Lecture Notes

Introduction to Plasma Physics II: Low-Temperature Plasmas

Winter Semester 2022/23

Ruhr University Bochum

A. von Keudell
V. Schulz-von der Gathen

September 9, 2026

Preface

These notes have evolved from the lecture 'Introduction to Plasma Physics II: Low-Temperature Plasmas' in the winter semester 2010/11 and subsequent semesters. The main sources used were the books by Liebermann and Lichtenberg (*Principles of Plasma Discharges and Materials Processing*), Reece Roth (*Plasma Processing*), Y. Raizer (*Gas Discharge Physics* and *RF Plasmas*), A. Fridman (*Plasma Physics and Engineering, Plasma Chemistry*), K. Wiesemann (*Gas Electronics*), A. Piel (*Plasma Physics*). Additionally, material was gathered from publications, which are cited as footnotes. These notes are not intended to replace these books and sources but are meant to supplement them. I would like to thank Tim Baloniak for proofreading.
Achim von Keudell, 2011

The version presented here includes modifications and corrections from the winter semester 2020/21, as well as a question catalog as an appendix. Furthermore, a chapter on plasma chemistry has been added with material from Jan Benedikt. I would like to thank Mr. Maik Budde for careful proofreading.
V. Schulz-von der Gathen, 2020

In the winter semester 2022/23, animations/visualizations of the different plasma phenomena were added, which are embedded in the script as links to YouTube (otherwise directly under https://www.youtube.com/@AchimvonKeudell). The underlying Python code is available at https://github.com/AchimVonKeudell/PhysicsVisualisations.

A. von Keudell, 2023

In 2026, an English translation is being generated. Thanks are also due to Julian Held, who contributed a chapter on plasma jets and plasma in liquids.

A. von Keudell, 2026

Contents

Chapter 1

Introduction

1.1 Definitions

Plasmas can generally be divided into **low-temperature plasmas** and **high-temperature plasmas**. High-temperature plasmas, in which ions and electrons reach very high temperatures, are fully ionized and are studied in fusion research. In contrast, low-temperature plasmas are often only partially ionized. The heavy particles such as ions and neutrals have, at low pressures, temperatures close to room temperature, whereas only the electrons possess high energies necessary for ionization and dissociation. At low pressures, there exists only a **local thermal equilibrium** among the electrons and the heavy particles themselves. Only at high pressures do the particle temperatures equalize, forming a **global thermal equilibrium**.
The specification of a temperature implies the existence of a **Maxwell distribution** of the particles, as shown in Fig. 1.1. The Maxwell distribution only develops in a system when collisions efficiently provide an equal distribution of energy. Deviations from this Maxwell distribution are especially observed at high electron energies, where either ionization or dissociation processes lead to a depletion of energetic electrons, or heating processes explicitly generate electrons with higher energy. In general, one can say that a Maxwell distribution rarely occurs in low-pressure plasmas, and that the concept of temperature is only used for a narrow energy window (e.g., Maxwell distribution with two excitation temperatures) or only for specific excitations (rotational temperatures, vibrational temperatures).
As mentioned initially, the local thermal equilibrium changes into a global one when the pressure is increased. Considering a plasma at constant power coupling per particle, it can be observed that as the pressure increases, the electron temperature decreases while the ion temperature increases; i.e., the

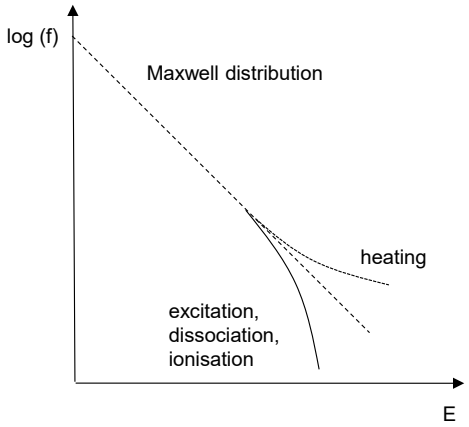

Figure 1.1: Distribution function of electrons in low-temperature plasmas.

temperatures equalize. At atmospheric pressure, a global thermal equilibrium is eventually reached. Increasing the pressure further leads to a slight temperature rise, as diffusion losses within the defined plasma volume become smaller. This is illustrated in Fig. 1.2.

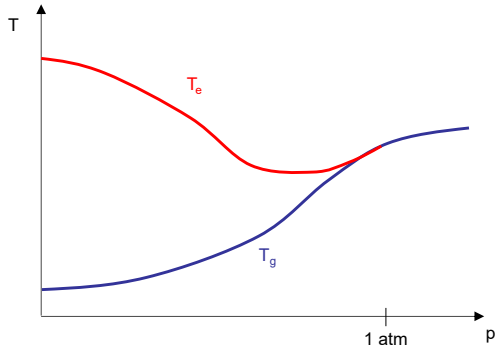

Figure 1.2: Dependence of the particle temperature on pressure in the discharge.

Low-temperature plasmas can exist in different forms that vary significantly in charge carrier densities, current-voltage characteristics, and temperatures. This can best be illustrated by the characteristic curve of a DC plasma, as shown in Fig. 1.3. When a current is set, the voltage applied to a gas gap behaves as follows:

- (Region 1 in Fig. 1.3, **Townsend discharge**) Charge carriers are

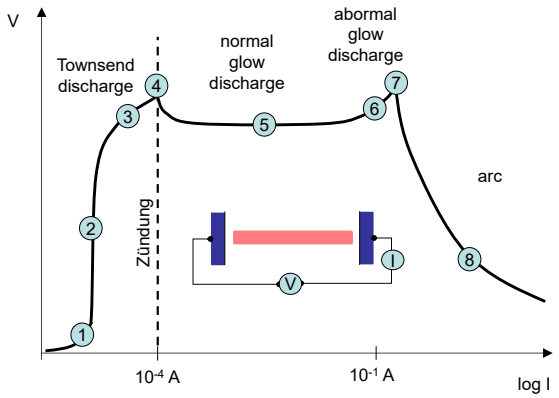

Figure 1.3: Characteristic curve of a DC discharge.

generated by an external source. With increasing voltage, all can be collected and the current rises.

- (Region 2 in Fig. 1.3, **Townsend discharge**) All charge carriers generated by the external source are collected, and a further increase in voltage does not change the current.

- (Region 3 in Fig. 1.3, **Townsend discharge**) The acceleration of charge carriers between collisions becomes so large that ionization can occur, forming an avalanche. The electrons multiply, and the current can increase further.

- (Point 4 in Fig. 1.3, **Breakdown**) From a certain point onward, secondary electron emission at the cathode increases so strongly that no external source is required to generate the first electrons of the avalanche. From this point, the discharge ignites and becomes a self-sustaining discharge.

- (Region 5 in Fig. 1.3, **Normal glow discharge**) A normal glow discharge burns between the electrodes where the voltage remains constant as the current varies. With increasing current, the plasma-filled region between the electrodes expands at constant current density.

- (Region 6 in Fig. 1.3, **Abnormal glow discharge**) From a certain point, the electrode is completely covered, and further current increase can only occur by raising the voltage. Since sheath voltage and current

scale as $j \propto V^{3/2}$, the voltage must increase to allow a larger current to flow. This is called an abnormal glow discharge.

- (Point 7 in Fig. 1.3, **Transition to arc**) At a certain point, the current becomes so large that macroscopic heating of the electrode occurs, and electrons are emitted thermionically. The transition to an arc takes place.

- (Region 8 in Fig. 1.3, **Arc**) The voltage decreases with increasing current because the plasma conductivity increases.

1.2 Methods of Power Coupling

Low-temperature plasmas have numerous applications where discharges at various pressures and geometries are used for light generation, coating, etching, or functionalization. Various methods exist for generating these plasmas, which differ significantly in their type of power coupling, as discussed below. Energy is coupled into a plasma by irradiating it with electric fields. In these fields, the electrons are accelerated:

$$E = E_0 e^{i\omega_{\mathrm{rf}} t} \tag{1.1}$$

The efficiency of power coupling can be evaluated according to three main criteria:

- *Confinement:*

  Confinement significantly affects coupling efficiency, as preventing losses or isolating the plasma from its surroundings allows for higher plasma densities and temperatures. Important parameters are pressure and any applied magnetic field: at higher pressures, collisions hinder particle transport to the plasma edges; with a magnetic field, particles are confined to their gyration orbits. Only collisions enable transport perpendicular to the magnetic field. For example, if a magnetic field is applied parallel to a surface, transport toward that surface is strongly suppressed.

- *Resonant heating:*

  Efficiency can be further increased when heating is resonant. The simplest form of resonant heating utilizes cyclotron motion. An electron follows a circular path with the **gyration radius** r_{L}:

$$\boxed{r_{\mathrm{L}} = \frac{m_{\mathrm{e}} v_{\perp}}{eB}} \tag{1.2}$$

with an angular frequency known as the **cyclotron frequency**:

$$\boxed{\omega_{\mathrm{c}} = \frac{eB}{m_{\mathrm{e}}}} \tag{1.3}$$

or

$$f_{\mathrm{c}} = 2.8B[\times 10^{-4}\mathrm{T}][\mathrm{MHz}] \tag{1.4}$$

For resonant heating to occur, the orbital motion given by r_{L} or the circumference $2\pi r_{\mathrm{L}}$ must be smaller than the mean free path λ_{m}:

$$\lambda_{\mathrm{m}} = \frac{1}{n_{\mathrm{g}} \sigma_{\mathrm{m}}} \tag{1.5}$$

with n_{g} the neutral gas density and σ_{m} the collision cross section. It is evident that at high pressures, the gyration radius must become very small, requiring very high magnetic fields. These high magnetic fields necessitate high frequencies of the alternating electric field to achieve resonance. Such conditions are economically challenging to realize. For low-pressure plasmas at pressures of a few pascals, magnetic fields of about 100 mT are required to achieve resonant heating at GHz frequencies. Both the magnetic fields and GHz radiation make this method technically demanding.

Resonant heating at lower magnetic fields or excitation frequencies can also be realized by macroscopic plasma oscillations, such as in **helicon plasmas**. However, these plasmas are very sensitive to the tuning of this resonance.

- *Heating volume:*

  The coupling into the vessel can also result in power being absorbed only in a small region of the volume, as the plasma, acting as a dielectric, may absorb the power too strongly, heating only the edge region.

  The penetration depth of an alternating electric field is typically on the order of the wavelength (see Fig. 1.4). For a given frequency, this yields:

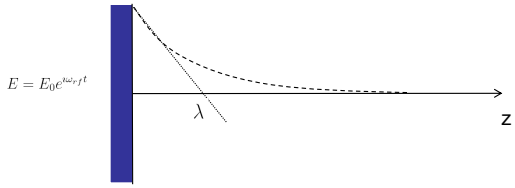

Figure 1.4: An electromagnetic wave penetrates a plasma approximately to the order of the wavelength.

$$\lambda_{\text{Vakuum}} = \frac{c}{f} \tag{1.6}$$

with c the speed of light and f the frequency ($2\pi f = \omega$). At MHz frequencies, this corresponds to a wavelength of about 300 meters, and at GHz frequencies, a wavelength of about 30 cm. However, one must consider that the wavelength in the plasma can be much smaller when the refractive index is taken into account:

$$\tilde{n} = \sqrt{1 - \frac{\omega_{\text{p}}^2}{\omega_{\text{rf}}^2}} \tag{1.7}$$

One can see that when the frequency ω_{rf} is much smaller than the plasma frequency ω_{p}, the refractive index becomes purely imaginary and the wave's penetration depth into the plasma becomes very small. In the general case, one must also consider the collision frequency in Eq. 1.7, which gives the refractive index a real part, further shortening the wavelength in the plasma. For MHz-driven discharges, this wavelength or penetration depth is typically several centimeters.

The plasma frequencies of electrons and ions are:

$$\boxed{\omega_{\text{pe}} = \sqrt{\frac{ne^2}{\epsilon_0 m_{\text{e}}}} \qquad \omega_{\text{pi}} = \sqrt{\frac{ne^2}{\epsilon_0 M}}} \tag{1.8}$$

or

$$f_{\text{pe}} = 9000\sqrt{n_{\text{e}}[\text{cm}^{-3}]}[\text{Hz}] \tag{1.9}$$

The possibilities of energy coupling and their efficiency can now be discussed for plasmas that are generated with different excitation frequencies of the electric field.

- *DC-...kHz-discharges* ($\omega_{rf} < \omega_{pi} < \omega_{pe}$)

  Discharges operated with direct current or with alternating voltages up to kHz behave similarly, as the excitation frequencies are lower than the plasma frequency of the ions and electrons. That is, both electrons and ions can follow the electric field. In these discharges, a DC current flows through the electrodes, which means that electrons must also be generated via secondary effects to maintain charge carrier conservation.

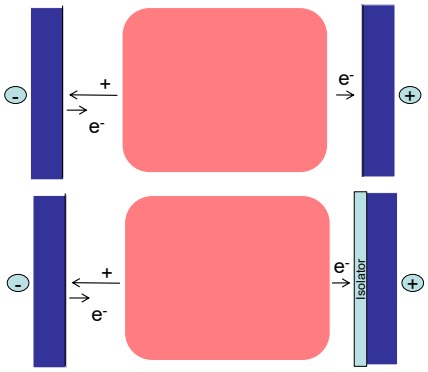

Figure 1.5: DC discharge with and without insulating electrode.

However, this current flow is simultaneously a limitation of the applicability of these plasmas, as charging occurs at insulating surfaces, leading to arcs (or arcing). This can only be avoided by temporarily changing the polarity of the discharge and thus compensating for the applied charge. At very high currents through the electrodes, thermal emission can also occur, resulting in an arc plasma.

Resonant heating is usually not possible at these frequencies, as the gyration radii become much larger than the mean free paths. However, additional magnetic fields can improve confinement and thus increase the efficiency of heating.

DC or kHz plasmas have a wide range of applications, as electrical power supply for very large technical plasmas can be provided cost-effectively in this way. The voltages are typically in the kV range.

- *MHz-discharges* ($\omega_{pi} < \omega_{rf} < \omega_{pe}$)

  In discharges operated in the MHz range, the excitation frequency is higher than the plasma frequency of the ions but lower than the plasma frequency of the electrons. That is, the ions can no longer follow the field oscillations in the first approximation. The wavelength of the radiation in the plasma is in the range of centimeters to meters, as the refractive index is very high.

  These plasmas are usually heated by the displacement current or by so-called stochastic heating, where electrons are heated in spatially varying electric fields that change periodically.

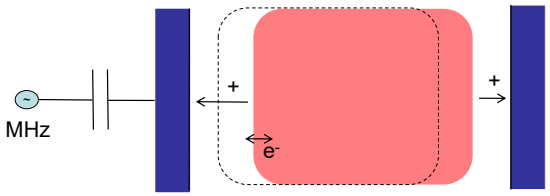

Figure 1.6: MHz discharge.

  Heating by displacement current also allows power to be coupled via insulating surfaces. Since the net current to the surface vanishes, charging effects are avoided. The voltages are in the range of several hundred volts to kilovolts. Resonant heating is usually not possible here either. Exceptions are collective excitations of the entire plasma, such as in helicon plasmas. These are, however, special cases.

- *GHz-discharges* ($\omega_{pi} < \omega_{rf} \approx \omega_{pe}$)

  As with the MHz discharges, ions can no longer follow the field. Since the plasma frequency for typical electron densities is also in the GHz range, the refractive index 1.7 is approximately 1. Partially, the electrons can also no longer follow the field, i.e., the plasma becomes transparent to the radiation.

  In the GHz discharge, heating occurs via the displacement current. However, stochastic heating is less efficient, as the absolute field strengths are smaller compared to the MHz discharge. Resonant heating is possible, as with a magnetic field of about 100 mT, the high-frequency field becomes synchronous with the cyclotron frequency.

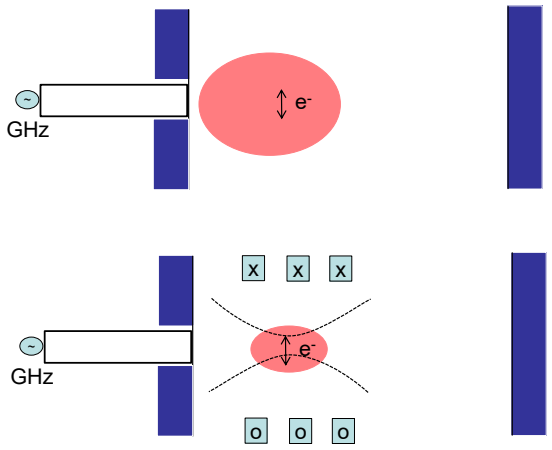

Figure 1.7: GHz discharge with and without magnetic field support.

A major difficulty with these plasmas is that the power is locally absorbed and a large plasma volume can hardly be filled with the GHz fields (see Fig. 1.7). The amplitude of the fields is in the range of below 100 V, and the wavelength is in the range of cm.

1.3 Overview of Discharge Types

1.3.1 High Pressure

The most prominent representatives of high-pressure plasmas are short-arc lamps, as used in projectors and spotlights. Between two electrodes, an arc plasma is ignited in a noble gas (see Fig. 1.8). In addition to the noble gas, a halide is always present in the lamp. This evaporates after ignition. Through collision processes with the halide atoms, the electrical resistance of the lamp increases and the efficiency of power conversion rises. This explains the typical warm-up behavior of these lamps, which reach their maximum light intensity only after a few seconds. Short-arc lamps are the most energy-efficient method for generating large amounts of light.

1.3.2 Atmospheric Pressure

At atmospheric pressure, the most common plasma applications are thermal plasma arcs, used for **plasma cutting** and **plasma welding**. Here, an

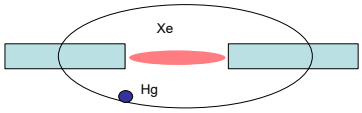

Figure 1.8: Principle of a short-arc lamp.

arc is ignited between two coaxial electrodes, and the flowing gas carries the flame onto the workpiece, which, depending on power, is either cut or welded (see Fig. 1.9). These thermal plasmas are highly prone to fluctuations and instabilities, which must be suppressed by gas vortexing or magnetic stabilization. Furthermore, the electrodes suffer from strong erosion at the arc root. This is also mitigated by moving the arc root on the electrode through electric forces.

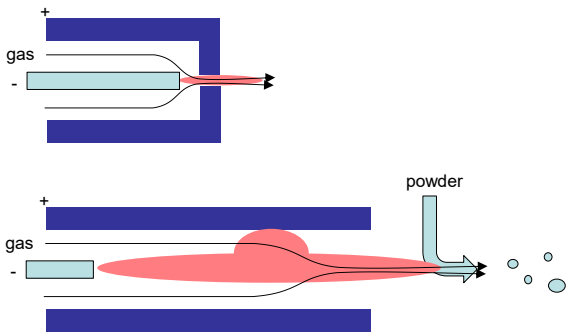

Figure 1.9: Arc plasmas for plasma welding, plasma cutting, and plasma spraying.

Thermal plasmas are also used for material processing. One field is **plasma spraying**, where a powder is injected into the arc (see Fig. 1.9). The material melts while traveling from the injection point to the surface within the arc and then rapidly solidifies on the workpiece. This process is, for example, used to create ceramic coatings on turbine blades.
Another application of material conversion is the thermal decomposition of waste, where the material passes through the arc or is destroyed in a crucible by the arc. This is particularly advantageous for highly hazardous substances that require high temperatures for decomposition (e.g., dioxins).
Finally, thermal arcs are also used for the synthesis of new substances, since

the arc can serve as a very homogeneous, high-temperature, short-time reactor. Many nonequilibrium reactions require a limited reaction time to initiate a reaction such as A → B, but to prevent further reaction B → C. Thermal plasmas are very well suited for this control.
A major area of application is **plasma switches** (see Fig. 1.10), which are used for switching large currents. In this application, a plasma must be prevented, since it causes strong erosion of the electrodes when the switch opens. For this purpose, the gas gap is filled with SF_6, which flows into the gap when the plasma switch opens and efficiently extinguishes the forming plasma, because fluorine, as a strongly electronegative gas, binds free electrons.

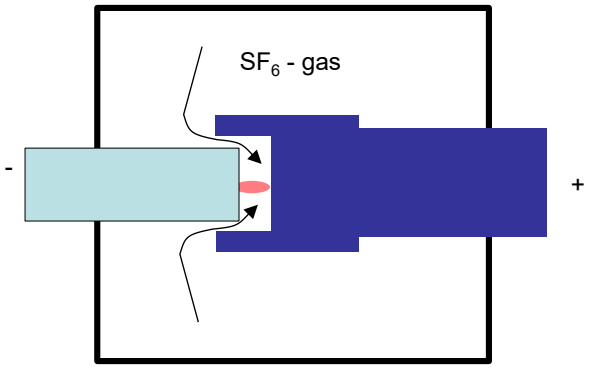

Figure 1.10: Plasma switch.

In addition to these hot arc plasmas, there are also cold atmospheric-pressure plasmas, where the formation of an arc is suppressed by removing the second electrode or by introducing a dielectric barrier that limits the current flow.
In the so-called **corona discharge**, a simple wire is placed at a high voltage (see Fig. 1.11). The surrounding electric field can ionize the air, forming a small discharge channel. In this channel, free electrons are generated, which, through electron-impact reactions in air, efficiently produce ozone. Corona discharges are used, for example, for flue gas dust removal in power plants. Dust particles are negatively charged in the corona discharge and then directed onto collectors by electric fields. This charge application also takes place in every photocopier and laser printer. On the drum, a charge layer is first applied by the corona discharge and then selectively discharged by a laser beam. At positions where the charge remains, toner particles are electrostatically accumulated and transferred to the paper.
A compact form of the corona discharge is the **barrier discharge** (see Fig.

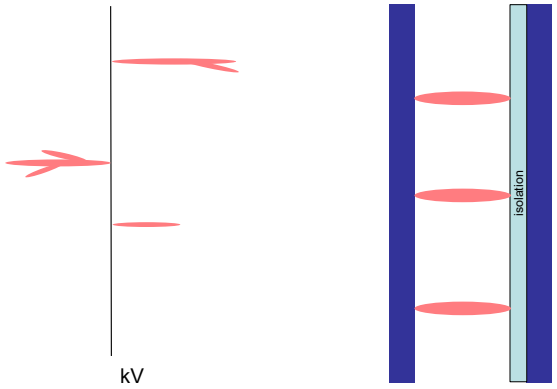

Figure 1.11: Corona and barrier discharge.

1.11). Here, a dielectric barrier is introduced between two electrodes to limit the current flow. This type of discharge can only be operated with alternating voltage, since the electrical charge of the barrier must be periodically neutralized. Such discharges are used for ozone generation for sterilization and water disinfection, as excimer lamps, and in plasma displays.
A newer type of atmospheric-pressure plasma is the **microplasma**, in which electrode spacing and gas flow are so small that plasma generation is primarily sustained by secondary electrons, while gas cooling is sufficient to prevent arc formation. In these microscopic plasmas, nonequilibrium reactions can dominate, similar to those long known from low-pressure plasmas.

1.3.3 Low Pressure

The simplest low-pressure discharge is the **DC discharge**, as used in fluorescent lamps. At low pressures, a gas is excited to emit light, and the emission is converted by suitable phosphors on the coating into the optimal spectral range.
Discharges operated in the kHz range are often used for the sputtering of a metal target to produce large-area inorganic layers such as oxides and nitrides on a substrate. By applying an additional magnetic field, the discharge is made more efficient. These are called **magnetron discharges**. In this process, a reactive component such as oxygen or nitrogen is added to the sputtering argon plasma. In the plasma, the gases are ionized, and the sputtered metal atoms, as well as the oxygen or nitrogen atoms, deposit on the workpiece to form the coating. Examples include magnetron discharges

used to coat architectural glass. The advantage of these discharges is that they can be scaled up to very large areas. In addition, their power supplies are technologically easy to implement.

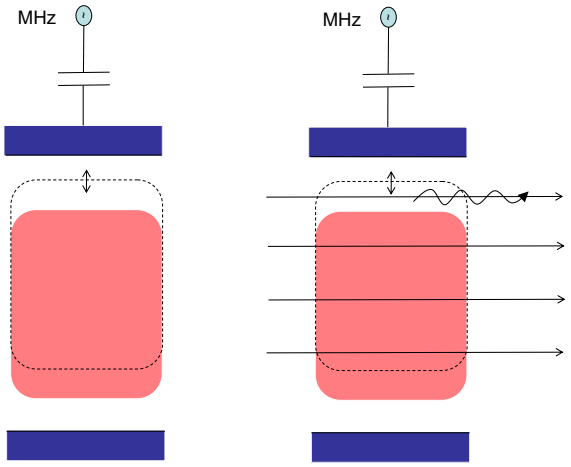

Figure 1.12: Capacitively coupled discharge.

Capacitively coupled MHz discharges (**CCP capacitively coupled plasma**) are used for plasma etching and plasma coating (Fig. 1.12). Confinement in these plasmas can be further enhanced by applying a superimposed magnetic field. These plasmas are among the most common types because they are highly versatile. Both conductive and insulating substrates can be treated. Using multiple frequencies, ion fluxes, and plasma density can also be controlled independently. However, capacitively coupled plasmas are not as easily scalable as kHz discharges. Especially for large areas on the order of meters, standing waves occur in these plasmas, leading to coating inhomogeneities. This remains an area of active research.
In inductively coupled systems, the plasma density is further increased, since here the plasma acts as the secondary winding of a transformer (see Fig. 1.13). This is called an **ICP inductively coupled plasma**. The coupling occurs via a dielectric electrode, which has the disadvantage that a metallic coating on this electrode can hinder the coupling. Scaling up this discharge is difficult because the secondary winding, the plasma, cannot be shaped arbitrarily. Therefore, these plasmas are often used as remote plasmas to generate an intense source of reactive particles. These then flow into a chamber and react with the substrate.
Finally, there are **microwave discharges** used to generate plasmas at high

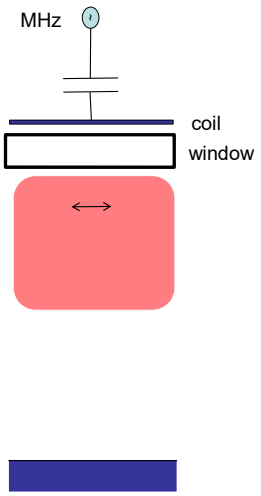

Figure 1.13: Inductively coupled discharge.

densities. The ion energies are comparatively low, so the surfaces of substrates are not strongly sputtered. Typical applications of microwave plasmas include the generation of oxygen or nitrogen atoms and the synthesis of polycrystalline diamond from methane-hydrogen mixtures.
Microwave plasmas can be transformed into **electron cyclotron resonance plasmas** (ECR electron cyclotron resonance) by applying a superimposed magnetic field. In a small resonance zone, a very intense plasma is generated. Both microwave and ECR plasmas are difficult to scale up, since power coupling is always spatially localized.

Chapter 2

Ignition

2.1 Excitation and Transport

The excitation and transport of electrons in a gas are decisive for the generation of a plasma, i.e., ignition. In an electric field, electrons absorb energy until ionization can take place, as illustrated in Fig. 2.11. This acceleration of the electrons depends on their collision rate with the background gas. The energy absorbed is partially lost again through elastic collisions, and the electrons become thermalized. A drift occurs. This acceleration of the electrons depends on their collision rate with the background gas. Some of the absorbed energy is lost through elastic collisions, and the electrons thermalize. A drift motion sets in. When electrons move in a high-frequency field, these collisions change the phase positions relative to the electric field. Only through this process is it possible to increase the energy of the electrons in an RF field. Furthermore, the collisions determine the confinement time of the charge carriers, since the ignition of a plasma always consists of a balance between the generation and loss of charge carriers.
Thus, the transport properties of electrons in a gas are very important for plasma ignition. In atmospheric pressure plasmas, for example, ignition in helium is significantly easier than in argon, even though the ionization threshold for helium is significantly higher at 24.8 eV than that for argon at 15 eV. However, the electrons do not lose as much energy in elastic collisions when accelerating in helium. This facilitates ignition. The key transport parameter is the mobility of the electrons in a gas, which links the drift velocity v_{drift} to the electric field E.

$$v_{drift} = \mu E \tag{2.1}$$

This drift velocity depends on the collision frequency and thus on the cross

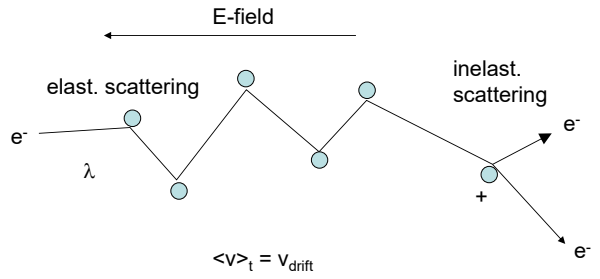

Figure 2.1: Movement of an electron in an electric field through a sequence of acceleration and elastic and inelastic collisions until the energy required for ionization is reached.

sections of the individual excitation processes, as explained below. These mobilities are measured in **Schwarmexperiments**. Here, the transit time of a swarm of electrons in an electric field is observed. This directly yields the mobility μ. There are several arrangements for this, as illustrated in Fig. 2.2.

- **(Fig. 2.2a) Pulsed arrangement:** Most methods are based on measuring the transit time of the electron swarm in a gas. In the simplest arrangement, a swarm of electrons is generated by a short flash of light in front of the cathode. These electrons travel through the gas to the anode, where a current pulse is measured after a time Δt. The drift velocity can be determined from this transit time and the distance traveled.

- **(Fig. 2.2b) DC arrangement with electric shutter:** It is also possible to measure the drift velocity of a uniform stream of electrons. This is based on the idea of a time-of-flight spectrometer in which two shutters interrupt the beam. If, at a certain frequency of this interruption, the period exactly matches the transit time between these two shutters, the electron swarm passes both shutters, and the drift velocity can be calculated again from the frequency or period and the distance traveled. It should be noted here that the shutter also becomes transparent at multiples of this frequency.

  These shutters are implemented by wires stretched in front of the cathode and anode. The cathode has a small filament electrode that emits electrons. An alternating voltage with a frequency f is applied to these

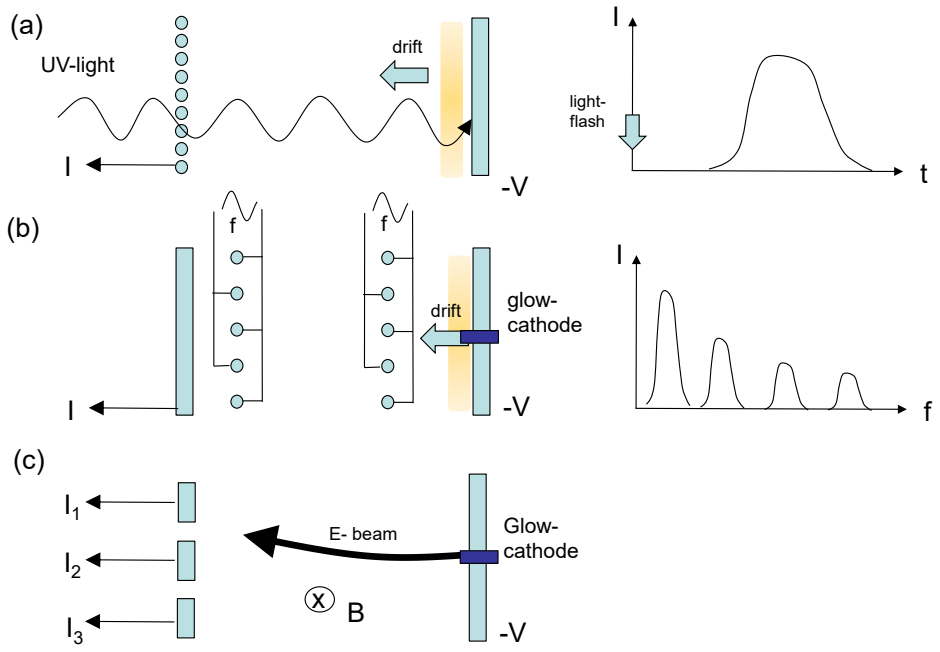

Figure 2.2: Swarm experiments: (a) pulsed arrangement, (b) DC arrangement with electrical locks, (c) deflection in a magnetic field.

wires, which generates an electric field perpendicular to the direction of flight of the electrons. This slows down the electrons and closes the shutter. However, when this AC voltage passes through zero, the shutter is open, and the electrons can pass through. At higher frequencies, the signal decreases because the opening time of the shutter becomes shorter and shorter.

- **(Fig. 2.2c) Deflection in a magnetic field:** Townsend's original experiment used the deflection of a swarm of electrons moving in the z-direction at a drift velocity v_z in a magnetic field according to $F_x = qv_zB$. This produces a deflection in the x-direction with a drift velocity $v_x = \mu F_x/q$. The deflection itself is measured by measuring the current on three electrodes.

Determining this mobility is a very integral measurement of the transport behavior of electrons, since a multitude of collision processes in equilibrium with the acceleration between collisions leads to this drift velocity.

2.1.1 Collision processes

Collision processes are generally described by a **cross section**, which can be measured and calculated in different ways. One starts with the **differential cross section** as the contribution to the scattering of an electron at an atom or molecule into a specific solid angle $\mathrm{d}\Omega$. This requires the kinematics of the collision and the interaction potential. From this differential cross section, the total cross section is finally determined as:

$$\sigma = \int \frac{\mathrm{d}\sigma}{\mathrm{d}\Omega}\mathrm{d}\Omega = 2\pi \int_0^\pi \frac{\mathrm{d}\sigma}{\mathrm{d}\Omega} \sin\Theta \mathrm{d}\Theta \tag{2.2}$$

To describe the transport, we set up an impulse balance equation for a flowing plasma. To do this, we need the cross section for the impulse loss. However, this is smaller than the total cross section, since the loss of impulse in a collision depends on the scattering angle Θ (see Fig. **??**):

$$\Delta p = p - p\cos\Theta = p(1 - \cos\Theta) \tag{2.3}$$

This means that the cross section for momentum loss σ_m becomes:

$$\sigma_\mathrm{m} = 2\pi \int_0^\pi \frac{\mathrm{d}\sigma}{\mathrm{d}\Omega}(1 - \cos\Theta) \sin\Theta \mathrm{d}\Theta \tag{2.4}$$

With this term, we can now calculate the **free path length $\boldsymbol{\lambda_\mathrm{m}}$**

$$\boxed{\lambda_\mathrm{m} = \frac{1}{n_\mathrm{g}\sigma_\mathrm{m}}} \tag{2.5}$$

or calculate the **collision frequency $\boldsymbol{\nu_\mathrm{m}}$**:

$$\boxed{\nu_\mathrm{m} = n_\mathrm{g}\langle v\sigma_\mathrm{m}\rangle} \tag{2.6}$$

We consider the following possible collision processes:

- *Ionization:*
  Ionization only occurs for energies greater than the ionization energy. Above this energy, the cross section increases sharply and, for most atoms and molecules, reaches its maximum at an electron energy of 70 eV.

- *Elastic scattering:*
  The elastic scattering of electrons among themselves can be described by normal Coulomb scattering. This process leads to the thermalization of the electrons. The collisions of electrons with ions can be described

using a shielded Coulomb potential, since the potential of the ion can be shielded by the surrounding electrons. When electrons collide with neutral particles, **polarization scattering (Langevin scattering)** occurs. The interaction potential decreases much more rapidly with the distance of the electron from the atom.

- *Inelastic scattering:*
  In inelastic scattering, part of the electron energy is used to generate internal excitation of the gas. The rotational and vibrational temperature increases.

- *Addition:*
  Electrons can also attach to atoms and molecules. Negative ions are formed. The cross section for this is very small. In addition, the electrons must have an energy close to the ionization energy.

- *Recombination:*
  If the electron collides with an ion, it can recombine. These reactions only occur at high pressure, since in two-particle recombination a third collision partner is always necessary to ensure conservation of momentum and energy. Furthermore, dissociative recombination can also occur, in which the neutral particle formed is first highly excited and then decays.

A typical course of cross sections is shown in Fig. 2.3 for the case of electron collision reactions of methane.

2.1.2 Transport in the fluid picture

The most common description of transport in a gas is the fluid picture, in which the totality of electrons is described by a density and a common mean velocity .
If a voltage is applied across a gas-filled space, charge carriers can be accelerated in it. The velocity of a single electron would continue to increase because it is an accelerated motion. However, the electron suffers collisions, so that a mean velocity is established, which is **drift velocity $\boldsymbol{v_\mathrm{d}}$**.

$$m\frac{\mathrm{d}^2 z}{\mathrm{d}t^2} = qE - m\frac{v_\mathrm{d}}{\tau} \stackrel{!}{=} 0 \tag{2.7}$$

with $\tau = \frac{1}{\nu_\mathrm{m}}$. It follows that:

$$\boxed{v_\mathrm{d} = \frac{qE}{m\nu_\mathrm{m}} = \mu E} \tag{2.8}$$

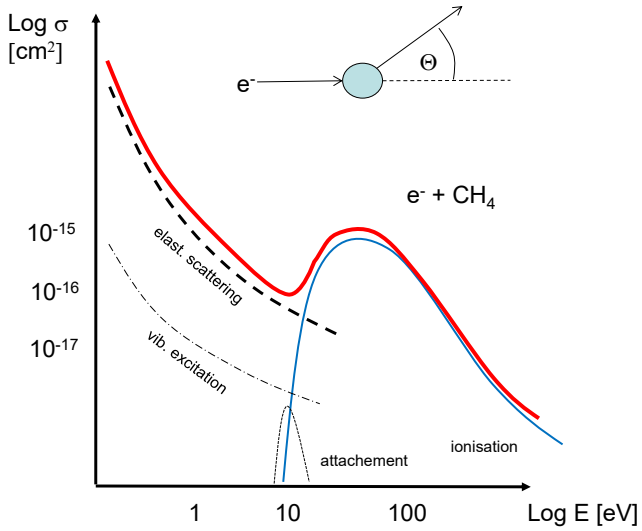

Figure 2.3: Principle course of a cross section for electron collision reactions using methane as an example.

with μ being the **mobility**. The current density that ultimately develops is:

$$j = nev_{\mathrm{d}} \tag{2.9}$$

2.1.3 Transport in the kinetic picture

The description of transport in the fluid picture assumes a Maxwellian distribution of the particles. This boundary condition does not always have to be given, since acceleration must explicitly lead to a deviation of the distribution function. The simplest description would be a Maxwell distribution that is shifted by the drift velocity in the direction of the electric field (see Fig.2.2). In general, the distribution function of the particles is found by solving the **Boltzmann equation**:

$$\boxed{\frac{\mathrm{d}f}{\mathrm{d}t} = \frac{\partial f}{\partial t} + \vec{v}\frac{\partial f}{\partial \vec{x}} + \frac{\vec{F}}{m}\frac{\partial f}{\partial \vec{v}} = \left.\frac{\partial f}{\partial t}\right|_{\text{collisions}}} \tag{2.10}$$

When deviating from equilibrium, the principle is to assume that the disturbance is small. In many cases, the system also has a preferred direction, e.g., due to the orientation of the electric field that accelerates the charge

carriers. This is taken into account in the so-called **2-term approximation**. The distribution function is divided into an isotropic component f_0 and an anisotropic component f_1 according to Fig.2.4:

$$f(\vec{v}) = f_0(|v|) + \frac{v_z}{v} f_1(|v|) \tag{2.11}$$

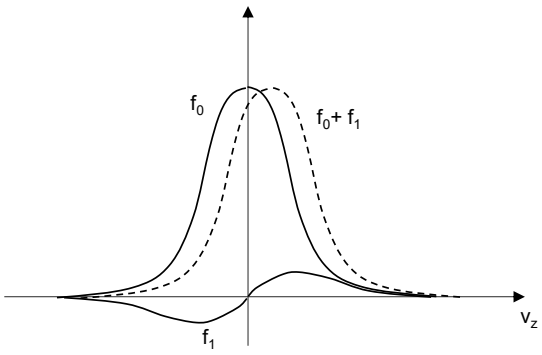

Figure 2.4: Division of a distribution function f into an isotropic component f_0 and an anisotropic component f_1.

i.e., the directional information is now contained in the prefactor of the anisotropic component, while the components of the distribution function f_0 and f_1 become functions of a scalar. With $\cos\Theta = \frac{v_z}{v}$, we can write:

$$f(\vec{v}) = f_0(|v|) + \cos\Theta f_1(|v|) \tag{2.12}$$

Depending on the angle Θ at which the distribution function is considered, a different form results. If we consider the distribution function for $\Theta = 0$, i.e., in the direction of the external electric field, we see the completely shifted distribution function $f_0 + f_1$. If we consider the distribution function for directions perpendicular to the electric field $\Theta = \pi/2$, we see no change and obtain only f_0. The impulse term on the right-hand side is determined by the impulse frequency for momentum transfer $\nu_m f_1$:

$$\boxed{\left.\frac{\partial f}{\partial t}\right|_{\text{Collision}} = -\nu_m f_1} \tag{2.13}$$

i.e., the anisotropic part of the distribution function decays due to collisions. In other words, by switching on the collisions, equilibrium is sought, and the distribution function f_0 is achieved.

Let us now consider the Boltzmann equation for electrons for a selected direction z in one dimension:

$$\frac{\partial f}{\partial t} + v_\mathrm{z}\frac{\partial f}{\partial z} - \frac{eE_\mathrm{z}}{m}\frac{\partial f}{\partial v_\mathrm{z}} = \left.\frac{\partial f}{\partial t}\right|_\mathrm{collisions} \tag{2.14}$$

The 2-term approximation can now be inserted into this equation; Eq. 2.14 becomes:

$$\frac{\partial f_0}{\partial t} + \cos\Theta\frac{\partial f_1}{\partial t} + ... \tag{2.15}$$

or

$$v_\mathrm{z} = v\cos\Theta \tag{2.16}$$

The equation is then multiplied by either $\sin\Theta$ or $\sin 2\Theta$ and integrated from 0 to π. This type of averaging over space separates the symmetric or antisymmetric part of the equation, and a balance equation for the part f_0 or f_1 of the distribution function is generated. After inserting the variable substitution from Eq. 2.15 and 2.16 into Eq. 2.14 and the corresponding integration over $\sin\Theta\mathrm{d}\Theta$, a balance equation for f_0 is obtained:

$$\frac{\partial f_0}{\partial t} + \frac{1}{3}v\frac{\partial f_1}{\partial z} - \frac{e\vec{E}_\mathrm{z}}{m}\frac{1}{3v^2}\frac{\partial}{\partial v}v^2 f_1 = 0 \tag{2.17}$$

The right-hand side of this equation only becomes zero if the isotropic distribution function cannot change due to, for example, collisions with heavy particles. This only applies for a mass $M \to \infty$ of the heavy particles. As a second variant, equation 2.14 is multiplied by $\sin 2\Theta$ and integrated from 0 to π to obtain a rate equation for f_1:

$$\frac{\partial f_1}{\partial t} + v\frac{\partial f_0}{\partial z} - \frac{e\vec{E}_\mathrm{z}}{m}\frac{\partial f_0}{\partial v} = -\nu_\mathrm{m} f_1 \tag{2.18}$$

It can be seen that the anisotropic component f_1 is modified by three terms: (i) by a flow in local space according to $\frac{\partial f_0}{\partial z}$ in which particles from neighboring phase space elements flow into the phase space element of f_1; (ii) by acceleration or deceleration according to an electric field E_z; (iii) or the loss of anisotropy due to collision processes according to a collision frequency ν_m. In this kinetic picture, mobility can now be derived again as follows. First, we assume spatially constant conditions and stationary conditions. This gives us:

$$-\frac{e\vec{E}_\mathrm{z}}{m}\frac{\partial f_0}{\partial v} = -\nu_\mathrm{m} f_1 \tag{2.19}$$

and can determine f_1 from this. The current is given by:

$$j = en\langle v\rangle = e\int v f_1 d^3v = \frac{4\pi}{3}\int v f_1 v^2 dv \tag{2.20}$$

Here we insert f_1 and obtain:

$$j = e\frac{4\pi}{3}\int v^3 \frac{e\vec{E}_z}{m\nu_m}\frac{\partial f_0}{\partial v}dv \tag{2.21}$$

Thus, the mobility becomes

$$n\mu = \frac{4\pi}{3}\int v^3 \frac{e\vec{E}_z}{m\nu_m}\frac{\partial f_0}{\partial v}dv \tag{2.22}$$

The individual collision processes are hidden in the collision frequency ν_m. At this point, the connection between the kinetic picture and the fluid picture becomes apparent. Often, the distribution function in the kinetic picture is sought by solving the Boltzmann equation (Boltzmann solver) and the transport quantities such as mobility are calculated from this. The solution in the kinetic picture can often be used for the entire plasma volume, since the transport of energy by the electrons is much more efficient than that of the particles themselves. This results in spatial gradients in density and less so in the electron energy distribution function. The distribution of electron density in space is then calculated in the fluid picture (this would require too much numerical effort in the kinetic picture) . The fluid picture provides densities and electric fields, which in turn are used in the Boltzmann equation. This allows a consistent solution for the plasma to be found iteratively.

2.2 Ignition of a plasma at low pressure

Let us first consider the formation of a discharge at low pressure. Here, a distinction is first made between a **dependent** and an **independent** discharge. The dependent discharge at low pressure is called a Townsend discharge. In a dependent discharge, an external source is necessary to generate the primary electrons. In a self-sustaining discharge, the plasma burns even without the presence of external ionization sources. The transition from a dependent to a self-sustaining discharge is also referred to as **ignition**.

2.2.1 The Townsend discharge

2.2.1.1 External ionization sources

Fig. 2.3 first shows the simple case of a parallel plate arrangement in which a cathode and an anode are placed at a distance d from each other. As the voltage increases, we pass through a characteristic curve. Let us first consider regions I and II of this characteristic curve (see Fig. 2.6) and distinguish between a surface effect and a volume effect as the determining factor in the generation of primary electrons.

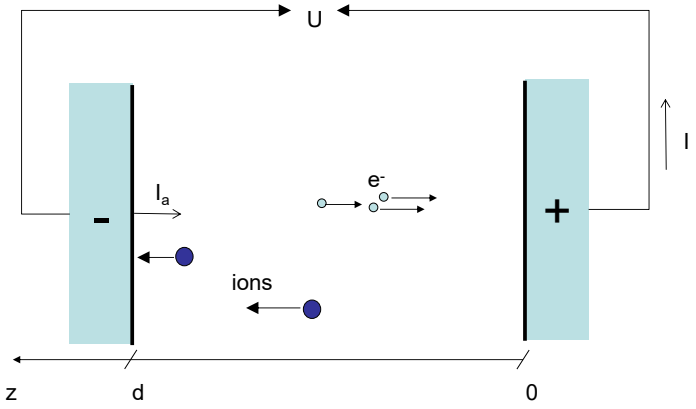

Figure 2.5: Townsend discharge - Movement of charge carriers in a gas gap.

- *Generation of primary electrons by photoelectric effect at the cathode*

  First, the electrons are generated by the photoelectric effect at the cathode. This results in a current of magnitude j_0 leaving the cathode. However, the total current j is slightly lower because some of

the electrons return to the electrode. According to the gas kinetics of an isotropically distributed electron gas of density n_e with a thermal velocity v_{th}, we obtain:

$$j = j_0 - \frac{1}{4} e n_e v_{th} \tag{2.23}$$

This current density must be equal to the current in the plasma volume, as it can be calculated from the electric field and the mobility:

$$j = e n_e v_d = e n_e \mu E \tag{2.24}$$

From this equation, we can determine the electron density n_e and obtain:

$$j = \frac{j_0 4 e \mu E}{4 e \mu E + v_{th}} \tag{2.25}$$

It can be seen that for small electric fields, the term v_{th} of the electrons dominates and the current increases linearly with the voltage. At higher voltages, the electrons have a greater chance of escaping loss to the surface due to their thermal motion and thus contributing to the current. In large electric fields, the thermal velocity is much smaller than the drift velocity, and the current is determined solely by the generation of primary electrons according to j_0.

- *Generation of primary electrons by ionization in the volume*

  In the second case, we consider the situation where volume ionization occurs at a frequency ν_0 and ions and electrons are produced simultaneously. As a balance of ion production, we obtain:

$$\frac{\mathrm{d}n_+}{\mathrm{d}t} = n_g \nu_0 - \frac{n_+}{\tau_{diff.}} - k n_+ n_e - \frac{n_+ v_d}{\frac{d}{2}} \tag{2.26}$$

  Here, we take into account that the charge carriers can also disappear radially from the space between the electrodes through diffusion (see Fig. 2.4), which we characterize with a diffusion time constant $\tau_{diff.}$. In addition, the charge carriers disappear through recombination with a rate constant k, or through drift to the electrodes. The drift time constant^{-1} is given as $v_d/d/2$. In the case where we can neglect recombination, we obtain the equilibrium density n as:

$$n = \frac{n_g \nu_0 d \tau_{\text{diff.}}}{2 v_d \tau_{\text{diff.}} + d} \tag{2.27}$$

The total current is given by the ion current plus the electron current, where the mobility of the electrons dominates. We obtain:

$$j = j_+ + j_e = 2ne\mu E = \frac{2e\mu n_g \nu_0 d \tau_{\text{diff.}} E}{2 v_d \tau_{\text{diff.}} + d} \tag{2.28}$$

For small diffusion lengths compared to d, the current increases with voltage, since the charge carriers are now more likely to reach the electrode before they are lost through diffusion. If the field is large, all charge carriers are effectively collected, and the current then depends only on the primary ionization rate ν_0.

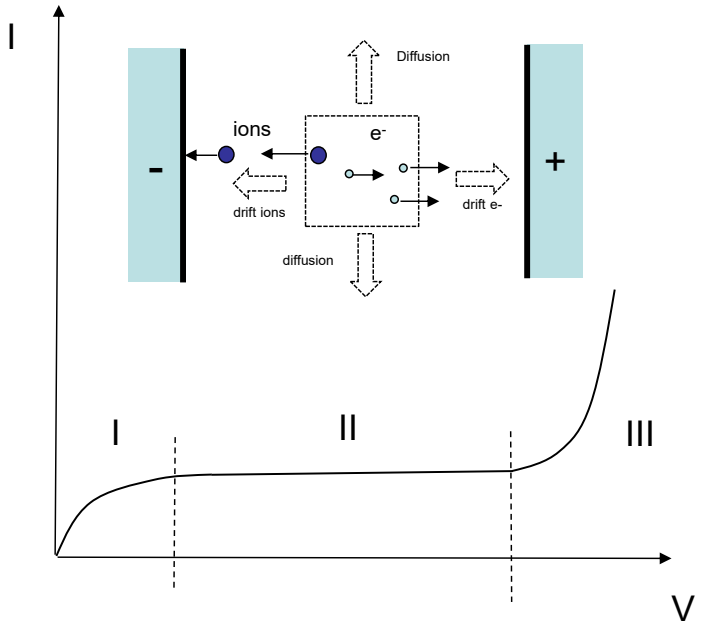

Figure 2.6: Current-voltage characteristic curve of a Townsend discharge.

Area II of the characteristic curve is typical for the operating mode of a counting tube as used for measuring radioactive radiation. Due to the fact that, at a given voltage, all charge carriers are collected at the electrodes,

the signal is proportional to the primary ionization flux, i.e., the external radiation from the radioactive source.

2.2.1.2 Current amplification

At sufficiently high voltages, ionization can be amplified by an electron avalanche, as shown in region III in Fig. 2.6. The increase in charge carrier current over a distance dz at an amplification factor α is:

$$\mathrm{d}n_\mathrm{e} = \alpha n_\mathrm{e}(z)\mathrm{d}z \tag{2.29}$$

α is the so-called first Townsend coefficient given as ionizations per length. If we perform the integration according to our drawing in Fig. 2.5, we obtain $n_\mathrm{e}(d) = n_0$ as the electron density in front of the cathode:

$$n_\mathrm{e}(z) = n_0 e^{\alpha(d-z)} \tag{2.30}$$

The current now depends on the location, since the charge carrier density changes spatially. We consider the change in the *external* current dI:

$$dI = \frac{dQ}{dt} = dQ\frac{v_{drift,e}}{d} \tag{2.31}$$

The drift velocity of the electrons and the electrode distance d determine the time interval dt in which the external current changes. In the microscopic picture, $dt = \frac{v_{drift,e}}{\lambda}$ with λ being the mean free path. However, the external current is sought, which is why the electrode spacing d is used in Eq. 2.31 (the gas-filled gap can also be regarded as a "black box" through which the current must be transported). Expression 2.31 takes into account that the amount of charge within the gas gap is not constant. Due to the current amplification, the total external current is obtained by integrating from 0 to d. To do this, $dQ(z)$ is first converted into a change in current $dI(z)$ in the depth interval dz. This gives us:

$$\mathrm{d}I = \mathrm{d}\left(\frac{Q}{t}\right) = \mathrm{d}\left(\frac{v_\mathrm{d,e}}{d}Q(z)\right) = \frac{v_\mathrm{d,e}}{d}en_\mathrm{e}(z)A\mathrm{d}z \tag{2.32}$$

where $v_\mathrm{d,e}$ is the drift velocity of the electrons. The electron density in front of the cathode can also be expressed by the start-up current I_a, which is the current leaving the cathode. From

$$I_\mathrm{a} = en_0 A v_\mathrm{d,e} \tag{2.33}$$

we finally obtain:

$$\boxed{n_\mathrm{e}(z) = \frac{I_\mathrm{a}}{eAv_\mathrm{d,e}} e^{\alpha(d-z)}} \tag{2.34}$$

With these definitions, we can now calculate the electron current as it falls on the anode by integrating along the electron movement:

$$I_\mathrm{e} = \int_{z=0}^{z=d} \mathrm{d}I_\mathrm{e} = \int_{z=0}^{z=d} \frac{I_\mathrm{a}}{d} e^{\alpha(d-z)} \mathrm{d}z = \frac{I_\mathrm{a}}{\alpha d} \left(e^{\alpha d} - 1\right) \tag{2.35}$$

However, the ion current also contributes to the current. For the movement of the ions, we use the continuity equation:

$$\frac{\mathrm{d}n_+}{\mathrm{d}t} + \nabla j = 0 \tag{2.36}$$

Ions are formed by electron collisions. Therefore, the change in ion density, electron density, and their drift velocity are relevant:

$$\mathrm{d}n_+ = \alpha n_\mathrm{e} \mathrm{d}z \tag{2.37}$$

$$\frac{\mathrm{d}n_+}{\mathrm{d}t} = \alpha n_\mathrm{e} \frac{\mathrm{d}z}{\mathrm{d}t} = -\alpha n_\mathrm{e} v_\mathrm{d,e} \tag{2.38}$$

The flux is expressed in terms of the drift of the ions:

$$\nabla j = \frac{\mathrm{d}}{\mathrm{d}z} n v_\mathrm{ions} = v_\mathrm{d,+} \frac{\mathrm{d}n_+}{\mathrm{d}z} \tag{2.39}$$

If we substitute the two expressions 2.38 and 2.39 into the continuity equation, we obtain:

$$\alpha n_\mathrm{e} v_\mathrm{d,e} - v_\mathrm{d,+} \frac{\mathrm{d}n_+}{\mathrm{d}z} = 0 \tag{2.40}$$

or

$$\alpha \frac{I_\mathrm{a}}{eA} e^{\alpha(d-z)} - v_\mathrm{d,+} \frac{\mathrm{d}n_+}{\mathrm{d}z} = 0 \tag{2.41}$$

This gives us the local ion density:

$$\mathrm{d}n_+ = \alpha \frac{I_\mathrm{a}}{eAv_\mathrm{d,+}} e^{\alpha(d-z)} \mathrm{d}z \tag{2.42}$$

or by integration along the generated electron avalanche from location z to the anode at location 0:

$$n_+ = \int_{z'=0}^{z} \alpha \frac{I_\mathrm{a}}{eAv_{\mathrm{d},+}} e^{\alpha(d-z')} \mathrm{d}z' \tag{2.43}$$

This yields:

$$\boxed{n_+ = \frac{I_\mathrm{a}}{eAv_{\mathrm{d},+}} e^{\alpha d} \left(1 - e^{-\alpha z}\right)} \tag{2.44}$$

At this point, it should be noted that the functional course of the electron density and the ion density is different, as illustrated in Fig. 2.7. *For Townsend discharge, quasi-neutrality does not apply!* The charge carrier densities are too low for this.

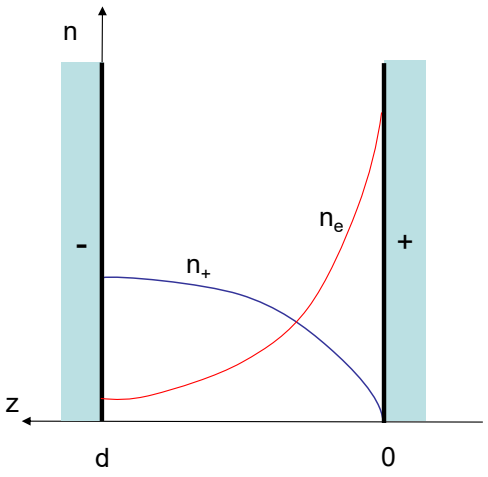

Figure 2.7: Spatial distribution of electron and ion density.

We obtain the total ion current by integrating along the current flow from the anode to the cathode:

$$\mathrm{d}I_+ = \frac{v_{\mathrm{d},+}}{d} e n_+ A \mathrm{d}z \tag{2.45}$$

$$I_+ = \int_{z=0}^{d} \frac{I_\mathrm{a}}{d} e^{\alpha d} \left(1 - e^{-\alpha z}\right) \mathrm{d}z = I_\mathrm{a} e^{\alpha d} + \frac{I_\mathrm{a}}{\alpha d} \left(1 - e^{\alpha d}\right) \tag{2.46}$$

Overall, the total current is given by:

$$\boxed{I = I_\mathrm{e} + I_+ = I_\mathrm{a} e^{\alpha d}} \tag{2.47}$$

Once again, we see a very simple relationship between the total current at the end and the starting current I_a. The factor $\exp(\alpha d)$ is referred to as the current amplification.

2.2.1.3 Secondary effects

Let us now consider the case where secondary effects influence the charge carrier balance. The simplest effect is the generation of γ_i secondary electrons per incident ion at the cathode. This means that the current of electrons at the cathode consists of two contributions: the externally applied start-up current I_a and the current of secondary electrons $\gamma_\mathrm{i} I_+$.

$$I_\mathrm{e}(d) = I_\mathrm{a} + \gamma_\mathrm{i} I_+(d) \tag{2.48}$$

The electron current as it starts at the cathode is:

$$I = I_\mathrm{e}(d) e^{\alpha d} \tag{2.49}$$

The ion current at the cathode is given as:

$$I_+(d) = e n_+(d) A v_{\mathrm{d},+} = e A v_{\mathrm{d},+} \frac{I_\mathrm{e}(d)}{e A v_{\mathrm{d},+}} e^{\alpha d} \left(1 - e^{-\alpha d}\right) \tag{2.50}$$

or

$$I_+(d) = I_\mathrm{e}(d) e^{\alpha d} \left(1 - e^{-\alpha d}\right) \tag{2.51}$$

We thus obtain the current of electrons as it starts at the cathode as:

$$I_e(d) = I_a + \gamma I_e(d) e^{\alpha d} \left(1 - e^{-\alpha d}\right) \tag{2.52}$$

or

$$I_\mathrm{e}(d) = \frac{I_\mathrm{a}}{1 - \gamma_\mathrm{i} \left(e^{\alpha d} - 1\right)} \tag{2.53}$$

The total current is then given as:

$$\boxed{I = \underbrace{I_\mathrm{a} e^{\alpha d}}_{\text{Primary amplification}} \quad \underbrace{\frac{1}{1 - \gamma_i \left(e^{\alpha d} - 1\right)}}_{\text{Secondary amplification}}} \tag{2.54}$$

The two factors are referred to as primary and secondary amplification of the current, which are expressed by the two **Townsend coefficients** α and γ.
However, several processes can contribute to the secondary amplification, as illustrated in Fig. 2.8:

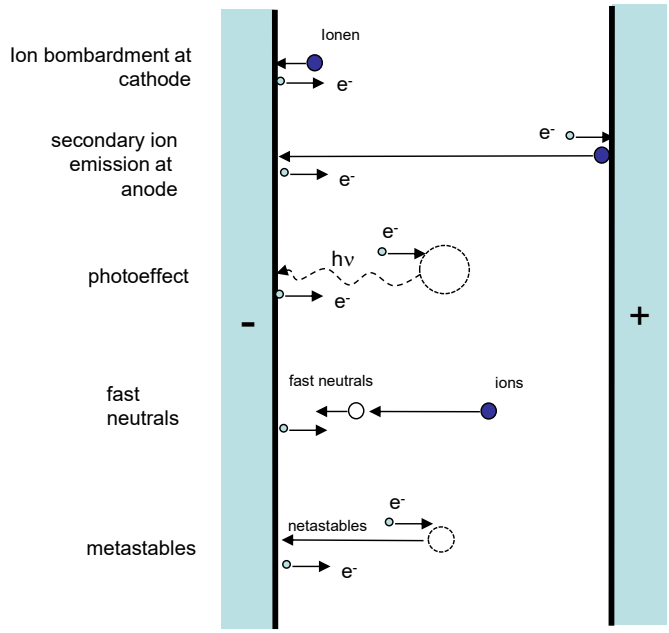

Figure 2.8: Possible secondary effects that contribute to γ in the Paschen curve.

- *Secondary electrons due to ion bombardment at the cathode*

  As just derived, secondary electrons can be generated by ion bombardment, which is expressed by the secondary electron coefficient due to ions:

$$\gamma = \gamma_{\text{ions}} \tag{2.55}$$

  The efficiency of secondary electron emission depends on the energy released when the ions strike the surface. At low energies (below keV), only the ionization energy is effectively converted into electronic excitation and thus into electron production via the Auger effect (see Plasma Interface Physics script). At high energies, the velocity of the incident ion becomes large enough that electronic excitations can also dominate due to the kinematic energy loss of the moving ion. A distinction is made between **potential emission** at low energies and **kinetic emission** at high energies. The triggered electrons have an energy dis-

tribution as illustrated in Fig. 2.9. The maximum is approximately at the work function of the material (eV). It is important to note that the energy of the triggered electrons does not depend on the energy of the ions. The energy of the ions alone determines the absolute quantity of secondary electrons. This is analogous to the theory of atomization.

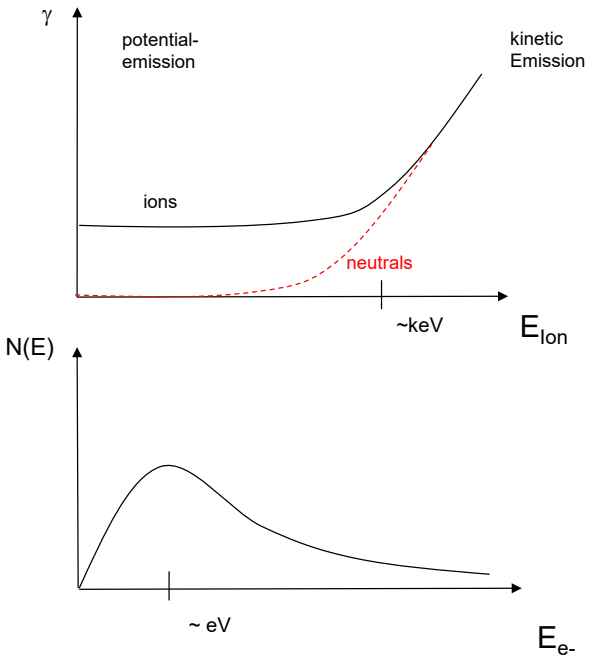

Figure 2.9: γ as a function of the energy of the incident ions (top) and energy distribution of the emitted electrons (bottom).

It is important to note that there is also a secondary electron coefficient for the incidence of electrons as primary particles. This can also influence the plasma, but the electrons usually strike the surfaces with very low energy. The secondary electron emission coefficient for incident electrons is often considered in electron accelerators.

- *Photoionization in volume*

  When electrons are accelerated in the gas space, the atoms and molecules are not only ionized but also excited. This excitation can be de-excited by photon emission, whereby these photons can trigger

further ionizations. The electron density is greatest at $z = 0$ in front of the anode. Thus, the number of photons per time becomes:

Finally, there is also the possibility that photons are created in the avalanche, which in turn trigger secondary electrons via the photoelectric effect with probability γ_{photons}. These photons depend on the electron density n_{e} and the rate of photon emission on an electrode g. In addition, only a fraction Θ of the excited atoms undergo de-excitation through radiation, and the photons are reabsorbed with an absorption length a^{-1}.

$$\Psi j_e(0) \tag{2.56}$$

where Ψ describes the efficiency of photon production. The photons are emitted to a fraction g in the direction of the cathode to generate a certain photon flux at location z. This flux is reduced by the reabsorption of photons in the volume. For this purpose, an absorption length a is used.

$$\Psi j_e(0) e^{-az} g \tag{2.57}$$

The photons in a location interval dz now ionize with a probability ξ

$$\xi a \Psi j_e(0) e^{-az} g dz \tag{2.58}$$

New ions and electrons are created. However, the contribution to the current is not only the electron-ion pair generated, but also the electron avalanche that moves from this location toward the anode. For this, we again use the amplification $e^{\alpha z}$. The contribution to the current due to photoionization in the depth interval dz is thus

$$dI = \xi a e^{\alpha z} \Psi j_e(0) e^{-az} g dz \tag{2.59}$$

Integrating this between 0 and d gives the proportion of current due to photoionization:

$$I_{by\ \ photons} = \frac{\xi a \Psi j_e(0) g}{\alpha - a} \left(e^{(\alpha - a)d} - 1 \right) \tag{2.60}$$

The total current through the discharge is given by.

$$I_{total,e} = ej_e(d)e^{\alpha d} + I_{total,e} \tag{2.61}$$

Eliminate $j_e(0)$ by replacing it with $j_e(d)$ and obtain $I_a = ej_e(d)$:

$$I = \frac{I_a e^{\alpha d}}{1 - \frac{\xi a \Psi g}{\alpha - a}\left(e^{(\alpha - a)z} - 1\right)} \tag{2.62}$$

This expression is similar to Eq. 2.54. From a comparison of coefficients, one can define an "apparent" γ_{photons} that depends on the gas parameters Ψ, ξ, a and g.

$$\gamma_{\text{photons}} = f(\xi, \Psi, a, g) \tag{2.63}$$

- *Secondary ions due to electron bombardment at the anode*

  One can additionally assume that the electrons at the anode release ions via electron-stimulated desorption. This has a probability of ω. The ions formed in this way reach the cathode, where they can in turn trigger secondary electrons. This corresponds to an apparent higher ion flux.

$$\gamma = \gamma_{\text{ions}}(1 + \omega) \tag{2.64}$$

- *Fast neutrals*

  Fast neutrals are created by charge transfer collisions of ions in the accelerating fields. A fast ion transfers its charge to a neutral particle and continues to fly as a fast neutral. With a coefficient γ_{n}, these then trigger secondary electrons. The conversion probability of an ion into a fast neutral particle is expressed by the probability b.

$$\gamma = \gamma_{\text{neutral}} b(1 + \omega) \tag{2.65}$$

Overall, all these processes can be expressed by an **effective coefficient** γ_{total}:

$$\gamma_{\text{total}} = \gamma_{\text{ions}}(1 + \omega) + \gamma_{\text{n}} b(1 + \omega) + \gamma_{\text{photons}}(\xi, \Phi, \xi, g) \tag{2.66}$$

The exact determination of which effects dominate the secondary electron yield can be evaluated experimentally by varying the electrode material, the gas type, and the geometry of the discharge. All these parameters have different effects on γ_{total}.

2.2.2 Ignition of a DC discharge

The ignition of an independent DC discharge can be characterized by the moment at which the secondary amplification becomes infinite. This results in the formation of a large number of charge carriers, and the initial assumptions of a vanishing space charge density are no longer justified. When the following condition is met, the discharge ignites:

$$\gamma \left(e^{\alpha d} - 1\right) \equiv 1 \tag{2.67}$$

A DC voltage discharge builds up, in which the current-voltage characteristic curve is determined by the current transport through the sheath at the cathode, as will be discussed further below.
For the coefficient α, we will now use a very simple heuristic model that expresses the electrons generated per path length:

$$\alpha = \underbrace{\sigma_\mathrm{m} n_\mathrm{g}}_{\lambda_\mathrm{m}^{-1}} \underbrace{\exp\left[-\frac{E_\mathrm{Ionisation}}{E_\mathrm{e}}\right]}_{\text{probability for ionisation}} \tag{2.68}$$

with the energy E_{e^-} that an electron can absorb between two collisions. This is calculated from the field strength $\vec{E}$ and the free path length λ_m as follows:

$$E_\mathrm{e} = \lambda_\mathrm{m} e\left|\vec{E}\right| = e\frac{V}{d}\frac{1}{\sigma_\mathrm{m} n_\mathrm{g}} \tag{2.69}$$

with $n_\mathrm{g} k_\mathrm{B} T = p$, we obtain:

$$\alpha = Ap\exp\left(-B\frac{p}{E}\right) = Ap\exp\left(-B\frac{pd}{V}\right) \tag{2.70}$$

for a given plate spacing d and voltage V with $E = V/d$. The parameters A and B are:

$$A = \frac{\sigma_\mathrm{m}}{k_\mathrm{B} T} \tag{2.71}$$

$$B = \frac{\sigma_\mathrm{m} E_\mathrm{Ionisation}}{e k_\mathrm{B} T} \tag{2.72}$$

Electron multiplication is therefore a function of the ratio of field strength to pressure or particle density. The value E/n is often given in the unit *Townsend* Td[$= 10^{-17}$ Vcm^2].
If we insert 2.70 into 2.67 and solve for V, we obtain:

	A / $cm^{-1}Torr^{-1}$	B / V $cm^{-1}Torr^{-1}$	$e\frac{B}{A}$ / eV
He	1.8	50	27.5
Ar	12	200	16.7
H_2	10.6	350	33
CO_2	20	466	23.3

Table 2.1: Parameters for the Townsend coefficient α.

$$\boxed{V = \frac{Bpd}{\ln(Apd) - \ln[\ln(1+\gamma^{-1})]}} \tag{2.73}$$

This equation yields the so-called **Paschen curve** (see Fig. 2.10). For large values of pd, the voltage at which ignition is possible increases linearly with Bpd. The factor B contains the ionization energy and therefore corresponds to a term that depends on the type of gas.

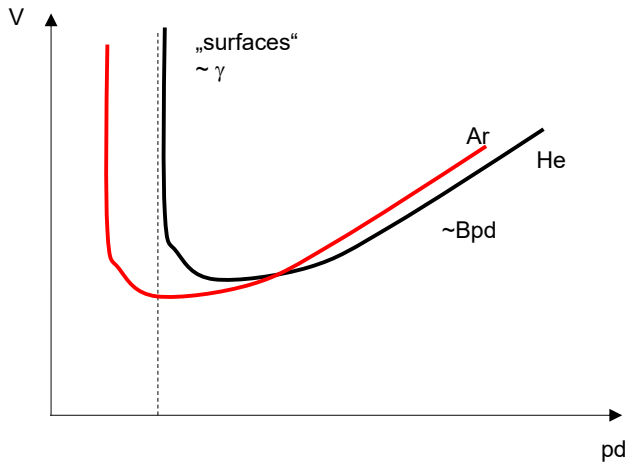

Figure 2.10: Paschen curve.

For small values of pd, a minimum value is obtained below which ignition is no longer possible. This limit is determined by the condition $Apd - \ln(1+\gamma^{-1}) = 0$. This includes the coefficient γ, i.e., this limit depends on the secondary coefficients, including the electrode material.
A list of parameters for calculating the Townsend coefficient α is shown in Table 2.1. From the definition of A and B, it can be seen that the ratio A/B is:

$$\frac{B}{A} = \frac{E_{\text{Ionisation}}}{ek_{\text{B}}T}\sigma_{\text{m}}\frac{k_{\text{B}}T}{\sigma_{\text{m}}} \approx \frac{E_{\text{Ionisation}}}{e} \tag{2.74}$$

As can be seen in the table, the values obtained are at least close to the true ionization energy of the gases mentioned.
When measuring ignition field strengths, in very special cases, some deviations can be observed, as illustrated in Fig. 2.11.

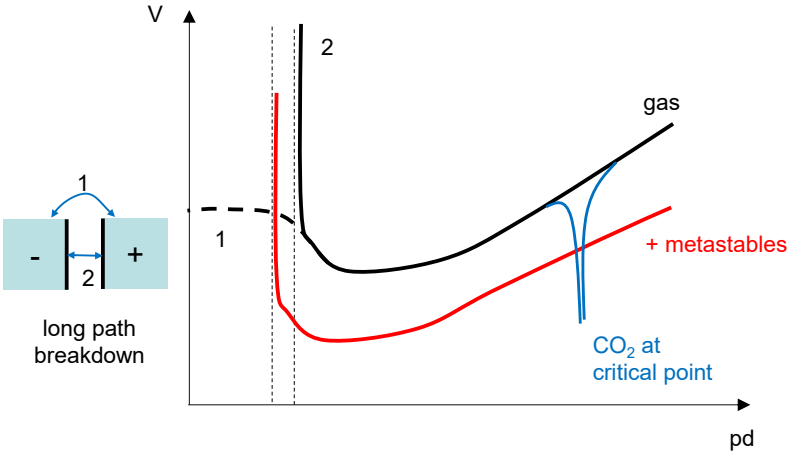

Figure 2.11: Deviations from the Paschen curve for selected examples.

- *Long Path Breakdown*

  When attempting to examine the Paschen curve at very high pressures and small distances, a kink in the Paschen curve was observed. This is caused by ignition via a longer path (path 1 in Fig. 2.8) instead of the direct path (path 2 in Fig. 2.8). To suppress this so-called *long path breakdown*, the discharge vessel must be radially enclosed.

- *Field emission*

  At very small distances, electron production can also occur via field emission. In this case, electrons can tunnel directly out of the solid state, as the strong electric field strongly bends the edge to the work function. However, the electrode distance should only be 5 μm.

  Furthermore, field emission can also occur at tips on the electrode. By applying carbon nanotubes as extremely sharp emitters, sources for electron beams can be produced.

- *Space charge effects*

  At high densities, such as at atmospheric pressure, the space charge density becomes so large that the electric field generated by the electrons in the avalanche is sufficient to continue ionization. In other words, the avalanche sustains itself. This mechanism is independent of the electrode material. This ignition mechanism is called a **streamer**.

- *Supercritical CO_2*

  At high pressure, CO_2 passes through the critical point at 73 bar and 304 K. At this critical point, there are strong fluctuations between the gaseous and liquid phases of CO_2. The temporary formation of bubbles creates regions in which the gas can ignite due to an externally applied voltage. This is visible in a reduced ignition voltage at the critical point.

Finally, let us discuss the temporal behavior of plasma ignition, as illustrated in Fig. 2.12. We distinguish between two time constants: the drift time of the ions to the cathode t_+ and the drift time of the electrons to the anode t_-. Most ions are formed in front of the anode. At this location, the electron density is at its maximum, n_0. This means that per drift time of the electrons t_-, we get:

$$\frac{\mathrm{d}n_+}{\mathrm{d}t} = \frac{n_0}{t_-}\left(e^{\alpha d} - 1\right) - \frac{n_+}{t_+} \tag{2.75}$$

The loss of ions is expressed by the drift time of the ions t_+. This change in the number of ions can be converted into a current $I_+ = \frac{\mathrm{d}n_+}{\mathrm{d}t}e$, and we obtain:

$$I_+ = \frac{en_0}{t_-}\left(e^{\alpha d} - 1\right)\left(1 - e^{-\frac{t}{t_+}}\right) \tag{2.76}$$

It can be seen that the current rise occurs over a characteristic time t_+, which is the time the ions need to reach the cathode. These times are typically in the range of μs. This is in contrast to ignition at high pressures. Here, the electron avalanche becomes so large and self-sustaining that it can bridge the entire discharge path and thus carry the current. In this case, the time constant is the drift time of the electrons. Due to their low mass, this is much shorter, and we obtain time constants in the range of ns.

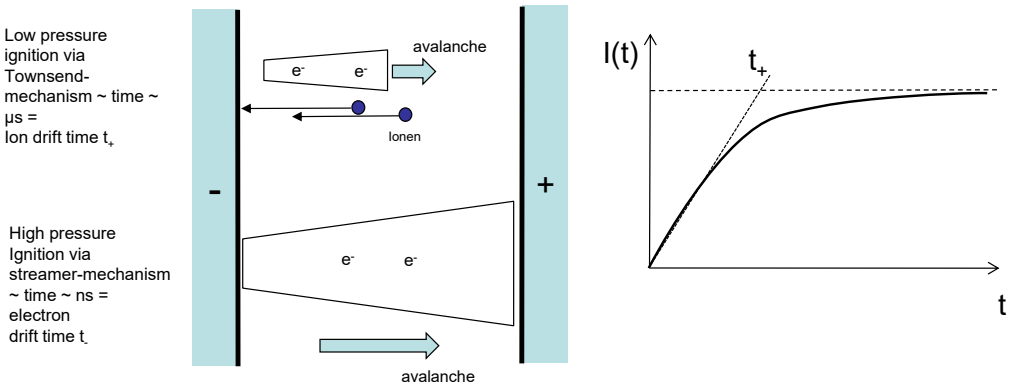

Figure 2.12: Time course of the current increase in a Townsend and a streamer discharge.

2.2.3 Ignition of an RF discharge

The ignition of a gas in an alternating electric field occurs in principle according to different mechanisms, since the stable operation of the discharge no longer has to be ensured by a DC current flow, but rather the displacement current alone maintains the discharge. To calculate the conditions for ignition, it is therefore necessary to establish an energy balance between the energy gain in the electric field and the energy loss in the collisions of the electrons with the neutral gas.

2.2.3.1 Average energy of an electron in the RF field

Let us first consider the simple case of the acceleration of an electron in an electric field:

$$E = E_0 e^{\imath\omega t} \tag{2.77}$$

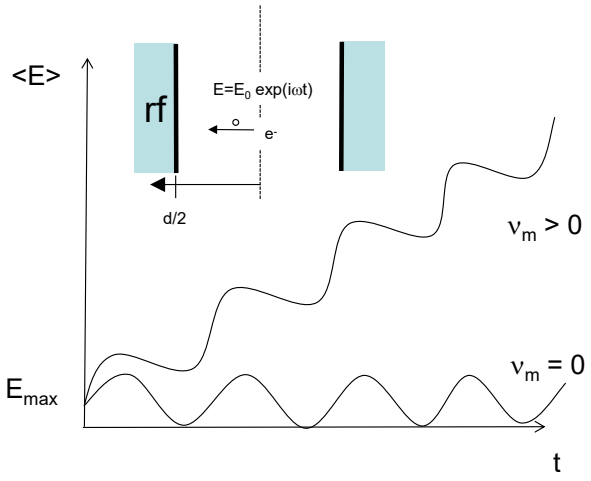

Figure 2.13: Average energy of an electron in an electric alternating field over time.

with the corresponding equation of motion:

$$m\frac{\mathrm{d}^2 z}{\mathrm{d}t^2} = qE_0 e^{\imath\omega t} \tag{2.78}$$

This is solved, and we obtain the following for position and velocity:

$$z(t) = -\frac{qE_0}{m\omega^2} e^{\imath\omega t} \tag{2.79}$$

$$v(t) = \imath\frac{qE_0}{m\omega} e^{\imath\omega t} \tag{2.80}$$

The electron oscillates around its rest position with a maximum velocity when passing through the rest position of:

$$v_{\max} = \frac{qE_0}{m\omega} \tag{2.81}$$

It can be seen that the velocity decreases as the frequency of the electric field increases. The maximum energy is:

$$E_{\max} = \frac{1}{2} m v_{\max}^2 = \frac{1}{2}\frac{q^2 E_0^2}{m\omega^2} \tag{2.82}$$

However, this energy is very small. If typical numbers are used, energies in the range of less than one eV are obtained. This energy is much lower than the ionization energy of the gases, and ignition could not take place. This can only be resolved if one takes into account that the electrons suffer collisions and thus run out of phase with the electric field, thereby increasing their average energy. Let us consider the equation of motion again, but this time taking damping into account:

$$m\frac{\mathrm{d}^2 z}{\mathrm{d}t^2} + \nu_{\mathrm{m}} m\frac{\mathrm{d}z}{\mathrm{d}t} = qE_0 e^{\imath\omega t} \tag{2.83}$$

For the velocity, this is solved by:

$$v(t) = \frac{eE_0(\nu_{\mathrm{m}} - \imath\omega)}{m(\omega^2 + \nu_{\mathrm{m}}^2)} e^{\imath\omega t} \tag{2.84}$$

From this, we can now determine the power, or the energy,that an electron absorbs from the electric field per unit of time. With $j = env$ and the power density $P = jE$, we get:

$$P = ne\frac{eE_0(\nu_{\mathrm{m}} - \imath\omega)}{m(\omega^2 + \nu_{\mathrm{m}}^2)} e^{\imath\omega t} E_0 e^{\imath\omega t} \tag{2.85}$$

This power is not purely imaginary, but also contains a proportion of active power, so that the time average is not zero. From $\Re\, P$, we obtain:

$$\langle P \rangle_{\mathrm{t}} = \frac{ne^2\nu_{\mathrm{m}} E_0^2}{2m(\omega^2 + \nu_{\mathrm{m}}^2)} \tag{2.86}$$

This formula can also be applied to the DC case with $\omega = 0$:

$$\boxed{P = \frac{ne^2 E_0^2}{2m\nu_\mathrm{m}}} \tag{2.87}$$

This corresponds to the power dissipated by an ohmic current. Comparing these two powers, the influence of the alternating electric field can also be expressed by an **effective electric field**:

$$\boxed{E_\mathrm{eff}^2 = \frac{\nu_\mathrm{m}^2}{\nu_\mathrm{m}^2 + \omega^2} E_0^2} \tag{2.88}$$

The power $\langle P \rangle_\mathrm{t}$ is absorbed on average over time. This is balanced with the energy loss per time that the electrons suffer during elastic collisions with the neutral gas. To do this, we consider the energy loss during a collision of an electron with mass m_e and average energy $\langle E \rangle$ with a neutral gas atom of mass m_g. We obtain:

$$T = \langle E \rangle \frac{m_\mathrm{e} m_\mathrm{g}}{(m_\mathrm{e} + m_\mathrm{g})^2} \approx \langle E \rangle \frac{m_\mathrm{e}}{m_\mathrm{g}} \tag{2.89}$$

This energy is lost by n electrons according to the collision frequency ν_m per time. Overall, we can write the following balance equation for power consumption and output:

$$\boxed{\frac{ne^2\nu_\mathrm{m} E_0^2}{2m_\mathrm{e}(\omega^2 + \nu_\mathrm{m}^2)} = n\nu_\mathrm{Ion.} E_\mathrm{Ion.} + \frac{m_\mathrm{e}}{m_\mathrm{g}} n\nu_\mathrm{m} \langle E \rangle + n\langle E \rangle \frac{1}{\tau_\mathrm{diff.}}} \tag{2.90}$$

The energy loss on the right-hand side consists of ionization at a rate $\nu_\mathrm{Ion.}$, energy loss in elastic collisions according to ν_m, and particle loss via diffusion with a confinement time $\tau_\mathrm{diff.}$.
In the simplest case, we want to neglect ionization and diffusion, since elastic scattering dominates. This gives us the average energy $\langle E \rangle$ of an electron from Eq. 2.90:

$$\langle E \rangle = \frac{m_\mathrm{g} e^2 E_0^2}{2m_e^2(\omega^2 + \nu_m^2)} = E_\mathrm{max} \frac{m_g}{m_e} \frac{\omega^2}{\omega^2 + \nu_m^2} \tag{2.91}$$

We see that the average energy can be a multiple of E_max, corresponding to the ratio $\frac{m_\mathrm{g}}{m_\mathrm{e}} \gg 1$. This result is obvious, since with an infinitely large mass difference $m_\mathrm{g}/m_\mathrm{e}$ during collisions, the electrons never lose energy and only change their phase to the electric field, thus always increasing their energy. The temporal evolution of the energy of an electron with and without collisions is illustrated in Fig. 2.13.

Animation

RF Ignition
Simulation of the energy increase of an electron with and without consideration of collisions.

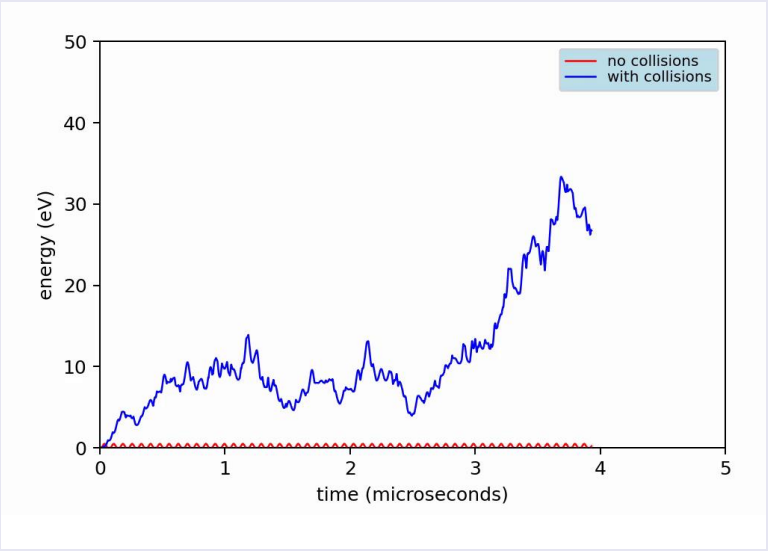

2.2.3.2 Diffusion-determined ignition

To evaluate the necessary ignition field strength E_0, it is now necessary to reconsider the balance equation 2.90. A simple ignition condition can be derived by balancing the charge carrier generation with the loss due to diffusion. To determine the density profile of electrons, To determine the density profile of electrons, we use the continuity equation:

$$\frac{\mathrm{d}n}{\mathrm{d}t} = n\nu_{\mathrm{Ion.}} + n_{\mathrm{g}}\nu_{\mathrm{extern}} + D_{\mathrm{e}}\frac{\partial^2 n}{\partial z^2} \tag{2.92}$$

At this point, we add ionization by an external source in order to be able to solve the density profile from the continuity equation alone. Without this term, all terms would be proportional to the electron density, which would cancel out, i.e., there would be no convergent solution. A convergent solution for this case can only be obtained by additionally solving a power balance equation for the discharge in order to determine its temperature. The continuity equation for a simple parallel plate arrangement yields a cosine-shaped density profile.

$$n(z) \propto \cos(z\sqrt{\frac{\nu_{\mathrm{Ion.}}}{D_{\mathrm{e}}}}) \tag{2.93}$$

From the boundary conditions, i.e., $n(\pm d/2) = 0$, we obtain a relationship between the geometry of the arrangement and the ratio of ionization and diffusion coefficients. This has the dimension of a characteristic length Λ^{-2}

$$\frac{\nu_{\text{Ion.}}}{D_{\text{e}}} = \left(\frac{\pi}{d}\right)^2 = \frac{1}{\Lambda^2} \tag{2.94}$$

This condition can be interpreted as the *ignition condition* of the plasma, since the solution precisely requires that

$$\boxed{\nu_{\text{Ion.}} = \frac{1}{\tau_{\text{diff.}}}} \tag{2.95}$$

must apply. However, both the ionization frequency and the confinement time are functions of the temperature of the plasma. This means that small changes in temperature lead, for example, to a higher ionization rate compared to the loss rate, and the electron density continues to increase. This would be the case for ignition and also explain why an energy balance is necessary for the independent determination of the temperature in order to determine the density profile of the discharge. We will now consider the two limiting cases of high and low pressure.

- $\nu_{\text{m}} \gg \omega$

  At high pressures, most particles reach a mean energy $\langle E \rangle$ equal to the ionization energy $E_{\text{Ion.}}$, because the loss to the walls is small. Elastic scattering dominates and we can neglect the first and third terms in Eq. 2.90. This means that we obtain the following for the ignition field strength E_0:

  $$E_0 = \left[\frac{m_{\text{e}}^2}{m_{\text{g}} e^2} E_{\text{Ion.}} (\nu_{\text{m}}^2 + \omega^2)\right]^{1/2} \tag{2.96}$$

  Since $\nu_{\text{m}} \gg \omega$, we see that because $\nu_m = n_{\text{g}} \langle v \sigma_{\text{m}} \rangle$, the ignition field strength increases linearly with the gas density or pressure. Furthermore, the ignition field strength is independent of the dimensions of the reactor.

- $\nu_{\text{m}} \ll \omega$

  If the pressure is low, we can neglect the elastic collisions. The balance equation 2.90 becomes:

  $$\frac{n e^2 \nu_{\text{m}} E_0^2}{2 m_{\text{e}} (\omega^2 + \nu_{\text{m}}^2)} = n \nu_{\text{Ion.}} E_{\text{Ion.}} + n \langle E \rangle \frac{1}{\tau_{\text{diff.}}} \tag{2.97}$$

The average energy of the particles becomes smaller than the ionization energy, since a significant portion of the particles is lost through diffusion before they can reach the ionization energy. If we use the ignition condition $\nu_{\text{Ion.}} = 1/\tau_{\text{diff.}}$ and $1/\tau_{\text{diff.}} = \frac{D_\text{e}}{\Lambda^2}$, we obtain the following for the ignition field strength:

$$E_0 = \left[\frac{D_\text{e} m_\text{e} \omega^2}{\Lambda^2 \nu_\text{m} e^2}(\langle E\rangle + E_{\text{Ion.}})\right]^{1/2} \tag{2.98}$$

Since $D_\text{e} \propto \nu_\text{m}^{-1}$, we see that the field strength scales with ν_m^{-1}, i.e., the ignition voltage increases again as the pressure decreases, as illustrated in Fig. 2.14. In addition, the ignition field strength depends on Λ and the geometry of the reactor.

At this point, it is important to note that this simple consideration neglects any secondary effects and the loss of charge carriers due to drift to the electrodes. Both contributions are particularly important at low pressures, so that measured ignition curves may deviate from the shape in Fig. 2.14 depending on the gas and the geometry of the setup.
The contribution of secondary electron emission (SEE) at the electrodes becomes important below a critical pressure, and the Paschen curve continues to decrease because there is now an additional production channel for the electrons. A "second minimum" is passed through. At low pressure, however, the point can be reached where the field strength becomes too high because the electrons are now lost again too quickly due to drift, so that ionization cannot take place again. Only when the voltage becomes very high can ionization take place again, even at low pressures. This characteristic curve can only be observed under special experimental conditions.
Normally, ignition curves are measured by increasing the voltage at constant pressure (path 1 in Fig. 2.14). The left branch of the RF Paschen curve for RF ignition in particular cannot be measured accurately in this way. To do this, it is necessary to first set the voltage at very low pressure and then increase the pressure (path 2 in Fig. 2.14).
This confinement can be further modified by superimposing a DC electric field. The effective confinement length Λ_eff is thus reduced according to:

$$\frac{\nu_{\text{Ion.}}}{D_\text{e}} = \frac{1}{\Lambda^2} + \frac{(2\mu E)}{dD_\text{e}} = \frac{1}{\Lambda_\text{eff}^2} \tag{2.99}$$

The quantity $\frac{(2\mu E)}{d}$ corresponds to the inverse of the drift confinement time. Furthermore, a superimposed magnetic field can greatly reduce the ignition

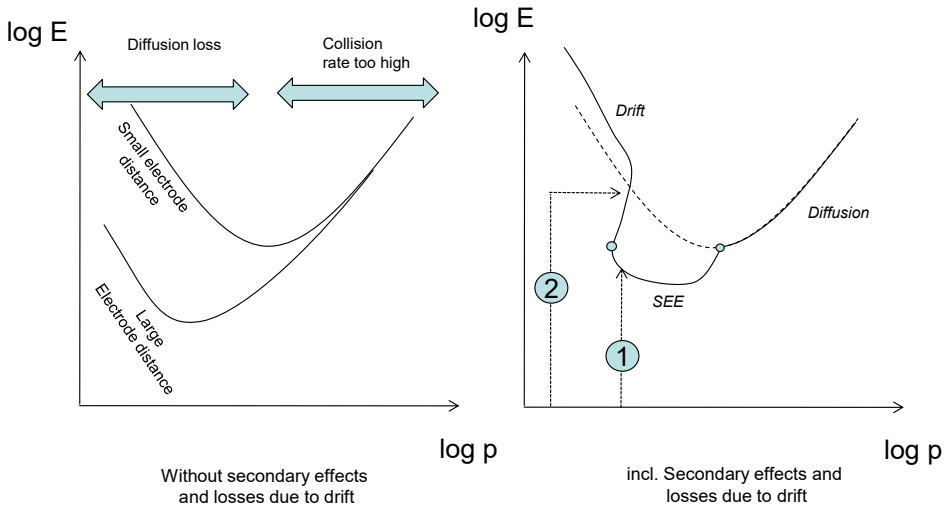

Figure 2.14: Ignition field strength in the alternating electric field as a function of pressure.

field strength at sufficiently low pressure, since the electrons can now be heated resonantly and the confinement can also be improved.
Finally, there is also the possibility of negative ion formation. This increases the ignition field strength because the loss of charge carriers becomes greater. Expressed by an attachment frequency ν_a, we obtain:

$$\frac{\nu_\mathrm{Ion.}}{D_\mathrm{e}} = \frac{1}{\Lambda^2} + \frac{\nu_\mathrm{a}}{D_\mathrm{e}} = \frac{1}{\Lambda_\mathrm{eff}^2} \tag{2.100}$$

2.2.3.3 Drift-determined ignition

As already mentioned, at low pressure and corresponding frequency, situations arise in which the amplitude of the oscillation reaches the order of magnitude of the distance between the electrodes. In this case, the loss of charge carriers becomes very large, and the ignition field strength increases accordingly. This transition is not gradual but occurs suddenly when the amplitude becomes too large at a certain frequency. This is illustrated in Fig. 2.15.

$$\frac{d}{2} = \frac{2e}{m\omega\nu_\mathrm{m}} E_0 \frac{\omega^2}{\nu_\mathrm{m}^2 + \omega^2} \tag{2.101}$$

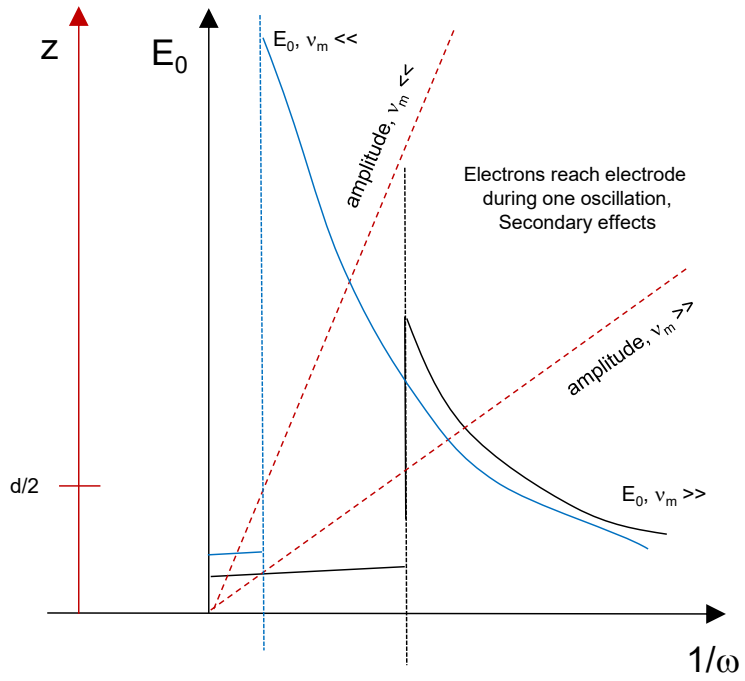

Figure 2.15: Ignition field strength in the alternating electric field as a function of frequency for different pressures and impact rates.

If we start at high frequencies, the ignition field strength changes only slightly. As the frequency decreases, the amplitude increases and the losses rise very slightly, as a small proportion of the electrons can reach the wall. This is visible in a very slight increase in the ignition field strength. If the amplitude of the oscillation reaches exactly the plate spacing, then the losses increase sharply, which must be compensated for by a strong increase in the ignition field strength. As the frequency is further reduced, the energy of the particles increases as they hit the electrode and the efficiency of the secondary electron emission increases. This means that a new mechanism effectively supplies electrons, which again leads to a reduction in the ignition field strength.
With the right frequency and plate spacing, these secondary effects can even build up, resulting in what is known as a **multipactor discharge**. These multipactor discharges are particularly parasitic discharges in evacuated waveguides for microwave supplies in large fusion plants.

2.3 Ignition at Higher Pressures

The previous description of ignition phenomena was always based on the fact that an externally applied field leads to an acceleration of the charge carriers until ionization occurs. The efficiency of this acceleration then depends on the reactor geometry, the frequency of the field, and the mean free path. However, it was always assumed that the charge carrier density is so small that the external fields are not influenced or shielded thereby. Exactly this assumption is no longer justified for ignition phenomena at higher pressures. Due to the high neutral gas density, so many electrons can be created in an avalanche that the local electric field in the vicinity of this avalanche becomes as large as the external field. That is, in the vicinity of this avalanche, ignition can be triggered by the avalanche itself. This effect is referred to as the **streamer mechanism**.

2.3.1 Streamer Mechanism

In the case of ignition at high pressures (or through the streamer mechanism), it is observed that the Paschen curve can no longer be used for description, since, for example, the influence of surfaces on the ignition voltage disappears. Moreover, the observed ignition field strengths are lower than expected: at one bar, the mean free path is approximately 1 μm. That is, to absorb energy of 10 eV to ionize, an electric field of the order of 10^7 V/m is required. In the experiment, however, only 10^6 V/m is observed. Finally, ignition also occurs much faster than at low pressure, since the time constant is determined by the drift of the electrons and no longer by the drift of the ions. That is, the streamer mechanism runs on the nanosecond time scale. A developed streamer can then even run through a gas path much faster than the drift velocity of the electrons, since ionization no longer occurs directly through electron impact but also through the electric field itself or through photoionization. These two processes naturally spread much faster compared to the drift velocity of the electrons. A photograph of a streamer discharge is shown in Fig. 2.16. It can be seen that at very short exposure times, the emission only comes from the head of the streamers. In this example, a bundle of streamer discharges is created, which branch out.
The influence of the electric field by a streamer is shown in Fig. 2.17. A streamer consists of a **streamer head**, the location with high charge carrier density, and a **streamer channel**, which extends along the direction of travel of the streamer. In the case of a negative streamer, the streamer head is negatively charged. At this point, the front of the electron avalanche has a correspondingly high electron density. This avalanche runs along the

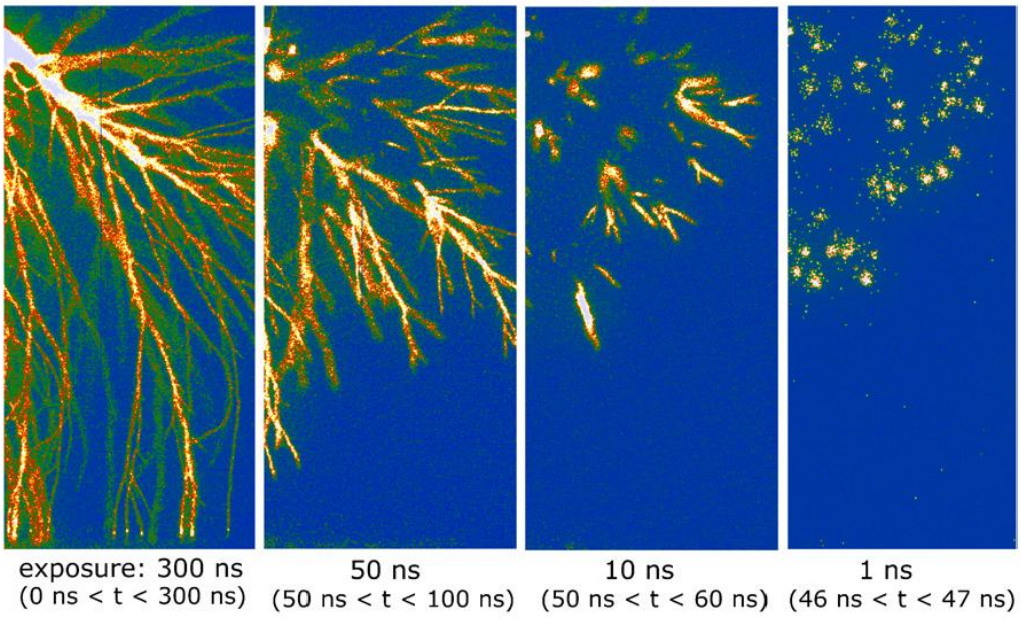

Figure 2.16: Photograph of a streamer discharge at different exposure times [16].

external electric field. However, the ionization itself is caused by the field strength of this large negative local charge. In the streamer channel, the positively charged ions remain, which cannot follow the rapid movement of the electron avalanche. If the electric field of the charge carriers in the streamer is superimposed with the external field, a field distribution as shown in Fig. 2.17 is obtained.
The field is particularly strong in the vicinity of the streamer head. The fields in the vicinity of the streamer channel are much weaker, but they cause electrons from the surroundings to be slowly collected in the streamer channel and a quasi-neutral channel to be built up. At the same time, a streamer widens as it progresses, since ionization at the streamer head can in principle occur in all directions. This leads to a decrease in the local electric field, and a free streamer can extinguish again after a certain running time.
In principle, a distinction is made between **negative** and **positive streamers**, as illustrated in Fig. 2.18:

- In the case of a negative streamer, an electron avalanche is created at the streamer head and the streamer moves in the direction of the anode, along the external electric field.

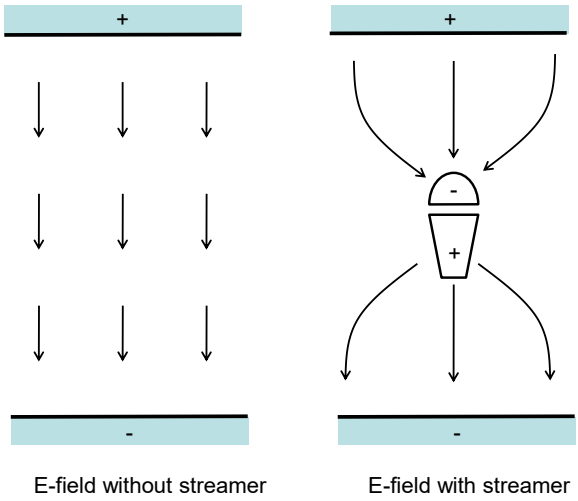

Figure 2.17: Electric fields in the vicinity of a streamer.

- In the case of a positive streamer, a large number of photons are also created in the electron avalanche, which in turn ionize the surroundings. In particular, also in the region in the direction of the cathode. An electron avalanche created there runs into the area of the channel and thus creates quasi-neutrality. However, a positive streamer head of the remaining ions remains, which moves towards the cathode via this mechanism. Unlike the negative streamer, we have a different direction of movement, and the direction of the positive streamers is also not as clear and straight as that of the negative streamer, since ionization always occurs through photons in all directions. Positive streamers can therefore only exist in gases that tend to efficient photoionization.

If there is a streamer discharge between two electrodes, this streamer can reach the surface and thus create a quasi-neutral plasma channel between the electrodes. This conductive channel causes a short circuit, and a large current flows at high pressure. This is then referred to as a **spark**.
A simple criterion for the occurrence of a streamer can be defined. For this purpose, we consider the electric field of the negative streamer head with a radius R in a gas gap with electrode spacing d. This is:

$$E_\mathrm{a} = \frac{e}{4\pi\epsilon_0 R^2} e\alpha d \tag{2.102}$$

The factor $e^{\alpha d} \gg 1$ denotes the primary amplification of the avalanche that prevails in the gas gap until the streamer head is formed. An independent

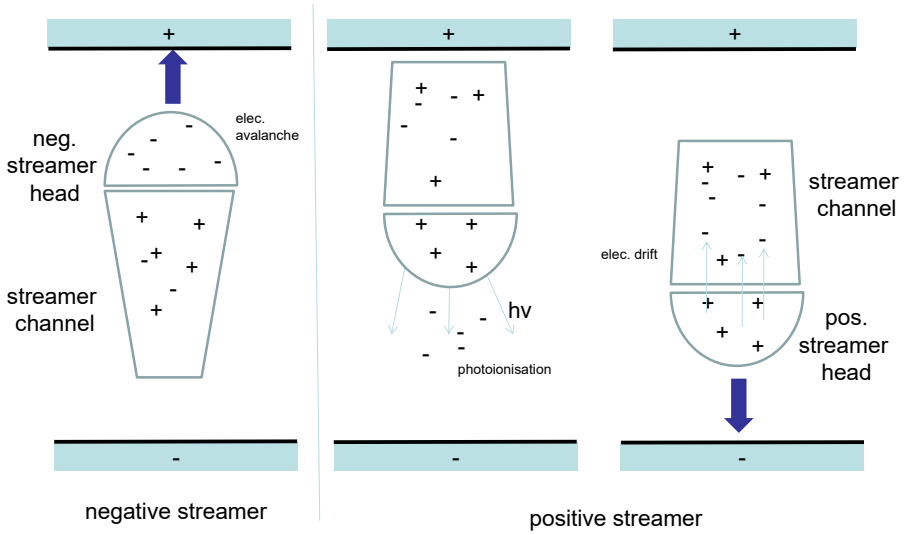

Figure 2.18: Negative and positive streamer.

streamer can be created if the electric field at the surface of the head becomes equal to the ignition field strength E_0 before the avalanche reaches the other electrode at a distance d. The expansion of the head corresponds approximately to the ionization length, i.e., $R = \frac{1}{\alpha}$. In this approximation, we obtain:

$$\alpha d = \ln \frac{4\pi\epsilon_0 E_0}{e\alpha^2} \approx 20 \tag{2.103}$$

Since E_0, according to Paschen's law, is a function of α, and the ignition field strength for a given gas is known, we can determine the term $\alpha d \simeq 20$ from this equation. From the primary amplification, this results in the minimum number of electrons in the streamer head $e^{20} \approx 10^8$ electrons. This is referred to as the **Meek criterion**. That is, given a field strength and thus a Townsend coefficient α, we need a distance d until the streamer is formed.

2.3.2 Streamer Model

In the following, we want to derive a very simple model[1] of the movement of a streamer, as illustrated in Fig. 2.19. The continuity equation for the electron density is:

[1] N. Babaeva and G. Naidis, *Modeling of streamer propagation*, in *Electrical Discharges for environmental purposes* ed. by E. Van Veldhuizen

$$\frac{\mathrm{d}n_\mathrm{e}}{\mathrm{d}t} + \nabla j = \nu_\mathrm{Ion} n_\mathrm{e} \tag{2.104}$$

We go into the reference system of the streamer moving with v and initially get a temporally constant electron density at the streamer head. That is, we have:

$$\nabla j = \nu_\mathrm{Ion} n_\mathrm{e} \tag{2.105}$$

The current in the reference system of the streamer is obtained if all velocities v are subtracted formally. Thus, from $\nabla j = \frac{\mathrm{d}}{\mathrm{d}z}(v_\mathrm{e} - v)n$. v_e denotes here the absolute drift velocity of the electrons. This can under certain circumstances be less than the velocity of the streamer itself, since a progression of the streamer head can also be carried by electric fields or photons.

$$\frac{\mathrm{d}}{\mathrm{d}z} n_\mathrm{e} \left(v_\mathrm{e} - v\right) = \nu_\mathrm{ion} n_\mathrm{e} \tag{2.106}$$

After the product rule, we solve the spatial derivative and obtain, under the assumption that v is spatially constant, as an equation for the electrons:

$$-v\frac{\mathrm{d}n_e}{\mathrm{d}z} + \frac{\mathrm{d}}{\mathrm{d}z}\left(n_\mathrm{e} v_\mathrm{e}\right) = \nu_\mathrm{Ion} n_\mathrm{e} \tag{2.107}$$

From a continuity equation for the ions, we get

$$-v\frac{\mathrm{d}n_+}{\mathrm{d}z} = \nu_\mathrm{ion} n_\mathrm{e} \tag{2.108}$$

At this point, we have used the fact that the movement of the ions with v_i is much slower than that of the electrons.
From these equations, it can now be derived by component comparison that:

$$n_\mathrm{e} v_\mathrm{e} = (n_+ - n_\mathrm{e})v \tag{2.109}$$

This means that by the movement of the streamer with v, which carries a net charge $n_+ - n_\mathrm{e}$, a current of the electrons $n_\mathrm{e} v_\mathrm{e}$ is induced, which moves absolutely with the drift velocity v_e. From this equation, it can also be read that $v \gg v_e$ is: the integral over the electron density alone is much larger than the integral over the net charge carrier density $n_+ - n_e$. Therefore, the equation can only be satisfied if, on the other hand, $v \gg v_e$ applies.
The ion density is obtained by additionally applying the Poisson equation:

$$\frac{\mathrm{d}E}{\mathrm{d}z} = \frac{e}{\epsilon_0}(n_+ - n_\mathrm{e}) \tag{2.110}$$

from:

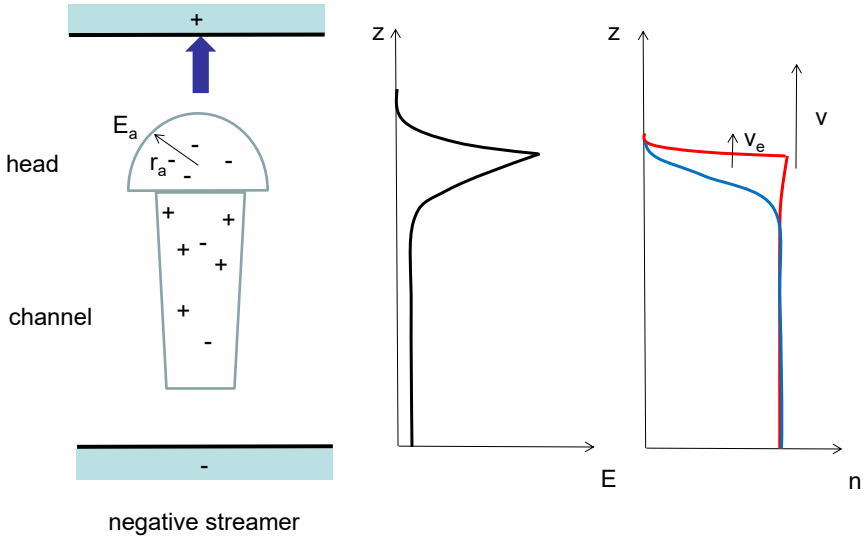

Figure 2.19: Electric field and charge carrier density of a single streamer.

$$
\begin{aligned}
-v\mathrm{d}n_+ &= \nu_{\mathrm{Ion}} n_{\mathrm{e}} \mathrm{d}z && (2.111)\\
&= \nu_{\mathrm{Ion}} n_{\mathrm{e}} \mathrm{d}E \frac{\epsilon_0}{e(n_+ - n_{\mathrm{e}})} && (2.112)\\
&= \nu_{\mathrm{Ion}} \frac{\epsilon_0}{e} \frac{v}{v_{\mathrm{e}}} \mathrm{d}E && (2.113)
\end{aligned}
$$

That is, the relationship between ion density and electric field is:

$$
-\frac{\mathrm{d}n_+}{\mathrm{d}E} = \frac{\epsilon_0}{e} \underbrace{\frac{\nu_{\mathrm{ion}}}{v_{\mathrm{e}}}}_{=\alpha} \tag{2.114}
$$

The term $\nu_{\mathrm{ion}}/v_{\mathrm{e}}$ corresponds exactly to the ions generated per distance, the ionization length α. If we again use the heuristic approach in the form:

$$
\alpha = Ae^{B/E} \tag{2.115}
$$

for α, we can integrate Eq. 2.114 to determine the ion density in the channel according to the electric fields that pass from E_{channel} to E_{head}

$$
n_{+,\mathrm{Kanal}} = \int_{E_{\mathrm{channel}}}^{E_{\mathrm{head}}} \frac{\epsilon_0}{e} A e^{-\frac{B}{E}} \mathrm{d}E \tag{2.116}
$$

In the approximation $E_{\text{channel}} \approx 0$, we get:

$$n_{+,\text{channel}} = \frac{\epsilon_0}{e}\alpha\frac{E_{\text{head}}^2}{E_{\text{head}} + B} \tag{2.117}$$

It can be seen that the ion density that builds up is proportional to the electric field of the streamer head and the ionization length. The electron density in the streamer head is now obtained from the continuity equation for the electrons:

$$-v\frac{\mathrm{d}n_\text{e}}{\mathrm{d}z} + \frac{\mathrm{d}}{\mathrm{d}z}n_\text{e}v_\text{e} = \nu_\text{Ion}n_\text{e} \tag{2.118}$$

Since v_e does not change spatially in the first approximation, this can be shortened to:

$$-v\mathrm{d}n_\text{e} + v_\text{e}\mathrm{d}n_\text{e} = \nu_\text{ion}n_\text{e}\mathrm{d}z \tag{2.119}$$

This can be solved by integration by integrating the electron density from the channel to the avalanche head, or in space along the radius R:

$$\int_{n_\text{e,head}}^{n_\text{e,background}} \frac{\mathrm{d}n_\text{e}}{n_\text{e}} = \int_0^R \frac{\nu_\text{ion}}{v_\text{e} - v}\mathrm{d}z \tag{2.120}$$

$$-\ln\left(\frac{n_\text{e,Kopf}}{n_\text{e,background}}\right) = R\nu_\text{ion}\frac{1}{v_\text{e} - v} \tag{2.121}$$

$$v \pm v_\text{e,head} \simeq \frac{R\nu_\text{Ion}}{\ln\left(\frac{n_\text{e,head}}{n_\text{e,background}}\right)} \tag{2.122}$$

The logarithmic dependence in the denominator on the particle density is very weak. This value is usually around 10. In the case of a very fast streamer (it holds $v_\text{e} \ll v$), it is observed that the velocity is proportional to the radius of the streamer head. This is correctly reproduced by this simple model. An example of a result of a complete fluid-dynamic description of a streamer is shown in Fig. 2.20. It can be seen very nicely how the electron density spreads, but only at the location of the streamer head is an electron excess formed, and locally the electric field is changed. A quasi-neutral streamer channel remains. Behind the streamer head, the field strength is lower compared to the initial situation, while it is significantly higher in front of the streamer. Furthermore, one can see the beginning of the division of the streamer head into two individual streamers (streamer branching).
In this streamer discharge at high pressure, conductive channels are created on the trail of the streamer. If the recombination is small, so-called **leaders**

can be created from these streamer discharges. These are conductive plasma channels as they form on thunderclouds before a breakdown occurs between the cloud and the ground.

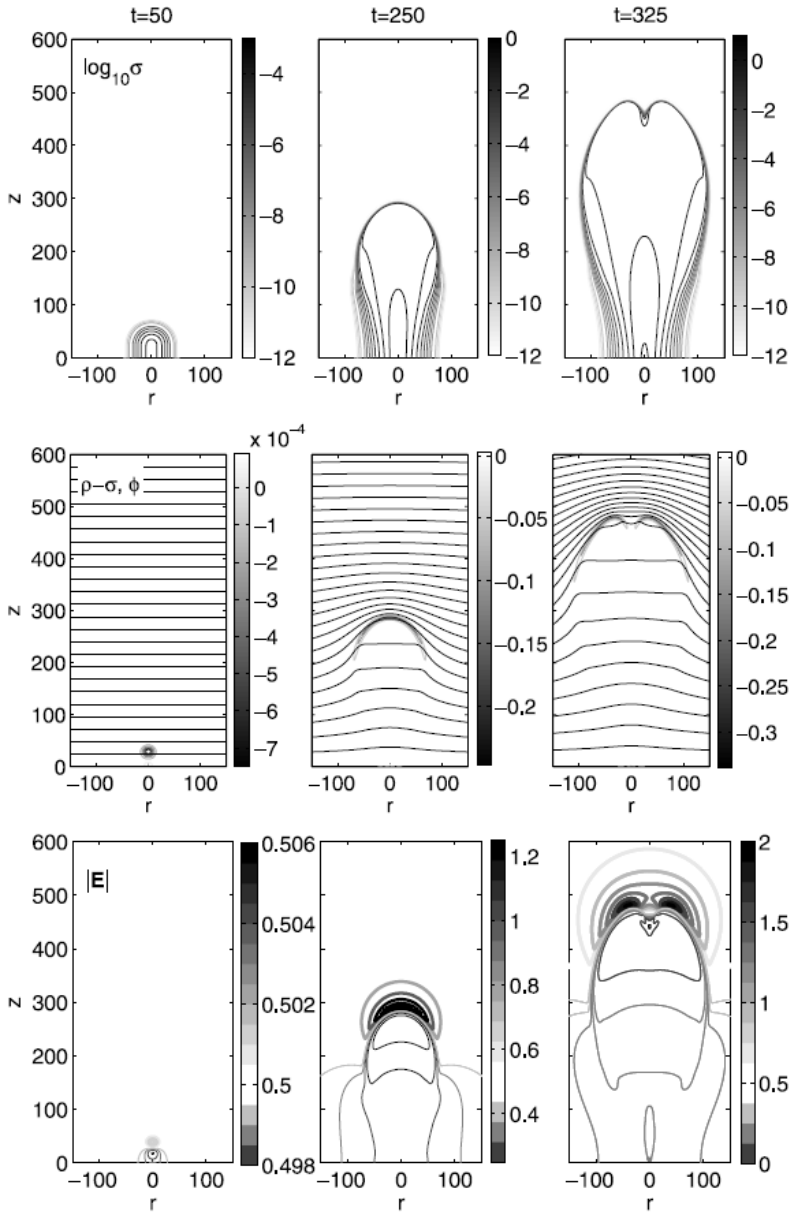

Figure 2.20: Calculation of the electron density (top row), the net charge and the equipotential lines (middle row) as well as the electric field of a streamer (bottom row) at different times [16].

2.4 Example - Ignition Phenomena in the Atmosphere

To conclude, we want to discuss an example in which all previous ignition phenomena come into play: the discharges in the upper atmosphere. From satellite and aircraft observations, it is now known that some discharges can occur not only between thunderclouds and the ground, but also between the thunderclouds and the upper atmosphere. An overview of these phenomena is shown in Fig. 2.21.

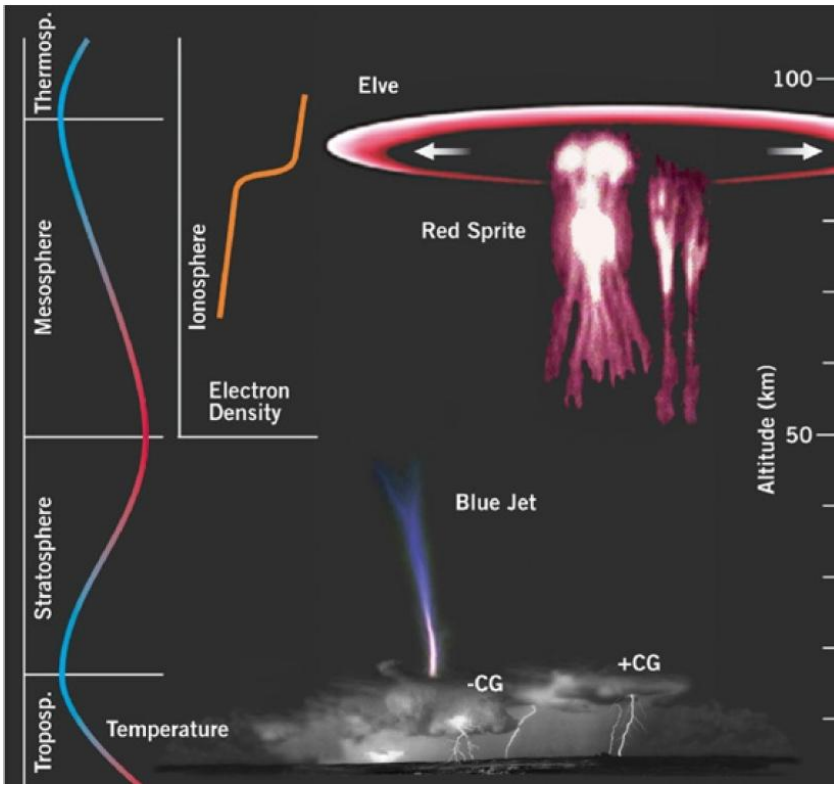

from T. Neubert, Science 300, 747 (2003)

Figure 2.21: Schematic representation of discharge phenomena in the upper atmosphere [36].

In a thunderstorm, the thunderclouds initially charge up. In the strong electric field, streamers are created, which bundle into leaders and finally discharge to the ground or the cloud in the form of a lightning bolt. However, these strong electric fields can also directly trigger streamer discharges above

the thunderclouds. Discharges that run upwards from the clouds are referred to as jets. Due to the excitation characteristics of nitrogen, these glow blue. A complex mechanism is the so-called sprite, which only occurs in connection with a lightning discharge, as illustrated in Fig. 2.22. In the ionosphere, a low charge density exists, as produced by cosmic radiation. With increasing altitude, the pressure decreases. A thundercloud has an electric dipole field that extends into the ionosphere. In this field, a discharge can ignite at sufficiently low density - a weak Townsend discharge in the upper atmosphere. If the positive charge at the upper end of the thundercloud now discharges to the ground, the field of the thundercloud changes and we suddenly get a very large electric field at great heights. This electric field is above the ignition field strength, and a streamer discharge can build up, which now runs down along the electric field (positive streamer). The color of this discharge again corresponds to the excitations of nitrogen, which are quenched to different degrees at different altitudes. These sprites can simultaneously trigger shock waves in the ionosphere, which are referred to as elves.

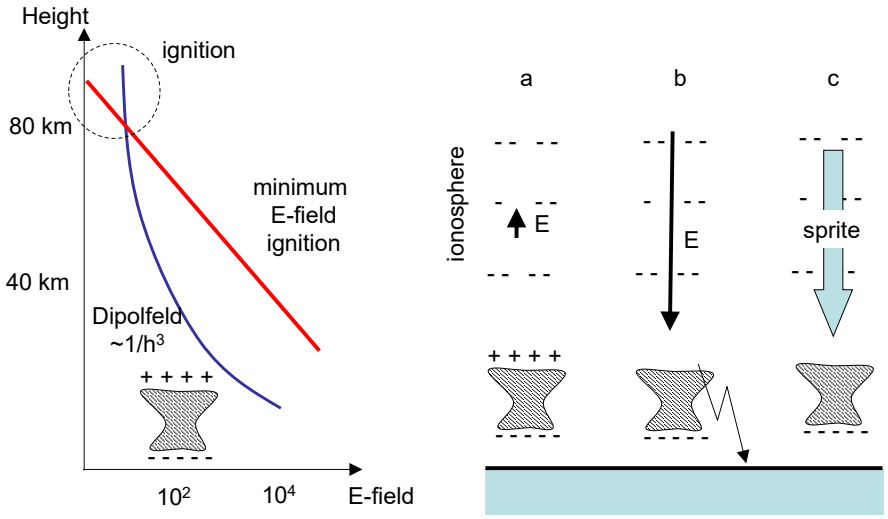

Figure 2.22: Field distribution above thunderclouds.

Chapter 3

Plasma Equilibrium

The achievement of the ignition criterion of a plasma initially corresponds to an exponential multiplication of the electrons (cf. secondary amplification of the Paschen criterion). The generated electrons finally form such a strong space charge zone that they shield the external electric field. That is, the generation comes to a halt, and a new equilibrium is established.
The equilibrium state of a plasma is equivalent to a balanced particle and energy balance, i.e., the inflow and outflow of particles as well as the absorbed power and the loss power are identical. The particle balance is largely determined by the boundary region, since at this boundary the particles leave the plasma or flow in. For the description of the energy balance, on the other hand, the heating processes and the losses through collision processes in the plasma are relevant.
This problem can be illustrated as a "Black-Box" in Fig. 3.1, where a particle flux j_{Teilchen} and energy input P lead to certain particle densities n_{e}, n_{i}, n^* and energy distribution functions $f(E)$ or temperatures T. To calculate this equilibrium, we will discuss the properties of the plasma sheath and the plasma heating in general in the following.

3.1 Plasma sheath

3.1.1 Space Charge Region

Given a quasi-neutral plasma in front of a surface. Depending on the charge carrier currents in the plasma and the potential of the surface, a so-called **sheath** is formed. The formation of this sheath is a consequence of the creation of the new equilibrium state after ignition. Especially in the boundary regions, the light electrons can leave the plasma very easily compared to the

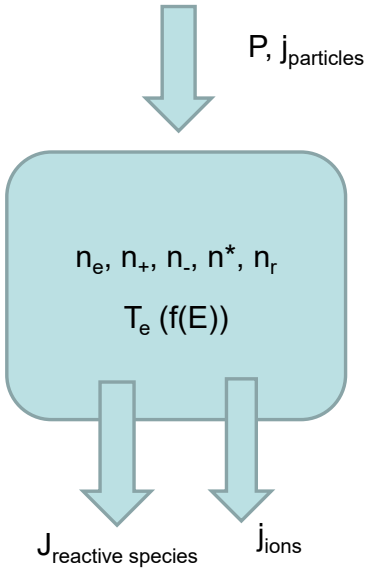

Figure 3.1: In equilibrium, the particle and energy flows into a plasma must balance the losses.

ions. Thus, the plasma would always charge positively. However, this charging creates an electric field in the boundary region that exactly counteracts this loss of electrons. That is, sheaths always compensate for the different mobilities or losses of the individual charge carrier species.

Animation

Density profile after turning on a plasma

Simulation of the formation of sheaths in a plasma with constant charge carrier density in the volume. The electrode at -0.05 m is biased with -100 V.

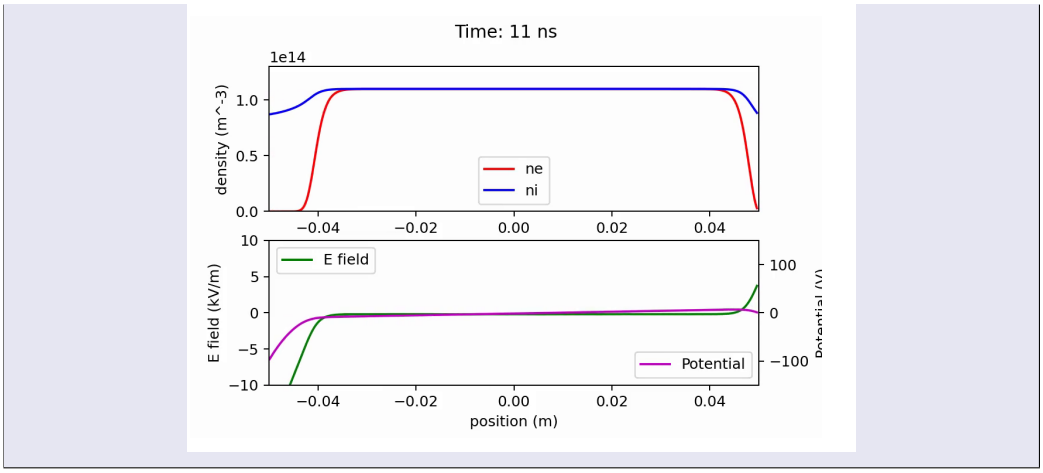

A distinction is made between an **ion sheath**, in which only ions are present in the sheath and the electrons are repelled by the electric field, and an **electron sheath**, in which the situation is reversed. In an ion sheath, the electric field points in the direction of the surface and thus keeps the electrons in the plasma, while it is the opposite in the electron sheath. An ion sheath can be easily recognized because the absence of electrons is visible as a dark zone in the plasma in which no electron impact reactions and thus also no light emission occur (see Fig. 3.2).
Which type of sheath is established depends on the charge carrier balance in the plasma. Thus, an ion sheath is usually formed at the cathode of a DC discharge, while an electron sheath may occur at the anode if the anode area is very small compared to the cathode area.

3.1.1.1 Space Charge Region of an Ion sheath

The simplest case is initially that of an ion sheath. In this sheath, the electron density is much smaller than the ion density, as illustrated in Fig. 3.3. The course corresponds to that of a pn junction in solid state physics. The positive space charge zone is the sheath of the plasma. The negative space charge zone is represented by a thin electron layer at the solid surface. To calculate the course of the ion density in the sheath, we first use the energy conservation of the ions according to:

$$\frac{1}{2}Mv_{\mathrm{i}}^2(x) + e\Phi(x) = \frac{1}{2}Mv_0^2 \tag{3.1}$$

v_0 is the velocity with which ions enter this space charge zone. In addition, current conservation applies:

$$n_{\mathrm{i}}(x)v_{\mathrm{i}}(x) = n_0 v_0 \tag{3.2}$$

Figure 3.2: Photo of an ion sheath in front of a substrate to which an external voltage is applied. A dark zone is visible in front of the surface. The external voltage displaces the electrons there and thus also suppresses the light emission in this region.

Solving this gives, with $E_0 = \frac{1}{2}Mv_0^2$:

$$n_\mathrm{i}(x) = n_0 \left(1 - \frac{2e\Phi(x)}{Mv_0 2}\right) -1/2 = n_0 \left(1 - \frac{e\Phi(x)}{E_0}\right)^{-1/2} \tag{3.3}$$

For the description of the electron density, the fact is used that, due to their high mobility, they directly map the course of the electric field. It is therefore permissible to simply use the Boltzmann relation:

$$n_\mathrm{e}(x) = n_0 e^{\frac{e\Phi(x)}{k_\mathrm{B}T_\mathrm{e}}} \tag{3.4}$$

Inserting both into the Poisson equation gives:

$$\frac{\mathrm{d}^2\Phi(x)}{\mathrm{d}x^2} = e\frac{n_0}{\epsilon_0}\left[\exp\left(\frac{e\Phi(x)}{k_\mathrm{B}T_\mathrm{e}}\right) - \left(1 - \frac{e\Phi(x)}{E_0}\right)^{-1/2}\right] \tag{3.5}$$

This equation corresponds to a differential equation for the potential profile $\Phi(x)$ in the sheath. However, this transcendental equation can only be solved numerically.
However, at least an estimate for the region of the sheath at $x \sim 0$ can be derived as follows. First, the equation is multiplied by $\frac{\mathrm{d}\Phi(x)}{\mathrm{d}x}$ and integrated over x. On the left side, we get

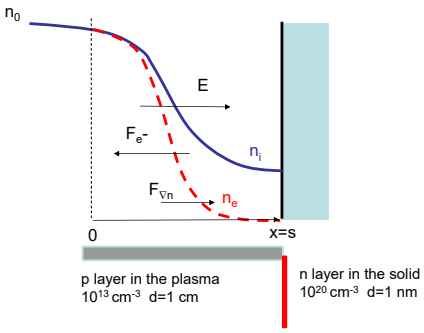

Figure 3.3: Profile of the charge carrier density in the sheath. A positive space charge zone is formed in front of the surface. This is compensated by a negative space charge zone directly at the surface. Due to the large differences in the charge carrier densities in the plasma compared to the solid, the thicknesses of these space charge zones are also very different.

$$\begin{aligned}
\int_0^x \frac{\mathrm{d}\Phi(x)}{\mathrm{d}x}\frac{\mathrm{d}^2\Phi(x)}{\mathrm{d}x}\mathrm{d}x &= \\
\int_0^x \frac{\mathrm{d}\Phi(x)}{\mathrm{d}x}\frac{\mathrm{d}}{\mathrm{d}x}\frac{\mathrm{d}\Phi(x)}{\mathrm{d}x}\mathrm{d}x &= \\
\int_0^x \frac{\mathrm{d}\Phi(x)}{\mathrm{d}x}\mathrm{d}\left(\frac{\mathrm{d}\Phi(x)}{\mathrm{d}x}\right) &= \\
\frac{1}{2}\left(\frac{\mathrm{d}\Phi(x)}{\mathrm{d}x}\right)^2 &
\end{aligned} \tag{3.6}$$

On the right side, we get

$$\begin{aligned}
\int_0^x \frac{\mathrm{d}\Phi(x)}{\mathrm{d}x} e\frac{n_0}{\epsilon_0}\left[exp\left(\frac{e\Phi(x)}{k_\mathrm{B}T_\mathrm{e}}\right) - \left(1-\frac{e\Phi(x)}{E_0}\right)^{-1/2}\right]\mathrm{d}x &= \\
\int_{\Phi(0)}^{\Phi(x)} e\frac{n_0}{\epsilon_0}\left[exp\left(\frac{e\Phi(x)}{k_\mathrm{B}T_\mathrm{e}}\right) - \left(1-\frac{e\Phi(x)}{E_0}\right)^{-1/2}\right]\mathrm{d}\Phi &
\end{aligned} \tag{3.7}$$

Thus, with the integration over Φ under the assumption that $\Phi(0) = 0$, we obtain:

$$\frac{1}{2}\left(\frac{\mathrm{d}\Phi(x)}{\mathrm{d}x}\right)^2 = \frac{en_0}{\epsilon_0}\left[k_\mathrm{B}T_\mathrm{e}e\frac{e\Phi(x)}{k_\mathrm{B}T_\mathrm{e}} - k_\mathrm{B}T_\mathrm{e} + 2E_0\left(1-\frac{e\Phi(x)}{E_0}\right)^{1/2} - 2E_0\right] \tag{3.8}$$

This equation requires that the right side becomes greater than zero for meaningful solutions. In the region $x \simeq 0$, both $e\Phi \ll k_\mathrm{B}T_\mathrm{e}$ and $e\Phi \ll E_0$ apply. Thus, an interesting relation can be derived if the right side is expanded to the second order:

$$k_\mathrm{B}T_\mathrm{e}\left(1+\frac{e\Phi}{k_\mathrm{B}T_\mathrm{e}}+\frac{1}{2}\left(\frac{e\Phi}{k_\mathrm{B}T_\mathrm{e}}\right)^2\right)k_\mathrm{B}T_\mathrm{e}+ \tag{3.9}$$

$$2E_0\left(1-\frac{1}{2}\frac{e\Phi}{E_0}-\frac{1}{8}\left(\frac{e\Phi}{E_0}\right)^2\right)2E_0 \leq 0 \tag{3.10}$$

This term must be greater than or equal to zero. Therefore, it can be concluded that:

$$\frac{1}{2}\frac{(e\Phi)^2}{k_\mathrm{B}T_\mathrm{e}} - \frac{1}{4}\frac{(e\Phi)^2}{E_0} \geq 0 \tag{3.11}$$

With $E_0 = \frac{1}{2}Mv_0^2$, the condition for the initial velocity v_0 is obtained:

$$\boxed{v_0 \geq \sqrt{\frac{k_\mathrm{B}T_\mathrm{e}}{M}} = v_\mathrm{B}} \tag{3.12}$$

This is referred to as the **Bohm velocity**. This velocity is equal to the **ion sound velocity**. This is an important result because it provides a boundary condition for the ion current that leaves the plasma. This current is *independent* of the exact profile of the sheath and an external voltage that might be applied to the surface. This initially appears surprising. However, the Bohm criterion only considers the conditions in the region where the sheath begins in the plasma and the positive charge carrier density must increase, and the potential must decrease. The further potential profile and the dynamics of the charge carriers within the sheath towards the surface are irrelevant for this.
We initially derived this condition formally from the solvability of the equation. However, this condition can also be physically motivated. For a sheath in equilibrium, the following must apply at the location where the ion sheath begins:

$$\boxed{\frac{\mathrm{d}(n_+ - n_-)}{\mathrm{d}\Phi} \leq 0} \tag{3.13}$$

with n_- the total density of negative charge carriers. This inequality means that the potential must decrease ($\mathrm{d}\Phi$ negative) while at the same time the net space charge increases ($\mathrm{d}(n_+ - n_-)$ positive). Only then does one obtain a uniform transition between the plasma and space charge zone. This condition is equivalent to the Bohm velocity. If the ions do not enter this space charge zone with a certain velocity, they could not build up this positive space charge at the boundary to the plasma sheath!
In describing the space charge zone, we assumed energy conservation of the ions and found a boundary condition, the Bohm velocity, which must be satisfied for the ions to enter this sheath. This naturally raises the question of how the ions are brought to this velocity. The acceleration of the ions to the Bohm velocity occurs in the so-called **presheath** (Fig. 3.4). Quasineutrality should prevail here:

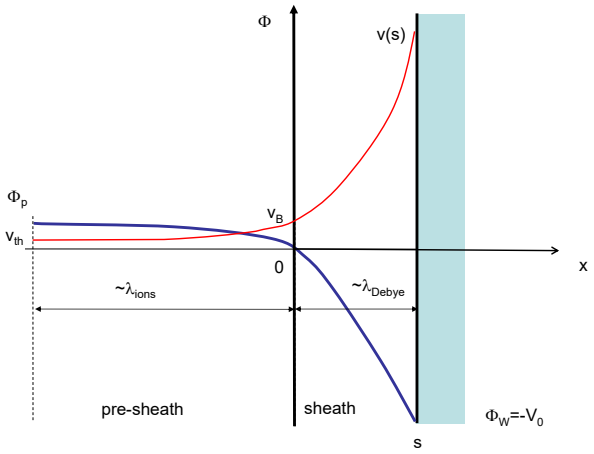

Figure 3.4: Potential profile in presheath and sheath. The extension of the presheath is of the order of the mean free path of the ions λ_{Ionen}, while the sheath has a thickness of the order of the Debye length λ_{D}.

$$n_{\mathrm{i}}(x) = n_{\mathrm{e}}(x) \tag{3.14}$$

From this, it can be derived that:

$$\frac{1}{n_{\mathrm{i}}(x)} \frac{\mathrm{d}n_{\mathrm{i}}(x)}{\mathrm{d}x} = \frac{1}{n_{\mathrm{e}}(x)} \frac{\mathrm{d}n_{\mathrm{e}}(x)}{\mathrm{d}x} \tag{3.15}$$

With $j_\mathrm{i} = n_\mathrm{i} e v_\mathrm{i}(x)$, we obtain:

$$\frac{1}{n_\mathrm{e}(x)}\frac{\mathrm{d}n_\mathrm{e}(x)}{\mathrm{d}x} = \frac{ev_\mathrm{i}(x)}{j_\mathrm{i}(x)}\frac{\mathrm{d}}{\mathrm{d}x}\frac{j_\mathrm{i}}{ev_\mathrm{i}(x)} = \frac{1}{j_\mathrm{i}(x)}\frac{\mathrm{d}j_\mathrm{i}(x)}{\mathrm{d}x} - \frac{1}{v_\mathrm{i}(x)}\frac{\mathrm{d}v_\mathrm{i}(x)}{\mathrm{d}x} \tag{3.16}$$

With the Boltzmann relation for the electrons, we finally obtain:

$$\frac{1}{v_\mathrm{i}(x)}\frac{\mathrm{d}v_\mathrm{i}(x)}{\mathrm{d}x} + \frac{e}{k_\mathrm{B}T_\mathrm{e}}\frac{\mathrm{d}\Phi(x)}{\mathrm{d}x} = \frac{1}{j_\mathrm{i}(x)}\frac{\mathrm{d}j_\mathrm{i}(x)}{\mathrm{d}x} \tag{3.17}$$

In the presheath, the local ion velocity $v_\mathrm{i}(x)$ must always be less than the Bohm velocity v_B. Therefore, from Eq. 3.17, the inequality is obtained according to:

$$\frac{1}{v_\mathrm{B}}\frac{\mathrm{d}v_\mathrm{i}(x)}{\mathrm{d}x} + \frac{e}{k_\mathrm{B}T_\mathrm{e}}\frac{\mathrm{d}\Phi}{\mathrm{d}x} < \frac{1}{j_\mathrm{i}}\frac{\mathrm{d}j_\mathrm{i}}{dx} \tag{3.18}$$

This equation can be satisfied by several conditions:

- **Ion friction**:

  In the case of current conservation ($\frac{\mathrm{d}j_\mathrm{i}(x)}{\mathrm{d}x} = 0$), the left side must explicitly become less than 0. This can be achieved if the increase in velocity of the ions is reduced by ion friction. That is, the change in $v_\mathrm{i}(x)$ is not equivalent to a change in $\Phi(x)$.

- **Geometry, Contraction**:

  Geometric effects can cause the current density to increase as it penetrates the sheath. For example, $\frac{\mathrm{d}j_\mathrm{i}}{\mathrm{d}x} > 0$ applies in a cylindrical arrangement.

- **Ionization**:

  The current through the presheath can increase due to the assumption of additional ionization. Here, too, $\frac{\mathrm{d}j_\mathrm{i}}{\mathrm{d}x} > 0$ applies.

It can be seen that collision processes, whether friction or ionization, are essential for the formation of the presheath in the plasma. Thus, it can be immediately concluded that the extent of the presheath must be of the order of the mean free path of the ions. For the description of the plasma sheath, there are thus two dominant but strongly different scales: the mean free path of the ions for the presheath in the range of typically several cm, and the Debye length for the space charge zone typically in the range of μm to mm. Now let us finally calculate the potential difference that is established in front of an insulating surface. This results from the condition that the ion

current and the electron current on an insulated surface must be equal. The ion current is given by the Bohm flux:

$$\Gamma_\mathrm{i} = n_0 v_\mathrm{B} \tag{3.19}$$

and the electron flux that hits the surface corresponds to the directed flux from the volume element directly in front of the surface. If the location of the surface is denoted by $x = s$ at which a potential Φ_W prevails, we obtain by means of the Boltzmann relation ($n(x = s) = n(x = 0)exp\left(\frac{e\Phi_\mathrm{W}}{k_\mathrm{B}T_\mathrm{e}}\right)$):

$$\Gamma_\mathrm{e} = \frac{1}{4} n(x = s) v_\mathrm{e,th} = \frac{1}{4} n_0 v_\mathrm{e,th} e^{\frac{e\Phi_\mathrm{W}}{k_\mathrm{B}T_\mathrm{e}}} \tag{3.20}$$

For the case of a so-called **floating** surface (i.e., the surface is not grounded) $\Gamma_\mathrm{e} = \Gamma_\mathrm{i}$ must apply, from which it follows:

$$n_0 v_\mathrm{B} = \frac{1}{4} n_0 v_\mathrm{e,th} e^{\frac{e\Phi_\mathrm{W}}{k_\mathrm{B}T_\mathrm{e}}} \tag{3.21}$$

$$\left(\frac{k_\mathrm{B}T_\mathrm{e}}{M}\right)^{1/2} = \frac{1}{4}\left(\frac{8k_\mathrm{B}T_\mathrm{e}}{\pi m}\right)^{1/2} e\frac{e\Phi_\mathrm{W}}{k_\mathrm{B}T_\mathrm{e}} \tag{3.22}$$

Thus, for the so-called **floating potential**, we obtain:

$$\boxed{\Phi_\mathrm{W} = -\frac{k_\mathrm{B}T_\mathrm{e}}{e} \ln\left(\frac{M}{2\pi m}\right)^{1/2}} \tag{3.23}$$

It can be seen that the potential becomes negative, i.e., the plasma is more positive than the surface. The voltage is a multiple of the electron energy. Also, between the sheath edge and the plasma volume, a potential must drop in which the ions are brought to the Bohm velocity. This can be easily derived from:

$$\frac{1}{2} M v_\mathrm{B}^2 = e\Phi_\mathrm{P} \tag{3.24}$$

From this, the so-called **plasma potential** is obtained:

$$\Phi_\mathrm{P} = \frac{k_\mathrm{B}T_\mathrm{e}}{2e} \tag{3.25}$$

All potentials are defined here with respect to the sheath edge. However, much more frequently one needs the potential with respect to the experimental mass of the reactor. This is then the plasma potential plus the floating potential.

3.1.1.2 Space Charge Zone with Multiple Ion Species

With the general formulation of the Bohm criterion 3.13, more general cases of a plasma sheath can be well described. For this purpose, we consider the case of a sheath of a plasma in which several different ion species are present. The charge carrier density ρ of a plasma with several ion species (index j) is generally:

$$\rho = e \sum_j n_j - e n_\mathrm{e} \tag{3.26}$$

For the evaluation of the Bohm criterion, we first need an expression of the form $\frac{\mathrm{d}n}{\mathrm{d}\Phi}$ for each charge carrier species. We start with the positive ions. The continuity equation for each ion species requires:

$$\frac{\mathrm{d}n_j}{\mathrm{d}t} + \frac{\mathrm{d}(n_j v_j)}{\mathrm{d}x} = 0 \tag{3.27}$$

In the steady state, this becomes:

$$n_j \frac{\mathrm{d}v_j}{\mathrm{d}x} + v_j \frac{\mathrm{d}n_j}{\mathrm{d}x} = 0 \tag{3.28}$$

or the momentum balance:

$$m_j n_j \left[\frac{\mathrm{d}v_j}{\mathrm{d}t} + v_j \frac{\mathrm{d}v_j}{\mathrm{d}x} \right] = n_j e E \tag{3.29}$$

From this, for steady cases, we get:

$$m_j v_j \frac{\mathrm{d}v_j}{\mathrm{d}x} = -\frac{\mathrm{d}\Phi}{\mathrm{d}x} e \tag{3.30}$$

Together with the continuity equation, this finally gives:

$$m_j v_j \frac{1}{-n_j} v_j \frac{\mathrm{d}n_j}{\mathrm{d}x} = -\frac{\mathrm{d}\Phi}{\mathrm{d}x} e \tag{3.31}$$

or

$$\frac{\mathrm{d}n_j}{\mathrm{d}\Phi} = \frac{e n_j}{m_j v_j^2} \tag{3.32}$$

For the relationship between electron density and potential, we simply use the Boltzmann relation:

$$\frac{\mathrm{d}n_\mathrm{e}}{\mathrm{d}\Phi} = \frac{e n_\mathrm{e}}{k_\mathrm{B} T_\mathrm{e}} \tag{3.33}$$

We insert the two terms of the form $\frac{\mathrm{d}n}{\mathrm{d}\Phi}$ for ions and electrons into our Bohm criterion

$$\frac{\mathrm{d}\rho}{\mathrm{d}\Phi} = e\sum_j \frac{\mathrm{d}n_j}{\mathrm{d}\Phi} - e\frac{\mathrm{d}n_\mathrm{e}}{\mathrm{d}\Phi} \leq 0 \tag{3.34}$$

or

$$\boxed{e\sum_j \frac{\mathrm{d}n_j}{\mathrm{d}\Phi} \leq e\frac{\mathrm{d}n_\mathrm{e}}{\mathrm{d}\Phi}} \tag{3.35}$$

and finally obtain:

$$\boxed{\sum_j \frac{en_j}{m_j v_j^2} \leq \frac{en_\mathrm{e}}{k_\mathrm{B}T_\mathrm{e}}} \tag{3.36}$$

We want to illustrate the application of Eq. 3.36 with two small examples:

- *a single ion species*

  If only one ion species is present, we get

  $$\frac{1}{mv_\mathrm{B}^2} \leq \frac{1}{k_\mathrm{B}T_\mathrm{e}} \tag{3.37}$$

  and we immediately get 3.12 again.

- *two ion species*

  For the simple case of two ion species, we get:

  $$\frac{n_1}{m_1 v_1^2} + \frac{n_2}{m_2 v_2^2} \leq \frac{n_\mathrm{e}}{k_\mathrm{B}T_\mathrm{e}} \tag{3.38}$$

  We transform this to:

  $$\frac{n_1}{v_1^2}\frac{k_\mathrm{B}T_\mathrm{e}}{m_1} + \frac{n_2}{v_2^2}\frac{k_\mathrm{B}T_\mathrm{e}}{m_2} \leq n_\mathrm{e} \tag{3.39}$$

  and we recognize the Bohm velocities of the individual ions according to:

  $$n_1\frac{v_{\mathrm{B},1}^2}{v_1^2} + n_1\frac{v_{\mathrm{B},2}^2}{v_2^2} \leq n_\mathrm{e} \tag{3.40}$$

i.e., this condition can be satisfied if each ion enters the sheath with its own Bohm velocity. This would be the case for low pressures. At higher pressures, collisions occur in the presheath that equalize the velocities of the ions. This means, however, that some ions enter the sheath slower, while others enter faster than their own Bohm velocity.

3.1.1.3 Space Charge Zone for Ions with a Distribution Function $f(v)$

Even the case where we have an ion species, but these ions hit the sheath with different velocities, can be easily mapped. The equation:

$$\boxed{\sum_j \frac{en_j}{m_j v_j^2} \leq \frac{en_\mathrm{e}}{k_\mathrm{B} T_\mathrm{e}}} \tag{3.41}$$

can be formally reinterpreted as a distribution over different velocities, and we get:

$$\boxed{\frac{en}{m} \int_0^\infty \frac{1}{v^2} f(v) \mathrm{d}^3 v \leq \frac{en_\mathrm{e}}{k_\mathrm{B} T_\mathrm{e}}} \tag{3.42}$$

This equation does not specify a fundamental velocity but requires a specific form of the ion energy distribution function to satisfy the Bohm criterion.

3.1.1.4 Space Charge Zone of an Electronegative Plasma

In technical plasmas, negative ions can also be formed, such as in oxygen- or fluorine-containing plasmas. In these cases, the Bohm criterion must take into account that part of the negative charge can also be present in the form of heavy ions. In this case, we must modify the Poisson equation to:

$$\nabla^2 \Phi = -\frac{e}{\epsilon_0} \left(n_+ - n_\mathrm{e} - n_- \right) \tag{3.43}$$

n_- denotes the density of negative ions. The degree of electronegativity is often expressed as a coefficient α:

$$\alpha = \frac{n_-}{n_\mathrm{e}} \tag{3.44}$$

Animation

Density profile of an electronegative plasma after 1200 ns

Density profile of an electronegative plasma after 1200 ns, starting with an electronegativity in the volume of 0.7/0.3. The cosine profile decays until an ion-ion consisting of negative and positive ions is formed.

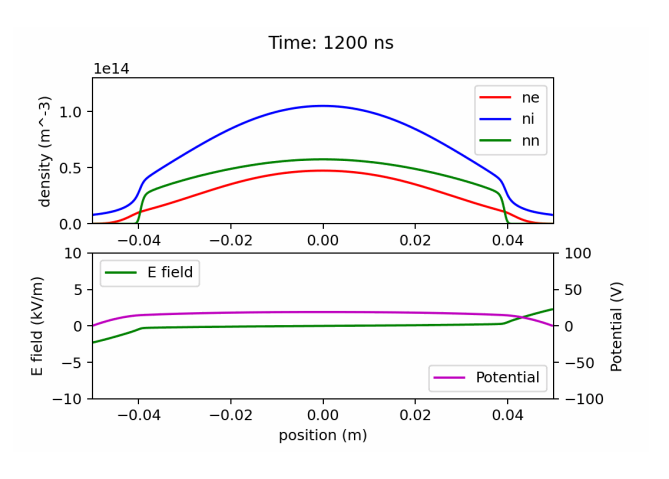

That is, the condition of quasi-neutrality can be formulated as:

$$n_+ = (1+\alpha)n_\mathrm{e} \tag{3.45}$$

In an ion sheath, the negative charge carriers are in equilibrium with the electric field, and we can simply use the Boltzmann relation in each case:

$$n_\mathrm{e} + n_- = n_{\mathrm{e},0} e^{\frac{\Phi}{k_\mathrm{B} T_\mathrm{e}}} + \alpha n_{\mathrm{e},0} e^{\frac{\Phi}{k_\mathrm{B} T_\mathrm{e}} \frac{T_\mathrm{e}}{T_\mathrm{i}}} \tag{3.46}$$

With the definition $\gamma = \frac{T_\mathrm{e}}{T_\mathrm{i}}$, this becomes:

$$n_\mathrm{e} + n_- = \frac{n_{+,0}}{1+\alpha} \left(e^{\frac{\Phi}{k_\mathrm{B} T_\mathrm{e}}} + \alpha e^{\frac{\Phi}{k_\mathrm{B} T_\mathrm{e}} \gamma} \right) \tag{3.47}$$

Thus, the change in the negative charge carrier density with the potential at the sheath edge ($\Phi(0) = 0$) becomes:

$$\frac{\mathrm{d}(n_\mathrm{e} + n_-)}{\mathrm{d}\Phi} = \frac{1}{k_\mathrm{B} T_\mathrm{e}} n_+ \left(\frac{1 + \alpha\gamma}{1+\alpha} \right) \tag{3.48}$$

According to the general formulation of the Bohm criterion 3.13, the change $\frac{\mathrm{d}(n_\mathrm{e}+n_-)}{\mathrm{d}\Phi}$ is equivalent to the condition:

$$\frac{k_\mathrm{B} T_\mathrm{e}}{M} \underbrace{\int_0^\infty \frac{1}{v^2} f(v) \mathrm{d}v}_{n + \frac{1}{v_\mathrm{B}^2}} \leq n_+ \left(\frac{1 + \alpha\gamma}{1+\alpha} \right) \tag{3.49}$$

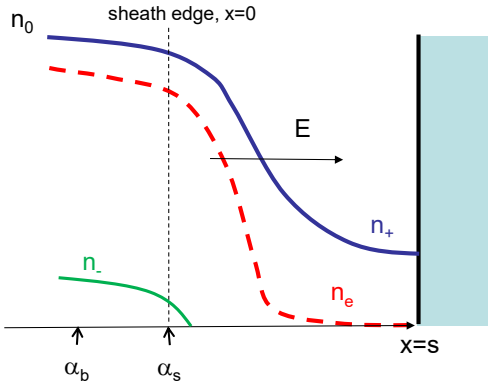

Figure 3.5: sheaths in electronegative plasmas. Part of the negative charge is present in the form of negative ions. Since their mobility is low, they are pushed back further into the plasma than the electrons. An electron boundary and a negative ion boundary are formed.

From this, we obtain the Bohm velocity:

$$\boxed{v_\mathrm{B} \geq \left(\frac{k_\mathrm{B} T_\mathrm{e}}{M} \frac{1+\alpha}{1+\alpha\gamma} \right)^{1/2}} \tag{3.50}$$

Several limiting cases can be distinguished for 3.50:

- $\alpha = 0$

  If α becomes zero, i.e., no negative ions are present, we get the simple Bohm criterion 3.12 again.

- $\gamma = 1$

  If $\gamma = 1$, the temperature of the electrons is equal to that of the negative ions. That is, in this case, both negative charge carriers can follow the electric field in the same way. Thus, they are no longer distinguishable from the electrons in this consideration, and we get the simple Bohm criterion 3.12 again.

- $\alpha > 0$ *and* $\gamma \gg 1$

  If γ is large, i.e., the electrons are much hotter than the ions, and α is not too small, i.e., the density of the negative ions is significant, the

Bohm velocity is strongly reduced, since the ions now no longer have to overtake only the light electrons at the plasma sheath edge, but are only in competition with the heavy negative ions.

The consideration of the Bohm velocity is, however, more complicated, since we now no longer have a clear boundary where the sheath begins. Due to their lower mobility, the heavy negative ions are stopped further away from the sheath, so that the electron density and the negative ion density do not become zero at the same location. Two interfaces are formed, as illustrated in Fig. 3.5. This means, however, that the parameter α changes spatially in the sheath, with a value in the plasma bulk α_{bulk} and a value α_{s} at the sheath edge of the electrons. For the charge carrier densities of the electrons at the sheath edge $n_{s,e}$ and in the plasma volume (bulk) $n_{bulk,e}$ as well as for the negative ions, we have:

$$n_{\mathrm{s,e}} = n_{\mathrm{bulk,e}} e^{\frac{e\Phi_{\mathrm{P}}}{k_{\mathrm{B}} T_{\mathrm{e}}}} \tag{3.51}$$

$$n_{\mathrm{s,-}} = n_{\mathrm{bulk,-}} e^{\frac{e\Phi_{\mathrm{P}}}{k_{\mathrm{B}} T_{\mathrm{i}}}} \tag{3.52}$$

This means:

$$\alpha_{\mathrm{s}} = \alpha_{\mathrm{b}} e^{\frac{e\Phi_{\mathrm{P}}(\gamma-1)}{k_{\mathrm{B}} T_{\mathrm{e}}}} \tag{3.53}$$

Often α_b is known. If we now want to calculate α_s, we still need the plasma potential Φ_P, which describes the voltage drop from the plasma bulk to the sheath edge. This voltage drop was for a plasma without negative ions:

$$e\Phi_{\mathrm{P}} = \frac{1}{2} k_B T_e \tag{3.54}$$

In analogy to Eq. 3.50, we get:

$$e\Phi_{\mathrm{P}} = \frac{1}{2} k_B T_e \frac{1+\alpha_s}{1+\alpha_s \gamma} \tag{3.55}$$

Thus, we now have a relationship between α_s, α_b, and Φ_P that can be solved numerically.

3.1.1.5 Double Layers

Double layers always form at locations where two plasmas with different plasma potentials are combined. This can be easily realized in the experiment through a two-chamber system in which a plasma flows into a second

one. Other examples are dusty plasmas in which the dust is spatially inhomogeneously distributed and a dust-loaded plasma and a dust-free plasma form an interface.
As illustrated in Fig. 3.6, the two plasma potentials Φ_1 and Φ_2 must match at this interface. A space charge zone is formed, with an electron layer and an ion layer. This is entirely analogous to the pn junction in solid state physics. Initially, energy conservation applies to the charge carriers in a spatially varying potential $\Phi(x)$

$$E_j = \frac{1}{2} m_j v_j^2 + q_j \Phi(x) \tag{3.56}$$

From the Poisson equation, we get the charge carrier density according to:

$$\frac{\mathrm{d}^2\Phi}{\mathrm{d}x^2} = -\frac{1}{\epsilon_0} \sum_j q_j n_j \tag{3.57}$$

with

$$\begin{aligned} n_j &= \int f_j(v) \mathrm{d}v \\ &= \int \frac{f_j(v)}{m_j v} \mathrm{d}E \\ &= \int \frac{f_j(E)}{\sqrt{2m_j(E - q_j\Phi)}} \mathrm{d}E \end{aligned} \tag{3.58}$$

we obtain:

$$\epsilon_0 \frac{\mathrm{d}^2\Phi}{\mathrm{d}x^2} = -\sum_j q_j \int_{E_1}^{E_2} \frac{f_j(E)\mathrm{d}E}{\sqrt{2m_j(E - q_j\Phi)}} \tag{3.59}$$

We multiply again with $\frac{\mathrm{d}\Phi}{\mathrm{d}x}$ and integrate over $\mathrm{d}x$ and obtain:

$$\frac{1}{2}\epsilon_0 \left(\frac{\mathrm{d}\Phi}{\mathrm{d}x}\right)^2 - \sum_j q_j \int_{E_1}^{E_2} f_j(E) \sqrt{2m_j(E - q_j\Phi)} \mathrm{d}E = \text{const.} \tag{3.60}$$

The solution of this equation gives the potential profile in the double layer. The movement of the charge carriers in this double layer can be expressed in a velocity-position diagram 3.7. It can be seen that both ions and electrons, if they come from the "wrong side", are simply reflected at the double layer (this is analogous to the mode of operation of a pn diode). These are referred to as trapped charge carriers. If the ions or electrons come from the other

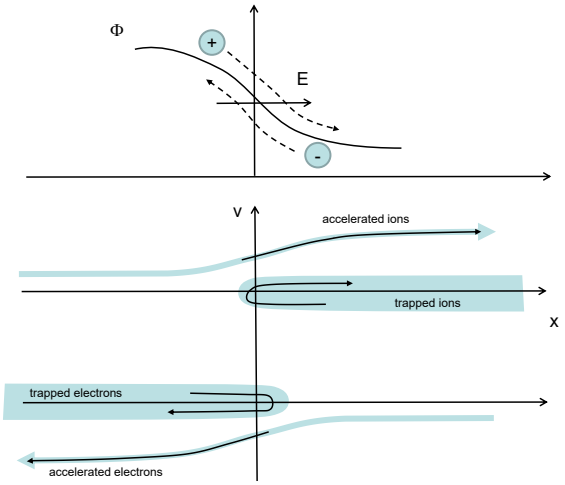

Figure 3.6: Phase space of a double layer.

side, respectively, they are accelerated and can penetrate the double layer. The local densities of the individual charge carriers are shown in Fig. 3.6. It can be seen that due to the superposition of the accelerated as well as the trapped charge carriers, a positive and a negative space charge zone is created.
Eq. 3.60 can now be solved in a simple approximation. For this purpose, we transform and use the electron and ion current again in the approach:

$$\epsilon_0 \frac{\mathrm{d}^2\Phi}{\mathrm{d}x^2} = -\frac{j_{\mathrm{Ionen}}}{v_{\mathrm{Ionen}}} + \frac{j_{\mathrm{e}}}{v_{\mathrm{e}}} \tag{3.61}$$

Again, we multiply by $\frac{\mathrm{d}\Phi}{\mathrm{d}x}$ and integrate over x. If the potential on the left side is Φ_0 and on the right side 0, and also the first derivatives are zero, we get on the left side:

$$\frac{1}{2}\epsilon_0 \left(\left(\frac{\mathrm{d}\Phi}{\mathrm{d}x}(x=L) \right)^2 - \left(\frac{\mathrm{d}\Phi}{\mathrm{d}x}(x=0) \right)^2 \right) = -\int \frac{j_{\mathrm{Ionen}}}{v_{\mathrm{Ionen}}} \mathrm{d}\Phi + \int \frac{j_{\mathrm{e}}}{v_{\mathrm{e}}} \mathrm{d}\Phi \tag{3.62}$$

With the velocities:

$$v_{\mathrm{Ionen}} = \sqrt{v_{\mathrm{Ionen},0}^2 + 2e\left(\Phi_0 - \Phi\right)\frac{1}{m_{\mathrm{i}}}} \tag{3.63}$$

$$v_{\mathrm{e}} = -\sqrt{v_{\mathrm{e},0}^2 + 2e\Phi\frac{1}{m_{\mathrm{e}}}} \tag{3.64}$$

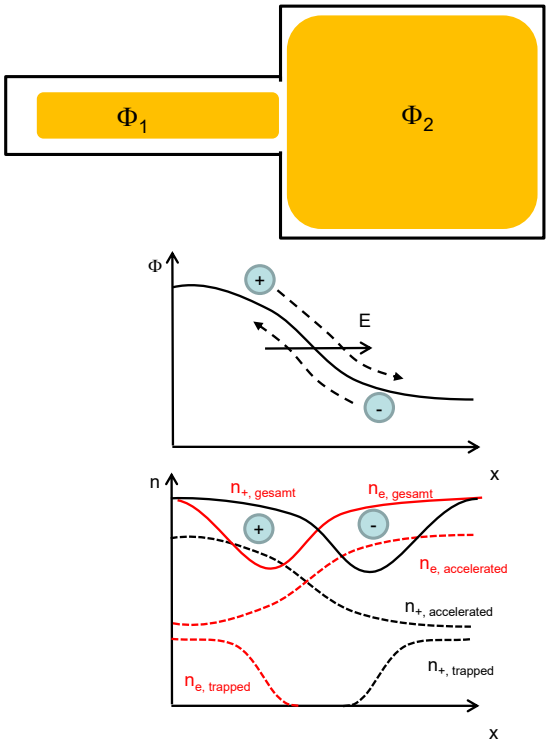

Figure 3.7: Potential profile and charge carrier densities in a double layer.

With the boundary conditions $v_{\mathrm{Ionen},0} = v_{\mathrm{e},0} = 0$, we finally get the so-called Langmuir criterion for a double layer in the limit $e\Phi_0 \gg k_\mathrm{B}T_\mathrm{e}$:

$$\frac{j_\mathrm{e}}{j_\mathrm{Ionen}} = \left(\frac{m_\mathrm{i}}{m_\mathrm{e}}\right)^{1/2} \tag{3.65}$$

i.e., the electron current dominates in the double layer. This can also be physically interpreted. The change in velocities of the electrons and ions, respectively, when passing through the sheath generates a corresponding force on the double layer. If the double layer is at rest, then the momentum of the ions and that of the electrons must cancel each other out. For this reason, the ratio must apply according to the Langmuir criterion.

3.1.1.6 Influences of Geometry

So far, we have only considered the case of an ion sheath. The formation of an ion or electron sheath depends on the particle balance and the corresponding

voltages of the plasma-exposed surfaces. To consider this, let us look at a parallel plate arrangement in which we can freely choose the area of the cathode A_c and the anode A_a. A high negative voltage is applied to the cathode. In the simplest case, the ions can leave the plasma. Their flux is given by the Bohm velocity at the sheath edges and the corresponding areas. One obtains:

$$I_{\text{Ionen}} = n_0 v_{\text{B}} \left(A_{\text{c}} + A_{\text{a}}\right) \tag{3.66}$$

The electrons can only reach the anode in this simple consideration, since the potential at the cathode is too large. The flux of electrons is:

$$I_{\text{e}} = \frac{1}{4} v_{\text{th}} n_0 e^{\frac{e\Phi}{k_{\text{B}} T_{\text{e}}}} A_{\text{a}} \tag{3.67}$$

with $v_{\text{th}} = \sqrt{\frac{8 k_{\text{B}} T_{\text{e}}}{\pi m_{\text{e}}}} \gg v_{\text{B}} = \sqrt{\frac{k_{\text{B}} T_{\text{e}}}{M}}$. It must be $I_{\text{Ionen}} = I_{\text{e}}$, from which it follows:

$$v_{\text{B}}(A_{\text{c}} + A_{\text{a}}) = \frac{1}{4} v_{\text{th}} e^{\frac{e\Phi}{k_{\text{B}} T_{\text{e}}}} A_{\text{a}} \tag{3.68}$$

or

$$\Phi = \frac{k_{\text{B}} T_{\text{e}}}{e} \ln \left[\frac{4 v_{\text{B}}}{v_{\text{th}}} \frac{A_{\text{c}} + A_{\text{a}}}{A_{\text{a}}} \right] \tag{3.69}$$

- $A_{\text{a}} \gg A_{\text{c}}$

  If the anode area A_{a} is much larger than the cathode area A_{c}, we get as an approximation:

  $$\Phi \simeq \frac{k_{\text{B}} T_{\text{e}}}{e} \ln \left[\frac{4 v_{\text{B}}}{v_{\text{th}}} \right] < 0 \tag{3.70}$$

  Since $v_{\text{th}} \gg v_{\text{B}}$, Φ becomes negative, which means that the potential decreases from the plasma to the surface, i.e., the electrons are repelled by the anode. This is intuitive, since the much more mobile electrons could easily leave the plasma and thus the charge carrier balance would no longer be balanced. This potential profile is almost typical for many technical low-pressure plasmas.

- $A_{\text{a}} \ll A_{\text{c}}$

  If now the anode area becomes very small and the ratio $v_{\text{B}}/v_{\text{th}}$ can compensate for it, Φ becomes positive.

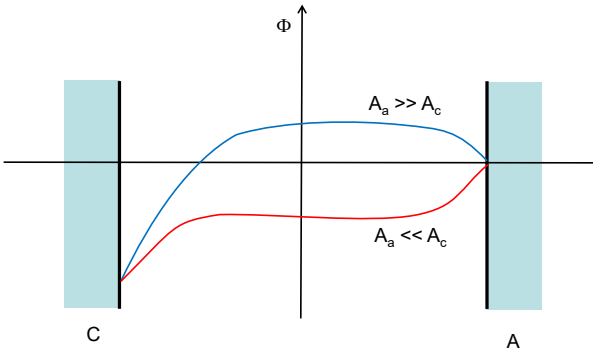

Figure 3.8: Potential profile depending on the geometry of the discharge.

$$\Phi \simeq \frac{k_\mathrm{B} T_\mathrm{e}}{e} \ln \left[\frac{4 v_\mathrm{B}}{v_\mathrm{th}} \frac{A_\mathrm{c}}{A_\mathrm{a}} \right] > 0 \tag{3.71}$$

Now the ion sheath at the anode turns into an electron sheath so that the electrons can effectively leave the plasma. Since the area of the anode in this example becomes very small, the loss of electrons must be made more effective by reversing the potential. This configuration is often found in high-pressure lamps, in which a small cathode but also a small anode are brought into contact with each other.

3.1.2 Sheaths with Applied Voltage

So far, we have considered a sheath that forms in front of a surface to balance the different mobilities of the positive and negative charge carriers. However, in plasmas, an external voltage is often applied to a surface, which additionally increases the sheath.
These sheaths with applied voltage play a major role in technical plasmas, as the sheath voltage simultaneously modifies the energy of the impinging ions. Processes such as sputtering (the physical dislodging of atoms from a solid by momentum transfer) depend in detail on the energy of the projectiles. Due to the formation of the electric field in the sheath, the ions also hit the surface perpendicularly. This is an essential component of anisotropic etching, in which the etching chemistry depends not only on the isotropic flux of neutral etching species (fluorine atoms, oxygen atoms, etc.) but also on the anisotropic flux of energetic ions. The direction of the ions determines

the etching direction of the microstructure. This is crucial in semiconductor technology for the production of electronic components such as memory cells.

3.1.2.1 Matrix Sheath

First, let us consider the simplest case where a high voltage pushes the electrons further back into the plasma and strongly accelerates the ions. In the simplest approximation, the violation of quasi-neutrality in the sheath can be described as a step function. If the ion density is assumed to be constant in the sheath, one speaks of the so-called **matrix sheath** (Fig. 3.9).

$$\frac{\mathrm{d}E}{\mathrm{d}x} = \frac{1}{\epsilon_0} e n_0 \tag{3.72}$$

$$E(x) = \frac{1}{\epsilon_0} e n_0 x \tag{3.73}$$

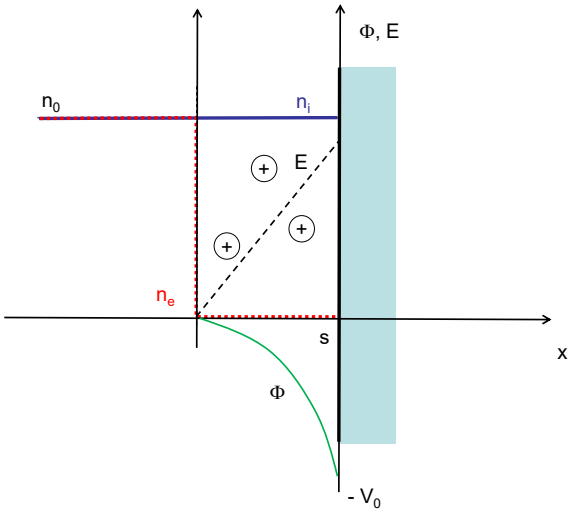

Figure 3.9: Profile of the charge carrier density in the matrix sheath.

From this, the potential profile is obtained:

$$\Phi(x) = -\frac{e}{\epsilon_0} n_0 \frac{1}{2} x^2 \tag{3.74}$$

With $\Phi(s) = -V_0$, we obtain

$$\boxed{s = \left(\frac{2\epsilon_0 V_0}{e n_0}\right)^{1/2} = \lambda_\mathrm{D} \left(\frac{2eV_0}{k_\mathrm{B} T_\mathrm{e}}\right)^{1/2}} \tag{3.75}$$

This result shows that the sheath can be many Debye lengths thick. In the description of the matrix layer, the acceleration of the ions in the electric field was neglected. This acceleration would, under the assumption of current conservation ($j_0 = n(x)v(x)$), lead to the fact that the density of the ions must decrease towards the surface. Despite this deficiency, the formulation of a matrix sheath is useful, since for the description of volume phenomena in the plasmas (see stochastic heating) often only a finite sheath thickness is important, and the fact that a certain amount of charge is stored in the sheath. Exactly this is correctly reproduced.
However, there are still some special cases in which a matrix layer is a good model. One such case is **Plasma Ion Immersed Implantation (PIII)**, in which a negative high-voltage pulse is applied to a workpiece. As a result, the electrons are quickly pushed back into the plasma, while the ions cannot initially follow the pulse; the matrix layer is formed. In this matrix layer, the ions then pass through the electric field and are implanted into the workpiece with high energies.
The advantage of this pulsed approach is the fact that the thickness of the sheath can be much thinner compared to a permanently applied voltage (Child-Langmuir sheath, see below). That is, given a plasma density n and voltage V, a cavity *can still* be filled, while the sheath thickness s in a uniformly operated plasma would be larger.

3.1.2.2 Child-Langmuir Sheath

The assumption of a constant ion density in the sheath is only valid if collisions in the sheath counteract the acceleration of the ions. In the case of a collision-free sheath, the ion density becomes lower with increasing acceleration, as illustrated in Fig. 3.10. As an approach, we get:

$$\frac{1}{2} M v^2(x) = -e\Phi(x) + \underbrace{\frac{1}{2} M v_0^2}_{\ll} \tag{3.76}$$

The second term on the right side can be neglected because the ions in the sheath are strongly accelerated and their initial energy according to v_0 is of minor importance. Current conservation provides:

$$e n(x) v(x) = j_0 \tag{3.77}$$

From Eq. 3.76 and 3.77, we obtain:

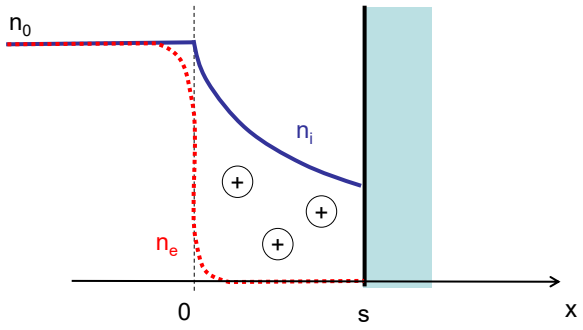

Figure 3.10: Profile of the charge carrier density in the Child-Langmuir sheath.

$$n(x) = \frac{1}{e} j_0 \left(-\frac{2e\Phi(x)}{M} \right)^{-1/2} \tag{3.78}$$

Thus, the Poisson equation gives:

$$\frac{\mathrm{d}^2\Phi(x)}{\mathrm{d}x^2} = -\frac{j_0}{\epsilon_0} \left(-\frac{2e\Phi(x)}{M} \right)^{-1/2} \tag{3.79}$$

At this point, the electron density in the sheath is neglected. This is a good approximation at high sheath voltage, since the electrons are effectively pushed back into the plasma volume.
Multiplication with $\frac{\mathrm{d}\Phi(x)}{\mathrm{d}x}$ and integration over x gives:

$$\frac{1}{2} \left(\frac{\mathrm{d}\Phi}{\mathrm{d}x} \right) 12 = 2\frac{j_0}{\epsilon_0} \left(\frac{2e}{M} \right) 1{-}1/2(-\Phi)^{1/2} \tag{3.80}$$

In the integration, the boundary conditions were used that $\Phi(0) = 0$ and $\frac{\mathrm{d}\Phi(x)}{\mathrm{d}x}\Big|_{x=0} = 0$. From this, for $\Phi(s) = -V_0$, we obtain

$$\boxed{j_0 = \frac{4}{9}\epsilon_0 \left(\frac{2e}{M} \right) 11/2\frac{V_0 13/2}{s^2}} \tag{3.81}$$

This equation suggests that the current j_0 would change with the voltage. However, in the case of a plasma sheath, j_0 is already given by the Bohm criterion. The actual dependence is between sheath voltages and sheath thickness. That is, with

$$j_0 = e n_0 v_\mathrm{B} \tag{3.82}$$

an expression for the sheath thickness s can also be derived:

$$\boxed{s = \frac{\sqrt{2}}{3} \lambda_\mathrm{D} \left(\frac{2eV_0}{k_\mathrm{B} T_\mathrm{e}} \right)^{3/4}} \tag{3.83}$$

These relationships provide a link between the particle density n_0, the thickness of the sheath s, the temperature of the electrons T_e, and the applied voltage V_0. The comparison with the matrix layer shows that the extent of the Child-Langmuir layer is greater. Due to the decrease in ion density according to the acceleration, the extent of the space charge zone must be greater in order to enclose the same amount of charge with the same voltage drop.
Eq. 3.81 is referred to as the **Child-Langmuir Law** ($V^{3/2}$-Law), as it applies to any space charge-limited current. A typical example is the maximum current in ion optics, where the distance between two electrodes/optics (corresponding to s in Eq. 3.81) is constant and Eq. 3.81 thus sets the maximum current density j_0 for a given voltage V_0.
The Child-Langmuir Law for describing a space charge-limited current was historically particularly important in the development of tube amplifiers. There, the law describes which current density could be switched at a given grid spacing s and voltage V. In the context of plasma physics, this "grid spacing" is variable, since now the current density is constant, namely plasma density times Bohm velocity, and the sheath thickness s adjusts itself in such a way that the voltage V drops across it.
For a given plasma process, the extent of the sheath can be estimated to decide to what extent a plasma can penetrate into the opening of a workpiece or not. These dependencies can be illustrated as follows:

- The sheath thickness increases with increasing voltage.
- The sheath thickness decreases with increasing electron density at a given sheath voltage.
- The sheath thickness decreases with increasing electron temperature.

For practical application, however, the exact quantitative relationship is essential. This, however, depends on the assumption of whether one may neglect collisions of the ions in the sheath or not.

3.1.2.3 Collision-Dominated Sheath

So far, we have assumed a sheath in which the velocity of the ions increases according to energy conservation. Collisions of the ions in the sheath were neglected. The other limiting case results from the assumption that collisions in the sheath limit the velocity, as expressed by the mobility. Initially, flux conservation applies in the sheath.

$$n_\mathrm{i}(x)v_\mathrm{i}(x) = n_0 v_\mathrm{B} \tag{3.84}$$

but the velocity is calculated by

$$v_\mathrm{i}(x) = \mu E \tag{3.85}$$

The mobility is given by:

$$\mu = \frac{e}{m\nu_\mathrm{m}} \tag{3.86}$$

with $\nu_\mathrm{m} = n_\mathrm{g}\langle\sigma_\mathrm{m}v\rangle$. For the description of the collision frequency, the velocity is important. Here, two different approaches can be chosen: (i) at high pressure, the collision frequency is given by the thermal velocity (ii) at low pressure and large mean free paths, the velocity is rather the drift velocity. These two cases give:

- ***p* small, constant mean free path $\boldsymbol{\lambda_\mathrm{m}}$ = const.**

  At low pressure, the mean free path $\lambda_\mathrm{m} = 1/n_\mathrm{g}\sigma_\mathrm{m}$ is constant, and for the collision frequency we directly set $\nu_\mathrm{m} = n_\mathrm{g}\sigma_\mathrm{m}v_\mathrm{i}$. The mobility becomes:

$$v_\mathrm{i}(x) = \mu E = \frac{e}{M\nu_\mathrm{m}}E = \frac{e\lambda_\mathrm{m}}{Mv_\mathrm{m}(x)}E \tag{3.87}$$

  From this, for a velocity-independent mean free path, we obtain:

$$v_\mathrm{i}(x) = \left(\frac{e\lambda_\mathrm{m}}{M}E(x)\right)^{1/2} \tag{3.88}$$

  This gives the ion density:

$$n_\mathrm{i}(x) = \frac{v_\mathrm{B}}{v_\mathrm{i}(x)}n_0 = v_\mathrm{B}n_0\left(\frac{e\lambda_\mathrm{m}}{M}E(x)\right)^{-1/2} \tag{3.89}$$

This is inserted into the Poisson equation under the neglect of the electron density in the sheath:

$$\frac{\mathrm{d}E}{\mathrm{d}x} = \frac{e}{\epsilon_0} n_0 v_\mathrm{B} \left(\frac{e\lambda_\mathrm{m}}{M} E(x) \right)^{-1/2} = \frac{1}{\epsilon_0} j_0 \left(\frac{e\lambda_\mathrm{m}}{M} E \right)^{-1/2} \tag{3.90}$$

As the current density, we obtain:

$$j_0 = \frac{2}{3} \left(\frac{5}{3} \right)^{3/2} \epsilon_0 \left(\frac{2e\lambda_\mathrm{m}}{\pi M} \right)^{1/2} \frac{V_0^{3/2}}{s^{5/2}} \tag{3.91}$$

It can be seen that the scaling is very similar to the Child-Langmuir Law. Only the dependence on the sheath thickness is somewhat different, since the ion density cannot decrease as quickly compared to free fall:

$$s \propto \lambda_\mathrm{m}^{1/5} V_0^{3/5} \tag{3.92}$$

The dependence on the mean free path is correspondingly weak.

A further comparison shows that the collision-determined sheath is equal to the Child-Langmuir layer multiplied by $(\lambda_\mathrm{m}/s)^{1/2}$. That is, the space charge-limited current is only reduced if the mean free path becomes smaller than the space charge zone.

- ***p* large, constant mobility ν_m = const.**

  At high pressure, the collision frequency is independent of the velocity, and the mobility becomes a constant. Thus, we obtain:

$$\frac{\mathrm{d}E}{\mathrm{d}x} = \frac{e}{\epsilon_0} \mu - 1 E - 1 \tag{3.93}$$

This solves to:

$$j_0 = \frac{9}{8} \epsilon_0 \mu \frac{V_0^2}{s^3} \tag{3.94}$$

This can be rewritten into a dependence of the sheath thickness s on the voltage V_0:

$$\boxed{s \propto \lambda_\mathrm{m} V_0^{2/3}} \tag{3.95}$$

It can be seen that depending on the boundary condition and prior assumption, the relationship between potential, voltage, and layer thickness is different.

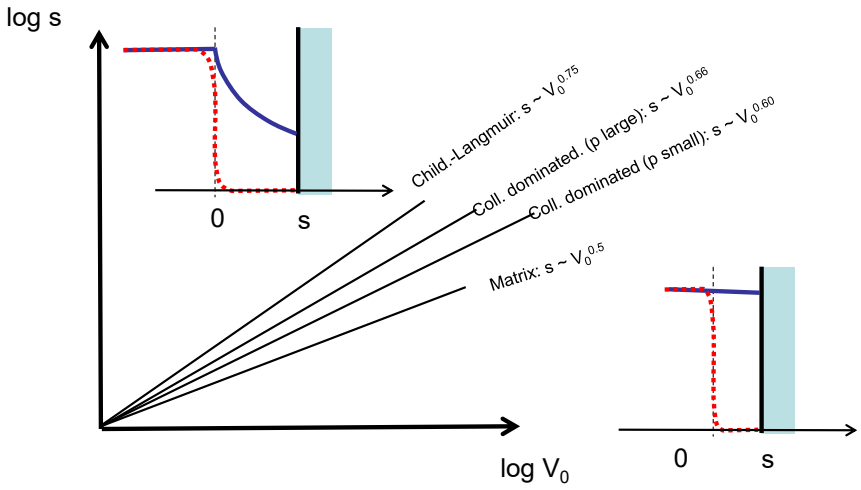

Figure 3.11: Dependence of the sheath thickness s on the voltage V_0, depending on the model as expressed by Eq. 3.83, 3.75, 3.92 and 3.95. Normally, one would expect a sequence of slopes with the pressure starting with the matrix layer at high pressure (strong ion friction) up to the Child-Langmuir layer (free fall); however, the dependence is not directly on the pressure but rather on the collision frequency, which can depend differently on pressure and velocity.

The different dependencies of the sheath thicknesses on the voltage V_0 depending on the model are illustrated in Fig. 3.11. The dependence in the case of the Child-Langmuir layer is the greatest, since due to the acceleration, the density of the ions in the sheath decreases strongly. To enclose the same amount of charge in the sheath at a given voltage, it must be correspondingly thick. The other extreme case is the matrix layer, in which the ion density does not vary. The sheath thickness can be thin in comparison, since even a thin sheath contains the required amount of charge. The collision-determined sheaths lie in between, since the acceleration of the ions is hindered and the velocity does not increase as strongly as in the Child-Langmuir layer. In the case of the collision-determined sheaths, it is also smaller at low pressure, since although the velocity increases, the collision frequency decreases again. This compensation falls away in the sheath at high pressure, which

is therefore also thicker in comparison in order to store the same amount of charge.

3.1.2.4 Energy Distribution of the Impinging Ions

The energy distribution of the ions that hit the surface is a direct measure of the sheath voltage. In addition, this energy distribution is changed by collision processes in the sheath. Here, so-called charge exchange collisions (CX) are important, in which an ion transfers its charge to a stationary neutral atom/molecule. The ion becomes a fast neutral atom/molecule and also reaches the sample surface. The stationary neutral particle becomes an ion and is accelerated from the location of its formation towards the surface. Since this charge exchange takes place inside the sheath, the potential difference that the new ion passes through is smaller than the sheath voltage. If we express the probability that a charge exchange occurs with p, we obtain after a distance x the form:

$$p \propto 1 - e^{-\frac{x}{\lambda_\mathrm{m}}} \tag{3.96}$$

with λ_m the mean free path of the ions in the sheath. That is, the probability of forming a stationary ion increases exponentially with x: if a stationary ion is formed at small x, the probability of surviving the rest of the flight path *without* a collision is much smaller than if this ion is formed at large x directly in front of the surface.
This behavior can also be observed in the experiment, as illustrated in Fig. 3.12. In the energy distribution of Ar^{++}, only a single peak is observed, since an Ar^{++} can only be formed in the plasma but not in a charge exchange collision. However, if Ne^+ ions are observed in a neon plasma, an exactly exponential increase in the ions at lower energies is observed at high pressure.

3.1.2.5 Sheaths in High-Frequency Plasmas

The behavior of high-frequency sheaths is essentially more complex, since the condition of balanced electron and ion currents to the surfaces only needs to be fulfilled on average over time. That is, the shape of the sheath can change strongly and sometimes only retain ions and sometimes only electrons. Furthermore, it depends on the frequency of the applied voltage whether the ions can follow the changes of the electric field or not.
In the simplest case, the frequency of the alternating voltage is large compared to the ion plasma frequency, and the ions can be considered as static. Then, the varying high-frequency voltage only pushes the electrons further

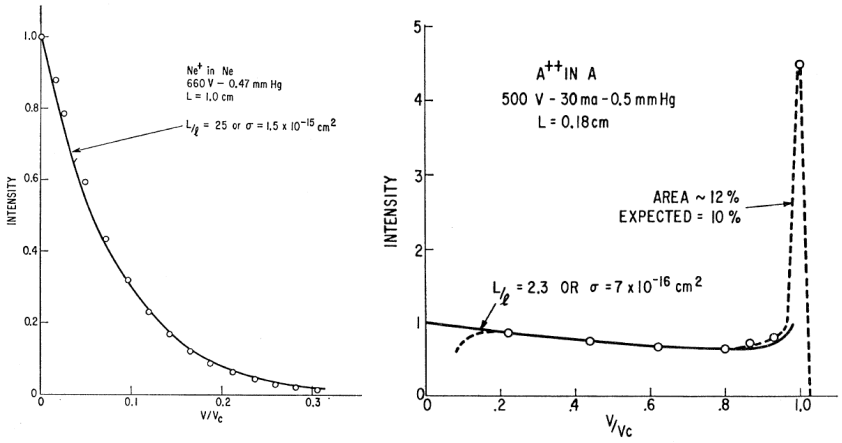

Figure 3.12: Measurement of the ion energy distribution of Ne^+ in a neon discharge and of Ar^{++} in an argon discharge at 0.5 Torr (1 mbar) [15].

into the plasma and out again. The ions, on the other hand, only see a time-averaged electric field in the sheath.
The energy distribution of the ions from a high-frequency sheath takes on very complex forms. If we apply a sinusoidal voltage and assume that the ions fall instantaneously through the sheath, i.e., their transit time τ is much smaller than $\omega_{\mathrm{rf}}^{-1}$, we obtain a characteristic bimodal distribution, as shown in Fig. 3.14 in the example of a CF plasma. Since the phases in which the sheath voltage becomes maximum or minimum are the longest, we obtain ions with high or low energies correspondingly more frequently than ions with medium energies. However, this is only a limiting case, since the transit time of the ions becomes longer with their mass.
This relationship can be best illustrated with a path-time diagram of the ion transport in a sheath (see Fig. 3.13). In a DC layer, an ion simply falls through the sheath to the surface, and one obtains a classical trajectory in the path-time diagram (this would be a parabola if the electric field in the sheath is constant, because $s = 1/2at^2$). In a high-frequency sheath, however, the sheath voltage changes sinusoidally and at the same time the extension of the sheath. This modulates the energy distribution. On the one hand because the electric field in the sheath changes continuously, but because depending on the mass of the ions and the excitation frequency, the sheath edge can also overtake the ions.
This complex behavior of ion acceleration in an RF sheath is best calculated

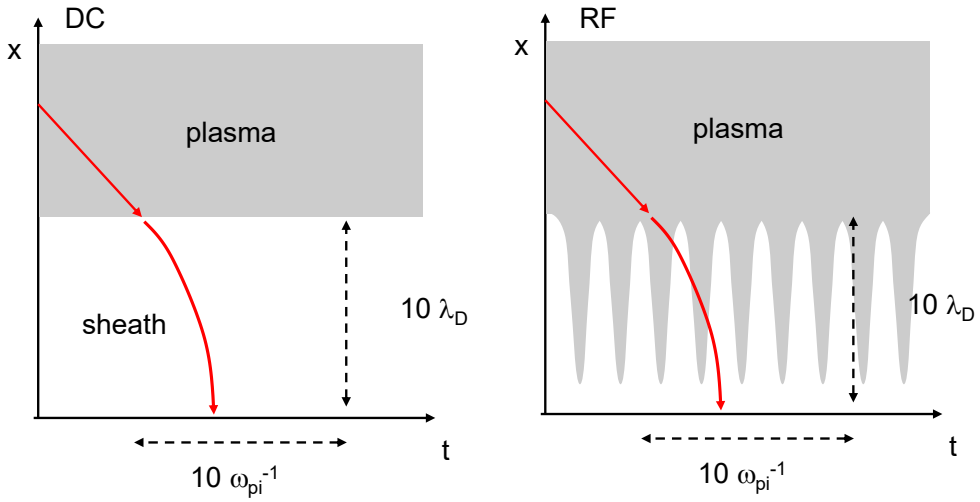

Figure 3.13: Path-time diagram of the ion trajectories in a DC sheath compared to an RF sheath.

with a computer simulation in which the ions are started with a random phase to the sheath oscillation in the plasma volume.

Animation

IEDF in an RF discharge without collisions IEDF in an RF discharge with collisions
Simulation of the energy gain of an electron with and without considering collisions.

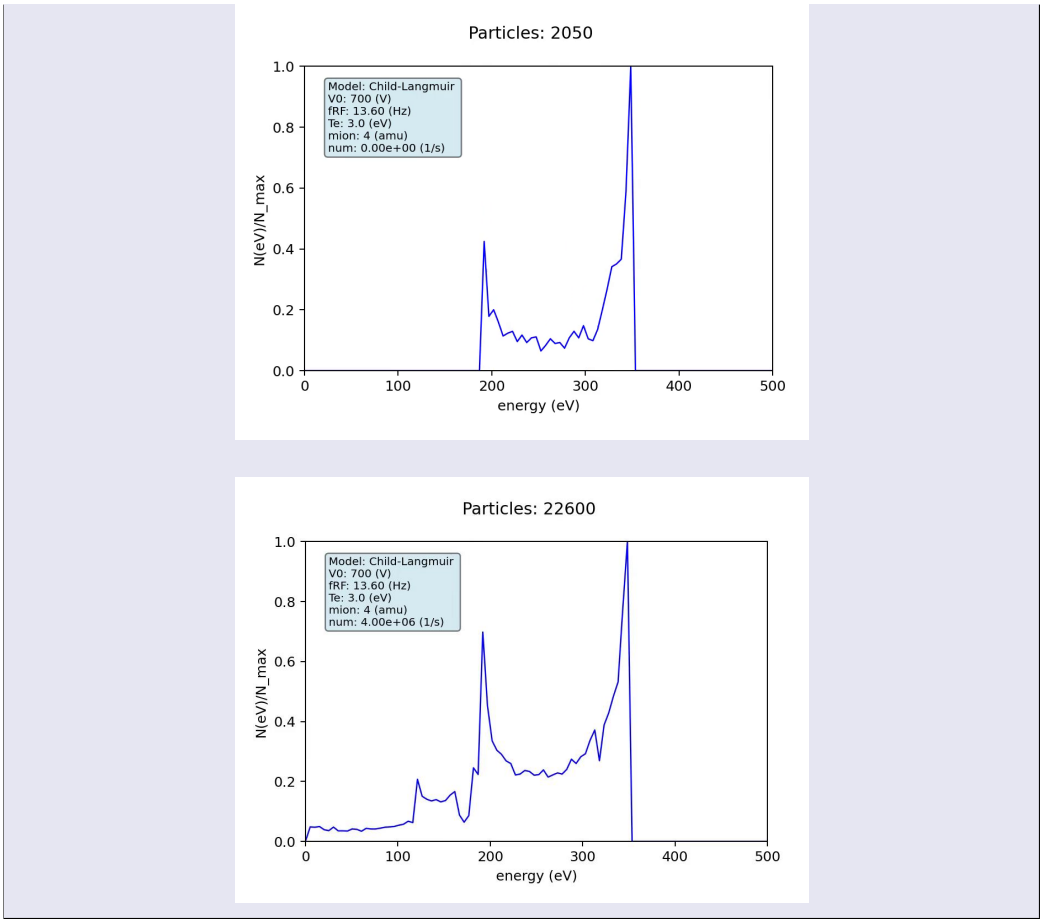

We nevertheless want to estimate the dependence of the energy distribution on frequency and ion mass. For this purpose, we consider the acceleration a of the ions in the sheath:

$$a = \frac{\mathrm{d}v}{\mathrm{d}t} = \frac{eE}{M} \tag{3.97}$$

Thus, with the sheath thickness $s = \frac{1}{2}a\tau^2$, the transit time becomes:

$$\tau = \left(\frac{2sM}{eE}\right)^{1/2} \tag{3.98}$$

Based on this equation, we can now distinguish two limiting cases:

- $\tau \gg \omega_{\mathrm{rf}}^{-1}$

  If the transit time τ is very long, the ions only see an averaged potential. The energy distribution will therefore be narrow. This is particularly the case for ions with heavy masses or for sheaths with high frequencies.

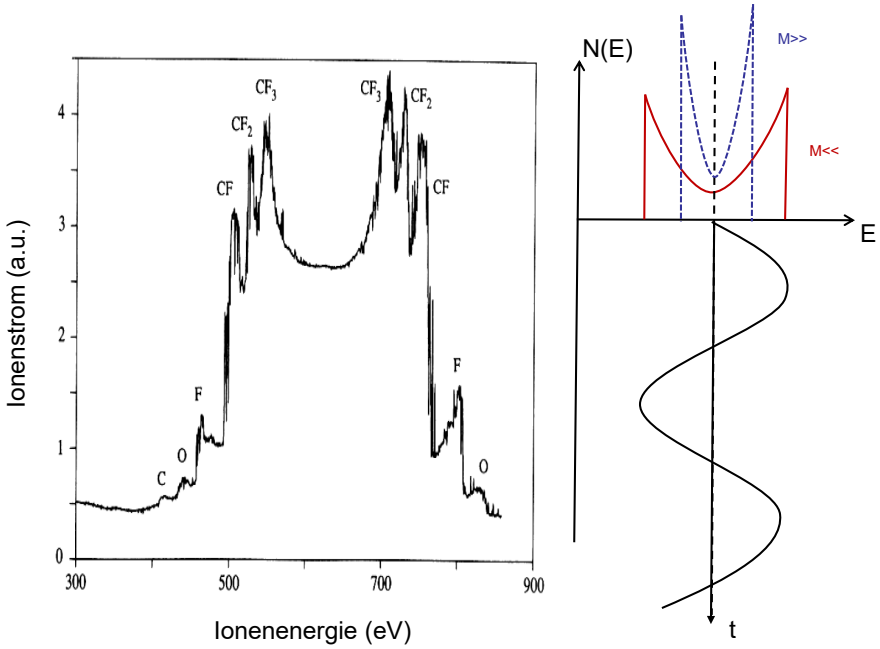

Figure 3.14: Measurement of the ion energy distribution in a CF-RF plasma [28].

- $\tau \ll \omega_{\mathrm{rf}}^{-1}$

  If the transit time is very short, the ions can almost follow the field, and the energy distribution will therefore be broad and take on its bimodal form.

The width of the ion energy distribution can thus be estimated as:

$$\Delta E \propto \frac{1}{\tau \omega_{\mathrm{rf}}} \propto \frac{1}{\omega_{\mathrm{rf}} \sqrt{M}} \tag{3.99}$$

An example of a measurement of such a distribution in a CF plasma is shown in Fig. 3.14. A superposition of bimodal distributions is observed, which becomes broader the lower the masses of the involved ion species are. The ion energy distribution in the high-frequency sheath was described so far for the case of a collision-free sheath at low pressures. In the case of a collision-determined sheath, the collision band at lower ion energies is added here. In general, one should initially expect this exponential increase in the frequency of the ions to smaller energies again. However, these secondary ions

are also modulated by the variation of the electric field. This is illustrated in Fig. 3.15. For this purpose, we consider the varying voltage as it changes in the sheath. The amplitude becomes smaller the closer the location is to the surface. That is, an ion that falls through this sheath sees a variation of the voltage as sketched in Fig. 3.15. If a charge exchange collision now occurs, events are more frequent in which this oscillation of the sheath voltage either shows a maximum or a minimum. This can be converted into an ion energy distribution analogously to the bimodal distribution. One recognizes a complex superposition of the bimodal distributions in the collision band to smaller energies.

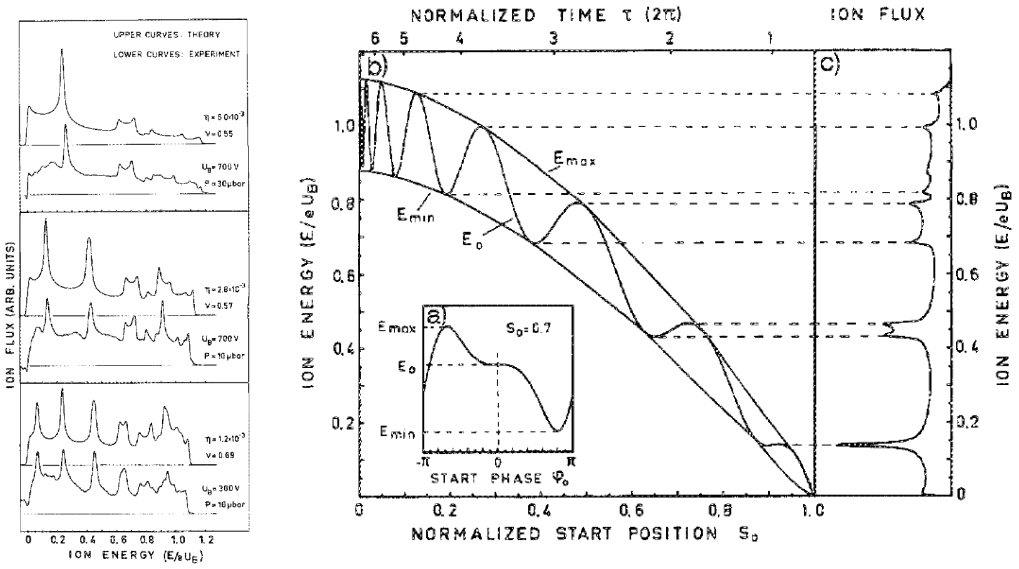

Figure 3.15: Collision-determined ion energy distributions in an RF sheath [51].

The sinusoidal voltage at an electrode is the most common form of time-dependent bias voltage. However, it may be advantageous to be able to explicitly tailor the ion energy distribution. This was particularly investigated in plasma etching, since a sharp energy distribution of the ions allows a particular selectivity of etching Si over SiO_2. To control the ion energy distribution, arbitrary signals are applied to the electrode via a function generator and amplifier: depending on the transit time of the ions and the modulation of the sheath edge, special ion energy distributions are obtained,

as illustrated in Fig. 3.16.

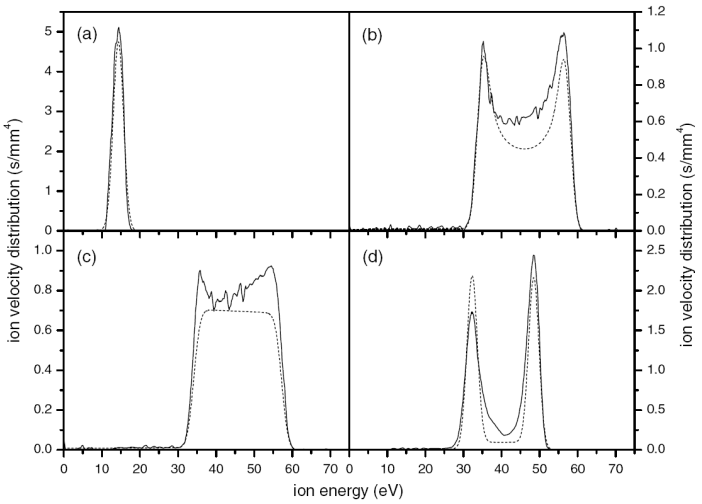

Figure 3.16: Ion energy distributions from an argon plasma with different variations of the substrate bias voltage [1]. (a) DC voltage, (b) sinusoidal voltage, Â© triangular voltage, (d) pulsed rectangular voltage.

3.2 Plasma Heating

3.2.1 General

The energy supply to a plasma initially occurs through the acceleration of electrons in an electric field. This field can be generated in various ways in the plasma, for example through external electrodes or coils that generate constant or time-varying E-fields. This does not yet correspond to heating, since an increase in the temperature of a plasma requires a uniform distribution of the directions of motion in space, as prescribed by the Maxwell distribution. Since the acceleration usually occurs in one spatial direction, heating actually involves two steps: first, the acceleration in the electric fields, and then the isotropization of the directions of motion through collisions of the electrons with each other or through collisions with the background gas. These two steps usually do not occur simultaneously and can be spatially and temporally separated from each other.
Traditionally, heating can be divided into several categories:

- *Ohmic Heating*

  Acceleration and isotropization occur almost at the same location and simultaneously in ohmic heating. Between two collisions with the background gas, an electron can absorb energy in the electric field and then release it again upon collision, which leads to the aforementioned isotropization when electrons collide with each other, and to excitation, ionization, or dissociation when they collide with heavy particles.

- *Stochastic Heating*

  Stochastic heating was traditionally introduced as a heating without collisions, which is not meaningful according to our definition. In stochastic heating, electrons gain their energy through collisions with temporally and spatially varying electric fields. However, in these collisions, they only absorb energy. The complete heating process still requires that these energetic electrons must be isotropized again to increase the temperature of the plasma. The term stochastic heating originates from the consideration that the electrons must collide with the oscillating electric fields in a random, i.e., stochastic phase to experience a net acceleration.

- *Wave Heating*

  In wave heating, electromagnetic waves are irradiated. In the non-resonant case, this is the acceleration in a high-frequency electric field.

In the case of resonant heating in a plasma with a superimposed magnetic field, this is the acceleration on the gyration path of an electron.

3.2.2 Ohmic Heating

Ohmic heating in a direct current (DC) or alternating current (RF) electric field can be derived in general. The oscillation of the potential (The limiting case $\omega \to 0$ corresponds to the DC case) at the electrode leads to time-varying electric fields in which the charge carriers are accelerated:

$$m\ddot{x} + m\nu_\mathrm{m}\dot{x} = eE_0 \sin \omega t \tag{3.100}$$

With the approach:

$$x = c_1 \sin \omega t + c_2 \cos \omega t \tag{3.101}$$

we obtain as a solution:

$$\dot{x} = -\frac{eE_0\omega}{m}\frac{1}{\omega^2 + \nu_\mathrm{m}^2}\left(\cos \omega t - \frac{\nu_\mathrm{m}}{\omega}\sin \omega t\right) \tag{3.102}$$

The absorbed power per electron is:

$$p = \frac{1}{\mathrm{d}t}\vec{F}\mathrm{d}x = \frac{1}{\mathrm{d}t}eE_0 \sin \omega t \mathrm{d}x = eE_0 \sin \omega t \dot{x} \tag{3.103}$$

A temporal average of the absorbed power $\bar{p}$ of a single electron is obtained from:

$$\bar{p} = \frac{1}{T}\int_0^T eE_0 \sin \omega t \dot{x} \mathrm{d}t \tag{3.104}$$

If we substitute the expression for $\dot{x}$, we obtain:

$$\bar{p} = \frac{e^2 E_0^2}{2m}\frac{\nu_\mathrm{m}}{\omega^2 + \nu_\mathrm{m}^2} \tag{3.105}$$

The total absorbed power per volume for an electron density n is:

$$P = n \cdot \bar{p} = \underbrace{\underbrace{\frac{ne^2}{m\nu_\mathrm{m}}}_{\sigma\mathrm{dc}}\frac{\nu_\mathrm{m}^2}{\omega^2 + \nu_\mathrm{m}^2}}_{\sigma\mathrm{rf}}\frac{1}{2}E_0^2 = \frac{1}{2}\sigma_\mathrm{rf}E_0^2 \tag{3.106}$$

The prefactors can be interpreted as DC conductivity σ_dc or RF conductivity σ_rf. This distinction between DC and RF conductivity can also be expressed equivalently by an effective field strength

$$E_{\text{eff}}^2 = E_0^2 \frac{\nu_{\text{m}}^2}{\nu_{\text{m}}^2 + \omega^2} \tag{3.107}$$

as already derived for the ignition of a plasma in the RF field. The power can also be represented as a function of the displacement current j_{rf}, because $j_{\text{rf}} = \sigma_{\text{rf}} E_0$:

$$P = \frac{1}{2}\sigma_{\text{rf}} E_0^2 = \frac{1}{2}\frac{1}{\sigma_{\text{rf}}} j_{\text{rf}}^2 \tag{3.108}$$

This is a power per volume V. The total absorbed power that is dissipated by a current $I_{\text{rf}} = A j_{\text{rf}}$ flowing through a plasma of thickness d is given by:

$$P_{\text{ges}} = \frac{1}{2} I_{\text{rf}}^2 \frac{1}{\sigma_{\text{rf}}} d \tag{3.109}$$

The formulation of power absorption according to Eq. 3.106 can also be rewritten as:

$$\begin{aligned} P &= \frac{e^2 n}{m} E^2 \frac{\nu_{\text{m}}}{\nu_{\text{m}}^2 + \omega^2} && (3.110)\\ &= 2\frac{e^2 n}{\epsilon_0 m}\frac{1}{2}\epsilon_0 E^2 \frac{\nu_{\text{m}}}{\nu_{\text{m}}^2 + \omega^2} && (3.111)\\ &= \underbrace{\frac{1}{2}\epsilon_0 E^2}_{\text{Energy E−Feld}} \quad \underbrace{2\omega_{\text{p}}^2 \frac{\nu_{\text{m}}}{\omega^2 + \nu_{\text{m}}^2}}_{\text{Energy transfer rate}} && (3.112) \end{aligned}$$

We recognize that the energy is transferred at an effective rate ν_*:

$$\nu_* = 2\frac{\omega_{\text{p}}^2}{\nu_{\text{m}}} \tag{3.113}$$

3.2.3 Stochastic Heating

3.2.3.1 Experimental Evidence

In the experiment, it is observed that the power absorption in high-frequency plasmas at low pressures does not completely disappear (ν_{m} becomes small because $\nu_{\text{m}} = n_{\text{g}}\langle\sigma_{\text{m}} v\rangle$). That is, despite the lack of collisions with the neutral gas, the electrons apparently can absorb energy from the oscillating field. This can be expressed by an *effective* collision frequency, which at low pressures approaches a constant value (see Fig. 3.17).

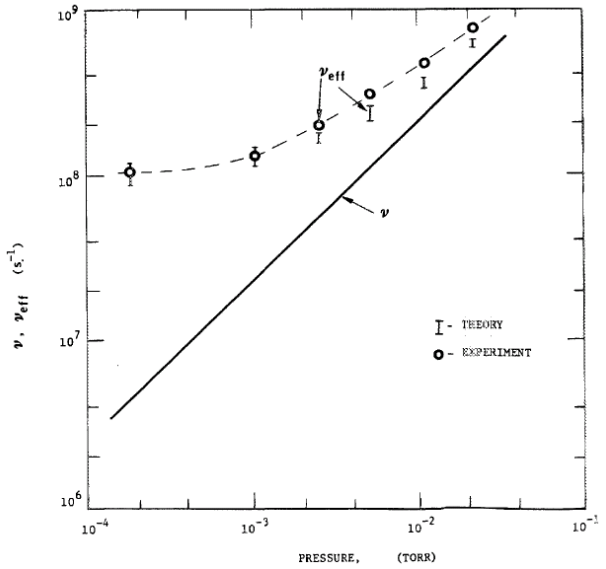

Figure 3.17: Effective collision rate in an RF plasma as a function of pressure [40].

An early explanation of this phenomenon is the reflection of the electrons at the oscillating sheaths. Through the collision with the spatially and temporally changing fields, an energy transfer can take place. This effect was initially introduced by Fermi as a possible explanation for the creation of high-energy particles in cosmic radiation.

Animation

Heating of an electron through collisions with an oscillating sheath. Stochastic heating of an electron through collisions with an oscillating sheath and neutral particle collisions.
Simulation of the energy increase of an electron through collisions with an oscillating sheath with and without considering collisions in the plasma volume.

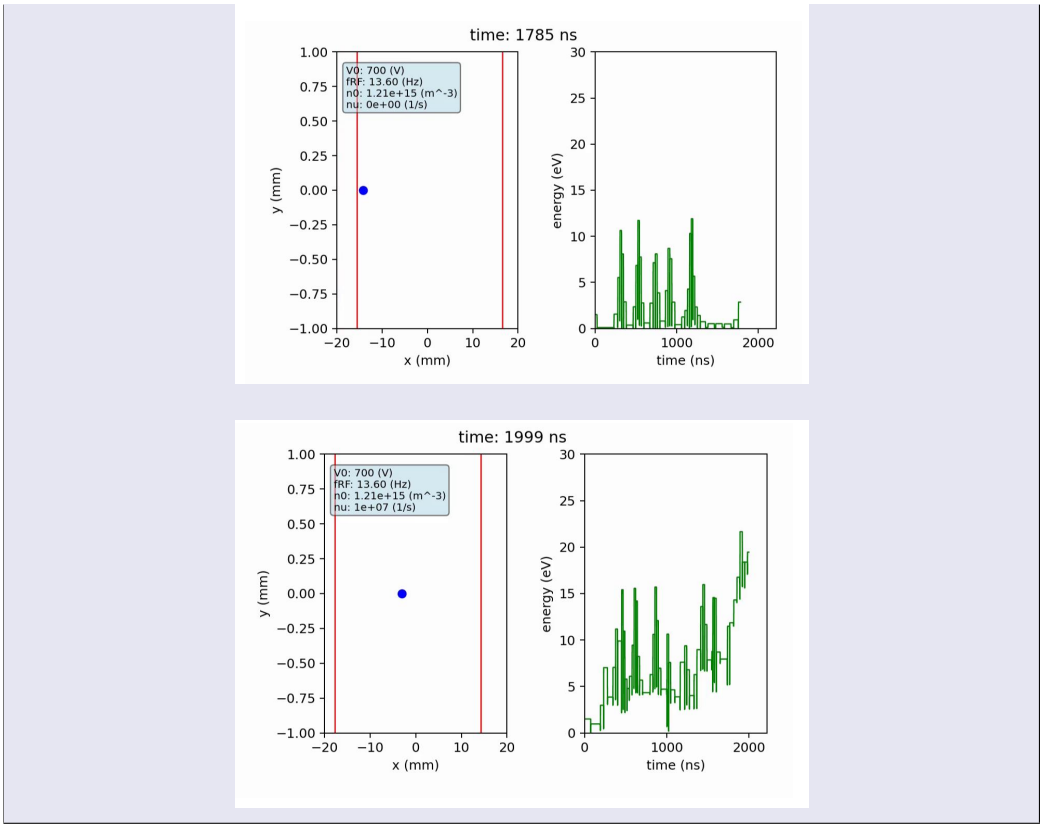

This acceleration of the electrons through collisions with the sheath has since also been observed experimentally many times. For this purpose, a parallel plate arrangement is considered, and the intermediate space of the discharge is observed time-resolved synchronously with the exciting alternating field. If emission lines are observed that have a short lifetime, an image of the exciting fast electrons is obtained. This method is referred to as **PROES (phase-resolved optical emission spectroscopy)**. These data are now plotted in a two-dimensional diagram, where one axis represents time and the other the location between the electrodes. According to the idea of stochastic heating, the collision at the sheath should lead to an electron beam that penetrates into the plasma, which is visible as a straight line in this PROES path-time diagram. The slope of this line is then the velocity of the electrons. Exactly this is the experimental finding, as shown in Fig. 3.18.
This PROES image shows only the acceleration of the electrons and not yet explicitly the heating of the discharge. For the electrons to experience a net energy gain, the phase of the electron relative to the oscillating field must change after a collision with the moving sheath. The electrons must therefore only collide with the sheath in a random phase. For this reason, it is referred to as **stochastic heating**.

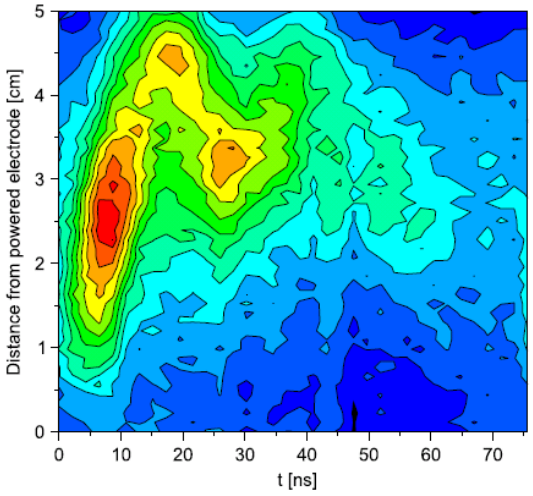

Figure 3.18: PROES data of an RF discharge [46].

3.2.3.2 Reflection of Electrons at Oscillating sheaths

In the following, we want to derive a simple model of stochastic heating. For this purpose, we first consider an electron with velocity v moving towards a sheath that is moving towards the electron with velocity v_{es}. After reflection, it has the velocity v_f (see Fig. 3.19). This velocity is greater than the initial velocity, which can be easily shown. For this purpose, we move into the rest frame of the moving sheath by subtracting v_{es} from all velocities:

$$v' = -v - v_{es} \tag{3.114}$$

$$v'_f = v_f - v_{es} \tag{3.115}$$

In the moving reference system, we approximate the sheath as a "hard wall", i.e., upon reflection of an electron, only the direction of the velocity changes, but not the energy of the electron and the magnitude of the momentum. Thus, we have:

$$v' = -v'_f \tag{3.116}$$

If we substitute this into Eq. 3.114 and 3.115, we obtain in the laboratory system:

$$v_f = -v + 2v_{es} \tag{3.117}$$

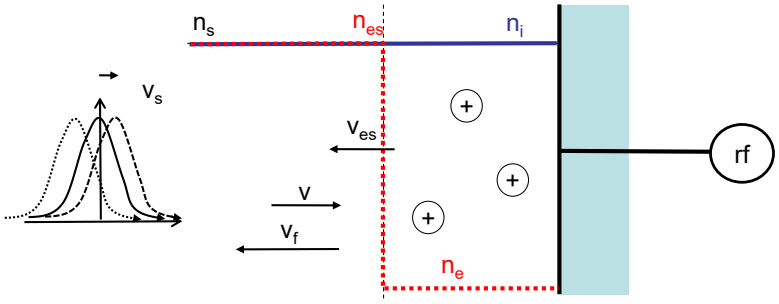

Figure 3.19: Fermi acceleration: Reflection of an electron with velocity v at a matrix layer with velocity v_{es}. If the electron and the sheath are moving towards each other, the velocity after reflection v_{f} is greater than v.

In this equation, it is important to note that the signs of the velocities must be considered. Thus, the velocity v_{es} points in the negative x-direction in Fig. 3.23. The energy gain then corresponds to:

$$\Delta E = \frac{1}{2} m_{\mathrm{e}} \left(v_{\mathrm{f}}^2 - v^2 \right) \tag{3.118}$$

Analogously, the reflection of an electron at the retreating sheath would also correspond to a deceleration ($v_{\mathrm{f}} = -v - 2v_{\mathrm{es}}$). However, the collisions of the electrons with the expanding and the retreating sheath are not equally probable, as will be discussed below.

3.2.3.3 Sheath with Homogeneous Ion Density Profile

The simplest model of an oscillating sheath is that of a matrix layer. The number of incident particles Δn with velocity v that collide with a surface element of the sheath per unit time Δt is

$$\frac{\Delta n}{\Delta t} = (|v| + |v_{\mathrm{es}}|) f(v) \mathrm{d}v \tag{3.119}$$

Analogously, the number of electrons hitting the retreating sheath would be:

$$\frac{\Delta n}{\Delta t} = (|v| - |v_{\mathrm{es}}|) f(v) \mathrm{d}v \tag{3.120}$$

Since $|v| + |v_{\mathrm{es}}| > |v| - |v_{\mathrm{es}}|$ applies, a net energy input is evident. Furthermore, it becomes clear that this model is only valid for the case that $v \gg v_{\mathrm{es}}$. Otherwise, the term $(v - v_{\mathrm{es}})$ would become negative, and the sheath would "overtake" the moving electron. This is referred to as the approximation of

a *slowly moving sheath* (**slow sheath approximation**). In the following, the contribution of the cooling of the electrons in the retreating sheath is neglected. The absorbed power per electron with velocity v is then:

$$\mathrm{d}P = \Delta E \frac{\Delta n}{\Delta t} = \frac{1}{2} m_\mathrm{e} (v_\mathrm{f}^2 - v^2)(v - v_\mathrm{es}) f(v) \mathrm{d}v \tag{3.121}$$

The term $(v - v_\mathrm{es})$ also takes into account the direction of the velocity vectors. That is, if, for example, v and v_es point in the same direction and are equal in magnitude, the heating disappears because no more collisions occur. The absorbed power by n electrons is obtained by integrating over the entire velocity space. If we also substitute Eq. 3.117, we obtain:

$$P = -2 m_\mathrm{e} \int_{v_\mathrm{es}}^{\infty} v_\mathrm{es} (v - v_\mathrm{es})^2 f(v) \mathrm{d}v \tag{3.122}$$

$$P = -2 m_\mathrm{e} \int_{v=v_\mathrm{s}}^{\infty} v_\mathrm{es} f(v) v^2 - 2 v_\mathrm{es}^2 v f(v) + v_\mathrm{es}^3 f(v) \mathrm{d}v \tag{3.123}$$

The velocity of the sheath is given as $v_\mathrm{es} = v_0 \cos \omega t$. The absorbed power corresponds to the **temporal average over an RF cycle**. As a result, the odd powers of v_s disappear upon averaging. If a Maxwell distribution is assumed for $f(v)$, we finally obtain:

$$\bar{P} = 2 m_\mathrm{e} v_0^2 \int_{v=\bar{v_\mathrm{s}}=0}^{\infty} v f(v) \mathrm{d}v = 2 m v_0^2 \frac{1}{4} v_\mathrm{th} n \tag{3.124}$$

or

$$\boxed{\bar{P} = \frac{1}{2} m_\mathrm{e} v_0^2 v_\mathrm{th} n} \tag{3.125}$$

The expression 3.125 can also be expressed through the RF current. For this purpose, we use:

$$j_\mathrm{rf} \cos \omega t = e n v_\mathrm{es}(t) = e n v_0 \cos \omega t \tag{3.126}$$

or

$$v_0 = \frac{j_\mathrm{rf}}{en} \tag{3.127}$$

Thus, the absorbed power per area through stochastic heating becomes:

$$\boxed{\bar{P} = \frac{1}{2} m_\mathrm{e} \frac{j_\mathrm{rf}^2}{e^2 n} v_\mathrm{th}} \tag{3.128}$$

At this point, we encounter a fundamental problem in the analytical description of stochastic heating. An important input parameter is the assumption about the distribution function of the electrons reflecting at the sheath edge. This distribution function $f_s(v)$ at the location of the sheath edge is certainly not identical to a Maxwell distribution $f(v)$ in the volume, since the acceleration process takes place there. That is, the model is not yet self-consistent. In the case of the matrix layer, we also get another problem: the oscillation at the electron sheath with an alternating current $n_{es}v_{es}$ cannot occur independently of the oscillation of the electrons in the plasma volume. There, the identical alternating current must flow with $n_s v_s$ (index s denotes the density and velocity of the electrons at the ion edge at $x = 0$). If we assume a matrix layer, $n_s = n_{es}$ applies. Thus, the oscillations of the velocities must also be equal, and no acceleration can occur. This can only be resolved by choosing a more realistic description of the sheath.

3.2.3.4 Sheath with Inhomogeneous Ion Density Profile

The model of stochastic heating with a homogeneous density profile leads to the contradiction that no heating can occur, since the electrons in the volume must oscillate with the same amplitude as the sheath edge itself. This can be resolved by choosing a more realistic model of the sheath. Fig. 3.20 shows such a sheath in which the ion density is approximately static in the first approximation and follows the typical course as in a Child-Langmuir sheath. We can define an ion sheath edge and a moving electron sheath edge. The electron density now oscillates with the applied RF voltage. Since the ion density in the sheath is lower than in the volume, the electron density at the electron sheath edge n_{es} must also be lower than in the volume (the densities at the ion sheath edge should be n_s). Since the RF current in the volume as well as at the electron sheath edge must now be equal, it is immediately apparent that the oscillation of the electrons in the volume must be smaller than the movement of the sheath edge. Thus, we obtain stochastic heating, since the electrons collide with a faster electron sheath edge. We now want to derive this quantitatively.
First, we consider the distribution function of the electrons in the plasma volume $f_s(v)$. Without the RF field in the volume, the distribution function is a simple Maxwell distribution $f_m(v)$. In the volume, the electrons oscillate with $v_s = v_0 \sin \omega t = v_0 \sin \phi$. As a result, the distribution function $f_m(v)$ moves back and forth with v_s, and we can set $f_s(v) = f_m(v - v_s)$. That is, our reference system for the electrons that hit the sheath edge moves with v_s. The densities in the volume are n_s and at the electron sheath edge n_{es}. The distribution functions integrated over velocity give the density of the

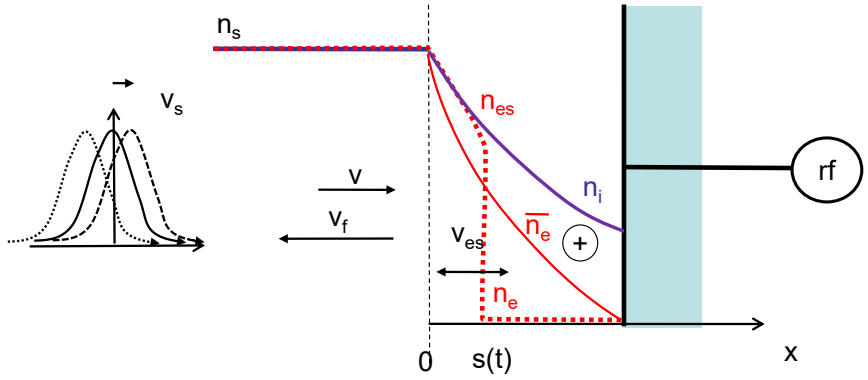

Figure 3.20: sheath with inhomogeneous ion density profile. An ion sheath edge at $x = 0$ with density n_s and an oscillating electron sheath edge at $x = s(t)$ with local density n_{es} are distinguished.

electrons at this location. Therefore, we have:

$$f_s(v) \propto n_s \tag{3.129}$$

$$f_{es}(v) \propto n_{es} \tag{3.130}$$

$$f_{es}(v) = \frac{n_{es}}{n_s} f_s(v) = \frac{n_{es}}{n_s} f_m(v - v_s) \tag{3.131}$$

If we now solve our question in the variable $v' = v - v_s$, we can consider the simple distribution function in the plasma volume for $f_m(v')$. The acceleration now arises from the relative velocity of the electrons in the volume v_s compared to the velocity v_{es} at the electron sheath edge.

$$v_R(\phi) = v_{es} - v_s = v_{es} - v_0 \sin\phi \tag{3.132}$$

That is, we now have to determine how the electron sheath moves in the inhomogeneous density profile, as illustrated in Fig. 3.24, to obtain $v_R(\phi)$. It should be noted that the movement of the sheath is fast compared to the inertia of the ions, i.e., they only see an averaged profile of the electron density $\bar{n}_e$. Initially, energy and flux conservation of the ions applies:

$$n_{\text{Ionen}}(x) v_{\text{Ionen}}(x) = n_0 v_B \tag{3.133}$$

$$\frac{1}{2} M v^2_{\text{Ionen}}(x) = \frac{1}{2} M v_B^2 - e\bar{\Phi} \tag{3.134}$$

with $\bar{\Phi}$ the temporally averaged potential that the ions see. The electric field in the region of the sheath is then:

$$\frac{\partial E}{\partial x} = \left\{ \begin{array}{ll} \frac{e}{\epsilon_0} n_{\mathrm{Ionen}}(x) & x > s \\ 0 & x < s \end{array} \right\}. \tag{3.135}$$

Charges and fields are connected via the Poisson equation:

$$\frac{\partial \bar{E}}{\partial x} = \frac{e}{\epsilon_0} \left(n_{\mathrm{Ionen}}(x) - \bar{n}_{\mathrm{e}} \right) \tag{3.136}$$

and

$$\frac{\partial \bar{\Phi}}{\partial x} = -\bar{E} \tag{3.137}$$

The averaged electron density in the sheath is given by the following simple approach:

$$\bar{n}\mathrm{e}(x) = \left(1 - \frac{2\phi}{2\pi} \right) n\mathrm{Ionen}(x) \tag{3.138}$$

with 2ϕ the length of the phase in the RF cycle at $x < s(t)$. That is, if we are approximately at the location x at the ion sheath edge, the electron sheath position is larger most of the time, i.e., ϕ is small, and thus $\bar{n}\mathrm{es}(x) = n\mathrm{Ionen}(x)$. Shortly before the surface, the length of the phase with $x > s(t)$ is very large. Thus, 2ϕ also becomes large, and we obtain $\bar{n}_{\mathrm{es}}(x) \approx 0$. This is illustrated in Fig. 3.21.
From equations 3.133 to 3.138, we obtain the spatial distribution of the ion density $n_{\mathrm{Ionen}}(x)$ as well as the velocity of the electron sheath $v_{\mathrm{es}}(t)$. This gives:

$$v_R(\phi) = \pm v_0 \frac{1}{8} \left(\frac{s_0^2}{\pi \lambda_D^2} \right) \left(-\frac{3}{2} \cos\phi + 3\phi \sin\phi + \frac{3}{2} \cos 3\phi + \phi \sin 3\phi \right) \tag{3.139}$$

The + sign is for the phases $\phi = [0, \pi]$ and the - sign for $\phi = [-\pi, 0]$. Here, s_0 is the effective amplitude of the electron oscillations in the plasma volume from

$$s_0 = \frac{j_{rf}}{e \omega n_s} \tag{3.140}$$

The description of stochastic heating in the homogeneous density profile was:

$$\bar{P} = -2 m_{\mathrm{e}} \int_{v_{\mathrm{s}}}^{\infty} v_{\mathrm{es}} \left(v + v_{\mathrm{es}} \right)^2 f_{\mathrm{es}}(v) \mathrm{d}v \tag{3.141}$$

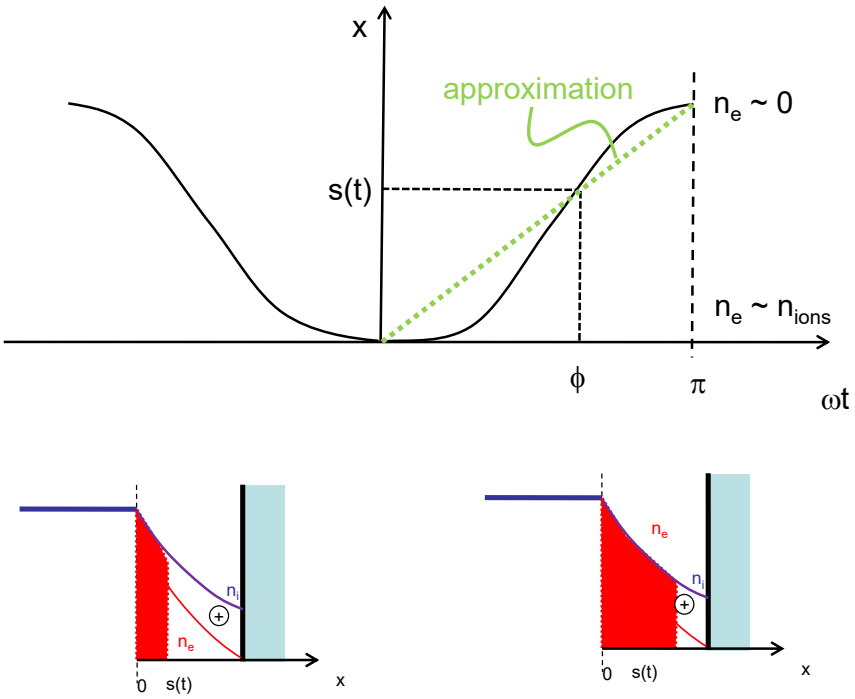

Figure 3.21: Linking the phase ϕ and the position of the electron sheath edge $s(t)$.

We first transform again into variables relative to the movement of the electrons in the plasma bulk, i.e., $v' = v - v_\mathrm{s}$, and additionally we use the connection of the distribution functions according to:

$$f_\mathrm{es}(v) = \frac{n_\mathrm{es}}{n_s} f_m(v - v_s) \tag{3.142}$$

Thus, we obtain:

$$P = -2m_\mathrm{e}\frac{n_{es}}{n_s}\int_{v_R}^{\infty} v_\mathrm{es}\left(v' + v_\mathrm{s} - v_\mathrm{es}\right)^2 f_m(v')\mathrm{d}v' \tag{3.143}$$

or

$$P = -2m_\mathrm{e}\frac{n_{es}}{n_s}\int_{v_R}^{\infty} v_\mathrm{es}\left(v'^2 - 2v'\underbrace{(v_\mathrm{es} - v_\mathrm{s})}_{v_R(\phi)} + \underbrace{(v\mathrm{es} - v_\mathrm{s})}_{v_R(\phi)}2\right) 2f_m(v')\mathrm{d}v' \tag{3.144}$$

The lower limits of the integrals can always be approximated to 0. Now we substitute $v_R = v_{es} - v_0 \sin\phi$ and $n_{es}v_{es} = n_s v_s$ and average over all possible ϕ (which corresponds to temporal averaging) and obtain

$$\begin{aligned} \bar{P} &= -2m_e v_0 \frac{1}{2\pi}\int_{-\pi}^{\pi} \sin\phi d\phi \int_{v_R}^{\infty} v'^2 f_m(v')dv' && (3.145)\\ &\quad +4m_e v_0 \frac{1}{2\pi}\int_{-\pi}^{\pi} \sin\phi v_R(\phi) d\phi \int_{v_R}^{\infty} v' f_m(v')dv' && (3.146)\\ &\quad -2m_e v_0 \frac{1}{2\pi}\int_{-\pi}^{\pi} \sin\phi v_R^2(\phi) d\phi \int_{v_R}^{\infty} f_m(v')dv' && (3.147) \end{aligned}$$

From the symmetry of the ϕ-dependence of $v_R(\phi)$, we can see that only the second term remains upon temporal averaging, and we obtain:

$$\bar{P} = 4m_e v_0 \frac{1}{2\pi}\int_{-\pi}^{\pi} \sin\phi v_R(\phi) d\phi \int_{v_R}^{\infty} v' f_m(v')dv' \qquad (3.148)$$

The integral over the distribution function gives exactly the thermal velocity of the electrons. By integrating over $d\phi$, we finally obtain:

$$\boxed{\bar{P} = \frac{3}{32}\pi \frac{s_0^2}{\lambda_{\mathrm{D}}^2} m_{\mathrm{e}} n_s v_{\mathrm{th}} v_0^2} \qquad (3.149)$$

Here, s_0 is the effective amplitude of the electron oscillations in the plasma volume and λ_{D} is the Debye length.
This result is in principle more accurate than Eq. 3.125 and is illustrated in Fig. 3.22 from [25]. The limiting case according to Eq. 3.125 is the upper limit, which is only reached if the electron density at the electron sheath edge is much smaller than that of the ion sheath. In this reference, a very simple estimate is also shown, which, however, already reproduces the behavior very well. For this purpose, the quantities in Eq. 3.125

$$P = \frac{1}{2} m_{\mathrm{e}} v_0^2 v_{\mathrm{th}} n \qquad (3.150)$$

are replaced by densities n_{es} and n_s and velocities v_{es} and v_{es} at the electron sheath edge and the ion sheath edge, respectively. Furthermore, it is assumed that the absorbed power depends on the relative velocity $v_{\mathrm{es}} - v_{\mathrm{s}}$ and the density of the electrons at the electron sheath edge n_{es} itself. Thus, we obtain:

$$P = \frac{1}{2} m_{\mathrm{e}} \left(v_{\mathrm{es}} - v_s\right)^2 v_{\mathrm{th}} n_{\mathrm{es}} \qquad (3.151)$$

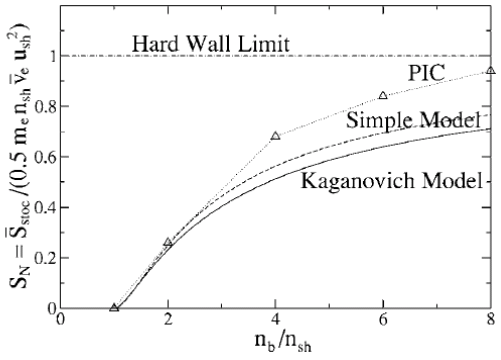

Figure 3.22: Efficiency of stochastic heating as a function of the ratio of electron density in the volume to electron density at the sheath edge [25]. The parameter on the x-axis is n_s/n_{es}.

With current conservation in the sheath

$$n_{\mathrm{es}} v_{\mathrm{es}} = n_s v_{\mathrm{s}} \tag{3.152}$$

we finally obtain

$$\boxed{P = \frac{1}{2} m_{\mathrm{e}} v_{\mathrm{es}}^2 \left(1 - \frac{n_{\mathrm{es}}}{n_s}\right)^2 v_{\mathrm{th}} n_{\mathrm{es}}} \tag{3.153}$$

It can be seen that the expression is reduced by a factor $\left(1 - \frac{n_{\mathrm{s}}}{n_0}\right)^2$ compared to the simplest description of the model of homogeneous ion density. If $n_{\mathrm{es}} \to n_s$, we obtain the model of homogeneous ion density and the heating disappears. If $n_{\mathrm{es}} \to 0$, we obtain a model in which an electron is accelerated by a collision with a hard wall.
The expression 3.153 describes how stochastic heating varies with the oscillation of the sheath: if $x \propto 0$, $n_{es} \propto n_s$ and the heating is inefficient, if $x \propto s_{max}$, the factor $(1 - n_{es}/n_s)$ is large but the number of electrons n_{es} that are accelerated at $x \propto s_{max}$ is very small.
However, some assumptions have been made in these models that limit their applicability:

- *Maxwell distribution*

The distribution function is always assumed to be Maxwell. However, the region at the sheath edge can certainly not be well described by a Maxwell distribution.

- *Self-consistency*

  The feedback of the electron oscillations in the plasma volume is assumed to be given and not self-consistently calculated as a result of the movement of the sheath.

Attempts have been made to remedy these deficiencies in the description through numerous analytical approaches. These have included different forms of the ion density distribution in the sheath, a strictly kinetic description of the distribution function at the sheath edge, or fluid methods in which the energy transfer at the sheath edge was encoded by very high local temperatures. None of these approaches could describe the absolute efficiency of stochastic heating. The analytical methods have in common that they essentially assume an almost undisturbed plasma bulk, which must be adapted in a suitable form to the boundary condition of an oscillating sheath. It is precisely this adaptation that influences the result of the calculation very sensitively.
The numerical variants usually refer to PIC codes that describe the dynamics of the electrons in a parallel plate arrangement. Here, too, the heating of the electrons at the expanding sheath and the cooling at the retreating sheath are observed. Both effects do not cancel each other out completely, and a net heating occurs. However, the absolute contributions of heating and cooling are so large that the difference, although it results in a net heating, remains with a large error.

3.2.3.5 Heating by Plasma Series Resonance or Higher Harmonics of the Excitation Frequency

A completely different approach to the problem of stochastic heating is chosen with an electrical equivalent circuit diagram of a discharge in which the heating corresponds to a damping term in the oscillation equation [34, 14]. In Fig. 3.23, this is illustrated. The sheaths are each capacitors, while the dissipation through collisions in the plasma bulk corresponds to an ohmic resistance and the inertia of the electrons corresponds to an inductance. With this approach, the acceleration at the oscillating sheath and the subsequent isotropization are no longer discussed separately, but an attempt is made to directly identify the dissipation of an alternating current as heating.

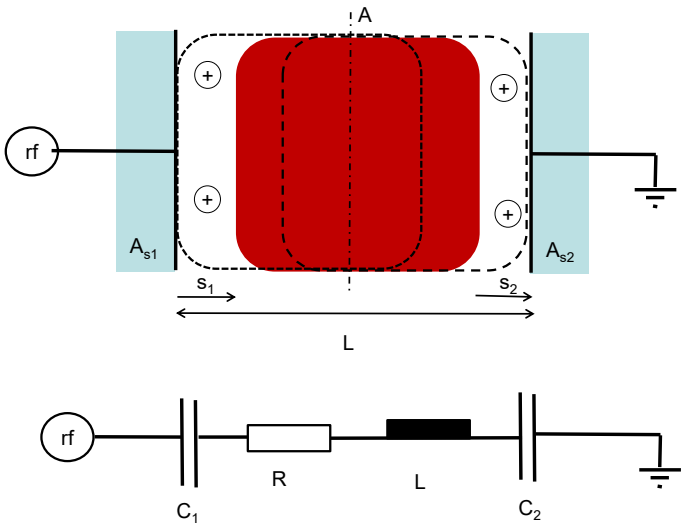

Figure 3.23: Simplest electrical model of a capacitive discharge.

For this purpose, we first consider a plasma between two electrodes. By applying an external alternating voltage, oscillations of the plasma bulk can be excited. This oscillation also has a natural frequency, which is given by:

$$\omega_{\mathrm{PSR}} \simeq \sqrt{\frac{s}{L}}\omega_{\mathrm{p}} \tag{3.154}$$

This frequency is referred to as **plasma series resonance**. It is lower than the plasma frequency ω_{p} of the electrons by the square root ratio of sheath thickness s and extension of the discharge L. Typical values are in the range of 100 MHz for a plasma frequency in the GHz range. That is, this frequency lies between the typical excitation frequency of 13.56 MHz and the plasma frequency. One also refers to this frequency as **geometric resonance**.
Now let us first consider this oscillation in the fluid picture:

$$mn\left[\frac{\partial v}{\partial t} + v\frac{\partial v}{\partial x}\right] = -enE - \nabla p - mvn\nu_{\mathrm{m}} \tag{3.155}$$

We assume that there is no spatial gradient in the velocity and no pressure gradients are present, and we obtain the free damped oscillation in the fluid picture according to:

$$\frac{m}{e}\left[\frac{\partial v}{\partial t} + \nu_{\mathrm{m}} v\right] = -E \tag{3.156}$$

or

$$\frac{m}{e}\left[\frac{\partial}{\partial t}+\nu_{\mathrm{m}}\right]v=\nabla\Phi \tag{3.157}$$

We replace the velocity by the current in the discharge $I = envA$ and obtain:

$$\frac{m}{e}\left[\frac{\partial}{\partial t}+\nu_{\mathrm{m}}\right]\frac{I}{enA}=\nabla\Phi \tag{3.158}$$

The potential drop across the plasma bulk U_{bulk} is obtained by integrating from one sheath edge to the opposite one. Thus, we obtain an equation that links the current I and voltage U_{bulk}:

$$\frac{m\bar{L}}{\bar{n}\bar{A}e^2}\frac{\mathrm{d}I}{\mathrm{d}t}+\frac{m\bar{L}}{\bar{n}\bar{A}e^2}\nu_{\mathrm{m}}I=U_{\mathrm{bulk}} \tag{3.159}$$

Here, we have expressed the integral

$$\int_{s_1}^{s_2}\frac{1}{n(s)A(s)}\mathrm{d}s=\frac{\bar{L}}{\bar{n}\bar{A}} \tag{3.160}$$

through averaged quantities $\bar{n}$, $\bar{L}$ and $\bar{A}$. In analogy to the equivalent circuit diagram, it can be seen that the term before $\frac{\mathrm{d}I}{\mathrm{d}t}$ corresponds to an inductance, while the term before I corresponds to an ohmic resistance.
The capacitor of the equivalent circuit diagram is given by the sheaths. For these, we again assume a matrix layer and calculate the voltage that drops across it:

$$\Delta\Phi=-\frac{e}{\epsilon_0}n_{\mathrm{s}} \tag{3.161}$$

In the case of the matrix layer, or under the approximation that, even in the case of another type of layer, the charge in the layer can be approximated as an average $\bar{n}_{\mathrm{s}}$, we obtain

$$\nabla\Phi=-\frac{e}{\epsilon_0}\bar{n}_{\mathrm{s}}z \tag{3.162}$$

or the potential of the sheath

$$U_{\mathrm{sheath}}=\int_0^s-\frac{e}{\epsilon_0}\bar{n}\mathrm{s}z\mathrm{d}z=-\frac{1}{2\epsilon_0}e\bar{n}\mathrm{s}s^2 \tag{3.163}$$

The charge in this sheath is:

$$Q=e\int_0^s\bar{n}\mathrm{s}A\mathrm{s}\mathrm{d}z=e\bar{n}_sA_ss \tag{3.164}$$

With this substitution, the relationship between voltage and charge becomes:

$$U_{\text{sheath}} = -\frac{1}{2\epsilon_0} e\bar{n}s \left(\frac{Q}{e\bar{n}\text{s}A_\text{s}} \right)^2 \tag{3.165}$$

We recognize that the voltage depends on the square of the charge in the sheath. This corresponds to the so-called **nonlinearity of the sheath** in contrast to a simple capacitor in which charge and voltage are directly proportional.
Thus, we obtain as the overall equation for a capacitive discharge with two sheaths, which is driven by an external voltage source U_rf under neglect of friction:

$$\boxed{U_\text{rf} = -\frac{1}{2\epsilon_0 e\bar{n}_\text{s}A_\text{s1}2} Q_1^2 - \frac{1}{2\epsilon_0 e\bar{n}_\text{s}A_\text{s2}2} Q_2^2 + \frac{m\bar{L}}{\bar{n}\bar{A}e^2}\ddot{Q}} \tag{3.166}$$

For the simple case of a symmetric discharge, we can transform this equation by first substituting $Q = -en_\text{s}A_\text{s}s$ again, and we obtain.

$$U_\text{rf} = \frac{1}{2\epsilon_0}\frac{s_1}{A_\text{s1}}Q_1 + \frac{1}{2\epsilon_0}\frac{s_2}{A_\text{s1}}Q_2 + \frac{m\bar{L}}{\bar{n}\bar{A}e^2}\ddot{Q} \tag{3.167}$$

In this equation, the quadratic dependence still exists, since naturally s_1 and s_2 change over time.
In the case of a symmetric discharge, the oscillating charge Q of both sheaths is equal, and $Q_1 = Q_2 = Q$ as well as $A_\text{s1} = A_\text{s2} = A_\text{s}$, or $\bar{A}_\text{s} = \bar{A}$. Furthermore, it is also evident that although s_1 and s_2 change, due to symmetry reasons $\frac{1}{2}(s_1 + s_2) = s = const.$ must apply. Thus, we obtain:

$$U_\text{rf} = \frac{1}{\epsilon_0}\frac{s}{A_\text{s}}Q + \frac{m\bar{L}}{\bar{n}\bar{A}e^2}\ddot{Q} \tag{3.168}$$

It can be seen that the nonlinearity disappears if a symmetric discharge is considered. From this, the plasma series resonance can now be directly read off according to:

$$\frac{A\bar{n}e^2}{m\bar{L}}U_\text{rf} = \underbrace{\frac{\bar{n}e^2}{\epsilon_0 m}\frac{s}{\bar{L}}}_{\omega^2\text{PSR}} Q + \ddot{Q} \tag{3.169}$$

This is the differential equation of a harmonic oscillator with a natural frequency ω_PSR.
Equation 3.167 can now be set up for the simple case of a strongly asymmetric discharge $\bar{A}\text{s}1 \ll \bar{A}\text{s}2$. Thus, the term of the second sheath disappears and $Q_1 = Q$. We obtain:

$$U_{\mathrm{rf}} = -\frac{1}{2\epsilon_0 e \bar{n}_{\mathrm{s}} A_{\mathrm{s}}^2} Q^2 + \frac{m\bar{L}}{\bar{n}\bar{A}e^2}\ddot{Q} + \frac{m\bar{L}}{\bar{n}\bar{A}e^2}\nu_{\mathrm{m}}\dot{Q} \tag{3.170}$$

In the case of a strongly asymmetric sheath, full modulation of the voltage occurs, and we obtain as a simple approach:

$$U_{\mathrm{rf}} = -\frac{\Phi_0}{2}\left(1 - \cos(\omega_{\mathrm{rf}} t)\right) \tag{3.171}$$

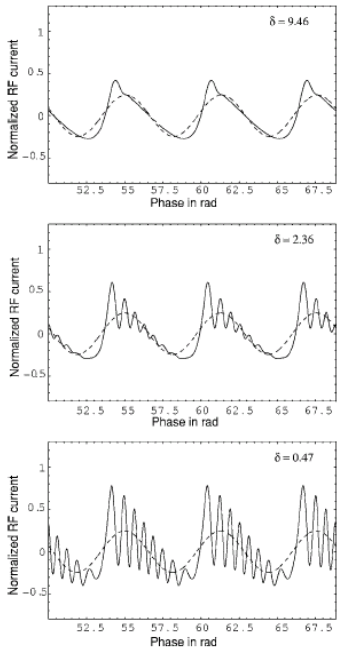

Figure 3.24: Model of the time dependence of the current in an asymmetric RF discharge for 20 Pa, 5 Pa and 1 Pa (from top to bottom) [34].

Equation 3.170 must now be solved to determine the current in the discharge that is generated at a given external voltage. However, this solution is not easy to set up due to the nonlinearity, and thus only numerical solutions or analytical approximations exist. Therefore, only the principal behavior of the solutions should be described here.
Due to the nonlinearity of the oscillation equation, it is clear that the solutions for Q or j contain higher harmonics. That is, the oscillation exists not

only at the fundamental frequency ω_{rf} but also at multiples thereof. These oscillations, however, cannot oscillate freely but are damped. An example of these solutions is shown in Fig. 3.24. It can be seen that especially at low pressures the oscillations build up in the phases of the RF cycle in which the sheath pushes the electrons into the plasma volume. These oscillations are more pronounced the lower the pressure is. In this figure, stochastic heating consists of the effect that at low pressures the displacement current increases and its ohmic damping thus leads to more efficient power absorption. That is, in the expression.

$$P_{\mathrm{ges}} = \frac{1}{2} I_{\mathrm{rf}}^2 \frac{1}{\sigma_{\mathrm{rf}}} d \tag{3.172}$$

Although the conductivity σ_{rf} becomes larger with low pressure, this is overcompensated by an increase in I_{rf} through the higher harmonics. A quantitative comparison of the efficiency of this model with the data shown in Fig. **??** achieves astonishing agreement. This model also means that stochastic heating must disappear in symmetric discharges, since the nonlinearities of both sheaths compensate each other. Exactly this is the observation in the experiment.

That the models based on the plasma series resonance work so well is surprising, since they make assumptions in principle that were forbidden in the previous models based on Fermi acceleration. That is, the assumption of a matrix layer is inadmissible and also in itself too coarse an approximation of a real RF sheath. The great advantage of the models based on the plasma series resonance is the fact that the entire plasma is considered as a whole and the heating is considered directly. The models based on Fermi acceleration, on the other hand, are of microscopic nature and initially only describe the acceleration but not the heating of the particles. It is precisely the second step of heating that requires assumptions about the transition of a sheath electron with its directed motion into an electron with undirected motion in the volume. It is precisely these assumptions that lead to contradictions and deviations between model and measurement. One recognizes from this discussion that the phenomenon of stochastic heating or the efficiency of heating at low pressures is not yet sufficiently understood, because all models so far do not yet correctly include the exact dynamics of the sheath and the bulk plasma, or the movement of ions and electrons.

At this point, the modified ohmic heating according to the plasma series resonance can be compared with the stochastic heating according to Eq. 3.128. The stochastic heating for an RF current flowing through a surface of an electrode is:

$$\bar{P}_{\text{stochastic}} = \frac{1}{2}\frac{m v_{\text{th}}}{n e^2} j_{\text{rf}}^2 \qquad \left[\frac{\text{W}}{\text{m}^2}\right] \tag{3.173}$$

This is a power per area. If we compare this with the ohmic power per volume (for small ω):

$$\bar{P}\text{ohmic} = \frac{1}{2}\frac{m \nu_{\text{m}}}{n e^2} j_{\text{rf}}^2 \qquad \left[\frac{\text{W}}{\text{m}^3}\right] \tag{3.174}$$

If we want to compare both expressions, we must multiply the ohmic power by the length L of the discharge to obtain a power per electrode area:

$$\bar{P}\text{ohmic} = \frac{1}{2}\frac{m \nu_{\text{m}} L}{n e^2} j_{\text{rf}}^2 \qquad \left[\frac{\text{W}}{\text{m}^2}\right] \tag{3.175}$$

From a comparison of Eq. 3.173 and 3.175, we recognize that the expression $\nu_{\text{m}} L$ is replaced by the thermal velocity v_{th}.
The plasma series resonance or the efficiency of power coupling is also practically used as a diagnostic. Via an electrode that is embedded in the chamber wall, the RF current to ground is measured. From the shape of the signal, the effective collision frequency as well as the electron density can be read off. At a high collision rate, the oscillations are strongly damped, while they can build up well at a low collision rate. The amplitude of the oscillations is proportional to the electron density. This type of diagnostics is particularly attractive for industrial processes, since the sensors react sensitively even before the actual failure of the process: if, for example, a mass flow controller drifts out of its set range, the plasma characteristics change, which can be read off from a change in the higher harmonics in the RF current. This change is measurable but still so small that the current substrates can still be processed before the system is shut down and the mass flow controller is corrected. The diagnostics thus function as an early warning system for the performance of the plasma system. These diagnostics are referred to as **SEERS (Self excited electron resonance spectroscopy)**.

3.2.4 Wave Heating

3.2.4.1 General

A distinction between ohmic, stochastic, and wave heating is partly arbitrary. In all cases, energy is transferred to the electrons by uniform or varying electric fields. In the case of electromagnetic waves, the frequency is so high that the wave itself, in contrast to electrostatic waves, generates a significant magnetic field of its own:

$$\nabla \times \vec{B} = \epsilon_0 \mu_0 \dot{\vec{E}} \tag{3.176}$$

At these high frequencies, resonant heating also becomes relevant, since the excitation frequency lies in the range of the cyclotron resonance frequency.

$$\omega_c = \frac{eB}{m} \tag{3.177}$$

The technical implementation of wave heating is very complex, since the resonance effect can only be generated in a limited plasma volume; in general, the generation of a magnetic field itself is very expensive, and finally, the radiation sources for the necessary GHz radiation are also complex.
First, we consider the propagation of an electromagnetic wave in a magnetized plasma (magnetic field $\vec{B}_0$). With the Maxwell equations

$$\nabla \times \vec{B}_0 = \mu_0 \vec{j} + \epsilon_0 \mu_0 \dot{\vec{E}} \tag{3.178}$$

$$\nabla \times \vec{E} = -\dot{\vec{B}}_0 \tag{3.179}$$

We finally obtain a wave equation of the form:

$$-\nabla \times \left(\nabla \times \vec{E} \right) = - \left(\nabla \left(\nabla \cdot \vec{E} \right) - \nabla 2 \vec{E} \right) = \mu_0 \dot{\vec{j}} + \frac{1}{c2} \ddot{\vec{E}} \tag{3.180}$$

From this, with the Fourier ansatz for waves of a certain wavenumber k and frequency ω, we obtain:

$$\vec{k} \left(\vec{k} \cdot \vec{E} \right) - k^2 \vec{E} = -\imath \omega \mu_0 \vec{j} - \frac{1}{c^2} \omega^2 \vec{E} \tag{3.181}$$

3.2.4.2 Waves in Magnetized Plasmas

We now want to consider the relationship between wavenumber and frequency in more detail for two limiting cases:

- *Waves $\perp$ to $\vec{B}_0$*

  We consider the case where the electromagnetic waves are incident on the plasma perpendicular to the external magnetic field $\vec{B}_0$. The force ansatz for this case is again:

$$m\frac{\partial \vec{v}_1}{\partial t} = -e\left(\vec{E}_1 + \vec{v}_1 \times \vec{B}_0\right) \tag{3.182}$$

  In the Fourier ansatz, this becomes:

$$-mi\omega\vec{v}_1 = -e\vec{E}_1 - e\left(\vec{v}_1 \times \vec{B}_0\right) \tag{3.183}$$

  With this description of the velocity, we can determine the current $\vec{j}$ and obtain.

$$\vec{j_1} = en\vec{v}_1 \tag{3.184}$$

  This quantity can now be inserted into the wave equation. After some transformations [1] we obtain, with the help of $ck = n\omega$, the dispersion to:

$$c^2k^2 = \omega^2 \underbrace{\left[1 - \frac{\omega_\mathrm{p}^2}{\omega^2}\frac{\omega^2 - \omega_\mathrm{p}^2}{\omega^2 - \omega_\mathrm{oh}^2}\right]}_{n^2} \tag{3.185}$$

  with the so-called **upper hybrid frequency**:

$$\omega_\mathrm{oh}^2 = \omega_\mathrm{p}^2 + \omega_\mathrm{c}^2 \tag{3.186}$$

  The quantity $1/n^2$ is illustrated in Fig. 3.25. At points where the refractive index becomes zero and $1/n^2 \to \infty$, a cut-off occurs. That is, the wave is reflected. These two characteristic frequencies ω_R and ω_L are given by:

$$1 - \frac{\omega_p^2}{\omega^2} = \pm\frac{\omega_c}{\omega_{R,L}} \tag{3.187}$$

  At the upper hybrid frequency, $n \to \infty$ and a resonance occurs. At this frequency, the gyration motion superimposes with the plasma oscillations and a resonance occurs.

[1] Section 5.2.2 in the script "Introduction to Plasma Physics"

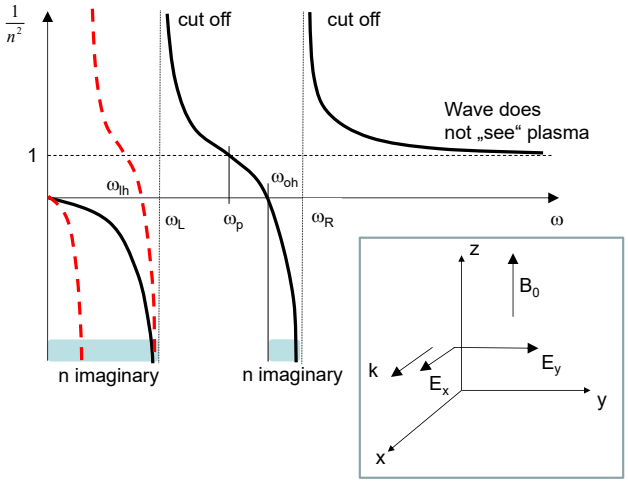

Figure 3.25: $1/n^2$ for waves in magnetized plasmas that propagate perpendicular to the magnetic field. The dashed lines (in red) refer to ion waves that can be excited since the ions can also follow the field oscillations at low frequencies.

This derivation has initially only considered the dynamics of the electrons. If we go to low frequencies, the ion motion can also be resonantly heated at the ion cyclotron frequency. Here, too, the plasma oscillations and the gyration of the ions superimpose. This resonance frequency is referred to as the **lower hybrid frequency**:

$$\omega_{\mathrm{uh}} = \omega_{\mathrm{ce}} \left(\frac{\omega_{\mathrm{ci}}^2 + \omega_{\mathrm{pi}}^2}{\omega_{\mathrm{pe}}^2 + \omega_{\mathrm{ce}}^2} \right) 1/2 \tag{3.188}$$

With the cyclotron and plasma frequency of the ions ω_{ci} and ω_{pi}, as well as the cyclotron and plasma frequency of the electrons ω_{ce} and ω_{pe}. For technical plasmas, these lower hybrids are interesting since the frequency may be in the radio range. However, this requires a very low gas pressure since the movement of the ions must proceed undisturbed on their gyration path in order to effectively absorb energy. If the electron density is high, $\omega_{\mathrm{pe}} \gg \omega_{\mathrm{ce}}$ applies, and the expression for the lower hybrid reduces to:

$$\omega_{\mathrm{uh}} = \left(\omega_{\mathrm{ci}} \omega_{\mathrm{ce}}\right)^{1/2} \tag{3.189}$$

- *Waves | to* $\vec{B}_0$

  The second limiting case is waves that propagate along the direction of the magnetic field. We start again with the wave equation:

$$\vec{k}\left(\vec{k}\cdot\vec{E}\right) - k^2\vec{E} = -\imath\omega\mu_0\vec{j} - \frac{1}{c^2}\omega^2\vec{E} \tag{3.190}$$

  and the momentum balance of an electron.

$$-\imath\omega m\vec{v}_1 = -e\vec{E}_1 - e\vec{v}_1 \times \vec{B}_0 \tag{3.191}$$

  with

$$\vec{j} = -en\vec{v}_1 \tag{3.192}$$

  If we insert this into the wave equation and consider the corresponding directions, we finally obtain the expression:

$$n2 = 1 - \frac{\omega_\mathrm{p}^2}{\omega^2}\frac{1}{1 \mp \frac{\omega_\mathrm{c}}{\omega}} \tag{3.193}$$

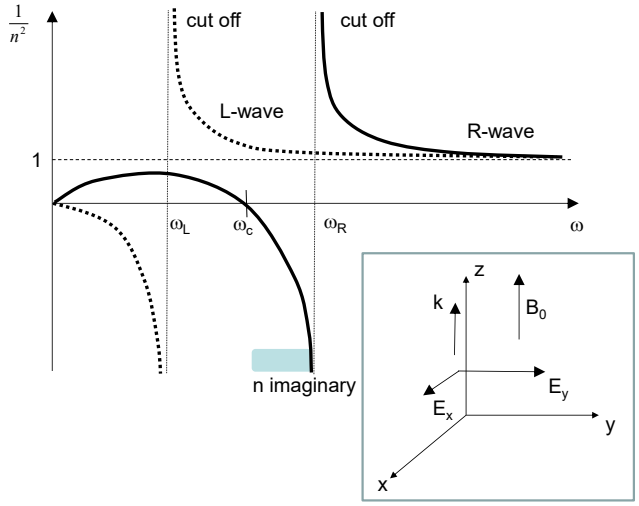

Figure 3.26: $1/n^2$ for waves in magnetized plasmas that propagate parallel to the magnetic field.

The two signs correspond to a right and a left circularly polarized wave. Here, too, it can be seen that a resonance occurs for the right circularly polarized wave at the cyclotron frequency ω_c ($n \to \infty$, see Fig. 3.26). The E-field circulates synchronously with the gyration motion. Since this depends on the direction of rotation, it is immediately clear that the left circularly polarized wave cannot heat this plasma.

Unlike the waves perpendicular to the magnetic field, here the plasma oscillations of the electrons do not superimpose. In the case of waves parallel to the magnetic field, the oscillations occur along this direction of propagation. That is, the fluctuating E-field of this oscillation is perpendicular to the direction of motion of the electrons on the gyration path and can thus not influence the resonance frequency.

3.2.4.3 Absorbed Power through Wave Heating

So far, we have considered the propagation of waves in magnetized plasmas and seen that, depending on the orientation, resonances occur at the cyclotron or the upper/lower hybrid frequency. In the following, however, we want to consider the ohmic power absorption in a collisional plasma. We consider the simple case of the equation of motion of the electrons in a configuration with a magnetic field in the z-direction and an E-field of the wave in the x-direction. Thus, we obtain:

$$m\frac{\mathrm{d}^2x}{\mathrm{d}t^2} + m\nu_\mathrm{m}\frac{\mathrm{d}x}{\mathrm{d}t} + eB\frac{\mathrm{d}y}{\mathrm{d}t} = -eE_0\sin\omega t \tag{3.194}$$

$$m\frac{\mathrm{d}^2y}{\mathrm{d}t^2} + m\nu_\mathrm{m}\frac{\mathrm{d}y}{\mathrm{d}t} - eB\frac{\mathrm{d}x}{\mathrm{d}t} = 0 \tag{3.195}$$

$$m\frac{\mathrm{d}^2z}{\mathrm{d}t^2} + m\nu_\mathrm{m}\frac{\mathrm{d}z}{\mathrm{d}t} = 0 \tag{3.196}$$

The motion in the z-direction is a simple damped motion. Therefore, it is sufficient to consider the dynamics of the electrons in the xy-plane.

$$\frac{\mathrm{d}^2x}{\mathrm{d}t^2} + \nu_\mathrm{m}\frac{\mathrm{d}x}{\mathrm{d}t} + \omega_\mathrm{c}\frac{\mathrm{d}y}{\mathrm{d}t} = -\frac{eE_0}{m}\sin\omega t \tag{3.197}$$

$$\frac{\mathrm{d}^2y}{\mathrm{d}t^2} + \nu_\mathrm{m}\frac{\mathrm{d}y}{\mathrm{d}t} - \omega_\mathrm{c}\frac{\mathrm{d}x}{\mathrm{d}t} = 0 \tag{3.198}$$

For the solution, we use the ansatz:

$$x = C_1 \sin\omega t + C_2 \cos\omega t \tag{3.199}$$
$$y = C_3 \sin\omega t + C_4 \cos\omega t \tag{3.200}$$

From a coefficient comparison, the quantities C_1 to C_4 are obtained. Furthermore, only C_2 is of importance here:

$$C_2 = -\nu_\mathrm{m} \frac{eE_0}{2\omega m} \left[\frac{1}{\left(\omega + \omega_\mathrm{c}\right)^2 + \nu_\mathrm{m}^2} + \frac{1}{\left(\omega - \omega_\mathrm{c}\right)^2 + \nu_\mathrm{m}^2} \right] \tag{3.201}$$

The absorbed power of a single electron is given by:

$$p = -F\frac{\mathrm{d}x}{\mathrm{d}t} = eE_0 \sin\omega t \frac{\mathrm{d}x}{\mathrm{d}t} \tag{3.202}$$

with the velocity $\frac{\mathrm{d}x}{\mathrm{d}t}$ according to:

$$\frac{\mathrm{d}x}{\mathrm{d}t} = C_1\omega\cos\omega t - C_2\omega\sin\omega t \tag{3.203}$$

We substitute this into Eq. 3.202 and recognize from a temporal average that only the component according to C_2 remains:

$$\langle p \rangle_\mathrm{t} = \langle eE_0C_1\omega\cos\omega t \sin\omega t - eE_0C_2\omega\sin^2\omega t \rangle_t = \frac{1}{2}C_2eE_0\omega \tag{3.204}$$

The total absorbed power of n electrons is:

$$\langle P \rangle_\mathrm{t} = n\langle p \rangle_\mathrm{t} = n\nu_\mathrm{m}\frac{1}{4}\frac{e^2E_0^2}{m} \left[\frac{1}{\left(\omega + \omega_\mathrm{c}\right)^2 + \nu_\mathrm{m}^2} + \frac{1}{\left(\omega - \omega_\mathrm{c}\right)^2 + \nu_\mathrm{m}^2} \right] \tag{3.205}$$

or:

$$\langle P \rangle_\mathrm{t} = \underbrace{\frac{1}{4}\epsilon_0 E_0^2}_{\text{Energy density E-Feld}} \underbrace{\frac{ne^2}{\epsilon_0 m}}_{\omega_\mathrm{p}^2} \underbrace{\nu\mathrm{m} \left[\frac{1}{\left(\omega + \omega_\mathrm{c}\right)^2 + \nu_\mathrm{m}^2} + \frac{1}{\left(\omega - \omega_\mathrm{c}\right)^2 + \nu_\mathrm{m}^2} \right]}_{\nu*} \tag{3.206}$$

From this equation, we recognize three characteristic quantities: (i) the energy density in the electric alternating field $\frac{1}{4}\epsilon_0 E_0^2$ (in a DC field, this would be $\frac{1}{2}\epsilon_0 E_0^2$. However, the temporal averaging in the alternating field produces an additional factor of 1/2); (ii) the plasma frequency as a characteristic oscillation of the electrons; (iii) an efficiency of the energy transfer from the

electric field to the electron oscillations. The last two quantities result in an effective **energy transfer rate** ν_*. This rate can be approximated for several limiting cases:

- $\nu_\mathrm{m} \ll \omega_\mathrm{c}$

  At low pressure, the collision frequency is much lower than the exciting frequency:

  $$\nu_* \approx 2\omega_\mathrm{p}^2 \nu_\mathrm{m} \left[\frac{\omega^2 + \omega_\mathrm{c}^2}{\left(\omega^2 - \omega_\mathrm{c}^2\right)^2} \right] \tag{3.207}$$

  If the exciting frequency is much smaller than the cyclotron frequency, we obtain:

  $$\nu_* \approx 2\frac{\omega_\mathrm{p}^2}{\omega_\mathrm{c}^2}\nu_\mathrm{m} \tag{3.208}$$

  From the size of the prefactors, it can be seen that the effective energy transfer rate is much smaller than in a direct current plasma. This is similar to the consideration of high-frequency ignition. In an alternating field, the electrons can absorb energy much less efficiently than in a direct current field. For the entire plasma, however, high-frequency heating is still more efficient since the charge carriers in the alternating field of the plasma are enclosed and can be continuously heated. In a DC plasma, each electron is only heated once on its single path through the plasma, but then leaves it again at the anode.

- $\nu_\mathrm{m} \gg \omega_\mathrm{c}$

  If the collision frequency becomes larger than the cyclotron frequency, we obtain:

  $$\nu_* \approx 2\omega_\mathrm{p}^2 \nu_\mathrm{m} \frac{1}{\omega^2 + \nu_\mathrm{m}^2} \tag{3.209}$$

  If the collision frequency is also much higher than the exciting frequency, we obtain:

  $$\nu_* \approx 2\frac{\omega_\mathrm{p}^2}{\nu_\mathrm{m}^2}\nu_\mathrm{m} \tag{3.210}$$

  This is identical to the result for the ohmic heating of an unmagnetized plasma 3.113.

- $\omega \approx \omega_c$ *and* $\nu_m < \omega_c$

  Finally, we want to consider the case where we heat at the cyclotron frequency and low collision rate. This corresponds exactly to the case that should be set for optimal wave heating:

$$\nu_* \approx 2\omega_p^2 \frac{1}{\nu_m} \left[\frac{2\omega^2 + \nu_m^2}{4\omega^2 + \nu_m^2} \right] \tag{3.211}$$

  If now the collision frequency becomes much smaller than ω_c, the efficiency of the resonant heating is obtained as:

$$\nu_* \approx 2\frac{\omega_p^2}{\nu_m}\frac{1}{2} \tag{3.212}$$

  This is identical to 3.113 except for a factor of 1/2. The reason lies again in the alternating field compared to a DC field, since we must temporally average over $E_0 2\sin 2(\omega t)$, which again gives the factor of 1/2.

The efficiency of the energy transfer rate 3.206 can now be optimized by several variants. By searching for the maximum, the following optimization criteria result from the derivative 3.206.

- *Optimization of the Applied Magnetic Field*

  If it is possible to freely choose the magnetic field, a maximum for $\langle P \rangle_t$ is obtained at:

$$\omega_{c,opt} \approx \omega \left(1 - \frac{\nu_m^4}{\omega^4} \right)^{1/2} \tag{3.213}$$

- *Optimization of* ω

  If the frequency is freely adjustable, an optimum of the energy transfer rate is obtained at:

$$\omega_{opt} \approx \omega_c^2 \left(1 + \frac{\nu_m^2}{\omega_c^2} \right) \left[\frac{2}{\sqrt{1 + \frac{\nu_m^2}{\omega_c^2}}} - 1 \right] \tag{3.214}$$

- *Optimization of Gas Pressure*

  For the operation of the plasma at different pressures, optimal heating is achieved if the following condition is met:

$$\nu_{\mathrm{m,opt}}^2 \approx \omega^2 - \omega_{\mathrm{c}}^2 \tag{3.215}$$

3.3 Global Models

In the previous sections, we have considered the boundary region as well as the power coupling into a plasma. Now we have derived all the components necessary to set up a simple but very powerful global model of a plasma.

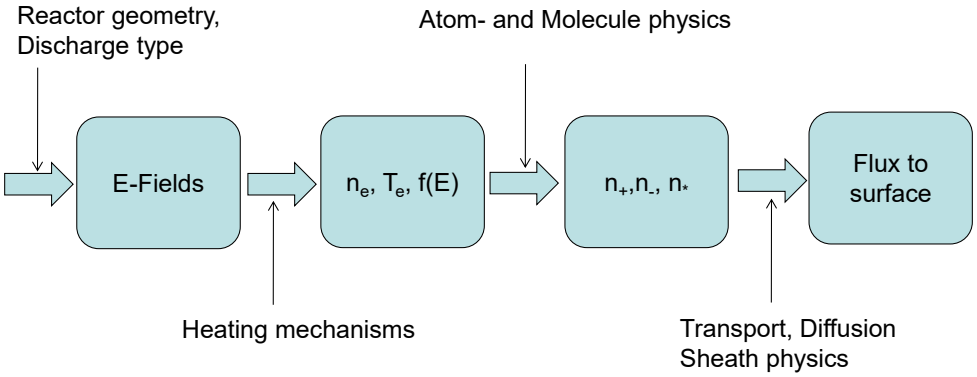

Figure 3.27: The energy and particle flow in a plasma can be described very schematically. Given a reactor geometry and concept, a certain configuration of electrical DC or AC fields is generated; these heat the plasma and result in a certain electron density and temperature; these in turn determine ionization, excitation, and dissociation; the particles formed are transported to the surfaces and disappear there or again dissipate the coupled energy.

In a global model, a zero-dimensional balance of the charge carriers and energy flow in a plasma is considered. This is schematically shown in Fig. 3.27: (i) the configuration of the electrodes, reactor geometry, etc., determines the electric fields present in the plasma; (ii) the power coupling according to the heating mechanisms determines to what extent electron densities and energies are established from these fields; (iii) given electron energies and densities, the reactive particles of a plasma are formed according to the dissociation or ionization energies; (iv) the reactive particles finally flow off via the sheaths and reach the surfaces. For this last step, the dynamics of the sheaths are essential. In the following, we want to discuss a few limiting cases of these global models.

3.3.1 Electropositive Plasma

3.3.1.1 Homogeneous Density Profile

The simplest global model considers a homogeneous density profile, i.e., transport to the surface is not dominated by diffusion. A *balance equation for the charge carriers* requires that the flux of ions through the surface A of the plasma is identical to the generation rate of the ions in the plasma volume V:

$$An_0 v_\mathrm{B} = n_\mathrm{g} n_0 k_\mathrm{Ionisation} V \tag{3.216}$$

with n_0 the electron density, n_g the neutral gas density, and $k_\mathrm{Ionisation}$ the ionization rate constant, which depends on the ionization threshold $E_\mathrm{Ionisation}$ in a simple relationship:

$$k_\mathrm{Ionisation} = k_0 e^{-\frac{E_\mathrm{Ionisation}}{k_\mathrm{B} T_\mathrm{e}}} \tag{3.217}$$

With the Bohm velocity, we finally obtain a relationship:

$$An_0 \sqrt{\frac{k_\mathrm{B} T_\mathrm{e}}{M}} = n_\mathrm{g} n_0 k_0 e^{-\frac{E_\mathrm{Ionisation}}{k_\mathrm{B} T_\mathrm{e}}} V \tag{3.218}$$

or

$$\boxed{\frac{k_\mathrm{Ionisation}}{v_\mathrm{B}} = \frac{1}{n_\mathrm{g}} \frac{A}{V}} \tag{3.219}$$

It can be seen from this equation that the electron density cancels out. That is, the charge carrier balance becomes a determining equation for the temperature of a plasma. This can be solved graphically, as illustrated in Fig. 3.28. With increasing surface-to-volume ratio, the temperature increases because the greater loss of charge carriers to the surfaces must be compensated. With increasing ionization energy, the temperature also increases because the loss to the surfaces cannot otherwise be balanced.
As a second balance equation, we can set up a *power balance*. For this purpose, we consider the coupled power that we can read from the heating mechanisms, or that is read at the generator in the experiment or directly measured in the experiment. The absorbed power is converted into reactions in the plasma. The particles generated flow out of the plasma, with each ion transporting its ionization energy as well as the energy $E_\mathrm{Randschicht} = eV_\mathrm{Randschicht}$, which it acquires in the acceleration in the sheath, out of the system. We obtain:

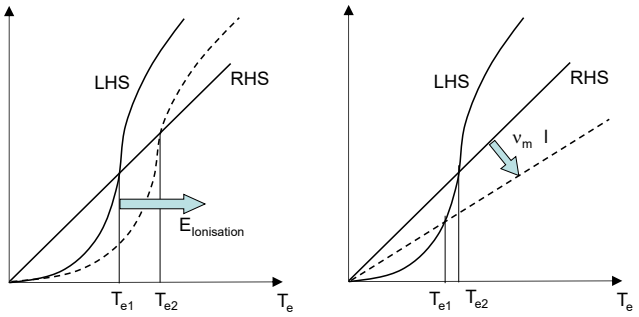

Figure 3.28: When changing the ionization energy or the volume-to-surface ratio, a new equilibrium electron temperature is established.

$$P_{\text{abs}} = P_{\text{Verlust}} = n_0 v_{\text{B}} A \left(E_{\text{Ionisation}} + E_{\text{Randschicht}} \right) \tag{3.220}$$

With known electron energy/temperature from the above charge carrier balance, the charge carrier density can now be determined from this power balance. In summary, it can be stated that according to the global model, the charge carrier and power balance each determine the other characteristic quantity contrary to intuition:

- **Charge carrier balance determines the electron temperature**
- **Power balance determines the electron density**

3.3.1.2 Inhomogeneous Density Profile

In a further case, we now consider the situation where diffusion determines the transport to the surfaces. From the continuity equation in the steady state, we obtain an equilibrium between the gradient in the flux and the generation rate of new charge carriers.

$$\frac{\mathrm{d}j}{\mathrm{d}x} = k_{\text{Ion.}} n_{\text{g}} n_{\text{e}} \tag{3.221}$$

This charge carrier current is driven by ambipolar diffusion:

$$j = -D_{\text{ambipolar}} \frac{\mathrm{d}n_{\text{e}}}{\mathrm{d}x} \tag{3.222}$$

In a simple parallel plate arrangement, the density profile for the case of dominant diffusion is a simple cosine, as illustrated in Fig. 3.29:

$$n_e(x) = n_0 \cos \beta x \tag{3.223}$$

with a coefficient $\beta = \frac{\pi}{l}$ corresponding to the chosen geometry. Thus, we obtain the flux of particles to the surface at the location $x = l/2$ by integrating Eq. 3.221 from the center of the discharge to the surface:

$$j(l/2) = k_{\text{Ion.}} n_g \int_0^{l/2} n_e(x) \mathrm{d}x = k_{\text{Ion.}} n_g n_0 \frac{l}{\pi} \tag{3.224}$$

This flux is driven by ambipolar diffusion if we substitute the density Eq. 3.223:

$$j(x) = D_{\text{ambipolar}} \beta n_0 \sin \beta x \tag{3.225}$$

or at the location $x = l/2$:

$$j(l/2) = D_{\text{ambipolar}} \frac{\pi}{l} n_0 \tag{3.226}$$

Thus, we obtain as an equilibrium:

$$\frac{\pi}{l} D_{\text{ambipolar}} = \frac{l}{\pi} k_{\text{Ion.}} n_g \tag{3.227}$$

With $D_{\text{ambipolar}} = \frac{k_B T_e}{M \nu_m} = \frac{k_B T_e}{M n_g k_m}$ we obtain the following condition:

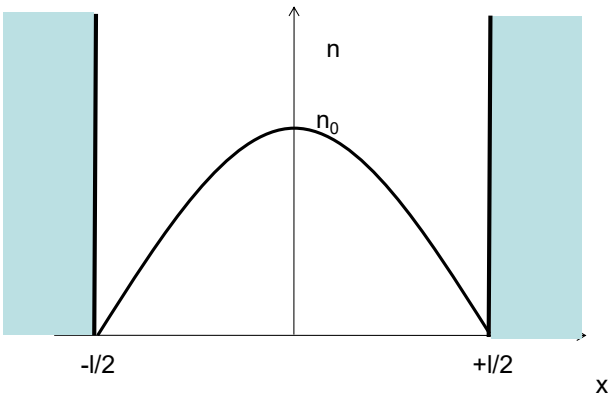

Figure 3.29: In the case of a diffusion-dominated density distribution, a cosine profile is established if the charge carrier generation is spatially constant.

$$\boxed{\frac{\left(k_{\mathrm{m}} k_{\mathrm{Ion.}}\right)^{1/2}}{v_{\mathrm{B}}} = \frac{\pi}{l n_{\mathrm{g}}}} \tag{3.228}$$

The power balance can be set up analogously to the model with a homogeneous density profile, and we obtain:

$$P_{\mathrm{Verlust}} = 2\Gamma_{\mathrm{i}}(l/2)e\left(E_{\mathrm{e}} + E_{\mathrm{i}}\right) + 2eE_{\mathrm{Ionisation}} \int_0^{l/2} k_{\mathrm{Ion.}} n_{\mathrm{g}} n_{\mathrm{e}} \mathrm{d}x \tag{3.229}$$

In this formulation, the losses due to the flux of electrons and ions out of the discharge are calculated with the electron energy $E_e = 2k_B T_e$ (see below) as well as the energy lost due to the sheath acceleration $E_i = eV$. The losses due to ionization in the volume are the third term. This can be simply summarized as:

$$P_{\mathrm{Verlust}} = 2\Gamma_{\mathrm{i}}(l/2)eE_{\mathrm{T}} \tag{3.230}$$

with $E_{\mathrm{T}} = E_{\mathrm{e}} + E_{\mathrm{i}} + E_{Ionisation}$.

$$n_0 = \frac{P_{\mathrm{abs}} l}{2\pi D_{\mathrm{ambipolar}} e E_{\mathrm{T}}} \tag{3.231}$$

3.3.1.3 Dissociation

The global model initially only describes the balance of the charge carriers according to:

$$A n_0 v_{\mathrm{B}} = n_{\mathrm{g}} n_0 k_{\mathrm{Ion.}} V \tag{3.232}$$

For a parallel plate arrangement, the ratio of volume to surface is exactly the plate distance l. That is, in the simplest approximation, we obtain:

$$\frac{k_{\mathrm{Ion.}}}{v_{\mathrm{B}}} = \frac{1}{n_{\mathrm{g}} l} \tag{3.233}$$

In the same sense, the electron density in the plasma is given by:

$$n_0 = \frac{P_{\mathrm{abs}}}{2eE_{\mathrm{T}} v_{\mathrm{B}} A} \tag{3.234}$$

From this equilibrium, a certain electron temperature and thus ionization rate is established in the plasma. From the comparison between dissociation and ionization, the dissociation rate can also be directly read off. For this purpose, we first consider both rate constants:

$$k_{\text{Diss.}} = k_{\text{Diss.},0} e^{-\frac{E_{\text{Diss.}}}{k_B T_e}} \tag{3.235}$$

$$k_{\text{Ion.}} = k_{\text{Ion.},0} e^{-\frac{E_{\text{Ion.}}}{k_B T_e}} \tag{3.236}$$

If we now set the rate coefficient for ionization $k_{\text{Ion.}}$ to the power of $\frac{E_{\text{Diss.}}}{E_{\text{Ion.}}}$, we obtain by substitution:

$$e^{-\frac{E_{\text{Diss.}}}{k_B T_e}} = \left(\frac{k_{\text{Diss.}}}{k_{\text{Ion.}}}\right)^{\frac{E_{\text{Diss.}}}{E_{\text{Ion.}}}} \tag{3.237}$$

If we substitute this into the rate coefficient for dissociation, we obtain:

$$k_{\text{Diss.}} \propto (k_{\text{Ion.}})^{\frac{E_{\text{Diss.}}}{E_{\text{Ion.}}}} \tag{3.238}$$

where the proportionality particularly contains the initial values for ionization and dissociation $(k_{\text{Diss.},0}, k_{\text{Ion.},0})$. The rate constant $k_{\text{Ion.}}$ is given by the global model, which results in a weak temperature dependence for dissociation after the quotient is only $\frac{E_{\text{Diss.}}}{E_{\text{Ion.}}} \approx 0.3...0.5$:

$$k_{\text{Diss.}} \propto \left(\frac{v_B}{n_g l}\right)^{\frac{E_{\text{Diss.}}}{E_{\text{Ion.}}}} \tag{3.239}$$

3.3.2 Electronegative Plasma

3.3.2.1 Balance Equations

As a final example, we want to consider the density profile in an electronegative plasma. The negative ions are essentially confined within the plasma volume, i.e., a balance of the production of negative ions cannot be simply described by generation in equilibrium with loss through drift and diffusion to the wall. The dominant loss channels for negative ions are, on the one hand, recombination with the positive ions and, on the other hand, de-excitation through collisions with metastables. That is, a model of an electronegative plasma must include at least the following reactions, as illustrated by the example of oxygen:

$$\begin{array}{rcll} e^- + O & \rightarrow & O^- & k_{\text{att}} \\ O^- + O^+ & \rightarrow & O_2 & k_{\text{recomb}} \\ O^- + O^* & \rightarrow & O_2 + e^- & k_{\text{det}} \\ e^- + O & \rightarrow & O^* + e^- & k_{\text{ex}} \end{array} \tag{3.240}$$

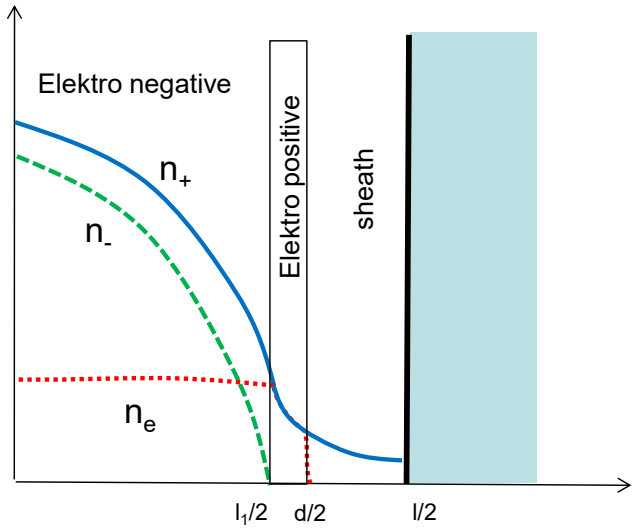

Figure 3.30: In an electronegative plasma, a complex boundary zone is formed because the negative ions are retained in the core of the plasma, while the lighter electrons can reach closer to the surface and form an electropositive boundary zone before the actual space charge zone begins in front of the surface.

The spatial distribution of the charge carriers of an electronegative plasma is significantly more complex than that of an electropositive plasma, as different sheaths can form for the electrons and the negative ions. As already discussed in the section on sheaths, the negative ions are retained in the core of the plasma due to their large mass, while the lighter electrons can reach closer to the surface due to their high mobility. That is, an electronegative volume and an electropositive sheath are initially formed before the actual space charge zone begins in front of the surface. This is schematically illustrated in Fig. 3.30.
Based on our simple chemical model, we can initially set up the continuity equations for the positive and negative ions, as well as the electrons and the metastables:

$$\nabla\Gamma_+ = n_\mathrm{g} n_\mathrm{e} k_\mathrm{ion} - k_\mathrm{recomb} n_+ n_- \quad (3.241)$$
$$\nabla\Gamma_- = n_\mathrm{g} n_\mathrm{e} k_\mathrm{att} - k_\mathrm{recomb} n_+ n_- - k_\mathrm{det} n^* n_- \quad (3.242)$$
$$\nabla\Gamma_e = (k_\mathrm{ion} - k_\mathrm{att}) n_\mathrm{g} n_\mathrm{e} \quad (3.243)$$
$$\nabla\Gamma_* = k_\mathrm{ex} n_\mathrm{e} n_\mathrm{g} - k_\mathrm{det} n_* n_- \quad (3.244)$$

The particle fluxes in this simple model are driven by drift and diffusion:

$$\Gamma_+ = -D_+ \nabla n_+ + n_+ \mu_+ E \quad (3.245)$$
$$\Gamma_- = -D_- \nabla n_- - n_- \mu_- E \quad (3.246)$$
$$\Gamma_e = -D_\mathrm{e} \nabla n_\mathrm{e} - n_\mathrm{e} \mu_\mathrm{e} E \quad (3.247)$$
$$\Gamma_* = -D_\nabla n_* \quad (3.248)$$

The equations are closed by the condition for flux conservation and quasi-neutrality.

$$\Gamma_+ = \Gamma_- + \Gamma_\mathrm{e} \quad (3.249)$$
$$n_+ = n_- + n_\mathrm{e} \quad (3.250)$$

3.3.2.2 Particle Densities

In the following, we consider the resulting solutions for the individual particle species:

- *excited species, n_**

  The simplest equations are obtained for the density of metastables. From the continuity equation, we obtain with $\Gamma_* = -D_* \nabla n_*$:

  $$\nabla\Gamma_* = -D_* \nabla^2 n_* = k_\mathrm{ex} n_\mathrm{e} n_\mathrm{g} - k_\mathrm{det} n_* n_- \quad (3.251)$$

  In most cases, the equilibrium of the metastables is determined by generation in the volume and loss in collisions with the reactor walls. That is, the term with k_det can initially be neglected for this equilibrium. The metastables reach the surface via diffusion, where they are de-excited with a loss probability γ_*. This can be expressed as an equilibrium in the volume element in front of the surface: the diffusive flux into this volume element from the plasma must be equal to the lost flux to the surface:

$$-D_* \nabla n_* = \frac{1}{4} \gamma_* n_* \bar{v}_* \tag{3.252}$$

with $\bar{v}_*$ the mean thermal velocity of the metastables. Since $k\mathrm{ex} \gg k_{\mathrm{det}}$ applies, the particle balance simplifies to:

$$-D_* \nabla n_* A = k_{\mathrm{ex}} n_{\mathrm{e}} n_{\mathrm{g}} V \tag{3.253}$$

Finally, we obtain:

$$n_* = \frac{4 k_{\mathrm{ex}}}{\gamma_* \bar{v}_*} n \mathrm{g} n_{\mathrm{e}} \frac{V}{A} \tag{3.254}$$

- *electrons,* n_{e}

  Since the electrons are confined in the plasma potential, we can approximate $\Gamma_{\mathrm{e}} \approx 0$ and we obtain:

$$-D_{\mathrm{e}} \nabla n_{\mathrm{e}} - n_{\mathrm{e}} \mu_{\mathrm{e}} E = 0 \tag{3.255}$$

  or with the Einstein relation and $E = -\nabla \Phi$:

$$\frac{k_{\mathrm{B}} T_{\mathrm{e}}}{e} \nabla n_{\mathrm{e}} + n_{\mathrm{e}} E = 0 \tag{3.256}$$

  This again leads to the Boltzmann relation for the electrons:

$$n_{\mathrm{e}} = n_{\mathrm{e},0} e^{\frac{e\Phi}{k_{\mathrm{B}} T_{\mathrm{e}}}} \tag{3.257}$$

- *positive ions,* n_+

  For the description of the positive ions, however, we must consider that their transport is determined by *ambipolar diffusion*. This in turn depends on the density and the mean mass of the negative charge carriers. If the density of the negative ions is high, the ambipolar diffusion is low. If the negative charge carriers are predominantly electrons, normal ambipolar diffusion occurs. The continuity equation for the positive ions in the drift-diffusion approximation is:

$$\nabla \left(-D_+ \nabla n_+ + n_+ \mu_+ E \right) = n_{\mathrm{g}} n_{\mathrm{e}} k_{\mathrm{ion}} - k_{\mathrm{recomb}} n_+ n_- \tag{3.258}$$

  Since the negative charge carriers are confined in the plasma, we can set $\Gamma_- \approx 0$ and $\Gamma_{\mathrm{e}} \approx 0$ in each case:

$$k_{\mathrm{B}} T_{\mathrm{i}} \nabla n_- + n_- E = 0 \tag{3.259}$$
$$k_{\mathrm{B}} T_{\mathrm{e}} \nabla n_{\mathrm{e}} + n_{\mathrm{e}} E = 0 \tag{3.260}$$

From this, we obtain:

$$\frac{\nabla n_-}{n_-} = \underbrace{\frac{T_{\mathrm{e}}}{T_{\mathrm{i}}}}_{=\gamma} \frac{\nabla n\mathrm{e}}{n_{\mathrm{e}}} \tag{3.261}$$

or from quasi-neutrality:

$$\nabla n_+ = \nabla n_- + \nabla n_{\mathrm{e}} \tag{3.262}$$

We now assume that the transport of the ions can be described by a net ambipolar diffusion constant $D_{\mathrm{a},+}$:

$$\Gamma_+ = -D_{\mathrm{a},+} \nabla n_+ \tag{3.263}$$

In the following, we want to derive an expression that gives the dependence of $D_{\mathrm{a},+}$ on the electronegativity of the plasma. The ion flux is initially:

$$\begin{aligned} \Gamma_+ &= -D_+ \nabla n_+ + n_+ \mu_+ E \\ &= -D_+ \nabla n_+ + (n_{\mathrm{e}} + n_-) \frac{D_+}{k_{\mathrm{B}} T_{\mathrm{i}}} E \end{aligned} \tag{3.264}$$

Now we substitute the drift-diffusion approximation for the negative charge carriers, and we obtain:

$$\Gamma_+ = -D_+ \nabla n_+ + \frac{D_+}{k_{\mathrm{B}} T_{\mathrm{i}}} \left[-\nabla n_{\mathrm{e}} k_{\mathrm{B}} T_{\mathrm{e}} - \nabla n_- k_{\mathrm{B}} T_{\mathrm{i}} \right] \tag{3.265}$$

At this point, it is now necessary to transform the gradients in n_{e} and n_- into a gradient in n_+ to obtain an equation of the form 3.263. From quasi-neutrality, we obtain with Eq. 3.261:

$$\frac{\nabla n_+}{n_\mathrm{e}} = \frac{\nabla n_-}{n_\mathrm{e}} + \frac{\nabla n_\mathrm{e}}{n_\mathrm{e}} \tag{3.266}$$

$$\frac{\nabla n_+}{n_\mathrm{e}} = \frac{\nabla n_-}{n_\mathrm{e}} + \frac{T_\mathrm{i}}{T_\mathrm{e}}\frac{\nabla n_-}{n_-} \tag{3.267}$$

finally:

$$\nabla n_+ = \nabla n_- \left(1 + \frac{T_\mathrm{i}}{T_\mathrm{e}}\frac{n_\mathrm{e}}{n_-}\right) = \nabla n_- \left(1 + \frac{1}{\gamma\alpha}\right) \tag{3.268}$$

That is, we can replace ∇n_- with an expression proportional to ∇n_+ according to:

$$\nabla n_- = \frac{\gamma\alpha}{1+\gamma\alpha}\nabla n_+ \tag{3.269}$$

Similarly, we obtain an expression for ∇n_e:

$$\nabla n_\mathrm{e} = \frac{1}{1+\gamma\alpha}\nabla n_+ \tag{3.270}$$

We now substitute this into Eq. 3.265 and from a comparison with 3.263 we obtain the expression for the ambipolar diffusion:

$$\boxed{D_{\mathrm{a},+} = D_+ \frac{1+\gamma+2\gamma\alpha}{1+\gamma\alpha}} \tag{3.271}$$

We recognize that for strongly electronegative plasmas, according to $\alpha \gg 1$, we obtain an ambipolar diffusion of

$$D_{\mathrm{a},+} = 2D_+ \tag{3.272}$$

If, on the other hand, the density of negative ions is low, we obtain $D_{\mathrm{a},+} \approx \gamma D_+$, which corresponds to normal ambipolar diffusion. This derivation shows that ambipolar diffusion in electronegative plasmas is strongly suppressed. That is, the ions flow off to the surfaces to a much lesser extent, and the confinement is much better than in electropositive plasmas.

- *negative ions, n_-*

  When determining the density of the positive ions, we had already derived that the flux $\Gamma_- \approx 0$. That is, the density of the negative ions is established from the equilibrium of generation and annihilation processes, less from diffusion. The continuity equation of the negative ions was initially given by:

$$\nabla\Gamma_- = k_{\text{att}} n_{\text{g}} n_{\text{e}} - k_{\text{recomb}} n_+ n_- - k_{\text{det}} n_* n_- \tag{3.273}$$

  If we now substitute the density of excited metastables from Eq. 3.254, we obtain:

$$\nabla\Gamma_- = k_{\text{att}} n_{\text{g}} n_{\text{e}} - k_{\text{recomb}} n_+ n_- - \underbrace{\frac{k_{\text{det}} 4 k_{\text{ex}}}{\gamma_* \bar{v}_*} \frac{V}{A}}_{k_*} n_{\text{g}} n_{\text{e}} n_- \tag{3.274}$$

  We want to abbreviate the three-body rate constant for de-excitation through collisions with metastables by k_*. The dominant loss channels for negative ions, recombination and de-excitation with metastables, depend on the pressure. Let us first consider a strongly electronegative plasma ($\alpha \gg 1$) and assume that recombination is stronger; then the following must apply:

$$k_{\text{recomb}} n_+ n_- k_* n_{\text{e}} n_- n_{\text{g}} \tag{3.275}$$

  This can be rewritten with $\alpha = \frac{n_-}{n_{\text{e}}}$ to:

$$\alpha = \frac{n_-}{n_{\text{e}}} > \frac{k_*}{k_{\text{recomb}}} \frac{n_-}{n_+} n_{\text{e}} \tag{3.276}$$

  If α becomes very large, we have a strongly electronegative plasma and $n_- \approx n_+$. Thus, the inequality becomes:

$$\alpha > \frac{k_*}{k_{\text{recomb}}} n_{\text{g}} \tag{3.277}$$

  At low pressure, corresponding to a small neutral gas density n_{g}, the inequality is satisfied, and the recombination of the negative ions with the positive ions dominates. At very high pressures, however, the inequality is no longer satisfied, and apparently the de-excitation through collisions with the metastables now dominates. This is also intuitively

understandable. At high pressures, the metastables are not so easily lost through collisions with the surfaces, and a high density can build up. Accordingly, de-excitation through collisions with metastables becomes more likely.

3.3.2.3 Model of an Electronegative Plasma

After this consideration, we can now set up a simple global model for an electronegative plasma. Unlike an electropositive plasma, we now need three equations because we have an additional charge carrier species. The particle balances for the positive and negative ions are:

$$k_{\mathrm{ion}} n_{\mathrm{e}} n_{\mathrm{g}} V - k_{\mathrm{recomb}} n_{+} n_{-} V - \Gamma_{+} A = 0 \tag{3.278}$$

$$k_{\mathrm{att}} n_{\mathrm{e}} n_{\mathrm{g}} V - k_{\mathrm{recomb}} n_{+} n_{-} - k_{*} n_{\mathrm{g}} n_{\mathrm{e}} n_{-} V = 0 \tag{3.279}$$

The coupled power is consumed for the ionization of the charge carriers and by the flux to the surfaces. Here, E_{i} is the energy of the ions that they take with them in the sheath, and E_{e} is the energy of the electrons when they hit the surfaces $E_{\mathrm{e}} \approx 2k_{\mathrm{B}}T_{\mathrm{e}}$. This energy loss due to the electrons can be derived from the energy loss S to the surface in the z-direction:

$$S = n\langle \frac{1}{2} m v^2 v_{\mathrm{z}} \rangle_v = 2k_{\mathrm{B}}T_{\mathrm{e}} \frac{1}{4} n\bar{v} \tag{3.280}$$

with the averaging over a Maxwell distribution. Since the flux of electrons to the surface ($\frac{1}{4}n\bar{v}$) must be equal to the ion flux due to the conservation of quasi-neutrality, a simple electron contribution to the loss of $\Gamma_{+} 2k_{\mathrm{B}}T_{\mathrm{e}}$ results. The energy balance is therefore:

$$P_{\mathrm{abs}} = k_{\mathrm{ion}} n_{\mathrm{e}} n_{\mathrm{g}} E_{\mathrm{Ionisation}} V + \Gamma_{+} A \left(E_{\mathrm{e}} + E_{\mathrm{i}}\right) \tag{3.281}$$

For determining the global equilibrium, we consider two limiting cases:

- *Volume processes dominate*

  If the losses in the volume dominate, we can neglect the term Γ_{+} in 3.278. Furthermore, the rate for attachment is much greater than that for detachment, and we obtain directly from the subtraction of Eq. 3.278 minus Eq. 3.279:

$$k_{\mathrm{ion}} = k_{\mathrm{att}} \tag{3.282}$$

From this equation, the electron temperature can initially be determined. From the particle balance 3.278 of the positive ions, we obtain a relationship between the electron density and the positive ion density for $n_+ \approx n_-$, according to:

$$n_\mathrm{e} = \frac{k_\mathrm{recomb}}{k_\mathrm{att}} \frac{n_+^2}{n_\mathrm{g}} \tag{3.283}$$

If we substitute this into the power balance 3.281, we obtain the density of the positive ions:

$$P_\mathrm{abs} = k_\mathrm{recomb} E_\mathrm{Ionisation} n_+^2 \tag{3.284}$$

and thus also the density of the electrons via Eq. 3.283.

- *Surface losses dominate*

  If, on the other hand, the surface losses dominate, we neglect the recombination and 3.278 becomes:

$$k_\mathrm{ion} n_\mathrm{e} n_\mathrm{g} V = \Gamma_+ A \tag{3.285}$$

For a strongly electronegative plasma, the ambipolar diffusion is strongly reduced, and we obtain:

$$\Gamma_+ = 2D_+ \nabla n_+ = 2D_+ \frac{n_+}{d_\mathrm{eff}} \tag{3.286}$$

Here, we have approximated the gradient in the ion density by an effective diffusion length d_eff. From the power balance 3.281, we can now directly determine the density of the positive ions:

$$P_\mathrm{abs} = A E_\mathrm{T} 2D_+ \frac{n_+}{d_\mathrm{eff}} \tag{3.287}$$

with $E_\mathrm{T} = E_\mathrm{Ionisation} + E_\mathrm{e} + E_\mathrm{i}$. The density of the electrons is determined from the balance of the negative charge carriers. Initially, quasi-neutrality applies:

$$n_+ = (1 + \alpha) n_\mathrm{e} \tag{3.288}$$

That is, we must determine α from Eq. 3.279 by dividing by $k_\mathrm{rec} n_- n_\mathrm{e}$, and we obtain:

$$\alpha = \frac{k_{\mathrm{att}} n_{\mathrm{g}}}{k_{\mathrm{rec}} n_-} - \frac{k_* n_{\mathrm{g}}}{k_{\mathrm{rec}}} - 1 \tag{3.289}$$

With $n_+ \approx n_-$ and $k_{\mathrm{att}} \gg k_* n_{\mathrm{g}}$ we obtain:

$$\alpha = \frac{k_{\mathrm{att}} n_{\mathrm{g}}}{k_{\mathrm{rec}} n_+} \tag{3.290}$$

From this, we obtain α and can finally determine n_{e}. Finally, we use Eq. 3.278 to determine the electron temperature:

$$k_{\mathrm{ion}} n_{\mathrm{e}} n_{\mathrm{g}} V = 2 D_+ \frac{n_+}{d_{\mathrm{eff}}} \tag{3.291}$$

It can be seen that when applying the global models to electronegative plasmas, the balance equations must be slightly extended. However, for the common case of strongly electronegative plasmas, very compact equations are obtained again, with the equilibrium temperatures being very low since the ambipolar diffusion constant is smaller than in electropositive plasmas. That is, the temperature decreases, while the charge carrier densities must increase accordingly at constant power.

3.3.2.4 Boundary Region of an Electronegative Plasma

In the boundary region of an electronegative plasma, an electropositive boundary zone is often formed, as illustrated in Fig. 3.30. This edge is stable if the particle flux driven by the electropositive edge is equal to the Bohm flux:

$$-D_{\mathrm{a}} \frac{\mathrm{d}n_+}{\mathrm{d}x}\bigg|_{x=d/2} = n + (d/2) v_{\mathrm{B}} \tag{3.292}$$

However, if the current of charge carriers from the electronegative plasma volume is equal to or greater than the Bohm flux across the electropositive edge, the electropositive region disappears. From the equality of the fluxes, we can determine the boundary to:

$$(n_{\mathrm{e}} + n_-) v_{\mathrm{B}\alpha} = n_{e0} v_{\mathrm{B}} \tag{3.293}$$

or

$$n_{\mathrm{e}0}(1 + \alpha) v_{\mathrm{B}\alpha} = n_{\mathrm{e}0} v_{\mathrm{B}} \tag{3.294}$$

with $v_{\mathrm{B}\alpha} = \left(\frac{k_\mathrm{B}T_\mathrm{e}}{M}\frac{1+\alpha}{1+\gamma\alpha}\right)^{1/2}$ the Bohm velocity at the edge of the electronegative plasma volume. For typical values of $\gamma \approx 100$, we obtain a limit value of α of approximately 8.5:

$$(1+\alpha)\left(\frac{1+\alpha}{\alpha}\right)1/2 = \gamma 1/2 \tag{3.295}$$

3.3.3 Pulsed Plasmas

Finally, we consider a global equilibrium for the case of a pulsed plasma. This application occurs relatively frequently since pulsing a plasma represents an additional control variable. By pulsing, the energy input into the system and thus the thermal load on the substrates or workpieces can be controlled while keeping the plasma conditions almost constant. Often, the goal is to generate a high plasma density so that the sheath thicknesses become small and the plasma can thus also penetrate into small cavities of the workpieces. A high continuous plasma density would, however, also be a high thermal load on the surfaces. This is resolved by pulsing, since the *time-averaged* power remains small and only the power in the pulse itself is high. The ratio of plasma on-time to off-time is referred to as the **duty cycle**. This case can also be discussed on the basis of the global models. For the general case of a time-dependent solution, we obtain the particle balance as:

$$V\frac{\mathrm{d}n_\mathrm{e}}{\mathrm{d}t} = k_\mathrm{Ion.}n_\mathrm{g}n_\mathrm{e}V - n_\mathrm{e}v_\mathrm{B}A \tag{3.296}$$

or

$$\frac{1}{n_\mathrm{e}}\frac{\mathrm{d}n_\mathrm{e}}{\mathrm{d}t} = \nu_\mathrm{ion} - \nu_\mathrm{loss} \tag{3.297}$$

That is, the relative density change depends on the difference between the generation rate ν_ion and the loss rate ν_loss. For the energy balance, we obtain:

$$\begin{aligned}\frac{\mathrm{d}}{\mathrm{d}t}\left(\frac{3}{2}k_\mathrm{B}n_\mathrm{e}T_\mathrm{e}V\right) &= P_\mathrm{abs} \\ &\quad -en_\mathrm{e}n_\mathrm{g}V\sum_i k_iE_i \\ &\quad -\left(eV_\mathrm{sheath} + \frac{5}{2}k_\mathrm{B}T_\mathrm{e}\right)n_\mathrm{e}v_\mathrm{B}A\end{aligned} \tag{3.298}$$

Here, the sum $\sum_i k_iE_i$ is the sum over all loss processes such as ionization, excitation, and elastic collisions. The term $5/2k_\mathrm{B}T_\mathrm{e}$ is composed of $1/2k_\mathrm{B}T_\mathrm{e}$

for the acceleration of the ions in the presheath and $2k_\mathrm{B}T_\mathrm{e}$ of the energy lost per electron at the wall. With the time derivative:

$$\frac{\mathrm{d}}{\mathrm{d}t}\left(\frac{3}{2}k_\mathrm{B}n_\mathrm{e}T_\mathrm{e}V\right) = \frac{3}{2}k_\mathrm{B}T_\mathrm{e}V\frac{\mathrm{d}n_\mathrm{e}}{\mathrm{d}t} + \frac{3}{2}k_\mathrm{B}n_\mathrm{e}V\frac{\mathrm{d}T_\mathrm{e}}{\mathrm{d}t} \tag{3.299}$$

The energy balance can be rewritten to:

$$\begin{aligned}\frac{1}{T_\mathrm{e}}\frac{\mathrm{d}T_\mathrm{e}}{\mathrm{d}t} \;=\; & \frac{P_\mathrm{abs}}{W_\mathrm{e}} - \\ & \left(\frac{2}{3}\frac{E_\mathrm{T}}{k_\mathrm{B}T_\mathrm{e}} + 1\right)\nu_\mathrm{ion} - \\ & \left(\frac{2}{3}\frac{eV_\mathrm{sheath} + 5/2k_\mathrm{B}T_\mathrm{e}}{k_\mathrm{B}T_\mathrm{e}} - 1\right)\nu_\mathrm{loss}\end{aligned} \tag{3.300}$$

with $W_\mathrm{e} = \frac{3}{2}k_\mathrm{B}T_\mathrm{e}n_\mathrm{e}V$ and $\nu_\mathrm{ion}E_\mathrm{T} = n_\mathrm{g}\sum_i k_i E_i$. We now want to consider this equation for the switching on and off of the plasma in the pulse, as illustrated in Fig. 3.31:

- *Switching on the plasma*

  At the beginning of the plasma, the loss rate is still low, i.e., we obtain:

  $$\frac{1}{n_\mathrm{e}}\frac{\mathrm{d}n_\mathrm{e}}{\mathrm{d}t} \approx \nu_\mathrm{ion} \tag{3.301}$$

  The power balance becomes:

  $$\frac{1}{T_\mathrm{e}}\frac{\mathrm{d}T_\mathrm{e}}{\mathrm{d}t} \approx \frac{P_\mathrm{abs}}{W_\mathrm{e}} - \left(\frac{2}{3}\frac{E_\mathrm{T}}{k_\mathrm{B}T_\mathrm{e}} + 1\right)\nu_\mathrm{ion} \tag{3.302}$$

  At the beginning, the ionization rate is still low, and we obtain a very strong increase in the electron temperature according to a slope of:

  $$\frac{1}{T_\mathrm{e}}\frac{\mathrm{d}T_\mathrm{e}}{\mathrm{d}t} = \frac{P_\mathrm{abs}}{W_\mathrm{e}} \tag{3.303}$$

  The maximum electron temperature in this phase is obtained from the power balance with the condition $\frac{1}{T_\mathrm{e}}\frac{\mathrm{d}T_\mathrm{e}}{\mathrm{d}t}\Big| T\mathrm{e},\mathrm{max} = 0$:

  $$\frac{P_\mathrm{abs}}{W_\mathrm{e}} = \left(\frac{2}{3}\frac{E_\mathrm{T}}{k_\mathrm{B}T_\mathrm{e,max}} + 1\right)\nu_\mathrm{ion} \tag{3.304}$$

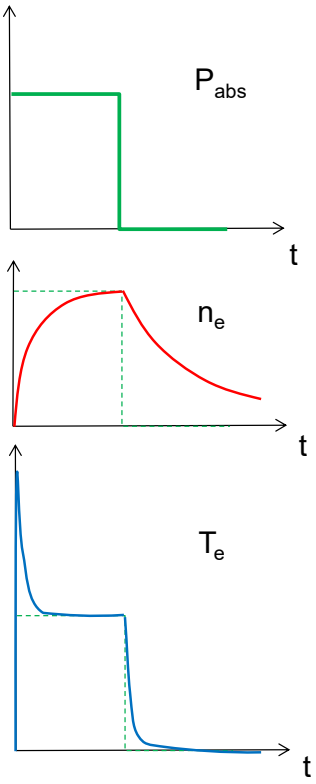

Figure 3.31: In a pulsed plasma, the change in electron temperature occurs much faster than the change in electron densities when switching the plasma on and off.

The electron density thus increases much more slowly than the electron temperature. The effect of the very high electron temperature right at the beginning is used to selectively drive certain chemical reactions in the plasma. Since many cross sections only come into play above a certain threshold energy, a very high electron energy specifically accelerates these reactions.

- *Switching off the plasma*

  When the plasma is switched off, ionization ceases. That is, we obtain a dynamics according to:

$$\frac{1}{n_e}\frac{dn_e}{dt} = -\nu_{loss} \tag{3.305}$$

and

$$\frac{1}{T_\mathrm{e}}\frac{\mathrm{d}T_\mathrm{e}}{\mathrm{d}t} = -\left(\frac{2}{3}\frac{eV_\mathrm{sheath} + 5/2k_\mathrm{B}T_\mathrm{e}}{k_\mathrm{B}T_\mathrm{e}} - 1\right)\nu_\mathrm{loss} \tag{3.306}$$

The decay of the density now depends on the loss time constant, which can be given by diffusion, for example. The decay time constant for the electron temperature is, however, orders of magnitude larger, as can be seen from the prefactor proportional to $eV_\mathrm{sheath}/k_\mathrm{B}T_\mathrm{e}$.

Chapter 4

Plasma Chemistry

In the description of chemical processes in plasmas, two areas can be separated: equilibrium reactions and kinetic reactions. In a plasma, depending on the boundary conditions, both areas can occur, or for some reactions, equilibrium can be achieved, while for others, this is not the case. Especially at low pressures and finite residence times of the particles in the plasmas, the reaction rates become important, as the system has no possibility to reach chemical equilibrium, where the forward and reverse reactions are in equilibrium. In the following, these two areas will be discussed.

4.1 Reaction Equilibrium

4.1.1 Thermodynamics of Chemical Reactions

Chemical reactions can take the following forms, for example, a dissociation:

$$AB \leftrightarrows A + B \tag{4.1}$$

a conversion of reactants A and B into the products C and D:

$$A + B \leftrightarrows C + D \tag{4.2}$$

as well as the recombination of reactants A and B to form AB.

$$A + B + X \leftrightarrows AB + X \tag{4.3}$$

In this so-called 2-to-1 reaction, a third collision partner X is often necessary to ensure both momentum and energy conservation in this reaction. If this third collision partner is missing, the product AB is initially an excited particle AB^*.

In chemical equilibrium, the different states of the system can be characterized by thermodynamic potentials and state variables. According to the first law of thermodynamics, the change in internal energy dU is composed of the change in heat δQ and the change in work δW. The latter is often, in the case of an ideal gas, $dW = -pdV$. Thus, we obtain:

$$dU = \delta Q - pdV \tag{4.4}$$

The expression δQ instead of dQ indicates that the change in the amount of heat cannot be independent of the path of the state change (although this is assumed in all practical cases). The change in the amount of heat is linked to the entropy:

$$dS = \frac{\delta Q}{T} \tag{4.5}$$

In the case of irreversible changes, the entropy always increases. From the perspective of an isolated system without external pressure, the first law is fully characterized by the change in internal energy. In chemistry and plasma chemistry, however, most processes occur under constant conditions of external pressure. In this case, during a state change, the system can also perform work against this external pressure. Therefore, one speaks here of the enthalpy of a state change:

$$H = U + pV \tag{4.6}$$

or its change.

$$dH = dU + pdV + Vdp \tag{4.7}$$

The external pressure should remain constant as plasmas develop slowly, i.e., we get:

$$dH = dU + pdV \approx dU \tag{4.8}$$

or approximately dU for very low pressures in the system. The enthalpy H is often used to distinguish chemical reactions into endothermic and exothermic reactions:

$$\underbrace{A + B}_{H_1(p,T,N_i)} \leftrightarrows \underbrace{C + D}_{H_2(p,T,N_i')} \tag{4.9}$$

$$\Delta H = H_2 - H_1 > 0 \qquad \text{endothermic} \tag{4.10}$$

$$\Delta H = H_2 - H_1 < 0 \qquad \text{exothermic} \tag{4.11}$$

Compound	$H_{Formation}(T_0)$ (kJ/mol)
CH	595.8
CCl_3	59
SiH	377
SiF	-19.3
SiF_3	-1025

Table 4.1: Formation enthalpies of some selected molecules and radicals

In reference works, one can find formation enthalpies that describe the transition from individual atoms to a molecule. From this comparison, the probability of the occurrence of a particularly favorable particle in a reaction mixture can be derived. Some examples are listed in Table 4.1.
The stoichiometry of a reaction can be taken into account with corresponding prefactors to establish the following energy balance:

$$A + B \leftrightarrows C + D \tag{4.12}$$
$$N_A H_A + N_B H_B \leftrightarrows N_C H_C + N_D H_D \tag{4.13}$$

Thus, the enthalpy of the reaction is the difference between the enthalpy of the reactants and the products:

$$\Delta H = \sum_p N_p H_p - \sum_r N_r H_r \tag{4.14}$$

4.1.2 Thermodynamics of an Ideal Gas

For the question of whether a reaction proceeds, however, not only the difference in enthalpies is decisive, but also the possible change in entropy. This is taken into account by the so-called Gibbs free energy:

$$G = H - TS \tag{4.15}$$

or its change

$$dG = dH - TdS - SdT \tag{4.16}$$

A reaction at a given constant temperature will always strive for a state of lower Gibbs free energy:

$$dG = dH - TdS < 0 \tag{4.17}$$

For this, it is necessary to also calculate the change in entropy during a reaction. One can see from this formula, for example, that in irreversible reactions in which the entropy increases, the factor dS is always positive and thus the Gibbs free energy decreases. That is, such reaction directions are favorable. For this, we consider:

$$dS = \frac{\delta Q}{T} = \frac{dH}{T} = \frac{C_p}{T} dT \tag{4.18}$$

due to $dH \approx \delta Q$ for very low pressures p and $dV \approx 0$.

$$S(p_0, T) = S(p_0, T_0) + \int_{T_0}^{T} \frac{C_p}{T'} dT' \tag{4.19}$$

- **Temperature dependence of entropy**: The temperature dependence of the entropy is, for constant pressure p_0 and for $C_p = \frac{5}{2} nRT$, given by:

$$S(p_0, T) = S(p_0, T_0) + \frac{5}{2} nRT \ln\left(\frac{T}{T_0}\right) \tag{4.20}$$

  In the case of a constant volume, we get

$$S(p_0, T) = S(p_0, T_0) + \int_{T_0}^{T} \frac{C_V}{T'} dT' \tag{4.21}$$

  with $C_V = \frac{3}{2} nRT$:

$$S(V, T) = S(V, T_0) + \frac{3}{2} nRT \ln\left(\frac{T}{T_0}\right) \tag{4.22}$$

- **Pressure dependence of entropy**: The pressure dependence of the entropy is obtained by first determining the temperature dependence of the entropy at constant pressure and then its dependence at constant volume.

$$S(p_0, T_0) \to S(p_0, T) \to S(p, T_0) \tag{4.23}$$

  This results in (n is the number of molecules):

$$\begin{aligned} S(p,T_0) &= S(p_0,T_0) + \frac{5}{2}nRT\ln\left(\frac{T}{T_0}\right) - \frac{3}{2}nRT\ln\left(\frac{T}{T_0}\right) \\ &= S(p_0,T_0) + nRT\ln\left(\frac{T}{T_0}\right) \end{aligned} \tag{4.24}$$

with

$$p_0V = nRT \tag{4.25}$$
$$pV = nRT_0 \tag{4.26}$$

Thus, we obtain

$$S(p,T_0) = S(p_0,T_0) - nRT\ln\left(\frac{p}{p_0}\right) \tag{4.27}$$

With this description of entropy, we can finally calculate the Gibbs free energy:

$$G = H - TS \tag{4.28}$$

$$dG = dH - TdS - SdT \tag{4.29}$$

$$\begin{aligned} dH &= dU + pdV + Vdp && (4.30)\\ &= \delta Q - pdV + pdV + Vdp && (4.31)\\ &= \delta Q + Vdp = TdS + Vdp && (4.32) \end{aligned}$$

Thus, we finally obtain the change in the Gibbs free energy as:

$$dG = Vdp - SdT \tag{4.33}$$

Now, for our system, the individual dependencies of $V(p)$ from the ideal gas law and $S(T)$ from Eq. 4.27 can be inserted, and the change in G can be calculated.
So far, we have always analyzed the Gibbs free energy for fixed particle numbers. In the following, it should be considered that the particle numbers can change during chemical reactions. This is achieved by:

$$dG = \underbrace{\frac{\partial G}{\partial p}}_{=V} dp + \underbrace{\frac{\partial G}{\partial T}}_{=-S} dT + \sum_j \underbrace{\frac{\partial G}{\partial N_j}}_{\mu_j} dN_j \tag{4.34}$$

The so-called chemical potential μ now describes the change in this Gibbs free energy with the particle number.

$$\mu_j = \left(\frac{\partial G}{\partial N_j}\right)_{p,T} \tag{4.35}$$

The chemical potential corresponds to the energy that is added to a system when the particle number is changed. In equilibrium, we first define the initial state at p_0 and T_0 as:

$$\mu^0 \equiv G^0 \tag{4.36}$$

$$\Delta G = \sum_{Products} N_i \mu_i^0 - \sum_{Reactants} N_j \mu_j^0 \tag{4.37}$$

The temperature dependence of the chemical potential at constant pressure is:

$$S = -\frac{\partial G}{\partial T} \qquad \Delta\mu = \int_{T_0}^{T} -S dT \tag{4.38}$$

$$\Delta\mu = \int_{T_0}^{T} \left[-S(p_0, T_0) - \frac{5}{2} nR \ln \frac{T}{T_0}\right] dT \tag{4.39}$$

$$\begin{aligned} \Delta\mu &= \mu_0(p_0, T_0) + (T - T_0)\left(-S(p_0, T_0)\right) + & (4.40)\\ &\quad (T - T_0)\frac{5}{2} nR - \frac{5}{2} nRT \ln \frac{T}{T_0} & (4.41) \end{aligned}$$

The pressure dependence of the chemical potential is:

$$V = \frac{\partial G}{\partial p} \qquad \Delta\mu = \int_{p_0}^{p} V dp \tag{4.42}$$

$$\Delta\mu = \mu_0(p_0, T_0) + nR \ln \frac{p}{p_0} \tag{4.43}$$

In a chemical equilibrium, however, the pressure changes during the reactions. In general, one speaks of partial pressures p_j:

$$p = \sum p_j \tag{4.44}$$

For each component of a gas mixture, a chemical potential can be defined that changes with the partial pressure according to:

$$\mu_j(p) = \mu_j(T) + RT \ln\left(\frac{p_j}{p_0}\right) \tag{4.45}$$

or with a mole fraction $x_j = p_j/p$

$$\mu_j(p) = \mu_j(T) + RT \ln\left(x_j \frac{p}{p_0}\right) \tag{4.46}$$

In the case of solids and liquids, the pressure ratio is replaced by the activity $a_j = \gamma_j x_j$, with γ_j the activity coefficient. In the case of pure solids and liquids, $x_j = 1$ and $\gamma_j = 1$. Thus, the chemical potential then has no pressure dependence.

4.1.3 Reaction Equilibria

4.1.3.1 Energy Balance

Now let's consider the chemical equilibrium in a closed system. As an example, we have:

$$3A + B \leftrightarrows 2C + 4D \tag{4.47}$$

with $J_1 = A$, $J_2 = B$, $J_3 = C$, $J_4 = D$, $\alpha_1 = -3$, $\alpha_2 = -1$, $\alpha_3 = 2$, and $\alpha_4 = 4$, we can define the stoichiometry of the reactions as:

$$\sum_i \alpha_i J_i = 0 \tag{4.48}$$

where the stoichiometric factors of the reactants are counted negatively and those of the products positively.
For reactions at constant temperature and pressure, we thus have:

$$dG = \sum_i \mu_i dN_i = \sum_i \alpha_i \mu_i dN \tag{4.49}$$

The system will then move to the state for which $\sum_i^M \alpha_i \mu_i = 0$ holds. We now insert the chemical potential with:

$$\mu_j(p) = \mu_j^0(T) + RT \ln\left(\frac{\bar{p}_j}{p}\right) \tag{4.50}$$

with $\bar{p}_j$ the equilibrium pressure of species j. For solids, we simply get $\mu_j(p) = \mu_j^0(T)$. Thus, we obtain:

$$\underbrace{-RT\sum_{j=1}^{M}\alpha_j \ln\left(\frac{\bar{p}_j}{p}\right)}_{\text{Sum of gas particles}} = \underbrace{\sum j = 1^M \alpha_j \mu_j^0(T)}_{\text{Sum of all particles}} \tag{4.51}$$

The logarithm on the left side can be transformed to:

$$\prod_{j=1}^{M}\left(\frac{\bar{p}_j}{p}\right)^{\alpha_j} = \kappa(T) \tag{4.52}$$

with an equilibrium constant $\kappa(T)$ according to

$$\kappa(T) = \exp\left(-\frac{G_r^0(T)}{RT}\right) \tag{4.53}$$

The index r now refers to the chemical reaction being considered. Thus, we finally obtain the central equation that describes the chemical equilibrium as:

$$\boxed{\prod_{j=1}^{M}\left(\frac{\bar{p}_j}{p}\right)^{\alpha_j} = \exp\left(-\frac{G_r^0(T)}{RT}\right)} \tag{4.54}$$

For the above reaction, we thus obtain:

$$\kappa(T) = \frac{\bar{p}_C^2 \bar{p}_D^4}{\bar{p}_A^3 \bar{p}_B^1} \frac{1}{p_0^{-3-1+2+4}} \tag{4.55}$$

$$\kappa = \prod_{j=1} M_g \bar{x}_j \alpha_j \left(\frac{p}{p_0}\right)^{\alpha_g} \tag{4.56}$$

with $\alpha_g = \sum_{j=1}^{M_g} \alpha_j$.
The pressure dependence of the equilibrium concentrations is obtained as follows. The equilibrium constant $\kappa(T)$ is initially independent of the pressure, but the equilibrium concentrations change:

$$\prod_{j=1} M_g \bar{x}_j \alpha_j = \left(\frac{p}{p_0}\right)^{-\alpha_g} \kappa(T) \tag{4.57}$$

The temperature dependence of the equilibrium concentration is obtained from $G_r(T)/(RT)$ as:

$$G = H + T\frac{\partial G}{\partial T} \tag{4.58}$$

Multiplying by $1/T^2$, we get:

$$-\frac{H}{T^2} = -\frac{G}{T^2} + \frac{1}{T}\frac{\partial G}{\partial T} = \frac{\partial}{\partial T}\left(\frac{G}{T}\right) \tag{4.59}$$

This is called the Gibbs-Helmholtz equation. With $\ln \kappa(T) = -\frac{G_r^0}{RT}$, we get:

$$\frac{\partial}{\partial T} \ln \kappa(T) = \frac{\partial}{\partial T}\left(-\frac{G_r 0}{RT}\right) = \frac{H_r 0}{RT^2} \tag{4.60}$$

With $H_r^0 \simeq const.$, we finally get:

$$\kappa(T) = \kappa(T_0) \exp\left(\frac{H_r^0}{T}\left(\frac{1}{T} - \frac{1}{T_0}\right)\right) \tag{4.61}$$

4.1.3.2 Direction of the Chemical Reaction

In which direction does the chemical reaction proceed?

$$G_r = G_r^0(T_0) + RT \ln Q(T) \tag{4.62}$$

with Q the reaction coefficient:

$$Q(T) = \prod_{j=1}^{M} \left(\frac{p_j}{p_0}\right)^{\alpha_j} \tag{4.63}$$

If $Q(T) > \kappa(T)$, the reaction shifts in the direction of the reactants; if $Q(T) < \kappa(T)$, the reaction shifts in the direction of the products. In equilibrium, $Q(T) = \kappa(T)$.

4.1.4 The Chemical Equilibrium in a System with Multiple Phases

In the case of multiple phases (g... gas, l... liquid, s... solid), one speaks of a heterogeneous equilibrium. That is,

$$dG = -\mu_g dN + \mu_l dN \tag{4.64}$$

In equilibrium, $\mu_g = \mu_l = \mu_s \equiv \mu$. For small changes in N, we get:

$$d\mu_g = -S_g dT + V_g dp \tag{4.65}$$
$$d\mu_l = -S_l dT + V_g dp \tag{4.66}$$

and

$$\frac{dp}{dT} = \frac{S_g - S_l}{V_g - V_l} \tag{4.67}$$

For the transition of the system from one phase to another, latent heat must be supplied, such as the enthalpy of vaporization $H_{evaporation}$ or the enthalpy of sublimation $H_{sublimation}$. For $S_g - S_l = \Delta S = H_{evaporation}/T$ and $V_g \gg V_l \simeq 0$, we finally obtain the **Clausius-Clapeyron equation**:

$$\frac{dp}{dT} = \frac{H_{evaporation}}{RT^2} p \tag{4.68}$$

In the case where the enthalpy of vaporization $H_{evaporation} \neq H_{evaporation}(T)$, we get:

$$p_j = p_{0j} \exp\left(-\frac{H_{evaporation}}{RT}\right) \tag{4.69}$$

or

$$p_j = p'0j \exp\left(-\frac{H_{sublimation}}{RT}\right) \tag{4.70}$$

4.2 Reaction Kinetics

The investigation of reaction equilibria assumes that the system can undergo sufficient collisions within the residence time of the molecules and atoms in a plasma so that the forward and reverse reactions are in equilibrium. This is only very rarely the case, as plasmas are often used to avoid exactly this equilibrium. An exception would be thermal plasmas as used, for example, for welding. Within the plasma, however, a quasi-equilibrium can also be described considering the electronically driven processes [43].

4.2.1 Rate Constants

Often, a so-called kinetic consideration is much more powerful, in which a gas flow passing through a plasma is considered. Depending on the residence time and reaction rates, the conversion of particle species can proceed to different extents. First, let's consider a typical reaction again:

$$\alpha_1 A + \alpha_2 B \leftrightarrows \alpha_3 C + \alpha_4 B \tag{4.71}$$

or the conservation equation for stoichiometry according to

$$\sum_j \alpha_j J_j = 0 \tag{4.72}$$

The reaction rate is then

$$R_{reaction}(T, p, n_i) = \frac{1}{\alpha_i} \frac{\partial n_i}{\partial t} \tag{4.73}$$

and the change of one of the particle species is thus:

$$\frac{\partial n_i}{\partial t} = \alpha_i R_{reaction}(T, p, n_i) \tag{4.74}$$

This reaction rate R is a function of T, p, and n_i and can be investigated in a plasma process or directly in particle beam experiments. We distinguish several types of reactions. First, an elementary reaction is defined as follows:

> *A reaction is an elementary reaction when, in a single step, all reactants collide simultaneously to produce the products. Example:* $2\,NO + O_2 \rightarrow 2\,NO_2$.

From the measurements, it is known that a reaction rate consists of the product of two factors: on the one hand, expressions according to the density of

the participating particles and, on the other hand, a parameter that depends on the temperature:

$$\frac{\partial n_i}{\partial t} = -\underbrace{[n_i]x[n_j]y}_{Densities} \quad \underbrace{k(T)}_{[m3(x+y-1)s-1]} \tag{4.75}$$

Here are some examples of different reaction orders:

- *Unimolecular* - First-order reaction

$$AB \rightarrow A + B \qquad \frac{\partial n_{AB}}{\partial t} = -[n_{AB}]^1 k_1(T) \tag{4.76}$$

- *Bimolecular* - Second-order reaction

$$A + B \rightarrow C + D \qquad \frac{\partial n_A}{\partial t} = \frac{\partial n_B}{\partial t} = -[n_A]^1[n_B]^1 k_2(T) \tag{4.77}$$

- *Trimolecular* - Third-order reaction

$$A+B+X \rightarrow AB+X \qquad \frac{\partial n_A}{\partial t} = -[n_A]^1[n_B]^1[n_X]^1 k_3(T) \tag{4.78}$$

From the units of the rate coefficient k, one can often also recognize the order of the reaction.
Let's compare the reaction kinetics with the chemical equilibrium for the reaction:

$$A + B \leftrightarrow C + D \tag{4.79}$$

with the rate coefficient for the forward reaction k_1 and the reverse reaction k_{-1}

$$\frac{\partial n_A}{\partial t} = \frac{\partial n_B}{\partial t} = -[n_A]^1[n_B]^1 k_1(T) \tag{4.80}$$
$$\frac{\partial n_C}{\partial t} = \frac{\partial n_D}{\partial t} = +[n_A]^1[n_B]^1 k_1(T) \tag{4.81}$$
$$\frac{\partial n_A}{\partial t} = \frac{\partial n_B}{\partial t} = [n_C]^1[n_D]^1 k_{-1}(T) \tag{4.82}$$
$$\frac{\partial n_C}{\partial t} = \frac{\partial n_D}{\partial t} = -[n_C]^1[n_D]^1 k_{-1}(T) \tag{4.83}$$

Assume that the particle species A is in equilibrium, i.e.,

$$\frac{\partial n_A}{\partial t} = 0 = -[n_A]^1[n_B]^1 k_1(T) + [n_C]^1[n_D]^1 k_{-1}(T) \tag{4.84}$$

From this, an equilibrium constant can be derived:

$$\frac{k_1(T)}{k_{-1}(T)} = \frac{[n_C]^1[n_D]^1}{[n_A]^1[n_B]^1} \tag{4.85}$$

It holds that:

$$\frac{k_1(T)}{k_{-1}(T)} = k(T) \exp\left(-\frac{G_r^0(T)}{RT}\right) \tag{4.86}$$

or

$$k(T) = \prod_{j=1} M_g \left(\frac{\bar{p}_j}{p_0}\right)^{\alpha_j} \tag{4.87}$$

Now let's consider the reaction kinetics in a theoretical example of a reaction chain:

$$A \rightarrow B \rightarrow C \tag{4.88}$$

with the rate coefficients k_A and k_B. Initially, only species A is present. The temporal development of the densities is shown in Fig. 4.1 for the case $k_A \ll k_B$ and for $k_A \gg k_B$. It can be seen that the slowest reaction is the rate-limiting step.
From the course of the densities over time, one can also learn something about the order of the individual reactions. Fig. 4.2 shows an experiment in which a closed reactor is initially filled with methane, and the course of the densities is observed after the plasma is ignited. It can be seen that the density of methane decreases and the densities of the reaction products increase. Furthermore, it can be seen that the densities of C_2H_6 and C_2H_4 increase linearly, indicating that these are primary products. The formation of C_2H_2, on the other hand, increases very slowly, i.e., methane is not directly involved in the formation channel here - these are secondary reactions.

4.2.2 Cross Sections, Mean Free Path, Collision Frequency

To determine reaction rates, chemical equilibria can be calculated or their variation under the influence of changes in external boundary conditions such as pressure and temperature. From a microscopic point of view, however,

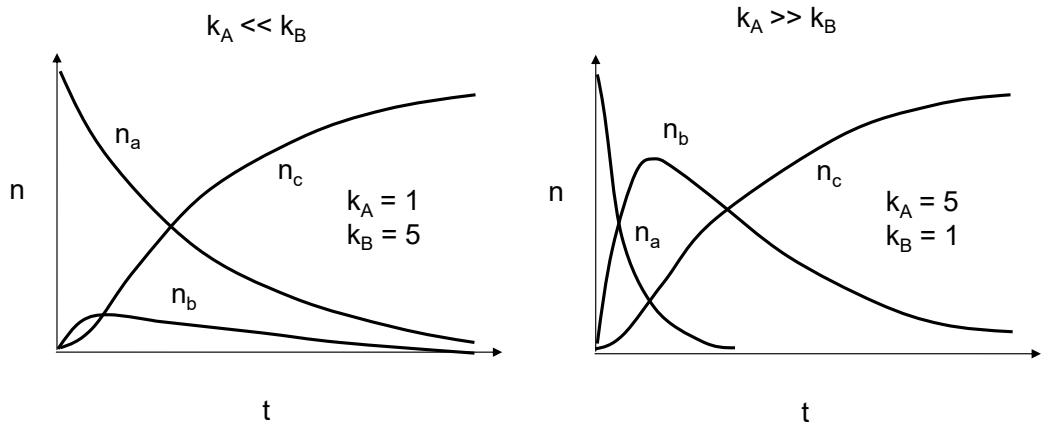

Figure 4.1: Variation of densities for different rate constants k_A and k_B.

every rate coefficient can be characterized by an elementary collision process between two particles. First, let's consider the probability of a collision p_{Stoss} along a flight path dx between a particle A with velocity v_A and a stationary particle species B with density n_B (see Fig. 4.3). This probability is linked to a hit area σ_{AB}, the so-called cross section.

$$p_{Stoss} = dx n_B \sigma_{AB}(v_A) \tag{4.89}$$

The frequency with which these collisions occur - the so-called collision frequency - is:

$$\nu_{AB} = v_A \sigma_{AB}(v_A) n_B \tag{4.90}$$

From this, the mean free path can be derived by considering the change in a particle flux Γ_A

$$d\Gamma_A(x) = \Gamma_A(x) n_B \sigma_{AB}(v_A) dx \tag{4.91}$$

and assuming $\Gamma_A(x) = \Gamma_{A,0} \exp(-x/\lambda)$:

$$\lambda = \frac{1}{n_B \sigma_{AB}} \tag{4.92}$$

From this, the reaction rate can now be derived from:

$$R_{AB} = n_A v_A \sigma_{AB}(v_A) n_B = n_A n_B v_A \sigma_{AB}(v_A) = n_A n_B k_{AB}(T) \tag{4.93}$$

In general, the reaction rate is given as:

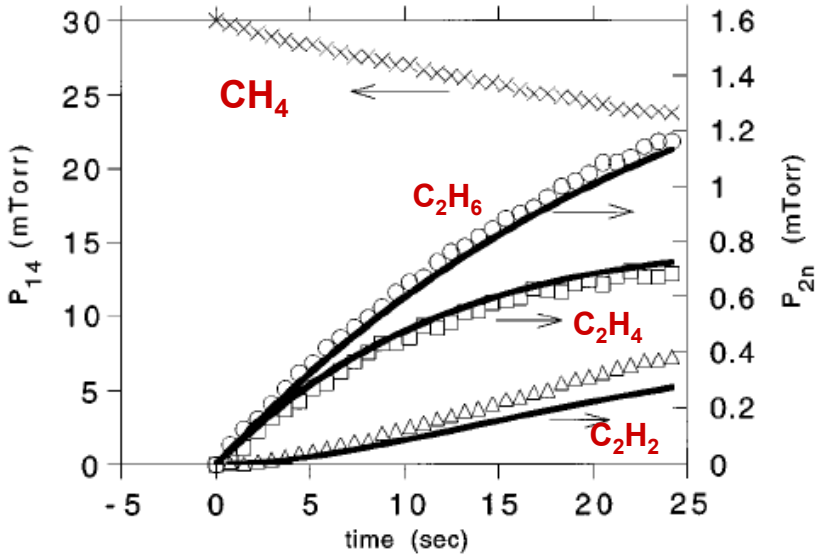

FIG. 5. C_2 partial pressures versus time for a 30 mTorr CH_4 discharge. Crosses; CH_4: circles: C_2H_6; squares: C_2H_4; triangles: C_2H_2. Solid lines are model results.

Figure 4.2: Variation of partial pressures in a methane plasma after the plasma is turned on. From Dagel, Mallouris, Doyle, J. Appl. Phys. 79, (1996).

$$R_{AB} = n_A n_B \int\int (v_A - v_B)\sigma_{AB}(v_A - v_B) f(v_A) f(v_B) dv_a dv_b = n_A n_B \langle \sigma(v) v \rangle \tag{4.94}$$

The rate coefficient is then

$$k_{AB} = \langle \sigma(v) v \rangle \tag{4.95}$$

The averaging, expressed by the symbols $\langle$ and $\rangle$, requires a distribution function for the frequency with which individual velocities occur in the ensemble. In the simplest case, this is also a Maxwell-Boltzmann distribution:

$$f(v) = 4\pi \left(\frac{m}{2\pi k_B T} \right)^{3/2} v^2 \exp\left(-\frac{m v^2}{2 k_B T} \right) \tag{4.96}$$

Databases for the individual cross sections can be found at NIST [1], at

[1]NIST Chemical Kinetics Database http://kinetics.nist.gov/kinetics/index.jsp De-

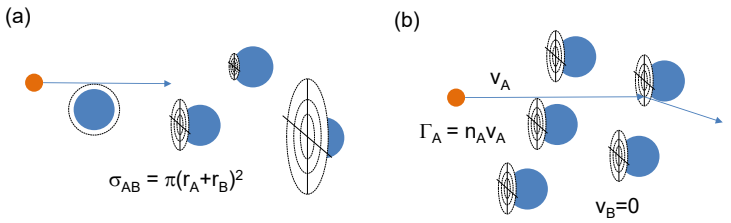

Figure 4.3: Collision processes between particles A and B with different cross sections (a) or as a transport problem where a projectile A flies through a quantity of particles B (b).

Gaphyor[2] and for astrochemical data at UMIST[3]

4.2.3 The Collision Process

For the calculation of cross sections, we need the calculation of a trajectory of the two colliding particles depending on the interaction, expressed by a potential $V(r)$, a relative velocity v, and an impact parameter describing the distance of the projectile to the symmetry axis (see Fig. 4.5). The particles with masses m_1 and m_2 and velocities v_1 and v_2 experience force and counterforce F_{12} and F_{21} according to:

$$m_1\dot{\vec{v}}_1 = \vec{F}_{12} = -\vec{F}_{21} = -m_2\dot{\vec{v}}_2 \tag{4.97}$$

The coordinate of the center of mass (cm) r_{cm} and its velocity v_{cm} is

$$r_{cm} = \frac{m_1 r_1 + m_2 r_2}{m_1 + m_2} \tag{4.98}$$

$$v_{cm} = \frac{m_1 v_1 + m_2 v_2}{m_1 + m_2} \tag{4.99}$$

Going to the center of mass system, we get new coordinates of the distance of the two bodies r as well as the relative velocity v_r and the reduced mass m_r as:

tailed Chemical Kinetic Combustion Model Database http://kinetics.nist.gov/CKMech/

[2]Gaphyor A Database for Atoms, Molecules, Gases and Plasmas http://gaphyor.lpgp.u-psud.fr/gaphyor/gaphyor.html

[3]The UMIST database for astrochemistry http://www.udfa.net/

$$r = r_1 - r_2 \tag{4.100}$$
$$v_r = v_1 - v_2 \tag{4.101}$$
$$m_r \dot{v}_r = F_{12}(r) \tag{4.102}$$
$$m_r = \frac{m_1 m_2}{m_2 + m_2} \tag{4.103}$$

The respective components in the laboratory system and in the center of mass system are shown in Fig. 4.4. As the scattering angle, we get

$$\tan\theta_1 = \frac{\sin\theta}{(m_1/m_2)(v_r/v_r') + \cos\theta} \tag{4.104}$$
$$\tan\theta_2 = \frac{\sin\theta}{v_r/v_r' - \cos\theta} \tag{4.105}$$

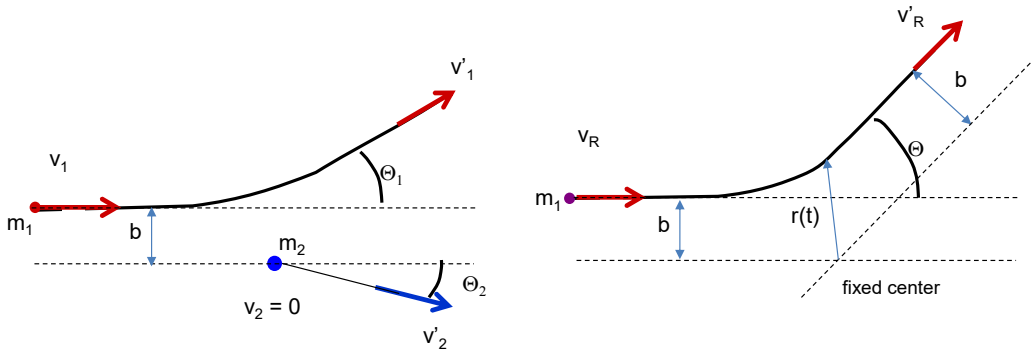

Figure 4.4: Collision processes in the laboratory system and in the center of mass system.

In the case of elastic scattering, $v_r = v_r'$. The differential cross section is

$$\frac{d\sigma}{d\Omega} = \frac{b}{\sin\theta}\frac{db}{d\theta} \tag{4.106}$$

Animation

Trajectory of Coulomb scattering
Trajectory of Langevin scattering
Simulation of trajectories in Coulomb and Langevin scattering.

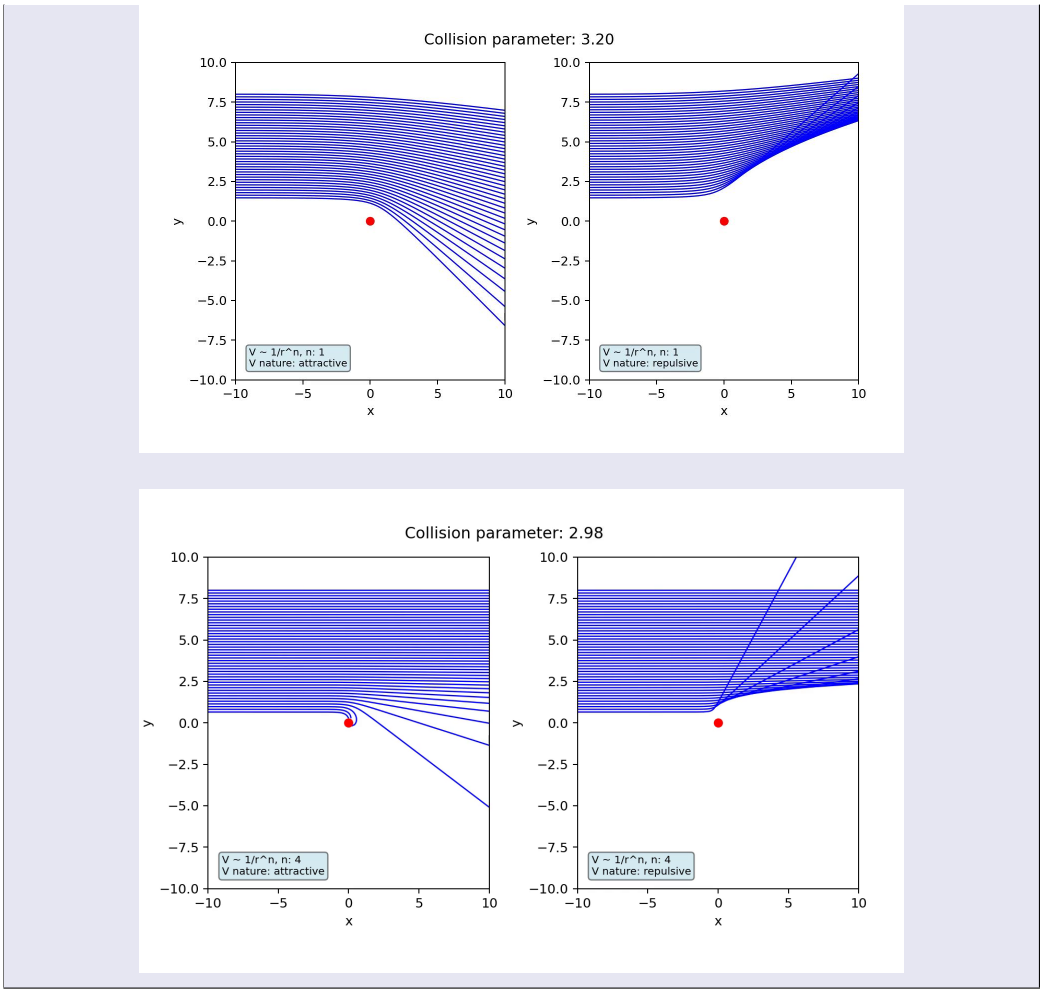

That is, a collision with a certain impact parameter leads to a characteristic deflection σ as illustrated in Fig. 4.5. From this, the total cross section for scattering (sc) can be calculated by integrating over all impact parameters:

$$\sigma_{sc} = 2\pi \int_0^\pi \frac{d\sigma}{d\Omega} \sin\theta d\theta \tag{4.107}$$

The cross section for momentum transfer (m) results directly from this:

$$\sigma_m = 2\pi \int_0^\pi (1 - \cos\theta) \frac{d\sigma}{d\Omega} \sin\theta d\theta \tag{4.108}$$

The additional factor $(1 - \cos\theta)$ weights the change in momentum during scattering. For example, if the deflection angle is very small $\theta \ll 1$, scattering does occur, but the momentum changes only slightly, since $\Delta p \simeq (1 - \cos\theta)$. In the case of a central potential, the scattering angle can be calculated as:

$$\theta = \pi - 2\int_{r_{min}} \infty \frac{bv_0/r^2}{\left[v_0^2 - \frac{2}{m_r}\left[V(r) + \frac{m_r b^2 v_0^2}{2r^2}\right]\right]^{1/2}} dr \tag{4.109}$$

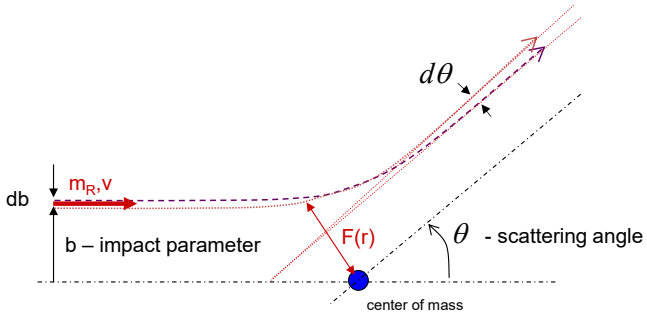

Figure 4.5: A collision with an impact parameter b leads to a deflection into a solid angle $2\pi d\Theta$.

- *Coulomb scattering*:

  In the scattering between two charge carriers, the Coulomb potential $V(r) = \frac{q_1 q_2}{4\pi\epsilon_0 r}$ initially applies, and we get:

$$\frac{d\sigma}{d\Omega} = \left[\frac{b_0}{4\sin^2(\theta/2)}\right]^2 \tag{4.110}$$

  with $b_0 = \frac{q_1 q_2}{4\pi\epsilon_0 E_0}$ the distance of closest approach, if E corresponds to the kinetic energy in the center-of-mass system. The collision integral, however, tends to infinity. Therefore, one could use the Debye length as the maximum distance in plasmas. However, it turns out that in the transport of particles in plasmas, the sum of many small-angle collisions dominates. We get:

$$\sigma_{90^\circ} = \frac{1}{4}\pi b_0^2 \tag{4.111}$$

  for a single collision and

$$\sigma_{90^\circ} = \frac{8}{\pi} b_0^2 \ln\Lambda \tag{4.112}$$

with $\Lambda = \lambda_d/b_0 \gg 1$ (often, for the so-called Coulomb logarithm, approximately $\ln \Lambda \simeq 10$ in many plasmas)

- *Polarization scattering*

  In the scattering between a charged particle and a neutral atom or molecule, the interaction is the induction of a dipole moment by the passing particle A in the atom or molecule B, as in Fig. 4.6. There, a dipole moment p_d is created

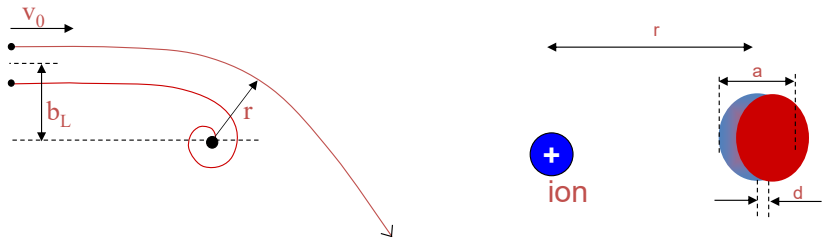

Figure 4.6: Polarization scattering for collisions between charged and uncharged particles. For impact parameters smaller than b_L, recombination occurs.

$$p_d = q_0 d = \frac{q a^3}{r^2} \tag{4.113}$$

The force between a charged particle and such a dipole moment is:

$$F = \frac{2 p_d q}{4\pi\epsilon r^3}\hat{r} = \frac{2 q^2 a^3}{4\pi\epsilon_0 r^5}\hat{r} \tag{4.114}$$

From this, a central potential of the form is obtained:

$$V(r) = -\frac{q^2 a^3}{8\pi\epsilon_0}\frac{1}{r^4} \tag{4.115}$$

The so-called **Langevin cross section** then becomes:

$$\sigma_L = \pi b_L^2 = \left(\frac{\pi\alpha_p q^2}{\epsilon_0 m}\right)^{1/2}\frac{1}{v_0} \tag{4.116}$$

with $E_0 = \frac{1}{2}mv_0^2$. Fig. 4.7 illustrates that particles with an impact parameter smaller than b_L can recombine with the molecule, which is referred to as particle capture.

- *Centrifugal barrier*

  For this interaction, however, the centrifugal force can become important, which may act as a barrier. A correction of the form is obtained:

$$V_{eff}(r) = V(r) + \frac{m_r b^2 v_0^2}{2r^2} \tag{4.117}$$

  The actual interaction potential can now be arbitrarily assumed $V(r) = C/r^i$ (in the case of the Coulomb potential, $i = 1$, in the case of polarization scattering, $i = 3$). Fig. 4.7 shows that in the case of normal Coulomb scattering, no barrier occurs. However, for higher exponents i, this centrifugal barrier is created.

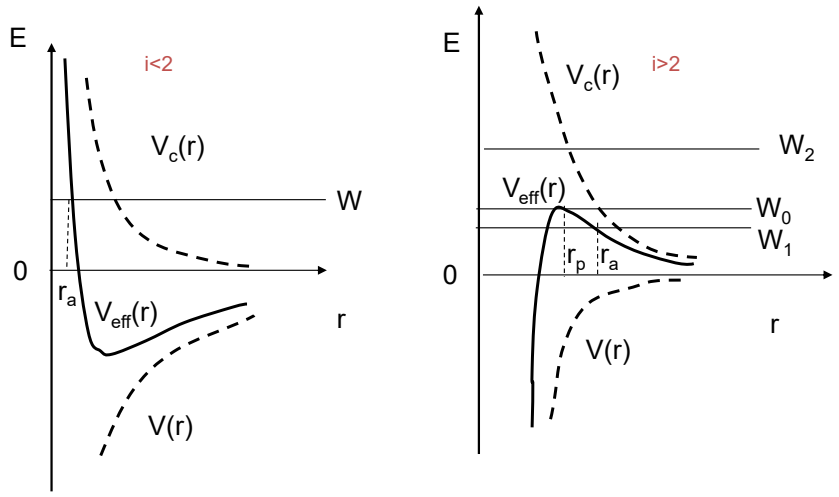

Figure 4.7: Depending on the exponent of the distance dependence of the potential $\propto 1/r^i$, an activation barrier is obtained, since the centrifugal force must be overcome.

- *Approximation for small-angle collisions*

  In the case of Coulomb scattering in plasmas, the Coulomb cross section can now be calculated as above. However, due to the high charge carrier

densities, the effect occurs that the efficiency of the succession of many collisions at small deflection angles, which occur more frequently, i.e., the cross section for the sum of these small-angle collisions, can be larger than the cross section for a single collision with a deflection of 90 degrees. Assume that the deflection angle $\theta \ll 1$. Thus, we get:

$$r = \left(b^2 + v_r^2 t^2\right)^{1/2} \tag{4.118}$$

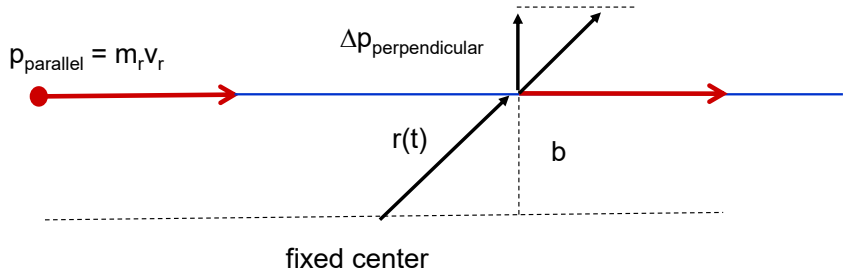

Figure 4.8: Approximation for small-angle collisions.

The change in the perpendicular momentum becomes

$$\Delta p_\perp = \int_{-\infty}^{\infty} \frac{b}{r} \left| \frac{dV}{dr} \right| dr \tag{4.119}$$

As well as

$$dt = \frac{r}{v_r} \frac{dr}{(r^2 - b^2)^{1/2}} \tag{4.120}$$

The deflection angle then becomes

$$\theta = \frac{\Delta p_\perp}{p_\parallel} = \frac{2b}{m_r v_r^2} \int_b^{\infty} \left| \frac{dV}{dr} \right| \frac{dr}{\sqrt{r^2 - b^2}} \tag{4.121}$$

Now assume that the initial kinetic energy is E_0. Furthermore, the interaction should be characterized by a potential in the form $V(r) = \frac{C}{r^i}$. With this approach, an analytical solution can be derived in the form:

$$\theta = \frac{A}{E_0 b^i} \tag{4.122}$$

with the factor A, which is derived from the gamma function Γ as:

$$A = \frac{C\sqrt{\pi}\Gamma((i+1)/2)}{2\Gamma((i+2)/2))} \tag{4.123}$$

Thus, we finally obtain a general expression for the differential cross section:

$$\frac{d\sigma}{d\Omega} = \frac{1}{i}\left(\frac{A}{E_0}\right)^{2/i} \frac{1}{\theta^{2+2/i}} \tag{4.124}$$

Some examples of the scattering of electrons on noble gas atoms or on hydrogen molecules are shown in Fig. 4.9. It can be seen that the cross section for large energies here, expressed as the square root of the acceleration voltage, decreases. However, for the noble gases Ar, Kr, Xe, a minimum is observed at small energies. This is the so-called **Ramsauer effect**, where the de Broglie wavelength of the scattering electron is approximately equal to the diameter of the atom. In this case, the scattering becomes very ineffective, i.e., a minimum is created. This occurs only in larger noble gas atoms and not in helium.

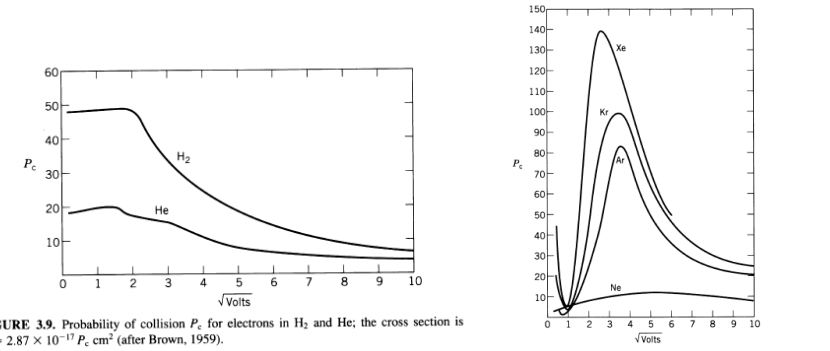

FIGURE 3.9. Probability of collision P_c for electrons in H_2 and He; the cross section is $\sigma \approx 2.87 \times 10^{-17} P_c$ cm^2 (after Brown, 1959).

FIGURE 3.10. Probability of collision P_c for electrons in Ne, Ar, Kr, and Xe, showing the Ramsauer minima for Ar, Kr, and Xe; the cross section is $\sigma \approx 2.87 \times 10^{-17} P_c$ cm^2 (after Brown, 1959).

Figure 4.9: Collision probabilities of electrons.

- *Ionization according to the Thomson model*

  Ionization by electron impact can only be correctly described by the laws of quantum mechanics. As a simple classical approximation, one can also consider the momentum transfer to a bound electron in the atomic shell. The energy transfer in such a collision process is:

$$\Delta E = E\, 2\frac{m_1 m_2}{(m_1+m_2)^2}(1-\cos\Theta_{cm}) \tag{4.125}$$

  Since small angles dominate, we make the approximation

$$\cos\Theta_{cm} \simeq 1 - \frac{\Theta_{cm}^2}{2} \tag{4.126}$$

  Eq. applies to the scattering angle in the center of mass system (cm - center of mass). In the laboratory system (lb - lab), $\Theta_{lb} \rightarrow \Theta_{cm}/2$ for collision partners with equal mass $m_1 = m_2$. In the following, we denote with Θ the scattering angle in the laboratory system. The energy transfer in the laboratory system becomes

$$\Delta E = \Theta^2 E \tag{4.127}$$

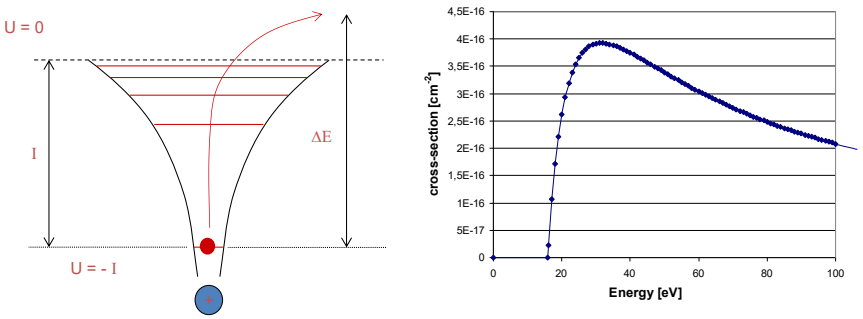

Figure 4.10: Ionization according to the Thomson model.

Similarly, the differential cross section in the center of mass system (cm) for small scattering angles Θ can be written ($\sin 4\Theta_{cm}/2 = \Theta 4$):

$$\left.\frac{d\sigma}{d\Omega}\right|_{cm} = \left(\frac{e^2}{4\pi\epsilon_0}\right)^2 \frac{1}{E^2}\frac{1}{\Theta^4} \tag{4.128}$$

convert to the laboratory system via $E_{cm} = \frac{1}{2}E_{lb}$ and $m_{cm} = \frac{1}{2}m_{lb}$:

$$d\sigma|\, lb = \left(\frac{e^2}{4\pi\epsilon_0}\right)^2 \frac{1}{E^2}\frac{1}{\Theta^4} 2\pi \underbrace{\sin\Theta}_{\propto\Theta} d\Theta \tag{4.129}$$

We switch from a solid angle element to an energy transfer ΔE with:

$$d(\Delta E) = E 2\Theta d\Theta \tag{4.130}$$

Thus, we get

$$d\sigma = \pi \left(\frac{e^2}{4\pi\epsilon_0}\right)^2 \frac{1}{E}\frac{1}{(\Delta E)^2} d(\Delta E) \tag{4.131}$$

We integrate this equation from the minimum energy transfer, given by the ionization energy, to the electron's total energy E.

$$\sigma(E) = \int_{E_{Ionization}}^{E} \pi \left(\frac{e^2}{4\pi\epsilon_0}\right)^2 \frac{1}{E}\frac{1}{(\Delta E)^2} d(\Delta E) \tag{4.132}$$

thus, we finally obtain the **Thomson cross section** for ionization (see Fig. 4.11):

$$\boxed{\sigma_{Ionization} = \pi \left(\frac{e^2}{4\pi\epsilon_0}\right)^2 \frac{1}{E}\left(\frac{1}{E_{Ionization}} - \frac{1}{E}\right)} \tag{4.133}$$

Some examples of ionization cross sections are shown in Fig. 4.11.

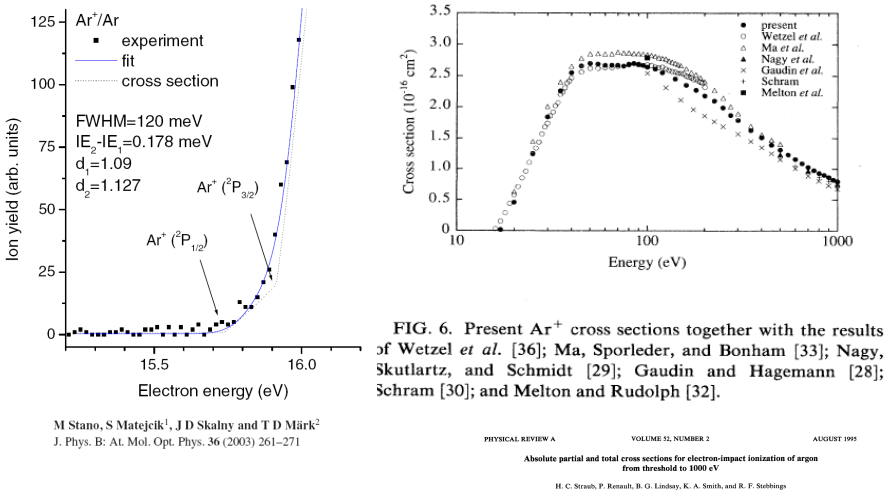

Figure 4.11: Ionization cross sections. From Stano, Matejcik, Skalny, MÃ¤rk, J. Phys. B 36, 261 (2003) and Straub, Renault, Lindsay, Smith, Stebbings, Phys. Rev A. 52(1995).

4.2.4 Molecular Collision Processes

Collision processes such as ionization and polarization scattering can already describe the behavior of plasmas quite well. However, molecules in plasmas have additional degrees of freedom, such as rotation and vibration. Furthermore, collisions between particles can also lead to dissociation or the creation of internal excitations.

4.2.4.1 The Molecular Bond

- *Electronic part of the bond:*

  First, let's consider a simple H_2 molecule, which, depending on the sign of the two 1s wavefunctions, can take on a bonding and a non-bonding state when the atomic orbitals are superimposed (LCAO - linear combination of atomic orbitals), as illustrated in Fig. 4.12. In the case of a bonding overlap of the orbitals, the system can lower its energy and a bound state is created. This electron can be excited into the non-bonding state, and thus dissociation occurs through electron transfer. The strength of this bond depends on the overlap of the wavefunctions. If the distance between the two atoms in the H_2 molecule is varied, the potential energy of the bonding and non-bonding states changes. At large distances, these approach each other, and dissociation occurs.

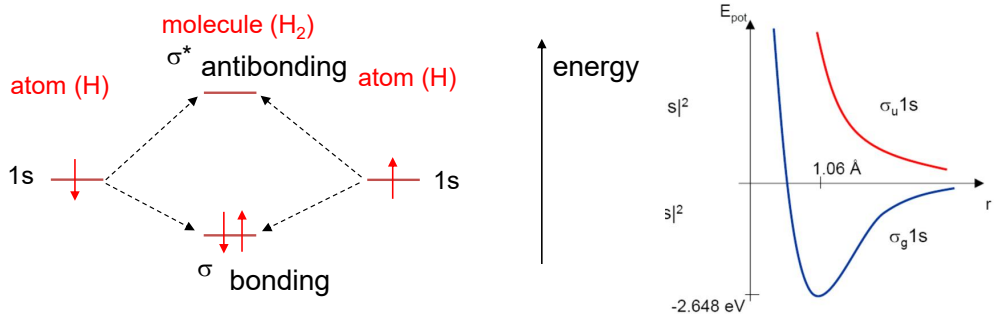

Figure 4.12: Superposition of 1s wavefunction in the H_2 molecule leads to a bonding σ and non-bonding state σ^*.

An example of the potential energy as a function of the atomic distance of the H_2, H_2^+, and H_2^- molecules is shown in Fig. 4.13. The ground state of the bonding state of H_2 is marked in blue, and that of the

non-bonding state in red. In addition to the ground state, a large number of excited states can be seen. This illustrates, for example, that dissociation can occur not only by separating the two atoms to large atomic distances but much more easily by excitation with electrons or photons from a bonding lower state to a non-bonding upper state.

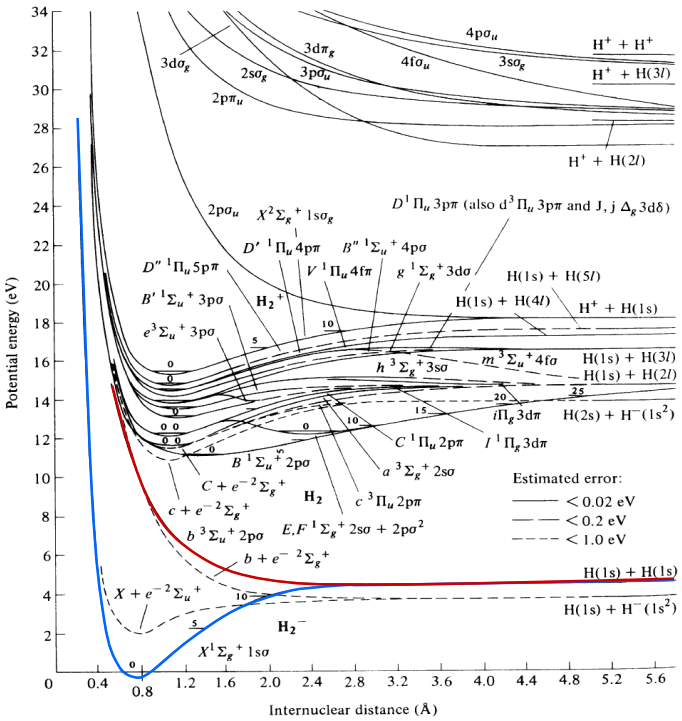

Figure 4.13: Energy diagram of H_2, H_2^+. From Jeffry, Steinfeld *Molecules and Radiation: An Introduction to Modern Molecular Spectroscopy*, MIT Press 1985.

- *Vibrational part of the bond:*

  The displacement of the atomic cores from the equilibrium position can lead to the excitation of vibrations. Such vibrations are represented with a potential energy corresponding to a parabola, and equidistant energy levels are obtained for small excitations. The energy diagram for this is shown in Fig. 4.14.

  The oscillator potential can be approximated as:

$$E_{pot}(r) = A\,[1 - \exp(-a(r - r_0))] \tag{4.134}$$

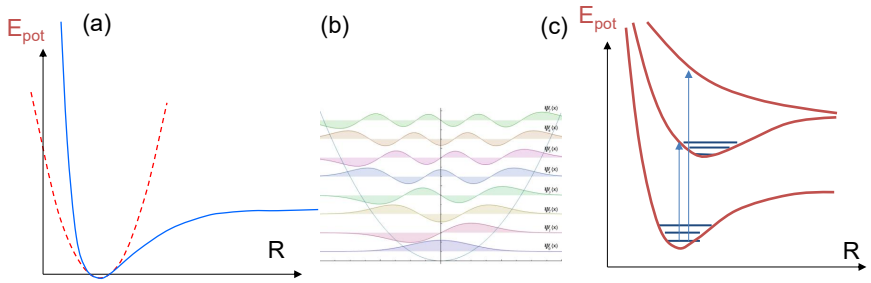

Figure 4.14: Energy diagram of a molecular vibration.

with r_0 the equilibrium distance and constants A and a. The energy eigenvalues in this potential well are:

$$E_n = \Delta E_0 \left(n + \frac{1}{2}\right) - \Delta E_0 x_e \left(n + \frac{1}{2}\right)^2 \tag{4.135}$$

with the anharmonicity $x_e = \Delta E_0/(4A)$ and $\Delta E_0 = \hbar\omega_0$. It can be seen in Fig. 4.14a that the oscillator potential is only an approximation for the lower states with small quantum numbers n. At higher excitations, the levels become increasingly closer together. In the case of CO_2, for example, the dissociation threshold is reached for $n = 21$. In this sense, dissociation in a plasma can also be increased if the collision partner for electron impact-induced dissociation is a vibrationally excited molecule.

The cross section for the electronic excitation of vibrationally excited molecules is particularly large when the overlap of the wavefunction in the lower and upper states is particularly large. A typical case is shown in Fig. 4.14c. From the wavefunction of the ground state (see Fig. 4.14b), it can be seen that the electron is initially localized in the region of r_0, the equilibrium distance. According to the Born approximation, the movement of the atomic cores always occurs much more slowly than the movement of the electrons in the atom, i.e., electronic excitations always occur vertically upwards in the energy diagram. This is referred to as the **Frank-Condon principle**. It can be seen that electronic excitation from the lower ground state to a vibrationally excited higher state occurs very efficiently if the wavefunction also shows a local extremum there (at constant position r_0). In the case shown here, this is for Ψ_2, Ψ_4, Ψ_6.

- *Rotational part of the bond:*

The quantization of the rotation of a simple diatomic molecule is derived from the equivalence of a classical rotor with moment of inertia I and angular frequency ω. Due to the symmetry in quantum physics, the angular momentum is quantized, and a rotational energy is obtained that scales with the quantum numbers $j(j+1)$. The rotational energies are much smaller than the vibrational energies, so that in an energy diagram (Fig. 4.15), a series of rotational levels is attached to each vibrational level. Here, too, the Frank-Condon principle applies again, so that transitions with large overlap of the wavefunctions in the ground and excited states are very likely.

$$E_{rot} = \frac{1}{2} I\omega^2 \tag{4.136}$$

$$L = I\omega = \hbar\sqrt{j(j+1)} \tag{4.137}$$

$$E_{rot} = \frac{\hbar^2}{2I}(j(j+1)) \tag{4.138}$$

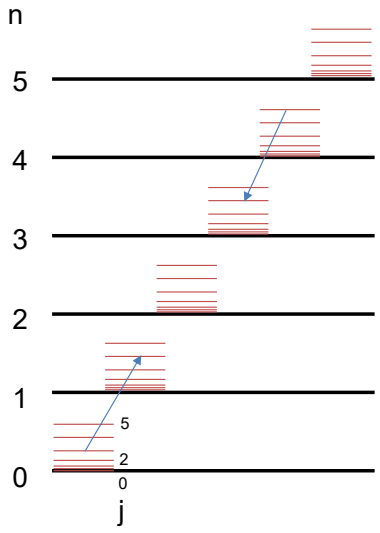

Figure 4.15: Energy diagram of the rotational bands.

That is, the rotational bands increase approximately quadratically with the quantum number j. Interesting in this context is the absorption of a photon and the generation of an excitation that can be electronic,

vibrational, and rotational. However, the conservation of angular momentum with respect to the annihilation of the angular momentum of the photon by the change in angular momentum of the excited electron or the rotation of the entire molecule must be considered. In excitations in the infrared, electronic excitations cannot occur due to the insufficient photon energy, but only vibro-rotational excitations. A pure vibrational excitation of a diatomic molecule, however, cannot occur through the absorption of a photon, as the conservation of angular momentum would be violated. For this reason, a vibrational-rotational excitation always occurs. This conservation of angular momentum conditions a transition between two rotational levels with different quantum numbers j (from different vibrational levels for a ro-vibronic transition). Since the energy of the individual rotational levels increases quadratically with the quantum number, different energies are also obtained at which such a molecule absorbs light, since $\Delta E_{j,j+1}$ scales approximately as j.

The energy exchange or time constants for the individual molecular excitations are as follows:

$$\tau_{e-collision} = 10^{-16}...10^{-15}s \quad (4.139)$$

$$\tau_{vibration} = 10^{-14}...10^{-13}s \quad (4.140)$$

$$\tau_{radiation} = 10^{-9}...10^{-8}s \quad (4.141)$$

That is, for example, electronic excitations occur much faster than the typical period of a vibration. We have already expressed this with the Frank-Condon principle. The time constant for a vibration is also decisive for dissociation. This must be related to the possibility of de-excitation or energy transfer during a collision with another particle or during de-excitation by the emission of a photon. The time constant for de-excitation by photons is in the nanosecond range, and the collision time in low-pressure plasmas is much shorter. Typically, we have

$$\tau_{electronic\ excitation} \ll \tau_{vibration} \simeq \tau_{dissociation} \ll \tau_{collisions} \ll \tau_{radiation} \quad (4.142)$$

However, in collisions between molecules, excited states can first be created. This is typically the case in recombination (2-to-1 reactions), as simultaneous energy and momentum conservation is only possible then.

4.2.4.2 Electron Collision Processes with Molecules

For the reactions of electrons with molecules, there are several cases:

- *Dissociation by electron impact*

$$e + AB \rightarrow A + B + e \tag{4.143}$$

In the simplest case, the transfer of an electron to a non-bonding state of the molecule occurs. As a result, the fragments move apart and have a kinetic energy corresponding to the initial state, as illustrated in Fig. 4.16a.

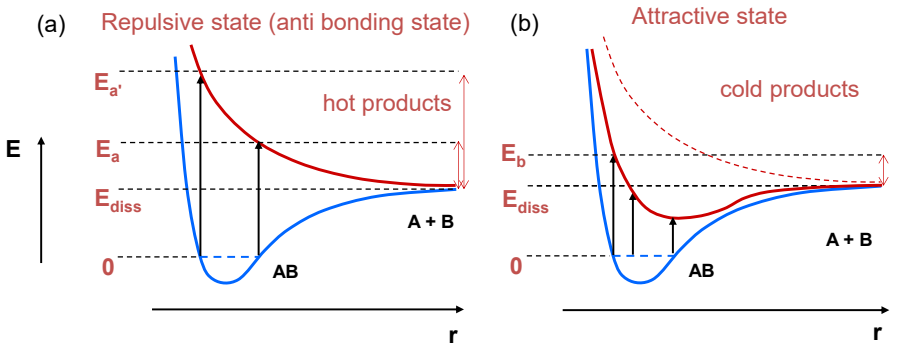

Figure 4.16: (a) Energy diagram of dissociation where the excited state is dissociative (a) or bonding (b). Here, thermally hot (a) or cold (b) reaction products are formed.

The cross section for such a transition is calculated analogously to the calculation of the excitation of atoms with a threshold energy E_a and an energy transfer ΔE.

$$d\sigma_i(E) = \frac{1}{(4\pi\epsilon_0)^2}\frac{\pi e^4}{E(\Delta E)^2}d(\Delta E) \tag{4.144}$$

with

$$\sigma_i(E) = \int_{E_a}^{\infty} d\sigma_i(E) \tag{4.145}$$

Such a dissociation does not have to occur only via a non-bonding state but can also occur via a bonded excited state, as illustrated in

Fig. 4.16b. Here, however, cases can also exist in which cold reaction products are formed.

In the excited state, the bonding and non-bonding states can overlap, as illustrated in Fig. 4.17a. Whenever the curves of the potential energy cross, it is possible for a configuration to transform into another energetically more favorable one. In this case, the excitation either directly produces two atoms A* and B from the molecule AB or initially a bonded excited state AB*. Through the crossing of the potential energy, this can decay into A* + B, or the excited molecule gives off its energy via a photon, thereby not reaching the ground state but the non-bonding state of A + B.

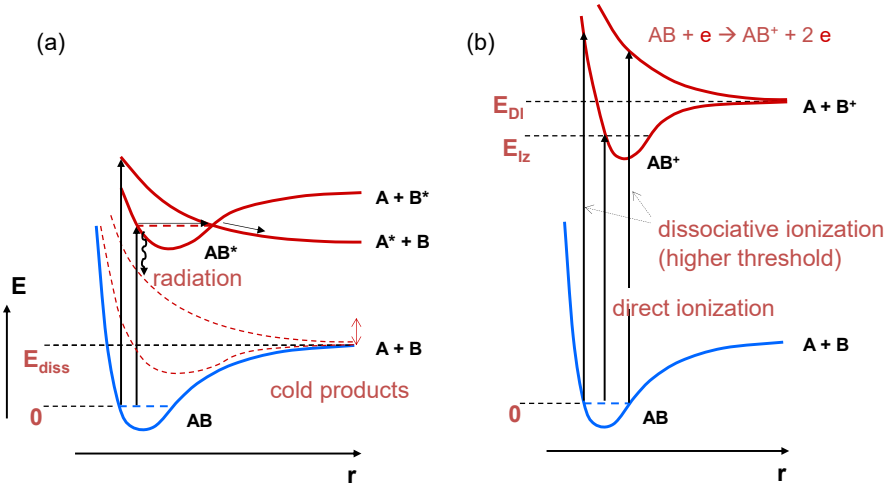

Figure 4.17: (a) Energy diagram of dissociation AB → AB* → A* + B. (b) Energy diagram of ionization and dissociative ionization.

A similar type of dissociation does not have to occur only via excited molecules but can also lead directly to ionization via the formation of a molecular ion AB^+ or directly to A + B^+, as illustrated in Fig. 4.17b.

The type of dissociative ionization can be very well measured with threshold mass spectrometry (appearance mass spectrometry). Here, the electron energy is varied, and at the threshold for the dissociative ionization of the corresponding fragment, the mass spectrometer measures a signal. This is shown in the example of C_2H_2 in Fig. 4.18. It can be seen that the lowest threshold is the simple ionization of C_2H_2. Here, only one electron has to be removed from the molecule. The more hydrogen atoms are detached in this collision process, the higher the

threshold energy, which increases in the order C_2H_2, C_2H, C_2. Finally, there is still the possibility of breaking the CC bond in the molecule, and a sequence of CH, CH_2, and C is obtained.

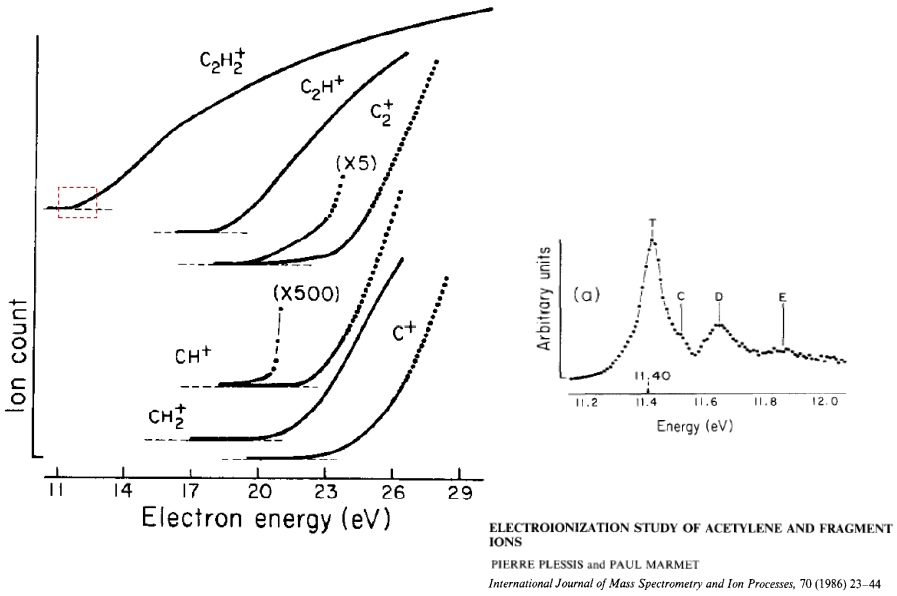

Figure 4.18: Energy dependence of the dissociative ionization of C_2H_2. From Plessis, Marmet Int. J. Mass Spec. and ion Proc. 70, 23 (1986).

- *Dissociation by electron attachment (dissociative electron attachment):*

  Another possibility for dissociation is the attachment of electrons. Here, a *negative ion* is initially formed, as illustrated in Fig. 4.19a. For this process, slow electrons are often important, i.e., this process occurs, for example, in the afterglow of plasmas where the electron temperature is small but the density of the electrons is still high. Initially, the electron is captured into an unoccupied excited state, which is referred to as a **negative ion resonance**. During de-excitation, this electron can be split off again (auto-detachment, blue curve in Fig. 4.19a). Or during the process, the molecule breaks apart, and a neutral and a negatively charged ion fragment are formed (red curve in Fig. 4.19a). In the exit channel of these two possibilities, either a free electron or a negatively charged ion is formed. The energy difference between these two possibilities is exactly the electron affinity (cf. Fig. 4.19a and b).

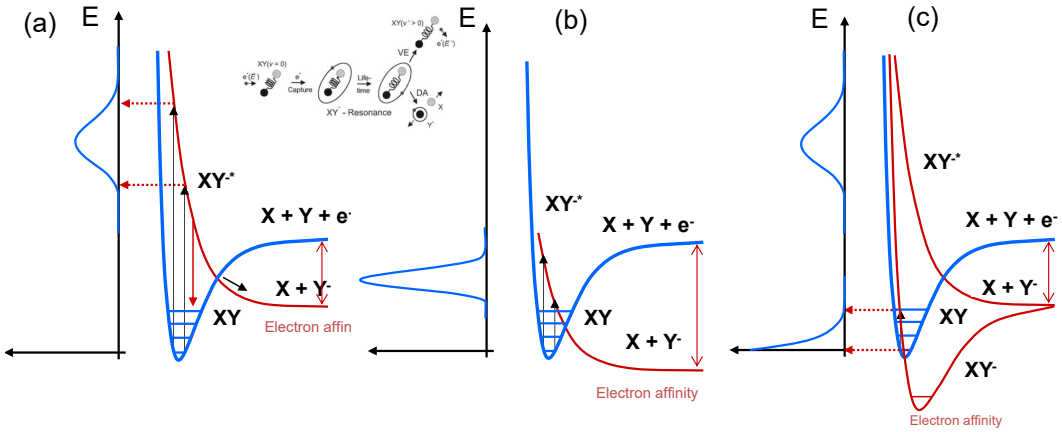

Figure 4.19: Negative ion resonance for a small (a) and large (b) electron affinity, or for the formation of an energetically more favorable ground state of the ion ÂⒸ. The energetic position of the transitions from the ground state to the excited state partly determines the cross section of this reaction, or the energy range of the electrons that can form such a resonance. In the case of a small electron affinity, the electron energy for formation is relatively high.

Finally, there is also the possibility (see Fig. 4.19c) that the state of the negative ion is energetically more favorable than that of the molecule. In this case, it is observed that even very low-energy electrons can lead to the formation of this negative ion. In addition, there is always the second contribution of the formation of an excited negative molecular ion, which then subsequently decays into a negative fragmentation or a free electron (auto-detachment). Some examples of attachment cross sections are shown in Fig. 4.20 and 4.21.

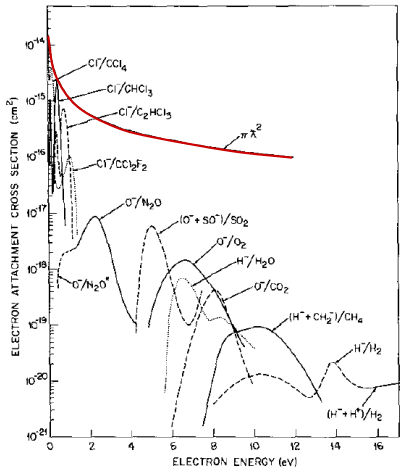

FIGURE 10. Dissociative attachment cross sections as a function of electron energy for a number of molecules. Some of

Figure 4.20: Cross sections for dissociative attachment.

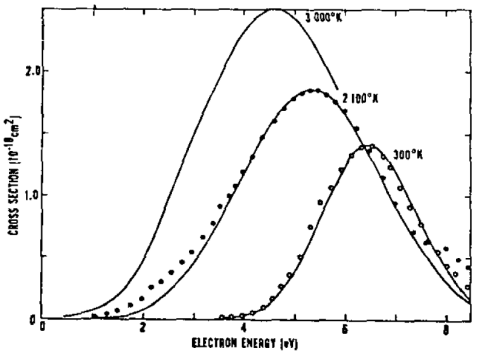

FIGURE 11. Total cross section for dissociative attachment of electrons to O_2 as a function of electron energy at the indicated temperatures: (···) experimental results (*57,58*); (——) theoretical results (*70*).

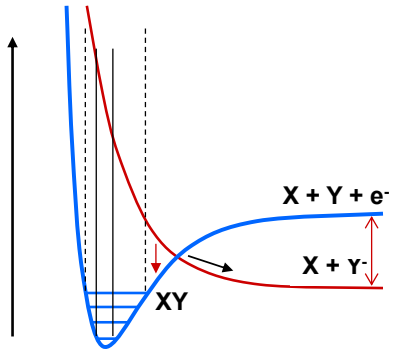

Figure 4.21: Cross sections for dissociative attachment of electrons to O_2.

- *Dissociation by recombination:*

  In the case of dissociative recombination, the following reaction is considered, as illustrated in Fig. 4.22:

$$AB^+ + e- \rightarrow A + B \tag{4.146}$$

  Here, an electron is initially captured by a molecular ion. Since this is a 2-to-1 reaction, one inevitably ends up in an excited molecular ion state, which subsequently decays. The rate for such a process depends on the Coulomb cross section; i.e., at high electron energies, the interaction is correspondingly smaller, and the rate of dissociation by recombination is low.

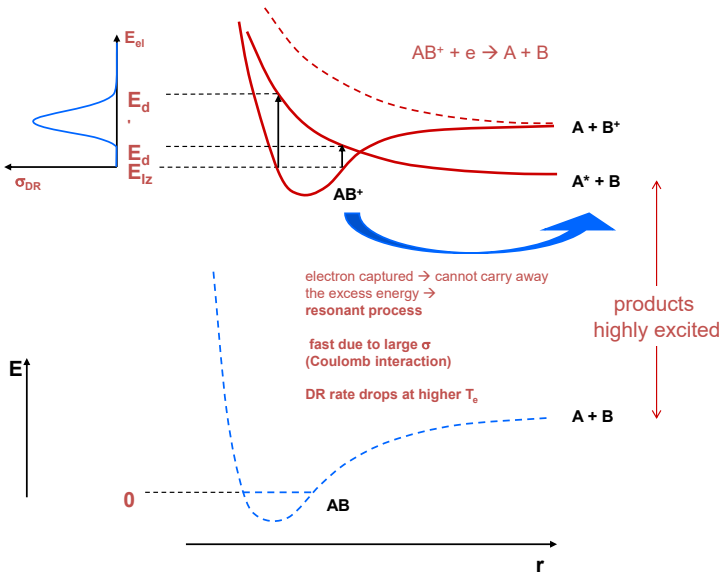

Figure 4.22: Dissociation by recombination.

In the decay channels, there are then numerous possibilities. These are typically measured in ion storage rings in which an electron cloud and an ion cloud can overlap for a longer time. The branching ratio for the recombination of an acetylene molecule is, for example:

$$
\begin{aligned}
C_2H_2^+ + e^- &\rightarrow C_2H + H + 5.8eV \quad (50\%) && (4.147)\\
&\rightarrow CH + CH + 1.2eV \quad (13\%) && (4.148)\\
&\rightarrow C_2 + H + H + 0.2eV \quad (30\%) && (4.149)\\
&\rightarrow CH_2 + C + 2.4eV \quad (5\%) && (4.150)\\
&\rightarrow C_2 + H_2 + 5.1eV \quad (2\%) && (4.151)
\end{aligned}
$$

It can be seen that the CH bond in the acetylene molecule is the easiest to break. In the case of plasmas, however, excited states of the reactants also exist, which is why the formation of $C_2H + H$ and $C_2 + H_2$ occurs more frequently here.

Finally, let's consider the comparison to the recombination of noble gas ions. In particular, at high pressures, excimer ions are formed there, which can then subsequently decay again by recombination with the electrons. The cross sections for excimer formation are:

$$
\begin{aligned}
He^+ + He + He &\rightarrow He_2^+ + He \quad (9 \cdot 10^{-32} cm^6/s) && (4.152)\\
Ar^+ + Ar + Ar &\rightarrow Ar_2^+ + He \quad (3 \cdot 10^{-31} cm^6/s) && (4.153)\\
Xe^+ + Xe + Xe &\rightarrow Xe_2^+ + Xe \quad (4 \cdot 10^{-31} cm^6/s) && (4.154)
\end{aligned}
$$

It can be seen that the cross sections for excimer formation increase with the size of the atoms.

4.2.4.3 Collision Processes Between Molecules

So far, we have investigated electron impact reactions. In the interaction of heavy molecules with each other, there are (i) the charge transfer between ions, (ii) the positive-negative ion recombination, (iii) the associative attachment in an ion impact, and finally the excitation transfer in collisions of neutral molecules with each other. The energy transfer in the case of equally heavy particles is much more efficient than in a collision between a molecule and an electron. The rates can, however, again be similar, since the lighter electrons move much faster. Whether such a transfer can take place can be estimated using the adiabatic *Massey criterion* (corresponding to a Heisenberg uncertainty relation):

$$\tau_{collision} = \frac{R_x}{v_i} \leq \frac{\hbar}{e\Delta E} \qquad (4.155)$$

with R_x the molecular diameter, v_i the relative velocity, and ΔE the energy transfer. In the following, we want to consider some methods of this energy transfer in more detail.

- *Charge transfer*

  To calculate the charge transfer, let's consider the interaction between an ion A^+ and a neutral atom or molecule B, as illustrated in Fig. 4.23. The Coulomb potential between an ion A^+ and an atom B at a distance r_{AB} from each other scales as:

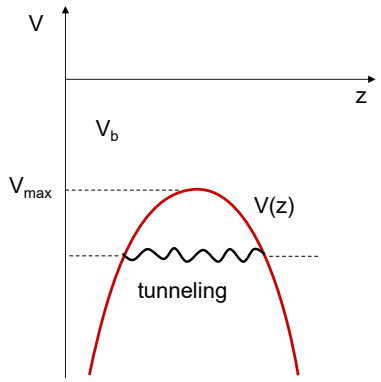

Figure 4.23: Charge transfer between two particles A and B.

$$V(z) = -\frac{e^2}{4\pi\epsilon_0 z} - \frac{e^2}{4\pi\epsilon_0 |r_{AB} - z|} \tag{4.156}$$

The potential barrier accordingly has a height of V_{max} as shown in Fig. 4.23.

$$V_{max} = -\frac{e^2}{\pi\epsilon_0 r_{AB}} \tag{4.157}$$

As the two particles A^+ and B approach each other, the binding energy of the electron in particle B can be described as follows. The binding energy of an electron at the location of atom B is then composed of the ionization energy of B (n are the quantum numbers of the excited states in B) and the attractive interaction with respect to the Coulomb attraction of A^+ (here, the quantum mechanical description in the near field is combined with the classical description in the far field).

$$E_B = -\frac{I_B}{n^2} - \frac{e^2}{4\pi\epsilon_0 r_{AB}} \leq V_{max} \tag{4.158}$$

A transfer can then take place if the binding energy becomes smaller compared to the potential barrier V_{max}. This occurs when the two particles approach each other to a distance $rmax_{AB} = \frac{3e2n^2}{4\pi\epsilon_0 I_B}$. From this, a cross section can be derived as:

$$\sigma_{CX}^{class} = \pi r_{AB} 2 = \frac{9e^4 n^4}{16\pi\epsilon_0^2 I_B^2} \tag{4.159}$$

or

$$\sigma_{CX} \simeq 36\pi \left(\frac{e^2}{8\pi\epsilon_0 I_B}\right)^2 \tag{4.160}$$

If, in addition to this classical picture, the tunneling effect is also taken into account, then we get:

$$\sigma_{CX}^{tunnel} \simeq \frac{1}{I_B}\left(\frac{\pi\hbar^2}{8me}\right)\left(\ln\frac{I_B d}{\hbar} - \ln v\right)^2 \tag{4.161}$$

At low energies, it often holds that $\sigma_{cs} = \frac{1}{2}\sigma_l$. The charge transfer is then particularly efficient when it occurs between similar ions/atoms, as here the energy levels in the atom and ion are almost identical, and the overlap of the wavefunctions during tunneling becomes very large. This is referred to as a **resonant charge transfer**. An example of such reaction cross sections is shown in Fig. 4.24. It can be seen that the cross section decreases with the relative velocity, as is typical for many cross sections. On the other hand, the cross section for elastic scattering (s) is smaller than that for charge transfer (T).

Fig. 4.25 now considers a **non-resonant** charge transfer between nitrogen and oxygen atoms according to:

$$N^+ + O \rightarrow N + O^+ \tag{4.162}$$
$$O^+ + N \rightarrow N^+ + O \tag{4.163}$$

These two reactions can initially be considered from the perspective of the formation of a molecular ion NO^+. Depending on the encounter,

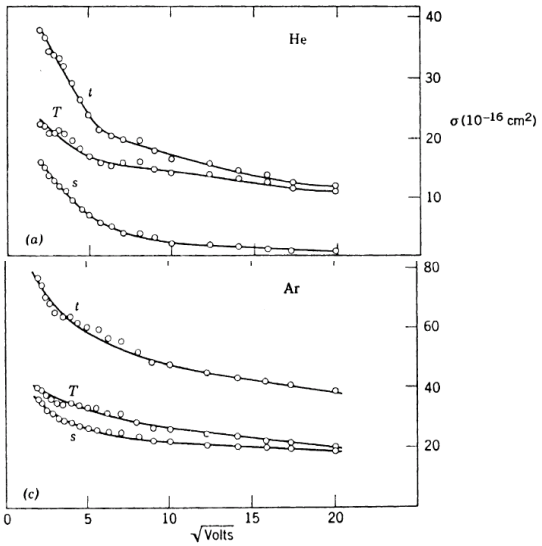

Figure 4.24: Cross section for charge transfer between two atoms as a function of the relative velocity expressed as the square root of the acceleration voltage. Here, the cross section for elastic scattering (s) is compared with that for charge transfer (T). (t) describes the sum of both cross sections.

there are different curves for the bonding and non-bonding states, depending on which ion, O^+ or N^+, is involved. When the two particles approach each other, however, the potential curves cross (marked as R_x in Fig. 4.25). At this point, a charge transfer can then take place, and for example $N^+ + O$ can be converted into $N + O^+$. It can be seen that the charge changes for energetic reasons and the energetically most favorable ion is formed. Here, the difference is 0.92 eV. A typical example that often occurs in plasmas is the formation of water cluster ions, which often have the most favorable formation energy for an ion. That is, in many collisions between charged noble gas ions and water cluster ions, the charge will ultimately be on the water cluster ions.

- *Positive-Negative Ion Charge Exchange*

  The charge exchange of positive and negative ions (charge recombination) can also be plotted in an energy diagram similar to charge transfer. For two heavy particles A and B, we can plot the potential curve that leads to the formation of the molecular ion AB^+, as well as the potential curves for A^- and B^+ and for $A + B^+$. The size of the electron affinity distinguishes the energy scale with respect to A

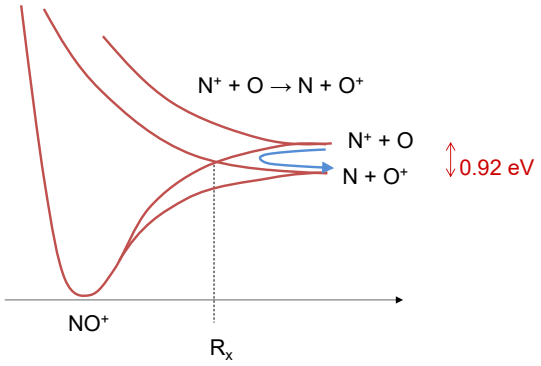

Figure 4.25: Non-resonant charge transfer between dissimilar atoms.

Recombination	Rate coefficient (cm^3/s)
$H^- + H^+ \rightarrow H + H$	$3.9 \cdot 10^{-7}$
$O^- + O^+ \rightarrow O + O$	$2.7 \cdot 10^{-7}$
$O^- + N^+ \rightarrow O + N$	$2.6 \cdot 10^{-7}$
$F^- + F^+ \rightarrow F + F$	$3 \cdot 10^{-8}$

Table 4.2: Rate coefficients for some recombination reactions

$+ B^+$, A^- and B^+. In this recombination, we again get a 2-to-1 reaction, i.e., after the recombination, an excited atom remains. In this sense, the potential curve for $A + B^+$ is also shown in Fig. 4.26. If the two components A^- and B^+ now approach each other, the intersection point with the potential curve $A + B^*$ occurs at a certain distance. The charge transfer takes place, and the two particles exchange the electron and fly apart again. Some typical rate coefficients are listed in Tab. 4.2.

The cross sections are typically of the order of $\sigma = 3000 - 10000 \cdot \pi a_0^2$. This scales with the kinetic energy and the electron affinity as $\sigma \propto E_{kin} - 0.5\epsilon_{affinity} - 0.5$.

- *Associative Detachment*

  In the so-called associative detachment, an atom and an ion recombine, but the electron is released. Here, too, the relationships can be derived by comparing the potential curves. First, we consider the formation of a molecular ion AB^-, which lies above the ground state of the molecule AB. This results in an intersection of the two potential curves (Fig.

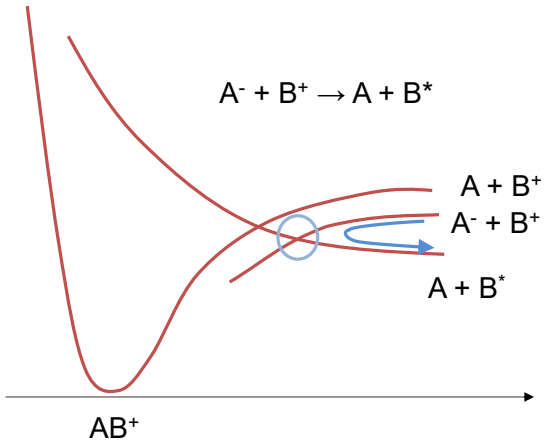

Figure 4.26: Recombination of positive and negative ions.

Recombination	Activation energy (eV)	Rate coefficient (cm^3/s)
$O^- + O_2 \rightarrow O_3 + e$	0.4	10^{-12}
$O_2^- + O \rightarrow O_3 + e$	-0.6	$3 \cdot 10^{-10}$

Table 4.3: Rate coefficients and activation energies for some recombination reactions

4.27) where the electron is removed, and a molecule AB can form. If the formation of a molecular ion is more favorable than that of the molecule, an activation barrier must be overcome during the collision for the formation of AB. An example is the collision of O^- with O_2 or of O_2^- and O to form ozone and an electron, as shown in Tab. 4.3.

It can be seen that the reaction of a negative oxygen molecular ion occurs exothermically, and thus the formation of ozone occurs with a high rate coefficient compared to the reaction of O^- with O_2.

- *Penning Collisions*

  Finally, let's consider the transfer of excitation energy. Here, the excitation can be transferred in the exit channel, but ionization can also occur. The following cases can be distinguished:

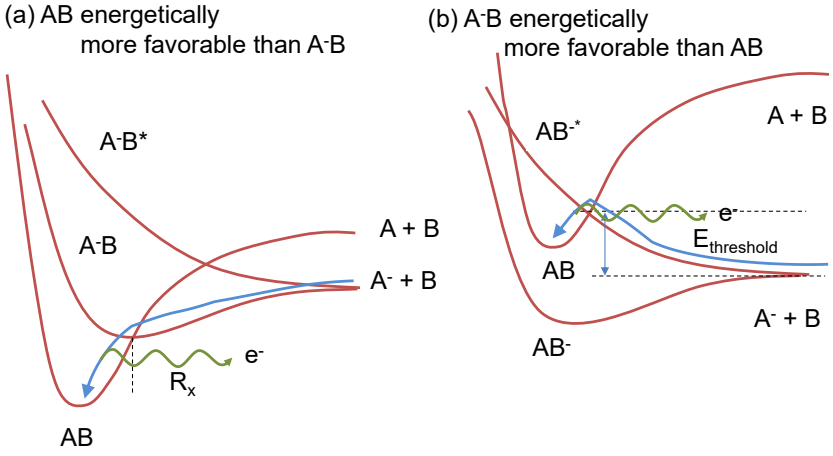

Figure 4.27: Associative detachment.

$$A + B^* \rightarrow A^+ + B + e \tag{4.164}$$
$$A + B^* \rightarrow AB^+ + e \tag{4.165}$$
$$A + B^* \rightarrow A^* + B \tag{4.166}$$

A typical case is the so-called Penning ionization (Fig. **??**a). Here, the excitation energy of metastable species is released, such as helium atoms in the singlet or triplet state where the second electron is in the $n = 2$ state. The excitation energies are here at 19.82 and 20.6 eV, which is much larger than the ionization energy of many other particles. The radius of these excited atoms is very large, which is why such Penning collisions usually have a large cross section. For example:

$$He^* + Ar \rightarrow Ar^+ + e + He \qquad \sigma = 10^{-15} cm^{-2} \tag{4.167}$$

These processes can also be illustrated in the potential diagrams, where different final products result depending on the energetic position of the intersection points (see Fig. 4.28).

- *Associative Ionization*

  In the case of associative ionization, the potential energy of the molecular ion is more favorable than that of the molecule. Accordingly, this ion is formed as the product, as illustrated in Fig. 4.28b.

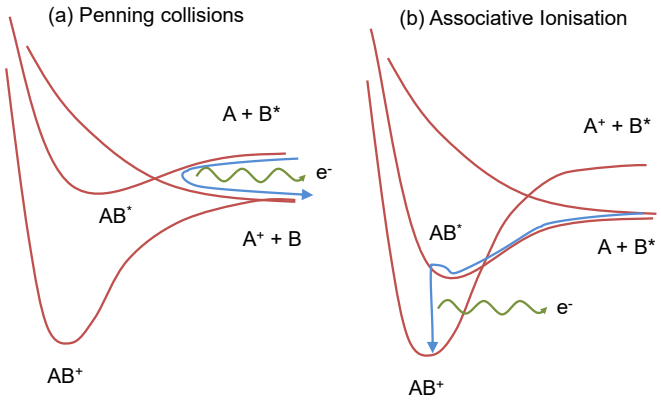

Figure 4.28: Excitation transfer through Penning collisions (a) or through associative ionization (b).

Chapter 5

Low-Pressure Plasmas

5.1 DC Plasmas

The technically simplest way to generate a discharge is to apply a direct voltage. These plasmas are referred to as DC discharges or glow discharges. However, this requires that a direct current can flow through the discharge, particularly through the adjacent sheaths of the plasma and through the surfaces of the reactor, which could be coated, for example. Maintaining this current is crucial for the characteristics of a DC discharge.

5.1.1 Zones of a DC Discharge

Based on their external appearance, a glow discharge can initially be divided into several zones, as illustrated in Fig. 5.1:

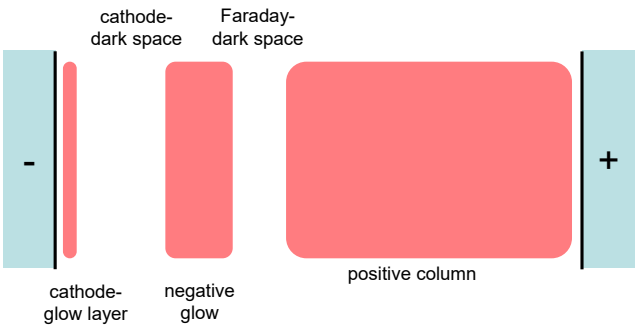

Figure 5.1: Zones of a DC glow discharge.

- **Cathode Glow**

  The cathode sheath or cathode glow is produced by secondary electrons that are ejected from the cathode by the ions. These electrons are accelerated in the electric field. Initially, they have low energies and can effectively excite gas atoms upon collision. With further acceleration, the cross section for excitation decreases, and a dark space follows.

- **Cathode Dark Space**

  In the cathode dark space, the electrons are strongly accelerated, and their density is still low. This dark space corresponds to the space charge zone of the sheath.

- **Negative Glow**

  The electrons accelerated in the sheath can be multiplied by gas collisions. Their current and density increase exponentially. Eventually, the electron current becomes so large that it is effectively sufficient to excite the neutral particles, and the negative glow is formed. This avalanche results in a high density of electrons at the end of the cathode dark space, creating a negative space charge zone. The corresponding electric field limits this negative glow towards the Faraday dark space.

- **Faraday Dark Space**

  The Faraday dark space separates the negative glow from the positive column.

- **Positive Column**

  The positive column connects the individual cathode layers to the counter electrode. The positive column can be of any length. Its existence is not essential for the operation of the discharge.

- **Anode Dark Space**

  In the anode dark space, the same conditions apply as in the cathode dark space. It is less extended because only a small voltage drop occurs here.

The individual layers of a DC discharge are also visible in the variation of the charge carrier density and the potential, as shown in Fig. 5.2. In particular, the negative net charge carrier density at the location of the negative glow generates an internal electric field that accelerates the electrons from the positive column towards this negative glow.

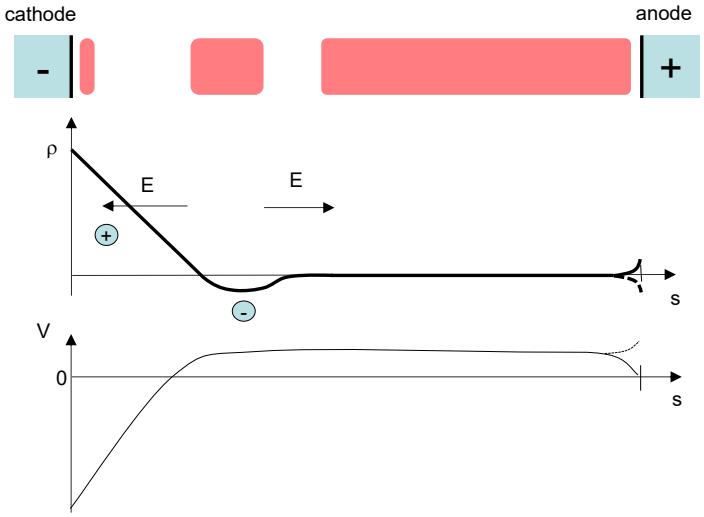

Figure 5.2: Variation of charge carrier density and electric potential along a DC discharge.

5.1.2 Characteristic Curve of a DC Discharge

For operating a direct voltage discharge, it is very important to operate it with a series resistor R (see Fig. 5.3). Since the conductivity of a plasma increases with ionization as the voltage increases, we obtain a negative resistance characteristic; i.e., without a series resistor, a too large current would be drawn after the plasma is ignited, which would destroy the power supply or cause the voltage to collapse. For this reason, a series resistor is used to limit the current through the plasma. The following applies:

$$V_{\mathrm{DC}} = V_{\mathrm{Plasma}} + RI \tag{5.1}$$

By varying the series resistor, the current can be adjusted to traverse the current-voltage characteristic of this DC glow discharge. A voltage V_{Plasma} is then established, as shown in Fig. 5.3. Several regimes of the discharge can be distinguished:

- **Townsend Discharge:**

  At low currents, the discharge burns unstably. To allow a higher current to flow, the voltage must be increased until all charge carriers are pumped away. Beyond this point, the current cannot be increased. Only when the voltage or field strength is sufficient to multiply the

charge carriers (according to the first Townsend coefficient α), the charge carrier density and thus the current continue to increase.

- **Subnormal Glow Discharge:**

  The ignition condition according to the Paschen curve is reached, and the discharge begins to burn independently. Initially, the extent of the plasma is reduced to a certain size so that the current density leads to a minimum voltage required for operating the discharge.

- **Normal Glow Discharge:**

  A further increase in current, at constant current density, leads to an enlargement of the plasma.

- **Abnormal Glow Discharge:**

  Once the entire electrode is filled, a further increase in current can only be achieved by a higher voltage. According to the Child-Langmuir law, the current increases proportionally to $V^{3/2}$.

- **Arc Discharge:**

  If the current becomes very large, the surface heats up significantly, and new charge carriers are formed by thermionic emission. The transition to an arc plasma occurs. This arc plasma is characterized by a high current at low voltage.

The transition from the unstable to the self-sustaining discharge, or from the dark discharge or Townsend discharge without quasi-neutrality to the glow discharge with layering and a positive column in which quasi-neutrality prevails, occurs at a certain space charge density. From this charge carrier density, the external field is shielded to such an extent that a sheath and a quasi-neutral positive column form in the volume. The current through the discharge remains constant and is:

$$j = j_+ + j_\mathrm{e} \tag{5.2}$$

According to Fig. 5.4, the following applies to the electron and ion currents:

$$\frac{\mathrm{d}j_\mathrm{e}}{\mathrm{d}x} = \alpha j_\mathrm{e} \tag{5.3}$$

$$\frac{\mathrm{d}j_+}{\mathrm{d}x} = -\alpha j_+ \tag{5.4}$$

$$j_\mathrm{e}(x=0) = \gamma j_+(x=0) \tag{5.5}$$

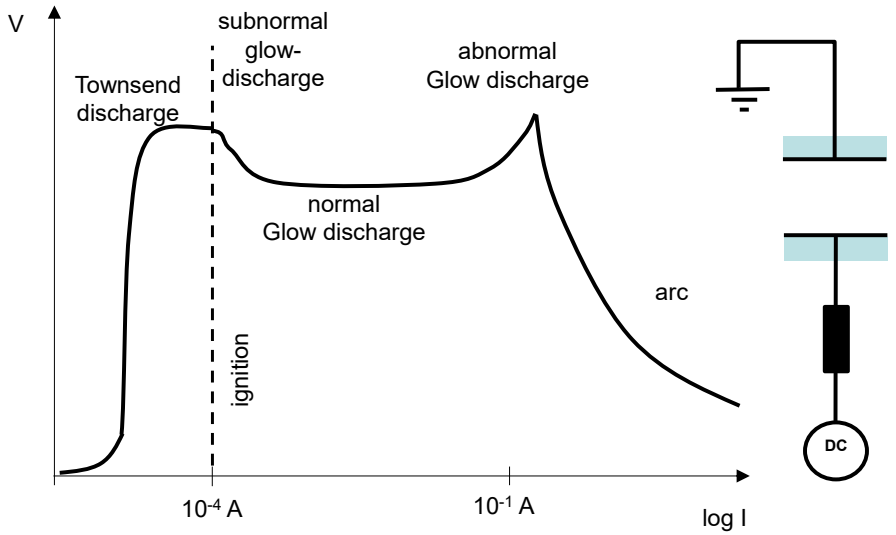

Figure 5.3: Current-voltage characteristic of a DC discharge. The current is determined by the choice of the series resistor R. The voltage of the plasma V_{plasma} is established accordingly.

with the additional boundary conditions $j_+(x = d_0) = 0$ and $j_e(x = d_0) = j$. The electric field in the gas gap is initially given as:

$$\frac{\mathrm{d}E}{\mathrm{d}x} = \frac{1}{\epsilon_0} e\,(n_+ - n_-) \tag{5.6}$$

In the plasma volume of a Townsend discharge, we can initially neglect the negative charge carrier density. The charge carrier density of the ions is thus $n_+ = \frac{j}{e\mu_+ E}$. As a solution, we obtain:

$$E = E_\mathrm{c}\sqrt{1 - \frac{x}{x_\mathrm{c}}} \tag{5.7}$$

with $x_\mathrm{c} = \frac{\epsilon_0 \mu_+ E_\mathrm{c}^2}{2j}$ a virtual point behind the anode where the electric field would be zero, and E_c the field strength at the location of the cathode. A critical current density j_c is now reached when this point x_c moves exactly to the location of the anode: $x_\mathrm{c} = d_0$. Then, the following applies:

$$d_0 = \frac{\epsilon_0 \mu_+ E_\mathrm{c}^2}{2 j_\mathrm{c}} \tag{5.8}$$

That is, from this current strength, the transition from the Townsend to the glow discharge begins.

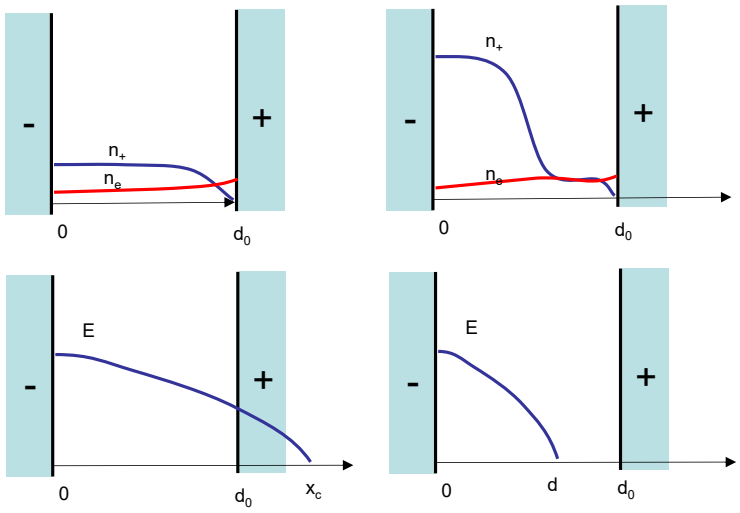

Figure 5.4: Transition from the Townsend discharge to the glow discharge. With increasing space charge density, the electric field in the gas gap decreases more and more until it can be completely dissipated in the sheath of the plasma. The plasma then divides into the cathode layer and the quasi-neutral positive column.

After the glow discharge has formed, the current transport is limited by the cathode sheath. For this purpose, we now consider the conditions in this layer, for which we assume a matrix layer in which the ions flow towards the cathode according to their mobility. The electric field in the sheath with an extension d is given as:

$$\frac{\mathrm{d}E}{\mathrm{d}x} = \frac{1}{\epsilon_0} n_+ e \tag{5.9}$$

The field at the cathode is E_c and becomes:

$$\frac{E_\mathrm{c}}{d} = \frac{1}{\epsilon_0} n_+ e \tag{5.10}$$

The current at the cathode consists of ion current and electron current. However, the electron current is formed solely by the secondary electrons. Thus, we obtain:

$$j = j_e + j_+ = j_+ + \gamma j_+ = (1+\gamma) j_+ \tag{5.11}$$

If we again express the ion current at the cathode through the mobility μ_+ and the field strength E_c at the cathode, we obtain:

$$j = (1+\gamma) e n_+ \mu_+ E_c = (1+\gamma) \epsilon_0 \mu_+ \frac{E_c^2}{d} \tag{5.12}$$

With $E_c = 2\frac{V_c}{d}$ we can insert the externally applied voltage $V_c = V_{plasma}$. The field directly in front of the cathode is exactly twice as large as V_c/d of an empty gas gap with a constant E-field, since the charge carrier density in the sheath is constant and the electric field must increase linearly. We finally obtain:

$$j = (1+\gamma) \epsilon_0 \mu_+ 4 \frac{V_c^2}{d^3} \tag{5.13}$$

The conditions for the applied voltage at the cathode layer are comparable to the ignition criterion in the Paschen curve. The loss of charge carriers due to the ion flux must be compensated by the multiplication of charge carriers by the electrons in the sheath. This so-called secondary amplification was given as:

$$\frac{1}{1 - \gamma \left(e^{\alpha d} - 1\right)}$$

This condition resulted in a certain sheath voltage V_c at which ignition occurred. This voltage was a function of the product pd. Since the equilibrium condition for the ignition of a discharge and the current retention in the sheath are identical, we also expect a dependence of the cathode layer voltage V_c on the product of pd, where the thickness d is now the thickness of the sheath. For the comparison of Eq. 5.13 with the Paschen curve, we first convert the right side of Eq. 5.13 into a function of pd. For this purpose, we first consider the pressure dependence of μ_+ according to $\mu_+ = \mu_+(p_0)\frac{p_0}{p}$ and divide Eq. 5.13 by p^2. Thus, we obtain:

$$\boxed{\frac{j}{p^2} = (1+\gamma) \epsilon_0 \mu_+(p_0) p_0 4 \frac{V_c^2}{(pd)^3}} \tag{5.14}$$

Now we only need a relationship between V_c and the extension of the cathode layer d. The secondary amplification in the sheath must at least maintain the ion current. This leads to the condition:

$$\alpha d = \ln\left(1 + \frac{1}{\gamma}\right) \tag{5.15}$$

With the relationship to the voltage V_c via the formulation of α

$$\alpha = Ape^{-B\frac{p}{E}} \tag{5.16}$$

with $E = E_c\left(1 - \frac{z}{d}\right)$ and $E_c = 2\frac{V_c}{d}$. In the sheath, the electric field is not constant but increases; i.e., we must integrate over the sheath and obtain:

$$\int_0^d \alpha(z)\mathrm{d}z = \ln\left(1 + \frac{1}{\gamma}\right) \tag{5.17}$$

or

$$\int_0^d Ape^{-Bp\frac{1}{E_c\left(1-\frac{z}{d}\right)}}\mathrm{d}z = \ln\left(1 + \frac{1}{\gamma}\right) \tag{5.18}$$

This integral cannot be easily calculated analytically and brought into the form $V_c = f(pd)$. The solution of the dependence of V_c on j/p^2 is shown in Fig. 5.5. A curve is recognized that is similar to the Paschen curve. At low current densities, the voltage increases sharply because the charge carrier density in the space charge zone becomes too low to ensure sufficient multiplication of the charge carriers. At very high current densities, the collisions increase to such an extent that this must also be compensated by a high voltage. A similar argumentation as in the Paschen curve is recognized, with the difference that the control variable here is j/p^2.
When increasing the current along our characteristic curve in Fig. 5.3, we are initially at low current densities and thus on the left side of the curve. At this point, the voltage can be reduced while simultaneously increasing the current density. In the circuit of the direct voltage discharge, this means a contraction of the plasma while the voltage drops. The operating point corresponding to the minimum of the curve is established. This is the transition that occurs in the subnormal glow discharge.
This behavior can be generalized: the so-called **Steenbeck Minimum Power Principle** states that the voltage over the plasma always adjusts to a minimum. This is equivalent to an energy minimization principle. This observation is initially only empirical but can be applied to many phenomena in plasma physics, such as contraction of arcs, instabilities, etc.
In the case of a normal DC glow discharge, two forms of appearance can be distinguished depending on the pressure of the discharge, the α and the γ-

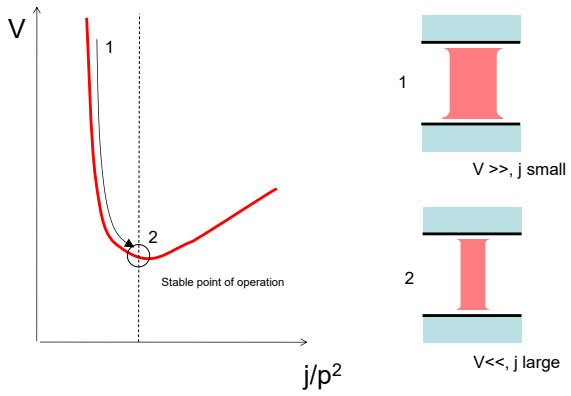

Figure 5.5: j/p^2-scaling of the voltage of a direct voltage discharge. The discharge automatically reduces the voltage $V_c = V_{plasma}$ by increasing the current density or by contracting the discharge.

mode[1]. This distinction refers to the essential ionization mechanism, which is characterized by the two Townsend coefficients.

- In the α-mode of a DC discharge, ionization is carried by the accelerated electrons in the volume. The light emission in a parallel plate arrangement occurs essentially homogeneously distributed between the plates.

- In the γ-mode, ionization is carried by secondary electrons at the electrodes. These are injected into the discharge by the high electric field in the sheath and cause strong light emission directly in front of the respective electrodes. The light emission in a parallel plate arrangement is strongly inhomogeneous.

At higher currents, when the electrode is completely filled, the current density must increase. That is, we move to the right side of the curve in Fig. 5.5, and the voltage increases. This is the region of the abnormal glow discharge. The variation from the subnormal, normal to the abnormal glow discharge is shown by experimental VI curves and emission patterns in Fig. 5.6. Initially, a Townsend discharge is recognized, the emission is distributed over the entire surface, and the discharge glows most strongly in front of the anode, as this is where the electrons reach their highest energy. The discharge itself glows

[1]This is to be distinguished from the emission profiles in a high-frequency discharge where a distinction is also made between an α and γ-mode.

very weakly and is diffuse. During the transition to the glow discharge, the voltage is reduced, and the plasma contracts to maintain the critical current density. The emission is maximum in the entire plasma volume. At very high currents, the entire discharge chamber is filled, the current increases again as the voltage increases. Now, the maximum emission is at the location of the negative glow, i.e., at the edge of the cathode fall.

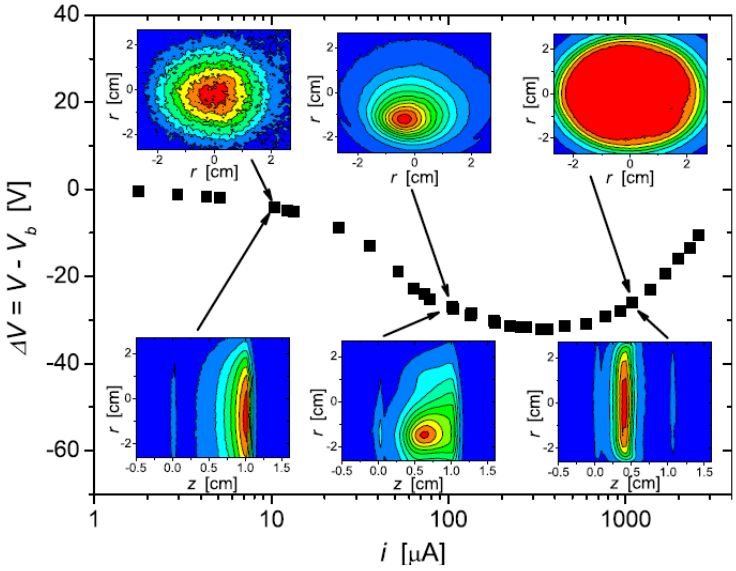

Figure 5.6: Measurement of the j/p^2-scaling for an argon direct voltage discharge at 200 Pa. The false-color representation shows the extent of the discharge in the region between subnormal discharge, normal discharge, and abnormal discharge - upper row from above, lower row from the side (cathode at $z = 0$ and the anode at $z = 1.1$). One can clearly see how the discharge expands with increasing current [31].

5.1.3 Instabilities of a Discharge

A direct voltage discharge can become unstable. One distinguishes *longitudinal* and *transverse instabilities*: longitudinal instabilities show a variation of the plasma parameters along the electric field, while transverse instabilities vary perpendicular to the electric field.

- *Thermal Instability*

One of the simplest instabilities is the thermal instability, a transverse instability, as illustrated in Fig. 5.7. A local disturbance of the electron density increases the gas temperature, which in turn causes the neutral gas density to decrease, as the pressure in the discharge remains constant. However, the reduced E-field E/n_g then increases, as does the ionization. That is, the electron density increases:

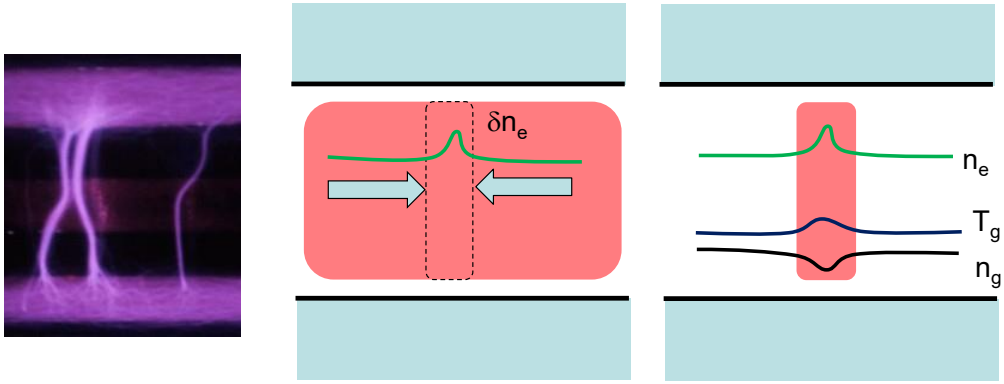

Figure 5.7: The thermal instability leads to a filamentation of the discharge. A local increase in the electron density leads to a heating of the gas and thus to a local reduction of the neutral gas density.

$$\delta n_e \uparrow \Rightarrow \delta T_g \uparrow \Rightarrow \delta n_g \downarrow \Rightarrow \delta \frac{E}{n_g} \uparrow \Rightarrow \delta n_e \uparrow$$

This instability only occurs at higher pressures, as only then is the thermal contact between electrons and neutral particles large enough so that an increase in the electron density also leads to an increase in the temperature. A filamentation is formed in which the local ionization is increased in thin filaments, and the discharge is thus short-circuited. If the current flow is not limited, the transition to an arc can occur. One way to suppress this instability is the use of helium. Helium has good thermal conductivity, so that inhomogeneities in the temperature profile cannot be stable.

- *Attachment Instability*

  In electronegative plasmas, attachment instabilities can form. Here, an increase in the electron density initially leads to a slight reduction of

the electric field, as the electrons shield the external field. That is, the following applies:

$$\frac{\delta n_\mathrm{e}}{n_\mathrm{e}} = -\frac{\delta E}{E} \tag{5.19}$$

This reduction of the electric field also reduces the electron temperature and thus the attachment frequency. However, if the attachment frequency decreases, the loss of electrons also decreases, and the electron density can continue to increase.

$$\delta n_\mathrm{e} \uparrow \Rightarrow \delta E \downarrow \Rightarrow \delta T_\mathrm{e} \downarrow \Rightarrow \nu_\mathrm{attachment} \downarrow \Rightarrow \delta n_\mathrm{e} \uparrow$$

- *Layers of a Discharge, Striations*

  The most famous instabilities of a direct voltage discharge are layers that can form (striations). Here, ionization waves or ion-acoustic waves can form along the positive column of a discharge. The fascinating phenomena are shown in Fig. 5.8. It can be seen that with variation of the gas and the pressure in the discharge, the existence of the layers and their periodicity change.

  The mechanism of striations is illustrated in Fig. 5.9. First, we consider a disturbance in the form of an oscillation of the ion density. The variation in the ion density is compensated by the electrons due to the conservation of quasi-neutrality. However, the oscillation in the electron density is smaller because the electrons are very mobile and any increase in density is compensated by ambipolar diffusion. As a result, we obtain a spatially alternating distribution of positive and negative space charge density.

  These local densities lead to alternating electric fields that superimpose the external field. This results in regions of high and low field strength. At locations of high field strength, ionization and thus the local electron density increase, further amplifying the disturbance. An instability with maxima in the electron density is created, which becomes visible as increased emission of the plasma at these locations. The layers thus formed in the discharge can be stationary or can also run along the discharge.

5.1.4 Hollow Cathode Plasma

So far, we have used the current retention in a cathode sheath for plasma generation. The electrons that were multiplied in the sheath contribute to

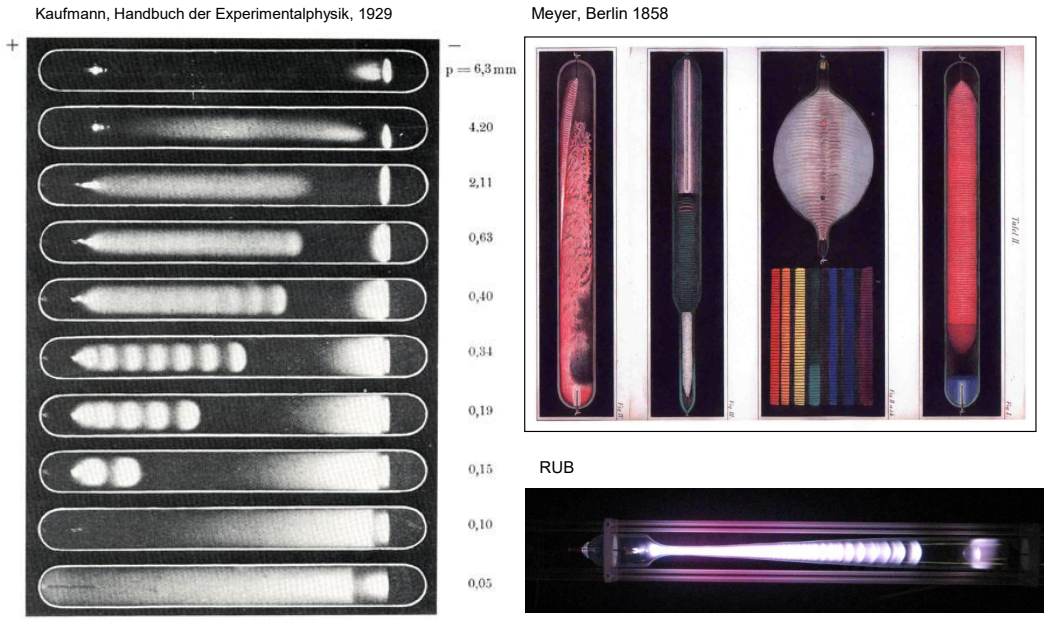

Figure 5.8: Longitudinal instabilities of a direct voltage discharge at different pressures (p refers to Torr) and plasma gases.

the electron density in the positive column and are lost from the discharge according to the current to the anode. However, there are configurations in which the electron flow does not have to be lost equally at the opposite electrode but can be captured by a second sheath with high sheath voltage. This situation is given in so-called hollow cathodes, which in some plasma discharges result in an intensive plasma emission in flanges of the system or boreholes in the workpiece.

Animation

Hollow cathode effect.
Simulation of an electron trajectory in a hollow cathode.

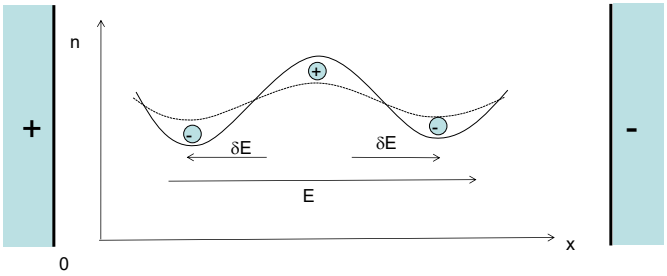

Figure 5.9: Mechanism of the formation of an ionization instability as the cause of the layers of a discharge. An oscillation of the ion density cannot be completely compensated by the oscillation of the electron density. As a result, a local increase in the electric fields and thus enhanced ionization occurs at these locations.

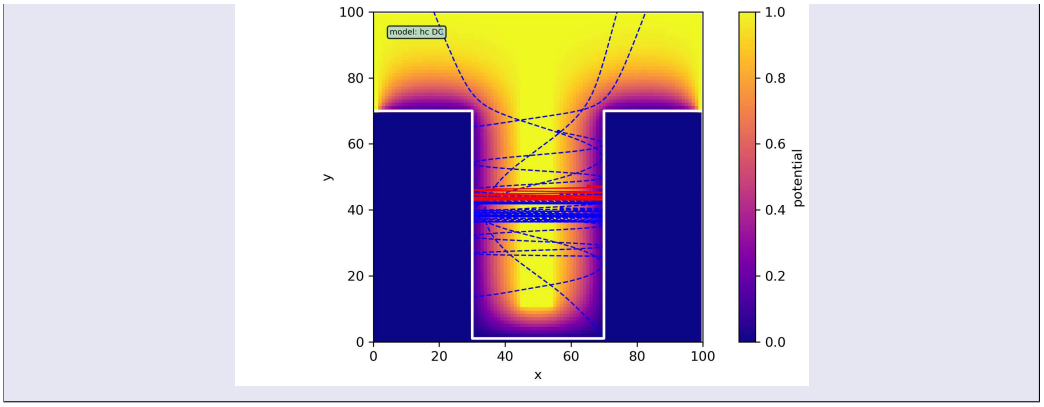

The conditions of a hollow cathode plasma are obtained if we assume that there is a depression in the cathode with a radius R, as shown in Fig. 5.10. The extension of the sheath relative to R is just large enough that opposite regions of the sheath can almost overlap. On one side of the hollow cathode, secondary electrons are initially created by the ion bombardment, which are accelerated in the sheath. They become so fast that they reach the opposite sheath and are reflected there. This group of hot electrons *pendulates* very efficiently between the two sheaths and remains well confined. This is the essential difference to a simple geometry in which the electrons are quickly lost at the anode after being accelerated in a sheath. On their pendulating path between the electrodes, these hot electrons give off energy through ionization. An intense plasma is created. The electrons that are created during ionization are generally cold and form the essential electron density in the plasma volume.
Such a hollow cathode plasma can be described by a simple global model in

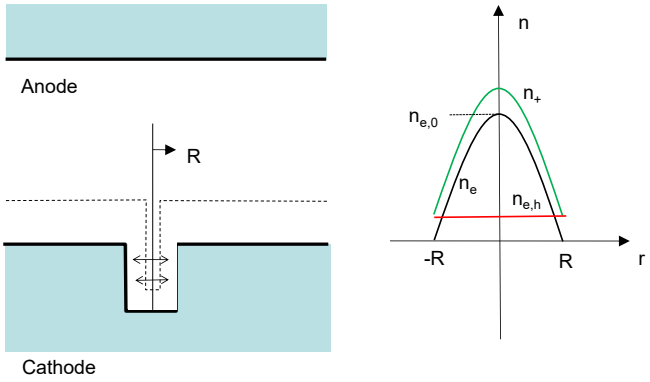

Figure 5.10: In the hollow cathode effect, the electrons pendulate between opposite sheaths. A group of hot electrons is formed.

a radial geometry in which the losses of ions through ambipolar diffusion are compensated by ionization by the hot electrons:

$$-D_\mathrm{a}\frac{1}{r}\frac{\mathrm{d}}{\mathrm{d}r}\left(r\frac{\mathrm{d}n_+}{\mathrm{d}r}\right) = k_\mathrm{ionization} n_\mathrm{g} n_\mathrm{e,h} \tag{5.20}$$

This equation is solved by a parabola. This is in contrast to a simple diffusion problem in which a dependence on the electron or ion density stands on the left and right side. Here, however, we consider the density of the hot electrons as spatially constant. This is a good approximation because these electrons, due to their high energy, have a long mean free path (which is why they can also pendulate well between the sheaths). The parabolic solution is:

$$n_+ = n_\mathrm{e,h} + n_\mathrm{e,0} - \frac{k_\mathrm{ionization} n_\mathrm{g} n_\mathrm{e,h}}{4D_\mathrm{a}} r^2 \tag{5.21}$$

The ion flows and electron flows to the electrodes then result again from the normal balances at the location R of the surface:

$$\Gamma_+(r) = 2D_\mathrm{a}\frac{n_\mathrm{e,0}}{R} \tag{5.22}$$

$$\Gamma_\mathrm{e,h}(r) = \gamma\Gamma_+(r) \tag{5.23}$$

5.1.5 Magnetron Plasmas

In a hollow cathode discharge, a high efficiency is achieved because the electrons pendulate between two cathode layers. The same effect can also be

achieved on a surface by using a magnetic field to guide the secondary electrons back to the surface. This is referred to as a magnetron plasma.

5.1.5.1 Electron Confinement

In a so-called magnetron discharge , magnets are placed behind a DC electrode. In this magnetic field, the electrons are magnetized and can follow the field lines. The magnetization of the charge carriers depends on the mean free path and the geometry and strength of the magnetic field. The gyration radii for electrons $r_{\mathrm{L,e}}$ and ions $r_{\mathrm{L,i}}$ are, for typical values for technical magnetron plasmas operated with a DC voltage V_{DC}:

$$r_{\mathrm{L,e}} = \frac{1}{B_0}\left(\frac{2mV_{\mathrm{DC}}}{e}\right)^{1/2} \approx 0.5\ cm \tag{5.24}$$

$$r_{\mathrm{L,i}} = \frac{1}{B_0}\left(\frac{2MV_{\mathrm{DC}}}{e}\right)^{1/2} \approx 1.3\ m \tag{5.25}$$

with m and M the electron and ion mass. It can be seen that the electrons can be well magnetized at low pressures, while the ions cannot follow the field lines before they are deflected again by collisions.

Animation

Confinement of an electron in a magnetron.
Simulation of an electron trajectory above a magnetron target.

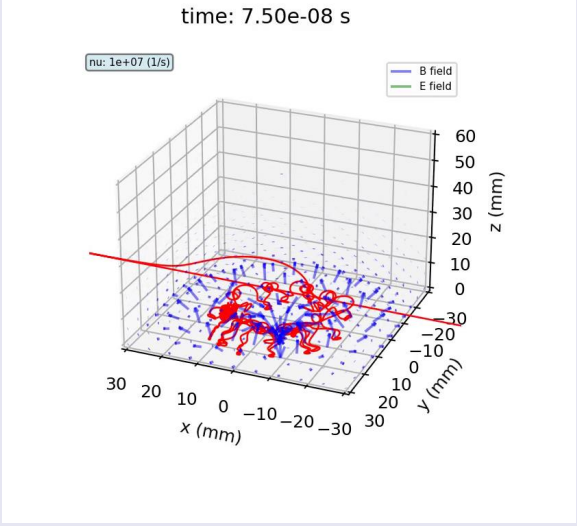

With appropriate geometry and magnetic field, the secondary electrons are initially accelerated in the sheath and can pendulate on an electrode back and forth along their gyration path, according to Fig. **??**. This pendulating of the electrons in the magnetic field is analogous to the movement in a magnetic bottle where the magnetic moment is a conserved quantity. In addition to the pendulating motion, the electrons also experience an $E \times B$-drift, where the static B-field and the E-field in the sheath are perpendicular to each other. That is, the footpoints of the electrons migrate on the surface in a defined direction.

Magnetrons come in different designs with the goal of producing metallic or ceramic materials. The surface of the electrode to which the voltage is applied is referred to as the target. The ions from the plasma are supposed to sputter this target, and the ablated atoms are deposited on an opposite substrate. A typical example is the coating of metallic films in an argon discharge. To increase the efficiency of the discharge, a magnetic field support is used. Here, the electrons are magnetized, and the good plasma confinement leads to an intense plasma and thus to an efficient sputtering rate.

The process of sputtering in magnetron discharges can be extended by adding reactive gases to the argon plasma. This is referred to as reactive magnetron sputtering. Typical examples are oxides that are formed by sputtering a metallic target in an argon-oxygen atmosphere. In reactive magnetron sputtering, however, a pronounced hysteresis is observed because not only the substrate but also the target is coated with an oxide layer. This behavior can be derived based on balance equations. In the balance equation of the target, sputtering dominates because the ion energy of the impinging ions is

very high:

$$n_0 \frac{d\Theta_t}{dt} = \underbrace{\Gamma_r s_r (1-\Theta_t)}_{Coating\ \ Target\ \ (1)^*} - \underbrace{\Gamma_{ions} Y_{film} \Theta_t}_{sputtering\ \ Target} = 0 \tag{5.26}$$

Here, Γ_r is the flux of reactive particles (e.g., O atoms) and Γ_{ions} is the flux of impinging ions. n_0 is the number of surface sites per area (typically 10^{15} cm^{-2}) Θ_t and Θ_s are the oxygen coverages of the target and substrate, respectively. s_r is the sticking coefficient of the reactive particles and Y_{film} is the sputtering coefficient at the target. The first term in Eq. 5.26 describes the deposition of oxide directly from the plasma.
In the balance equation of the substrate, sputtering is negligible because the ion energy of the impinging ions is very low. However, target atoms are transported to the substrate by sputtering at the target. These terms are proportional to the respective coverages on the substrate and target:

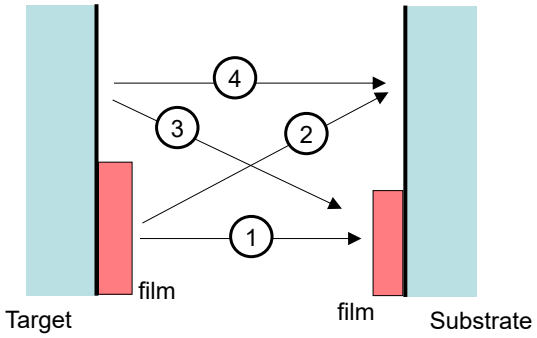

Figure 5.11: Particle fluxes between target and substrate in magnetron sputtering.

$$\begin{aligned} n_0 \frac{d\Theta_s}{dt} = & \underbrace{\Gamma_r s_r (1-\Theta_s)}_{Coating\ \ substrate\ \ (1)^{**}} + \\ & \underbrace{\Gamma_{ions} Y_{film} \Theta_t (1-\Theta_s)}_{transport\ \ film\ \ target \rightarrow substrate\ \ (2)} - \\ & \underbrace{\Gamma_{ions} Y_{metall} (1-\Theta_t)(\Theta_s)}_{transport\ \ metal\ \ target \rightarrow substrate\ \ (3)} \end{aligned} \tag{5.27}$$

Here, Y_{metall} is the sputtering yield of the metal atoms on the substrate.

From these two equations, the consumption of the source gas can be derived as:

$$\frac{dN_r}{dt} = \Gamma_r s_r \left[\underbrace{(1-\Theta_t)A_{Target}}_{Process\ (1)*} + \underbrace{(1-\Theta_s)A_{Substrat}}_{Process\ \ (1)**} \right] \tag{5.28}$$

The consumption of reactive particles is described by this equation. The sputtering yield of metal atoms at the target is:

$$\Gamma_{sputtering\ \ Metal} = \Gamma_i \left[Y_{Metall}(1-\Theta_t) + Y_{film}\Theta_t \right] \tag{5.29}$$

To achieve a certain composition of a film, the yield of sputtered metal atoms and the consumption of reactive particles must be in a fixed ratio to each other. However, one does not initially control the partial pressure in the chamber but rather the flux that is introduced into the chamber.

$$\Phi_{IN} = \Phi_{pump} + \Phi_{Target} + \Phi_{Substrat} \tag{5.30}$$

The partial pressure is then established from the losses to the surface and to the pump. If we now plot the sputtering rate $\Gamma_{sputtering}$ as a function of the consumed reactive gas $\frac{dn_r}{dt}$, we obtain Fig. 5.12 (the curve is traversed with increasing coverage Θ_t).

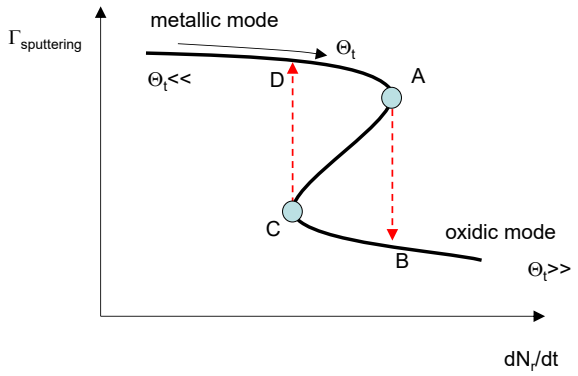

Figure 5.12: Hysteresis in magnetron sputtering: when varying the supplied amount of reactive gas Φ_{IN}, a non-linear dependence of the reactive gas consumption $\frac{dN_r}{dt}$ on the surface coverage is obtained. The discharge jumps directly from A to B when increasing Φ_{IN}, or directly from C to D when decreasing Φ_{IN}.

It can be seen that at low reactive gas consumption, the sputtering yield of metal is high, and the target is operated in the so-called metallic mode. At high reactive gas consumption, the metal sputtering rate is low, and the target is in the coated mode (often referred to as the oxide mode, as oxides are a common application of reactive magnetron sputtering).
In the intermediate range, the discharge is bistable and spontaneously jumps directly from the metallic to the oxide mode (A to B) or from the oxide to the metallic mode (C to D). Why is that?
To understand this, consider the following experiment. Using an external flow controller, we slowly increase the supply of reactive gas Φ_{IN}. This increases the coverage Θ_t and the consumption of reactive gas through the surface processes. Eventually, we reach point A. When further increasing Φ_{IN}, the reactive gas consumption $\frac{dn_r}{dt}$ now *decreases*, although the coverage Θ_t continues to increase! Since the surface losses according to $\frac{dn_r}{dt}$ become smaller, the partial pressure $p_{ReactiveGas}$ continues to increase, which leads to a higher flux Γ_r and thus to a further increase in Θ_r. That is, a runaway effect is created until point B is finally reached. From a similar argument, one can deduce that when decreasing the set flow Φ_{IN} from point C, one spontaneously reaches point D. This hysteresis arises because one controls the flow Φ_{IN} *not* but the partial pressure $p_{ReactiveGas}$, which is crucial for the coverage!
This can only be achieved if the partial pressure $p_{ReactiveGas}$ in the plasma is *actively* controlled. Often, a measurement variable for the partial pressure of reactive particles (e.g., emission line of O atoms) is used to control the gas flow regulator. This allows stable operation of the discharge in the transition region AC. Through this control, any coverage on the magnetron target can be set, and the stoichiometry of the deposited films, which is a direct reflection of the composition of the target, can be controlled simultaneously.
The morphology of many inorganic materials produced by magnetron sputtering depends on the pressure and substrate temperature. By varying the pressure, the ion energy distribution of the impinging ions changes. On the one hand, the sheath voltage decreases, and the collisions of the ions in the sheath lead to a smaller average ion energy. Depending on the input of ion bombardment and substrate temperature, a different microstructure is obtained, ranging from completely amorphous to polycrystalline, as illustrated in the so-called **Thornton diagram** in Fig. 5.13. The individual phase boundaries show that a lower substrate temperature can be compensated to some extent by an increase in ion bombardment. That is, the crystallinity of a material can be achieved even at a lower substrate temperature if the ion bombardment contributes sufficiently to the film growth. The control parameter here is the dissipated energy per incorporated atom in the layer.

If we assume that all ions with the flux Γ_{Ions} and energy E_{Ions} contribute to the layer growth, as well as the flux of neutral particles $\Gamma_{Neutrals}$, we obtain the characteristic energy per incorporated particle $E_{dissipated}$ as:

$$E_{dissipated} = \frac{\Gamma_{Ions} E_{Ions}}{\Gamma_{Ions} + \Gamma_{Neutrals}} \tag{5.31}$$

One can see that high values for $E_{dissipated}$ can be achieved when the ion flux is significant compared to the neutral flux. When considering the morphology of the resulting layers, four regions can be distinguished:

- **I**

  The film shows columnar growth with a relatively porous structure. At the low substrate temperatures, the porosities cannot be filled.

- **II**

  The film still shows columnar growth, but the porosity decreases significantly because the surface diffusion is now sufficient to fill the voids. The surface is relatively smooth due to the ion bombardment. These films are suitable for many applications.

- **III**

  The diffusion becomes so strong that crystalline columns form. The surfaces become rougher because the crystallinity of the material predominates.

- **IV**

  The diffusion becomes so strong that a polycrystalline material with a correspondingly compact structure and rough surface is formed.

5.1.5.2 Deposition of Insulating Layers Bipolar Sputtering, Dual Magnetron Sputtering, Dual Anode Sputtering

In the production of oxides and nitrides by magnetron plasmas, electrically insulating coatings are created on the surfaces of the substrate and the chamber walls. This hinders the flow of current in the DC plasma, and the efficiency decreases with increasing process duration. One speaks of the problem of the *disappearing anode*. Due to the insulating layers, a charging of the surfaces occurs, which in the worst case can lead to the formation of short-circuit arcs (arcing) between the surface and the plasma or between the top side of the insulating layer and the conductive electrode underneath.

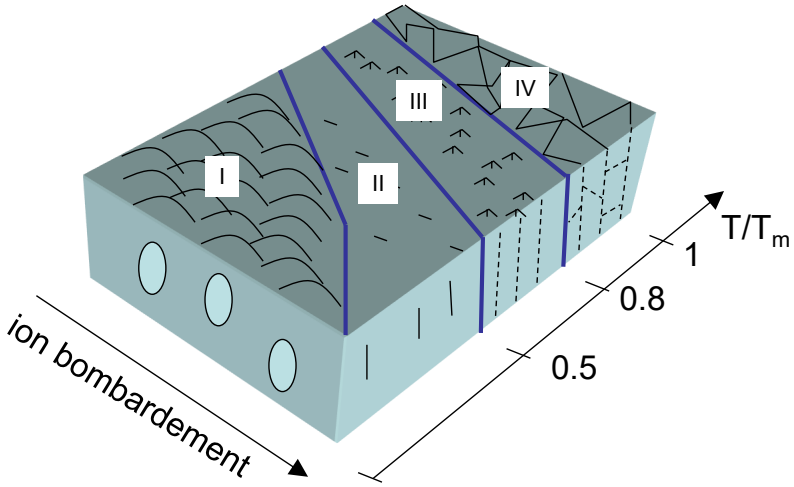

Figure 5.13: Thornton diagram.

A way out would be high-frequency plasmas or RF magnetrons with a capacitive coupling and a vanishing net current to the surface. In this configuration, however, heating is done by the displacement current, and the pendulum effect of the electrons in the magnetic bottle is no longer utilized. In this sense, an RF magnetron is conceptually nonsensical. In contrast to the magnetron effect, the better formulation would actually be an RF plasma in which the confinement is supported by an additional magnetic field[2]. However, there is another reason why high-frequency magnetrons appear unfavorable, as the technical realization of a plasma at high power density with a direct voltage power supply is much simpler and more cost-effective. For this reason, several schemes exist to counteract the charging effects despite DC plasmas.

- *Bipolar Sputtering*

  In the so-called bipolar sputtering, the polarity of the power supply is inverted for a short time (hence bipolar), as illustrated in Fig. 5.14. In this phase, electrons are collected from the plasma. This happens directly at the cathode. By adjusting the corresponding duty cycle, charge conservation for the plasma can be achieved. Due to the high

[2]A practical example would be MERIE plasmas (magnetically enhanced reactive ion etching) in which a magnetic field parallel to the surface reduces the loss of electrons

sheath voltages at the cathode, this surface is always kept clean and retains its metallic conductivity.

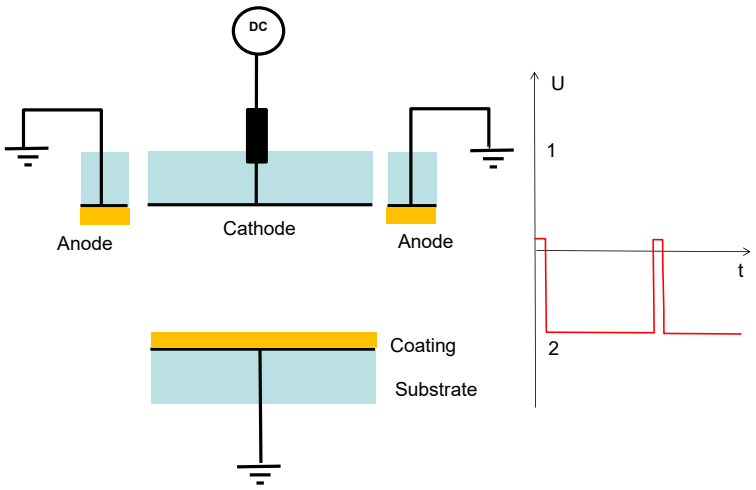

Figure 5.14: In bipolar sputtering, the polarity at the cathode is inverted for a short time to collect electrons intentionally.

- *Dual Magnetron Sputtering*

  In bipolar sputtering, the temporal structure of the pulsing must be precisely chosen so that a slow charging of the surfaces does not occur over time. This can be avoided if two magnetrons are used, which are alternately operated with a positive and negative voltage (see Fig. 5.15). Thus, the cathode and anode alternate. In the cathodic phase, any insulating coating on the anode is removed again. These discharges are spatially extended. However, large glass substrates are often coated, which are moved under the magnetrons to achieve a uniform layer thickness.

- *Dual Anode Magnetron Sputtering*

  Finally, it is also possible to apply a negative or positive voltage selectively to the anode itself. By switching between two anodes, the one with the most negative voltage is allowed to sputter effectively (see Fig. 5.16). This is achieved, for example, by superimposing an AC signal on a double anode so that both anodes become more negative than the DC potential and thus part of the cathode, which is effectively sputtered.

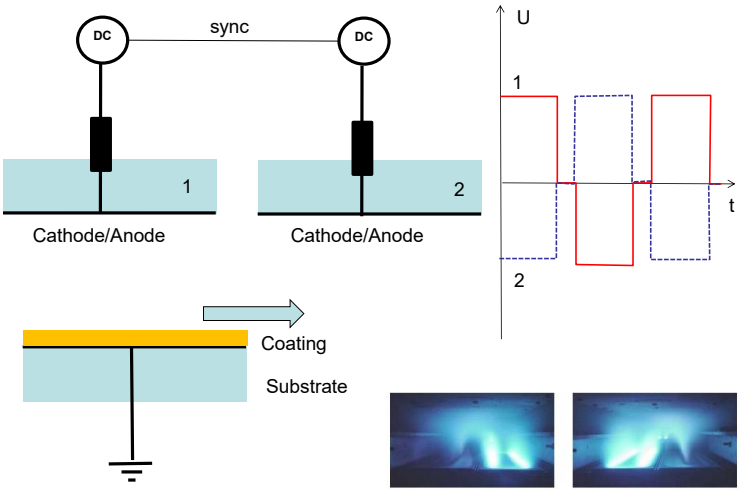

Figure 5.15: Dual-magnetron sputtering (photos Fraunhofer FEP). By alternately operating as cathode and anode, the surfaces of the targets are always kept metallically clean.

The mentioned methods can only function if the cathode surface is not also covered with an insulating layer. This is the case in the so-called **target poisoning**. That is, in a reactive plasma process (addition of O_2, N_2 to the argon plasma), the reactive gas can also react at the target itself. If this happens, the surface switches to an oxidized mode and can thus be sputtered less effectively. Thus, the sink for the reactive particles disappears, and the partial pressure continues to rise. This situation is unstable, and the process can only be operated in two strongly different modes depending on the supply of reactive particles: the metallic mode with high sputtering rate and the oxide mode with very low sputtering rate. Starting an intermediate state is not possible without active control. When varying the supply of reactive gas, both regimes are not reached uniformly, but a hysteresis is formed.

5.1.5.3 High Power Pulsed Magnetron Sputtering (HPPMS)

As mentioned at the beginning, control of the film properties is possible through control of the ion energies. Ultimate control, however, requires fully ionized plasmas, as only charged particles can be manipulated in their energy by applying electric and magnetic fields. Exactly this is achieved by means of so-called HPPMS plasmas (HPPMS - High Power Pulsed Magnetron Sputtering).
In this case, a pulse with high voltage (1...4 kV) is applied to the target for

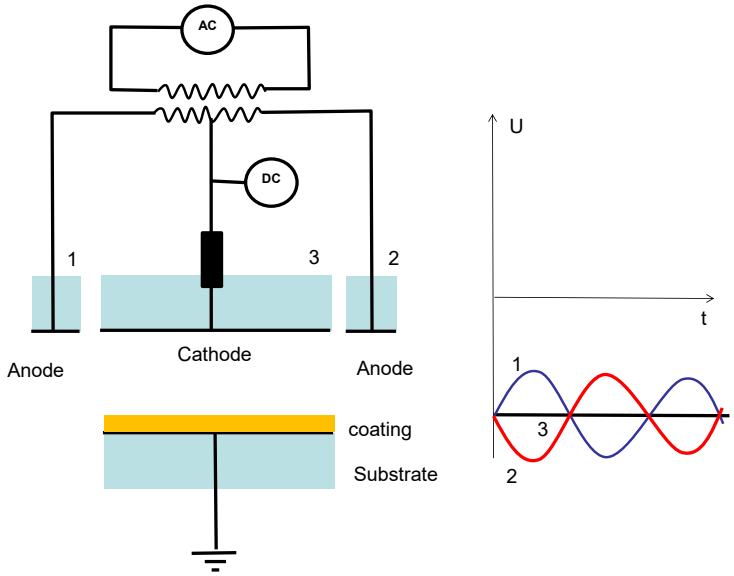

Figure 5.16: Dual anode magnetron sputtering.

a short time ($\approx$ 100 μs). The power supplies are designed to also deliver a high current in this time (up to 1000 A). That is, in this short phase of the plasma pulse, powers in the MW range are implemented. In continuous operation, the system and the substrates would be thermally destroyed. For this reason, these discharges are only operated in a pulsed manner with a duty cycle of 1% and a pulse frequency in the range of $\approx$ 100 Hz [3].
The development of the HPPMS plasma creates some peculiarities, as illustrated in Fig. 5.17. When the plasma is turned on, an almost fully ionized argon plasma is initially created, resulting in a high ion current to the target surface. This in turn results in a high ablation of metal atoms, which are effectively ionized in the high-density plasma in front of the surface. These metal atoms can in turn return to the target surface and sputter there. Here, a chain reaction is hidden because the yield for self-sputtering (i.e., metal sputters metal) can become greater than one depending on the metal and the ion energy. As a result, the density of metal atoms multiplies and displaces the argon ions (rarefaction) due to the high density that builds up. Since the ionization energy of metal atoms is generally much lower than that of noble gas atoms, a very intense pure metal plasma is thus created, which

[3] A current review on HIPIMS can be found in *J.T. Gudmundsson "High power impulse magnetron sputtering discharge", Journal of Vacuum Science & Technology A 30 (2012) 030801*

is fully ionized. This transition to self-sputtering does not occur instantaneously when the pulse is turned on but must first develop, which can be seen from a time-delayed increase in the current[4].

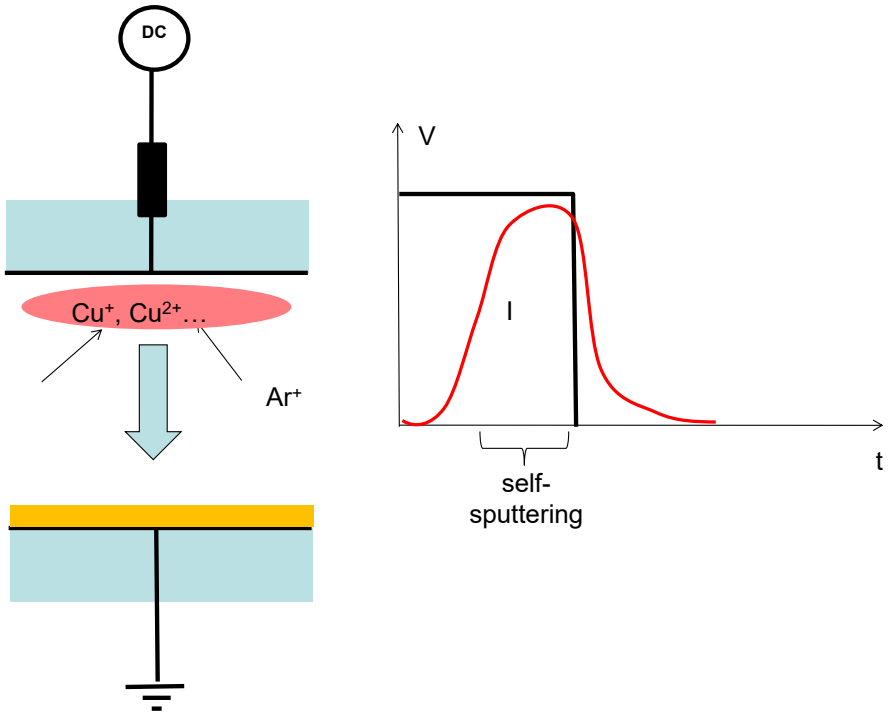

Figure 5.17: In a High Power Pulsed Magnetron Sputtering (HPPMS) process, a high power is provided by a power supply. In the plasma pulse itself, a fully ionized metal plasma is formed through self-sputtering.

In the following, we want to sketch some properties of HiPIMS plasmas:

- **Pulse Length and Duty Cycle:** The duty cycle is typically ¡1% to keep the thermal load on the target low. The pulse lengths are approximately 100 μs. After about 50 μs, the transition from an argon to a metal plasma occurs.
- **Gas Depletion:** Due to the intensive sputtering, the metal atoms displace the argon atoms in front of the target after about 40 μs. Since

[4] A current tutorial on reactive magnetron sputtering can be found in *A. Anders "Tutorial: Reactive high power impulse magnetron sputtering (R-HiPIMS)"; Journal of Applied Physics 121, 171101 (2017)*

the ionization energy of metals is generally lower than that of argon, a metal plasma is created.

- **Ionization Degree, Power Densities:** HiPIMS plasmas require powers in the range of kW/cm^2 target area or current densities in the range ¿1 A/cm^2. An ionization degree of 50% and higher is then created.

- **Current/Voltage Characteristics:** Many power supplies initially generate a rectangular voltage pulse. The voltage or power is regulated via a simultaneous current measurement. In the current curve, either a continuous increase to a plateau is seen, or a continuous increase to the end of the pulse if the self-sputtering is very high.

- **Return Effect:** In front of the target in the region of the magnetic confinement, there is an electric field in the direction of the target. If the energy of the ions is too low, they cannot leave this region in the direction of the substrate and return to the target (return effect). That is, the high degree of ionization can only be partially utilized. If the coating is normalized to the average (integrated over time) power, the growth rate in HiPIMS is only 30% of that of DCMS plasmas.

- **Instabilities, Structure Formation:** Due to the high densities and gradients, waves and instabilities are formed. Prominent here are the "spokes" with a dispersion of gradient waves, which typically rotate at 10 km/s along the sputtering trench. Their speed is greater than that of the ions at 1 km/s and less than that of the electrons in the ExB motion at approximately 100 km/s. These waves generate azimuthal electric fields that enhance the transport from the target to the substrate.

5.2 Capacitively Coupled Plasmas (CCP)

5.2.1 Current-Voltage Characteristic

In a DC discharge, the power coupling is bound to the ohmic DC current flowing between the parallel plates. When operating this system with alternating current, much higher charge carrier densities can be achieved because the plasma is heated by the displacement current and the ohmic current represents only a very small fraction. The AC voltage shifts the plasma volume back and forth between the electrodes and drives this displacement current through the sheaths with the extensions s_a and s_b, as illustrated in Fig. 5.18. This is referred to as capacitive coupling (CCP, capacitively coupled plasma).

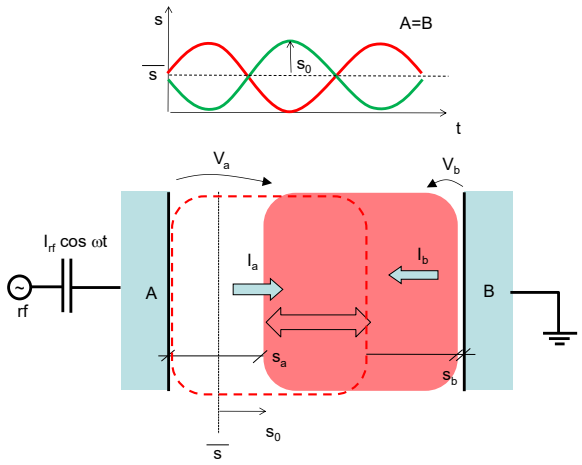

Figure 5.18: Model of a capacitively coupled RF discharge.

The conditions for high-frequency plasmas regarding dimensions and frequencies can be defined as follows:

- *Ions see only the time-averaged E-field*

  If the plasma frequency of the ions ω_{pi} is much smaller than the exciting high frequency ω_{rf}, then the ions see only the time-averaged electric fields. The following must apply:

$$\omega_{\mathrm{pi}} \ll \omega_{\mathrm{rf}} \tag{5.32}$$

- *Electrons see the E-field directly*

Since the plasma frequency of the electrons ω_{pe} is much larger than the exciting frequency, the electrons can follow the electric fields and be heated. This is satisfied for:

$$\omega_{pe}^2 \gg \omega_{rf}^2 \left(1 + \frac{\nu_m^2}{\omega_{rf}^2}\right)^{1/2} \tag{5.33}$$

- *vanishing electron density in the sheath*

  At the considered high voltages, the extensions of the sheaths are significant. As a first approximation, we can assume the electron density in the sheath to be zero if the following applies:

$$\lambda_D \ll s \tag{5.34}$$

- *no standing wave effects*

  Finally, we want to initially limit the consideration to smaller CCPs in which no standing waves can yet be formed. That is, the following must apply:

$$\lambda_{rf} \gg d \tag{5.35}$$

With typical plasma densities in the range $n_e \simeq 10^{10}$ cm^{-3}, this results in frequencies in the MHz range. Often, 13.56 MHz is used as the HF frequency, as this frequency is released for technical use. However, this release may not necessarily be fulfilled by plasmas. Due to the nonlinearity of the sheath (see stochastic heating), higher harmonics are also excited, which then no longer fall into the released frequency band. For this reason, it is always necessary to shield a reactor for a high-frequency plasma well against scattered HF power.

Animation

RF Plasma.
1d3v PIC Simulation of a high-frequency plasma.

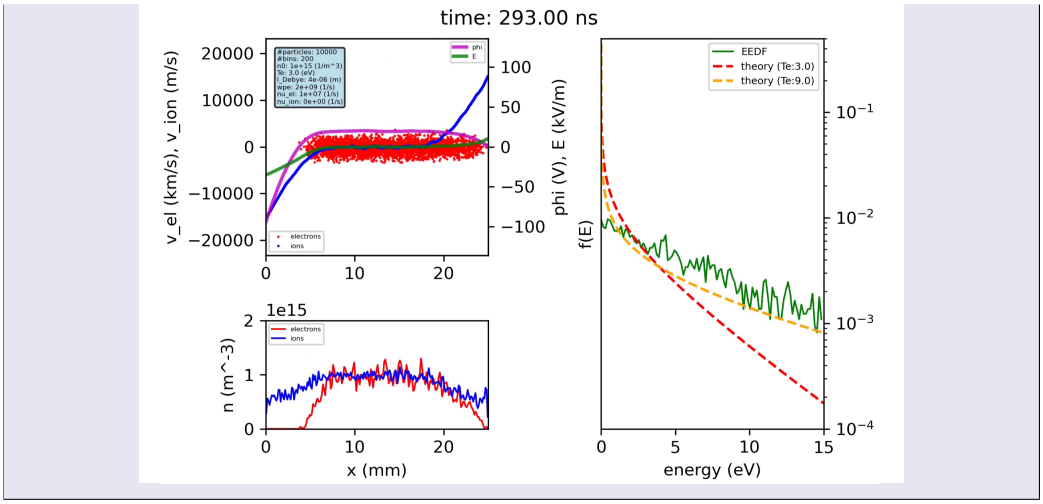

The course of the voltage in a symmetric high-frequency plasma with equally large electrode areas is shown in Fig. 5.19. One electrode is referred to as driven, as the voltage oscillates sinusoidally between $\pm V_0$ there. The other electrode is grounded. If the voltage is zero, there is a small voltage drop in front of both electrodes with respect to the positive plasma potential. If the voltage becomes negative ($-V_0$), we have the potential profile with a large sheath in front of the driven electrode. If, however, the voltage becomes positive, the picture is reversed, and the large voltage drop occurs in front of the grounded electrode. The sheath voltage is also a measure of the ion bombardment of the surfaces, and thus in a symmetric arrangement, both electrode surfaces are exposed to the same ion bombardment.
To describe the voltage characteristics of a high-frequency discharge, we start with the simplest sheath model, a matrix layer. The signs of all voltages and currents refer to the directions as shown in Fig. 5.18. The field in the space charge zone is calculated as:

$$\nabla E = \frac{e}{\epsilon_0} n \tag{5.36}$$

$$E(x,t) = \frac{en}{\epsilon_0} \left[x - s_\mathrm{a}(t)\right] \tag{5.37}$$

The displacement current, which is generated by the oscillation of the sheath between electrode a and the plasma (see Fig. 5.18), is given by:

$$I_\mathrm{a} = \epsilon_0 A \frac{\partial E}{\partial t} = -enA \frac{\partial s_\mathrm{a}}{\partial t} \tag{5.38}$$

with A the area of electrode a. This displacement current must be equal to the RF current in the external circuit:

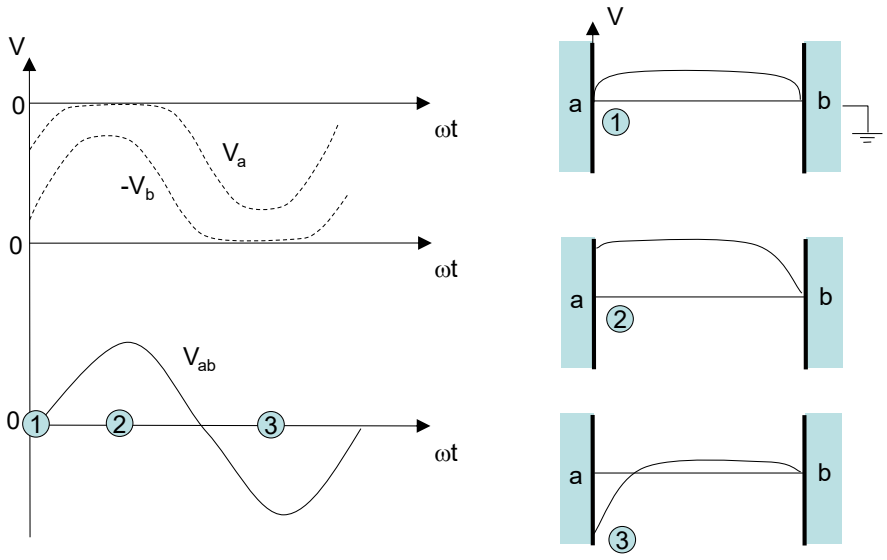

Figure 5.19: Voltage profiles between plasma and surface as well as between the electrodes (left). Potential profile in a symmetric arrangement (right). Here, $V_{\mathrm{ab}} = V_{\mathrm{a}} - V_{\mathrm{b}}$.

$$I_{\mathrm{a}} = I_{\mathrm{rf}} \cos \omega t \tag{5.39}$$

From this, it follows that the thickness of the sheath is obtained by integration of Eq. 5.38 as:

$$s_{\mathrm{a}}(t) = -\frac{I_{\mathrm{rf}}}{\underbrace{en\omega A}_{s_0}} \sin \omega t + \bar{s} \tag{5.40}$$

or

$$s_{\mathrm{a}}(t) = -s_0 \sin \omega t + \bar{s} \tag{5.41}$$

Here, $\bar{s}$ is the integration constant. The voltage across sheath a from Eq. 5.37 is, according to $V_{\mathrm{a}} = -\int_0^{s_{\mathrm{a}}} E \mathrm{d}x$:

$$V_{\mathrm{a}} = \frac{e}{\epsilon_0} n \frac{1}{2} s_{\mathrm{a}}^2(t) \tag{5.42}$$

Substituting $s_{\mathrm{a}}(t)$ gives:

$$V_a = \frac{1}{2}\frac{en}{\epsilon_0}(\bar{s}^2 + \frac{1}{2}s_0^2 - 2\bar{s}s_0 \sin\omega t \frac{1}{2}s_0^2 \cos^2\omega t) \tag{5.43}$$

Analogously, the displacement current at electrode b with area B is:

$$I_\mathrm{b} = -enB\frac{\partial s_\mathrm{b}}{\partial t} \tag{5.44}$$

Since the current is contained in the charge, according to our arrow directions for the currents in Fig. 5.18, the following must apply $I_\mathrm{a} = -I_\mathrm{b}$. Thus, we obtain:

$$I_\mathrm{a} + I_\mathrm{b} = 0 = -en\frac{\mathrm{d}}{\mathrm{d}t}(As_\mathrm{a} + Bs_\mathrm{b}) = 0 \tag{5.45}$$

The quantity $As_\mathrm{a} + Bs_\mathrm{b}$ corresponds to the total volume of the sheaths and is thus proportional to the total net charge in the parallel plate arrangement. This total charge is conserved, which is an equivalent formulation of charge conservation.
Next, we want to consider the simple case of a symmetric discharge where the electrode areas A and B are equal. For this case, the following must apply:

$$\frac{\mathrm{d}}{\mathrm{d}t}(s_\mathrm{a} + s_\mathrm{b}) = 0 \tag{5.46}$$

That is, the expansion of the plasma volume (plate distance-$(s_\mathrm{a} + s_\mathrm{b})$) does not change, but oscillates in its position during the RF cycle back and forth between the electrodes. The solution for s_a must therefore be inversely proportional to the solution for s_b in a symmetric discharge, so that the sum remains constant. That is, the following applies:

$$s_\mathrm{b}(t) = \underbrace{\frac{I_\mathrm{rf}}{en\omega A}}_{s_0}\sin\omega t + \bar{s} \tag{5.47}$$

and $s_\mathrm{a} + s_\mathrm{b} = 2\bar{s}$. The voltage across sheath b is:

$$V_\mathrm{b} = \frac{1}{2}\frac{en}{\epsilon_0}(\bar{s}^2 + \frac{1}{2}s_0^2 + 2\bar{s}s_0 \sin\omega t \frac{1}{2}s_0^2 \cos^2\omega t) \tag{5.48}$$

According to our convention for the voltages across the sheaths, the external voltage V_rf is composed of the voltages across the sheaths:

$$V_\mathrm{rf} = V_\mathrm{ab} = V_\mathrm{a} - V_\mathrm{b} \tag{5.49}$$

This results in:

$$V_{\mathrm{rf}} = \frac{2e}{\epsilon_0} n\bar{s} \frac{I_{\mathrm{rf}}}{en\omega A} \sin \omega t \tag{5.50}$$

One can see that the voltage oscillates phase-shifted by 90 ° to the current ($I = I_{\mathrm{rf}} \cos \omega t$). This is a result of the fact that the voltage drives a capacitance, the sheath.
So far, the integration constant $\bar{s}$ has not been specified. This is obtained from the condition that the electron flux to a surface must compensate for the Bohm flux of the ions. This can only be achieved for the matrix layer by assuming that the layer collapses briefly during an RF cycle ($s_a(t) = 0$). That is, according to Eq. 5.41, the following must apply:

$$0 = -s_0 + \bar{s} \tag{5.51}$$

From this, it becomes clear that the quantity $\bar{s}$ corresponds to the average sheath thickness. With this boundary condition, the voltage drop across a sheath is:

$$V_{\mathrm{a}} = \frac{e}{2\epsilon_0} n s_0^2 (1 - \sin \omega t)^2 = \frac{1}{2\epsilon_0} \frac{I_{\mathrm{rf}}^2}{enA^2} \frac{1}{\omega^2} (1 - \sin \omega t)^2 \tag{5.52}$$

Thus, the relationship between RF current and RF voltage is:

$$\boxed{V_{\mathrm{rf}} = \frac{2e}{\epsilon_0} n \left(\frac{I_{\mathrm{rf}}}{en\omega A} \right)^2 \sin \omega t} \tag{5.53}$$

The course of the individual components of the voltage is shown in Fig. 5.19. One can see that the sheath voltages in front of the electrodes are small for long periods within the RF cycle. The sheath voltage is alternately large at electrode a and then at b. In the external circuit, however, the voltage follows a simple law $V_{\mathrm{rf}} \propto \sin \omega t$ again.
Fig. 5.19 also shows the spatial distribution of the potential under the assumption that electrode b is grounded and an alternating voltage is applied to electrode a. This profile can be easily understood if one realizes that the potential of the plasma must always be the most positive in the system electrode-plasma-electrode. If this were not the case, the electrons could simply leave the plasma[5].

[5] Only in a few cases does this rule not apply. In hydrogen plasmas, for a short period in the RF cycle, a so-called field reversal occurs, in which the electric field no longer points in the direction of the plasma volume. This enhances the electron current out of the plasma. This is necessary because otherwise the quasi-neutrality cannot be maintained, as the ion current through the very light and thus fast hydrogen ions cannot be compensated by the loss of thermal electrons in front of the surface.

In the positive half-cycle of the voltage source, the plasma potential follows the potential of electrode a in order to always remain more positive than the external potentials. The potential difference drops in front of electrode b. In the negative half-cycle, the sheath forms in front of electrode a, while the sheath voltage at electrode b remains low.
The ion energy distribution of the ions hitting the surfaces in a symmetric RF discharge results from the statistics of the time intervals in which the sheath voltage assumes certain values. From Fig. 5.19, one can see that the number of ions hitting the surfaces at lower sheath voltages and thus lower ion energies is greater than those at higher energies. This results in a bimodal distribution (as in Fig. 3.14) which is actually asymmetric with a higher peak at low energies. This asymmetry, however, becomes smaller when moving to very asymmetric discharges. For a large electrode b, the amplitude of the sheath voltage V_b becomes very small and the externally imposed sinusoidal course of V_rf is carried along by the oscillation of V_a, which must therefore also be almost perfectly sinusoidal. Since most measurements of ion energy distributions are carried out in strongly asymmetric discharges, numerous publications show almost perfectly symmetric bimodal distributions.

5.2.2 Absorbed Power of an RF Discharge

5.2.2.1 Power Scaling

The absorbed power in a high-frequency discharge consists of ohmic and stochastic heating:

$$P_\mathrm{ohmic} = \frac{1}{2} I_\mathrm{rf}^2 \frac{m\nu_\mathrm{m}}{e^2 n} d \tag{5.54}$$

$$P_\mathrm{stochastic} = \frac{1}{2} I_\mathrm{rf}^2 \frac{m v_\mathrm{th}}{e^2 n} \tag{5.55}$$

The absorbed power according to these mechanisms is, according to a global model, in equilibrium with the loss of power through ionization and energy transport through the sheaths. This loss occurs in the parallel plate arrangement at both sheaths, so we get:

$$P_\mathrm{ohm} + P_\mathrm{stochastic} = 2Aenv_\mathrm{B} \left(E_\mathrm{sheath} + E_\mathrm{ionisation} + E_\mathrm{e}\right) \tag{5.56}$$

The power balance determines the electron density to:

$$n = \frac{1}{2} I_\mathrm{rf} \left[\frac{m\left(\nu_\mathrm{m} d + 2v_\mathrm{th}\right)}{Ae^3 v_\mathrm{B} \left(E_\mathrm{sheath} + E_\mathrm{ionisation} + E_\mathrm{e}\right)}\right]^{1/2} \tag{5.57}$$

When operating a high-frequency plasma, the voltage is often freely adjusted from the outside. This was:

$$V_{\mathrm{ab}} = \frac{1}{2}\frac{en}{\epsilon_0}s_0^2 \sin \omega t \tag{5.58}$$

This voltage controls the voltage at the sheath V_{a}:

$$V_{\mathrm{a}} = \frac{en}{2\epsilon_0}s_0^2 \left(1 - \sin \omega t\right)^2 \tag{5.59}$$

We substitute the current according to $s_0 = \frac{I_{\mathrm{rf}}}{en\omega A}$ and consider the time averaging of $\langle (1 - \sin \omega t)^2 \rangle_{\mathrm{t}} = \frac{3}{2}$:

$$\bar{V_{\mathrm{a}}} = \frac{3}{4}\frac{I_{\mathrm{rf}}^2}{A^2 e\epsilon_0 n\omega^2} \tag{5.60}$$

If we substitute the current in Eq. 5.55, we get a scaling of the power according to:

$$P_{\mathrm{ges}} = P_{\mathrm{ohmic}} + P_{\mathrm{stochastic}} = \frac{1}{2}\frac{4}{3}\bar{V_{\mathrm{a}}}\omega^2 e\epsilon_0 n A^2 \left(\frac{m\nu_{\mathrm{m}}}{e^2 n}d + \frac{mv_{\mathrm{th}}}{e^2 n}\right) \tag{5.61}$$

Since the thermal electron velocity as well as the electron collision rate scale with $\sqrt{T_{\mathrm{e}}}$, we get an absorbed power with a dependence on:

$$\boxed{P_{\mathrm{ges}} \propto \omega^2 \bar{V_{\mathrm{a}}} \sqrt{T_{\mathrm{e}}}} \tag{5.62}$$

At this point, one recognizes a fundamental problem of high-frequency discharges. In applications, one often wants to control two quantities independently of each other: the plasma density and thus the rate of the process (e.g., etch rate or growth rate), as well as the energy of the ions hitting the surfaces. This is not possible. The plasma density is directly related to the absorbed power via the global model, which in turn can only be adjusted by increasing the sheath voltage. That is, a high plasma density also implies a high sheath voltage and thus a high ion bombardment. This is particularly disadvantageous for the field of plasma etching in microelectronics, where the structures are to be etched quickly but electronic defects must not be introduced by the ion bombardment. A way out of this dilemma is offered by other types of discharges as well as the use of multiple and higher frequencies, as discussed below.

5.2.2.2 α-, γ- and Ω-Mode of an RF Plasma

In the external appearance of a high-frequency plasma, several heating modes can be distinguished depending on which processes predominantly contribute

to the energy transfer from the electric field to the electrons. These heating modes are:

- α-mode: stochastic heating of the electrons in collisions with the sheath.
- γ-mode: heating of the plasma by injection of secondary electrons from the surface.
- Ω-mode: heating in drift fields in the plasma volume at high-pressure plasmas.

First, one distinguishes a $\boldsymbol{\alpha}$- and a $\boldsymbol{\gamma}$-mode. The γ-mode is significantly carried by the secondary electron multiplication at the electrodes. Due to the strong electron flows into the plasma, a structure is formed which, similar to the sequence of a DC discharge, consists of negative glow, Faraday dark space, and positive column. In the emission, this is visible in three maxima of the emission between the electrodes. In the α-mode, on the other hand, heating takes place primarily by displacement current, especially in front of the electrodes where the oscillating sheaths accelerate the electrons and shoot them into the plasma. This behavior can be observed in the experiment as shown in Fig. 5.20. Due to the high current density in the γ-mode, the discharge also contracts.
When considering the Ω-mode, we first need to motivate that an electric drift field is created in atmospheric pressure plasmas in the plasma volume. To do this, we consider a simple global model consisting of continuity and momentum equations for the electron current j_e:

$$\frac{\partial n_e}{\partial t} + \frac{\partial n_e v_e}{\partial x} = S \tag{5.63}$$

with S the ionization rate. The momentum balance is:

$$m_e n_e \left[\frac{\partial v_e}{\partial t} + v_e \frac{\partial v_e}{\partial x}\right] = -eEn_e - \frac{\partial p_e}{\partial x} - m_e n_e v_e \nu_m \tag{5.64}$$

With the electron flux $\Gamma_e = n_e v_e$ we get:

$$\frac{\partial \Gamma_e}{\partial t} = -\frac{eE}{m_e} n_e - \frac{1}{m_e}\frac{\partial p_e}{\partial x} - \Gamma_e \nu_m - \frac{\partial v_e \Gamma_e}{\partial x} \tag{5.65}$$

Now we use the electrical current densities $j_e = en_e v_e$ and $j_{therm} = en_e\sqrt{k_B T_e/m_e}$ and $p_e = n_e k_B T_e$ and solve everything for the electric field E:

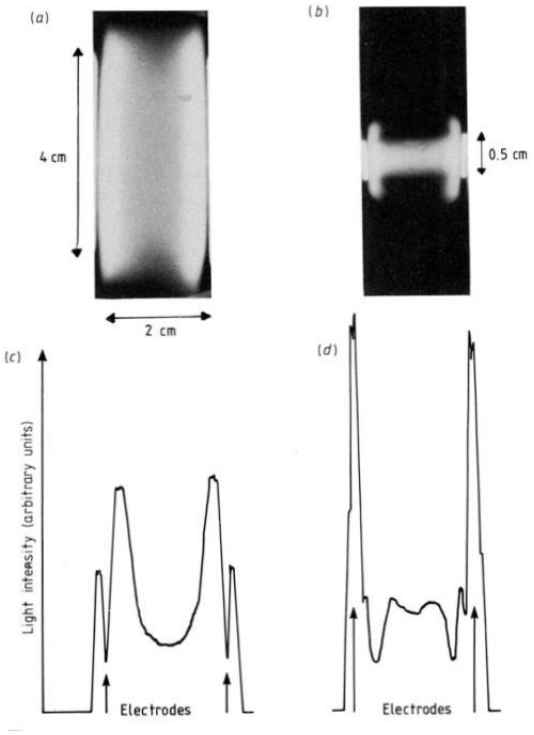

Figure 5.20: α- and γ-RF discharge [50].

$$E = \frac{m_e}{n_e e^2}\left(\underbrace{\frac{\partial j_e}{\partial t}}_{displacement} + \underbrace{\nu_m j_e}_{drift} + \underbrace{\frac{1}{en_e 2}\left(j_e^2 - j_{therm}^2\right)\frac{\partial n_e}{\partial x}}_{ambipolar\ \ field} + \frac{j_e S}{n_e}\right) \tag{5.66}$$

One recognizes several contributions to the electric field in the plasma. The ambipolar field is particularly large in regions with a strong density gradient such as at the edges of the discharge near the sheaths. However, a large drift field is also created in the case of high collision frequencies ν_m, i.e., this electric field must accelerate the electrons in the volume against the high collision rate to ensure current continuity in the volume. The name Ω-mode is derived from the ohmic heating in the plasma volume.

5.2.3 Geometry of an RF Discharge

In a symmetric RF discharge, due to symmetry reasons, the voltage swing at both sheaths is identical. If a parallel plate arrangement with different electrode areas is used, a different voltage drop can be forced. This is a direct consequence of the conservation of the RF current in the arrangement. For two electrodes a and b, the following must apply, according to the convention for the current direction in Fig. 5.21:

$$I_\mathrm{a} = I_\mathrm{b} \tag{5.67}$$

This displacement current is carried by the change in the amount of charge in the sheath:

$$\dot{Q}_\mathrm{a} = \dot{Q}_\mathrm{b} \tag{5.68}$$

For a periodic signal, we can also integrate this over one period and must therefore demand that the amount of charge itself must also be identical in the time average.

$$\frac{1}{T}\int_0 T\dot{Q}_\mathrm{a}\mathrm{d}t = \frac{1}{T}\int_0 T\dot{Q}_\mathrm{b}\mathrm{d}t \tag{5.69}$$

$$\bar{Q}_\mathrm{a} = \bar{Q}_\mathrm{b} \tag{5.70}$$

If now the areas of the electrodes in an asymmetric RF discharge are different, the average amount of charge in the sheath in front of this small electrode can only remain the same as the amount of charge in front of the large electrode if the thickness of this sheath increases compared to a symmetric discharge. Exactly this equilibrium is established, and a negative voltage is formed at the small electrode, which leads to an expansion of the sheath. This so-called Self-Bias Effect we want to quantify now.
The plasma can be seen as a series connection of two capacitors C_a and C_b. Each sheath (or capacitor) carries an average charge $\bar{Q}$, which is maintained by the time-averaged voltage $\bar{V}_\mathrm{a}$ or $\bar{V}_\mathrm{b}$. According to the expression for the capacitance of a plate capacitor, we get for the two sheaths:

$$\bar{Q}_\mathrm{a} = \bar{V}_\mathrm{a}C_\mathrm{a} = \bar{V}_\mathrm{a}\frac{A}{\bar{s}_\mathrm{a}}\epsilon_0 \tag{5.71}$$

$$\bar{Q}_\mathrm{b} = \bar{V}_\mathrm{b}C_\mathrm{b} = \bar{V}_\mathrm{b}\frac{B}{\bar{s}_\mathrm{b}}\epsilon_0 \tag{5.72}$$

with A and B the areas of electrodes a and b and $\bar{s}_\mathrm{a}$ and $\bar{s}_\mathrm{b}$ the average thicknesses of the sheaths. Since $\bar{Q}_\mathrm{a} = \bar{Q}_\mathrm{b}$ applies, it immediately follows:

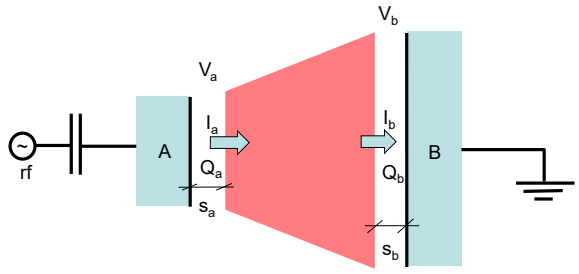

Figure 5.21: Scheme of an asymmetric RF discharge.

$$\frac{\bar{V}_\mathrm{a}}{\bar{s}_\mathrm{a}} A = \frac{\bar{V}_\mathrm{b}}{\bar{s}_\mathrm{b}} B \tag{5.73}$$

Since the plasma is characterized by a unique density, a second relationship between sheath thicknesses and sheath voltages can be derived. According to the Child-Langmuir law, sheath voltage and sheath thickness are linked as:

$$j_0 \propto n v_\mathrm{B} \propto \frac{\bar{V}^{3/2}}{\bar{s}^2} \tag{5.74}$$

Since the current density on both electrodes a and b must be equal, we obtain as a second equation:

$$\frac{\bar{V}\mathrm{a}^{3/2}}{\bar{s}_\mathrm{a}^2} = \frac{\bar{V}\mathrm{b}^{3/2}}{\bar{s}_\mathrm{b}^2} \tag{5.75}$$

Dividing equation 5.73 by equation 5.75, we obtain:

$$\boxed{\frac{\bar{V}_\mathrm{a}}{\bar{V}_\mathrm{b}} = \left(\frac{B}{A}\right)^4} \tag{5.76}$$

That is, by a very asymmetric choice of the electrode areas, the average voltage that drops between surface and plasma becomes very large at small electrodes. The exponent 4 essentially arises from the assumption of the Child-Langmuir law. In a matrix layer, this exponent is 2. In the experiment, one rather observes a dependence with an exponent of 2.5. The course of the sheath voltage at an RF electrode is shown in Fig. 5.22.
For the asymmetry of the voltage drop on the two electrodes a and b to be ensured according to Eq. 5.76, a DC voltage is set at electrode a, the DC

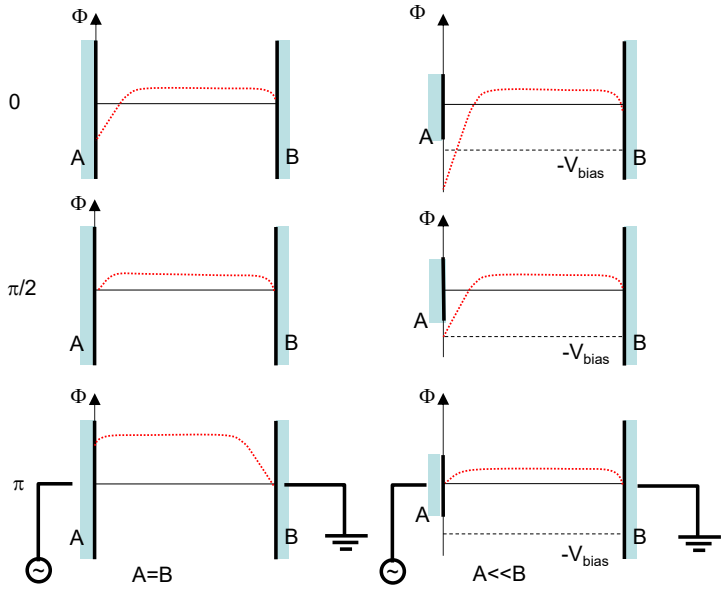

Figure 5.22: Course of the potential between two electrodes with symmetric electrode areas $A = B$ and asymmetric electrode areas $A \ll B$.

Self-Bias $\boldsymbol{V_{\mathrm{bias}}}$: the generator initially generates an alternating voltage V_{rf} with an average of 0, which is connected to the electrode via a capacitor. This capacitor galvanically isolates the generator from the electrode. Thus, it is possible for an additional DC voltage to be set at the electrode, which is superimposed on the alternating voltage. At the electrode, a voltage swing of amplitude V_{rf} is created, but the average of this amplitude is shifted to negative voltages by V_{bias}.
This DC Self-Bias, however, cannot assume arbitrary values, since the net currents to electrode a must always result in zero. That is, during an RF cycle, the sheath must collapse at a certain point in time to allow the electrons to reach the electrode. This is illustrated in Fig. 5.23. In strongly asymmetric discharges, the voltage across the sheath at electrode a has an almost sinusoidal course. A maximum DC Self-Bias $V_{\mathrm{bias,max}}$ is set in such a way that $V_{\mathrm{bias,max}}$ is exactly equal to the amplitude of the externally applied alternating voltage V_{rf}. This ensures that the sheath collapses at one point in time and the electron current to the electrode is exactly equal to the ion current to electrode a.
For arbitrary ratios of the electrode areas, V_{bias} is set in such a way that Eq. 5.76 is satisfied. The temporal course of the voltages at the electrode Φ_{a} and

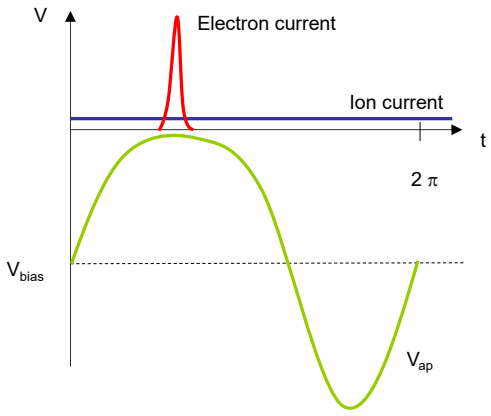

Figure 5.23: Course of the currents in front of electrode A in a strongly asymmetric discharge with $A \ll B$.

in the plasma Φ_p is illustrated in Fig. 5.24.
The strong dependence of the DC Self-Bias on the ratio of the electrode areas is rarely achieved in experiments. This is due to the fact that at high pressure, the model of a collision-determined sheath is more appropriate. In this case, the current density scales as:

$$j \propto \frac{V^{3/2}}{s^{5/2}} \tag{5.77}$$

which results in a scaling of

$$\frac{\bar{V}_a}{\bar{V}_b} = \left(\frac{B}{A}\right)^{2.5} \tag{5.78}$$

which is much closer to the measured values of 2...2.5. The DC Self-Bias is often also used as a simple control variable for the operation of a high-frequency plasma. In addition, the average energy of the ion bombardment can be determined in principle from the DC Self-Bias. However, in very large plasma reactors, the area ratio becomes more symmetric, i.e., the DC Self-Bias becomes smaller and is then no longer a good control variable.

5.2.4 Impedance Matching

When operating a high-frequency discharge, one wants to couple the power output of an RF transmitter into the plasma as efficiently as possible. For

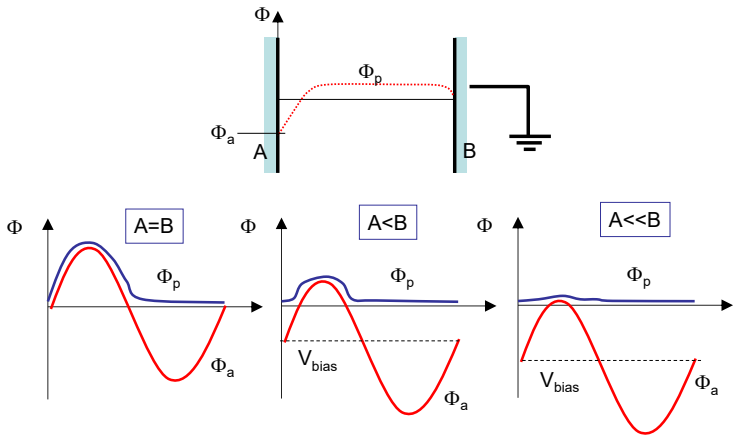

Figure 5.24: Temporal course of the plasma potential Φ_p and the potential Φ_a at the electrode a for different ratios of the electrode areas A and B.

this purpose, however, the current and voltage of the RF transmitter must be as in phase as possible.

$$\bar{P} = \frac{1}{2}\Re\left\{V_\mathrm{rf} I_\mathrm{rf}\right\} \tag{5.79}$$

This is not possible with a purely capacitive or inductive load of a plasma. For this reason, there is an impedance matching network (Matching) between the RF transmitter and the plasma. The purpose of this matching network is to make the complex resistance consisting of matching and plasma real. One can also consider this as a series resonant circuit with the capacitors "plasma" and capacitors in the matchbox, as well as the inductances in the matchbox and in the plasma. Together, this resonant circuit is to be driven by an alternating voltage in which current and voltage are in phase.
There are several variants for the matching network, as illustrated in Fig. 5.25. A network of 2 reactive components is referred to as an L-network. Networks of three components can either be designed as a Π-network or as a T-network. The networks with three components can be adjusted more precisely in their frequency response.
The impedances in the network according to Fig. 5.25 are:

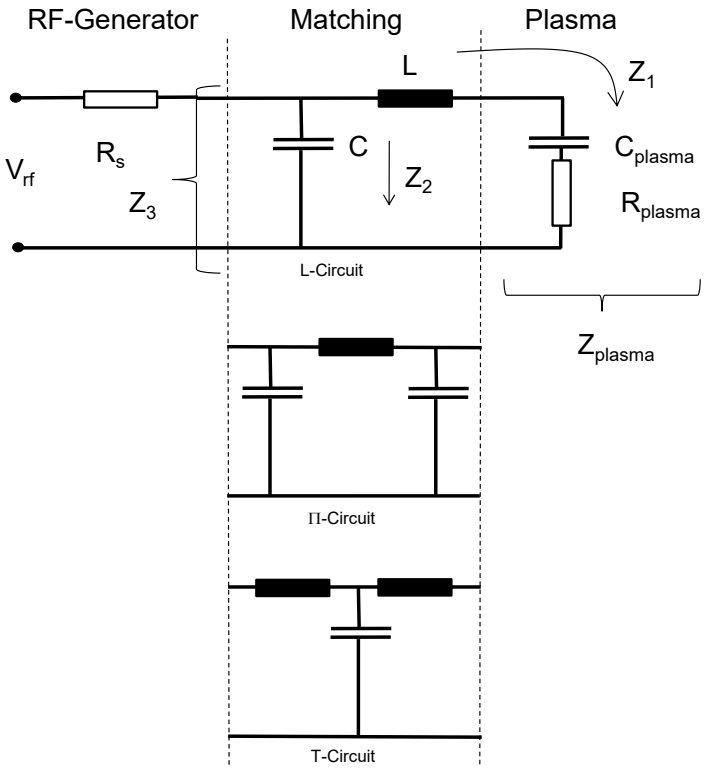

Figure 5.25: Impedance matching between transmitter and plasma using a matching network. Depending on the quality of the matching, one can choose between a network with two components (L-network) or with three components (Π-network or T-network).

$$Z_{\text{plasma}} = R_{\text{plasma}} + \frac{1}{\imath\omega C_{\text{plasma}}} \tag{5.80}$$

$$Z_1 = \imath\omega L + R_{\text{plasma}} + \frac{1}{\imath\omega C_{\text{plasma}}} \tag{5.81}$$

$$Z_2 = \frac{1}{\imath\omega C} \tag{5.82}$$

This combines to an impedance Z_3, which the RF transmitter sees. This should be as real as possible, i.e., the imaginary part of Z_3 should become zero so that the power is effectively dissipated in R_{plasma}.

$$\frac{1}{Z_3} = \frac{1}{Z_1} + \frac{1}{Z_2} \tag{5.83}$$

5.2.5 Multifrequency Discharges

For many applications, it is necessary to be able to control the plasma density and sheath voltage separately. In a simple DC discharge, this is not possible because with increasing current density and thus generated plasma density, the sheath voltage must also increase, according to the Child-Langmuir law for the abnormal glow discharge. This also applies to high-frequency discharges, as discussed with reference to Eq. 5.62.

5.2.5.1 Plasma Heating

However, it is possible in high-frequency discharges to vary an additional characteristic, the frequency. A simple variant would be to apply a high (HF) and a low (LF) frequency simultaneously to the driven electrode and thus generate a multifrequency plasma. According to Eq. 5.62, one can thus set the plasma density and sheath voltage independently of each other:

$$\begin{aligned} P_{\text{abs}} \propto V_{\text{LF}}\omega_{\text{LF}}^2 &\rightarrow \text{boundary layer voltage} \\ P_{\text{abs}} \propto V_{\text{HF}}\omega_{\text{HF}}^2 &\rightarrow \text{plasma density} \end{aligned}$$

At a low frequency, a high sheath voltage can be chosen without the plasma density increasing, since the term ω_{LF}^2 is very small. Conversely, a small voltage V_{HF} is sufficient for a high plasma density, since the absorbed power becomes very efficient due to the term ω_{HF}^2. Typical values for ω_{LF} are in the range of 1 to 2 MHz, for ω_{HF} at 50 to 200 MHz.
This very simple picture of a perfect decoupling of the effects of both frequencies cannot be found quite in the experiment. In particular, the variation of the sheath voltage of the low frequency leads to a slight variation of the efficiency of the power coupling through the high frequency. This has two reasons:

- *Stochastic heating without loss of electrons*

  Consider for this purpose a typical course of the voltage in a dual-frequency discharge (2 MHz and 27 MHz) as shown in Fig. 5.26. In normal heating with one frequency, a small current of electrons is always lost to the electrodes per period to ensure that the total current to the driven electrode is zero. This is not necessary in a multifrequency discharge. The high-frequency component causes an oscillation of the sheath edge at a location determined by the sheath extension of the low-frequency component. The charge balance only takes place when the sheath collapses at a point in the phase of the low-frequency sheath.

That is, for a large part of the period, the high-frequency field can effectively heat the electrons without them being lost.

- *Higher speed of the sheaths*

  The speed of the sheath depends on the ion density at the location of the sheath edge. In the Child-Langmuir sheath, the ion density decreases towards the electrode surfaces and accordingly the sheath edge moves quickly there. Since stochastic heating depends on the speed of the sheath edge, this heating mechanism is more effective if it takes place near the surface of a sheath with a high absolute sheath voltage.

  This fundamental behavior is also found in experiments as can be seen from the PROES data of a dual-frequency discharge with 2 MHz and 27 MHz (see in Fig. 5.26). Actually, one should find about 13 electron beams in the PROES recording, corresponding to the oscillations of the high-frequency component during the period of the low-frequency component. However, intense emission is only observed when the speed of the sheath edge in front of the electrode is high.

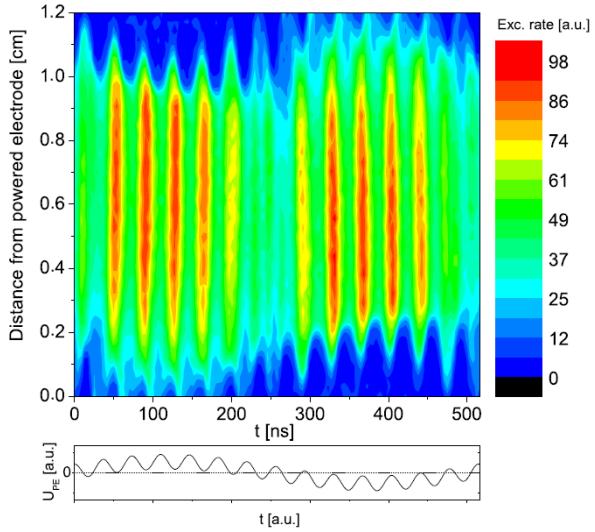

Figure 5.26: PROES images of a discharge driven with 2 and 27 MHz. The voltage curve is shown in the lower panel [45].

In the technical implementation of these multifrequency plasmas, several hurdles have to be overcome. Initially, high-frequency supplies in the range of

50...100 MHz are technically complex and costly; on the other hand, the wavelength of the RF radiation becomes correspondingly small, so that the dimensions and line lengths must be matched very precisely. When operating with multiple frequencies, the impedance networks must also be protected against the feedback of the respective other frequency. That is, it is necessary to insert corresponding bandpass filters. In addition to these technical difficulties, however, new physical phenomena also exist in these plasmas, which still hinder the application to large-area etching or coating.

5.2.5.2 Standing Waves, Skin Effect

With increasing frequency, the wavelength decreases to a range in which standing waves can occur in the plasma discharge. At the same time, the high-frequency electric field generates a variation in the B-field and electromagnetic effects begin to play a role (at low frequencies it is sufficient to simply calculate electrostatically). In the most general formulation, the Maxwell equations must be satisfied, assuming that only the displacement current is important:

$$\nabla \times \vec{B} \simeq \mu_0 \epsilon_0 \epsilon_\mathrm{r} \dot{\vec{E}} \tag{5.84}$$

$$\nabla \times \vec{E} = -\dot{\vec{B}} \tag{5.85}$$

The properties of the plasma can be mapped with a dielectric constant:

$$\epsilon_\mathrm{r} = 1 - \frac{\omega_\mathrm{p}^2}{\omega^2} \frac{1}{1 - \imath \frac{\nu_\mathrm{m}}{\omega}} \tag{5.86}$$

We now consider again the parallel plate arrangement as illustrated in Fig. 5.27. The components of the electric and magnetic field are coupled as follows:

$$\frac{\partial B_\phi}{\partial z} = \imath \omega \mu_0 \epsilon_0 \epsilon_\mathrm{r} E_\mathrm{r} \tag{5.87}$$

$$\frac{1}{r} \frac{\partial r B_\phi}{\partial r} = \imath \omega \mu_0 \epsilon_0 \epsilon_\mathrm{r} E_\mathrm{z} \tag{5.88}$$

$$\frac{\partial E_\mathrm{r}}{\partial z} - \frac{\partial E_\mathrm{z}}{\partial r} = -\imath \omega B_\phi \tag{5.89}$$

Due to the high ϵ_r we get a shielding of the radial electric field E_r with the penetration into the plasma according to:

$$E_\mathrm{r} = E_{\mathrm{r},0} e^{-\alpha z} \tag{5.90}$$

with $\alpha = \frac{1}{\delta}$ and δ the skin depth. This skin depth can be derived from the Maxwell equations, and one gets with a simple force approach for the linkage between displacement current and movement of the electrons in the limit of small collision frequencies ($\nu_\mathrm{m} \ll \omega$):

$$\delta = \frac{c}{\omega_\mathrm{p}} = \left(\frac{\epsilon_0 m_\mathrm{e} c^2}{n e^2} \right)^{1/2} \tag{5.91}$$

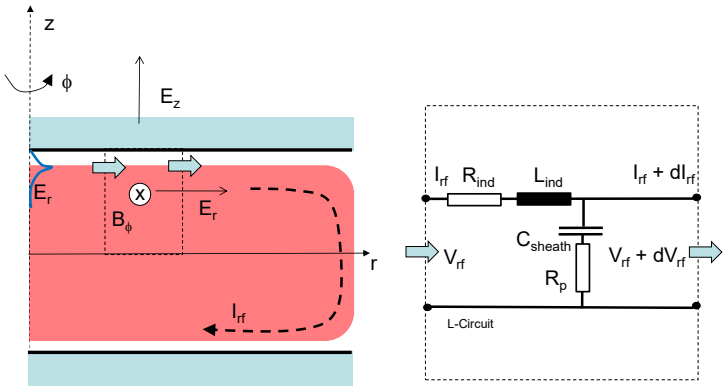

Figure 5.27: Electromagnetic effects in a high-frequency discharge. Equivalent circuit diagram of the propagation of the RF current in the plasma.

This shielding of the electric field leads to a different distribution of the high-frequency current in the discharge, which now no longer flows directly through the discharge but runs in the outer region corresponding to the skin depth from the driven to the grounded electrode (see Fig. 5.27 and 5.28). This effect is advantageous, as can be seen from the ion flux measurements in a high-frequency discharge in Fig. 5.28. At low powers, the field penetrates far into the plasma, since the electron density is small and the skin depth is large. Standing waves are formed, which lead to a strongly inhomogeneous plasma density profile with increasing frequency. If, however, the power is increased to the same extent, the skin depth becomes smaller again, and the RF current flows over the outer sides of the plasma.
The asymmetries that arise from standing waves and the skin effect are opposite and can partially cancel each other out. However, this compensation requires that the operating point with respect to plasma density and RF

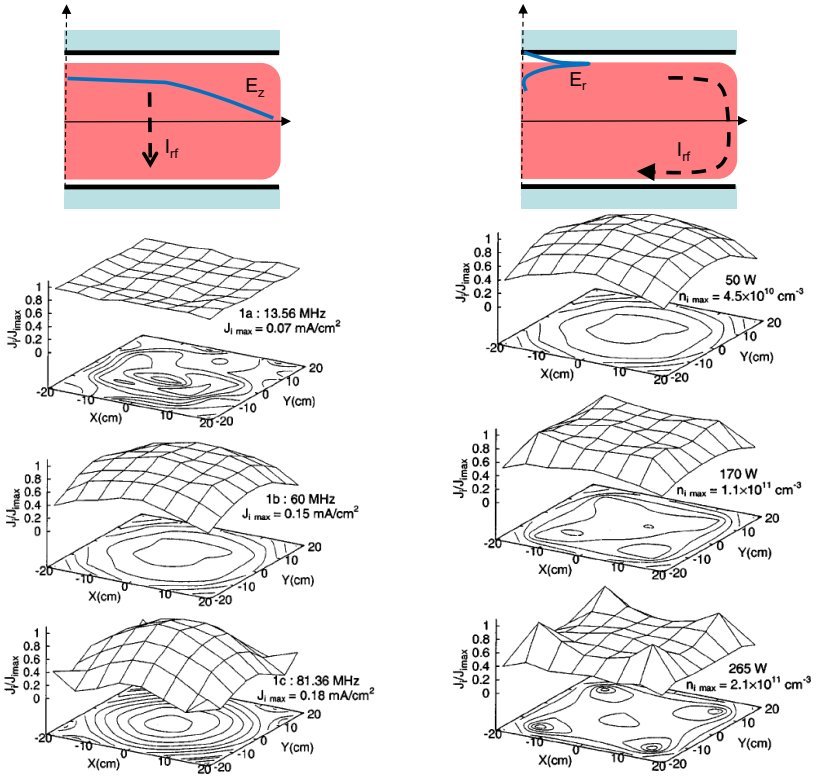

Figure 5.28: Distribution of the ion flux on an electrode as a function of the excitation frequency (left side) and at 60 MHz but increasing power [38].

current is exactly selected or can be selected. In addition, there is always a residual inhomogeneity that in some applications is not permissible. There, one wants to achieve a homogeneity of the treatment of the surfaces in the range of less than one percent. For this reason, other concepts have been developed to make a high-frequency plasma homogeneous. This is achieved by manipulating the standing waves or by manipulating the RF current that flows through the discharge.

- *dielectric lens*

  In a dielectric lens, as shown in Fig. 5.29, the shape of the electrode is adapted and covered by a dielectric. The shape of this electrode and the dielectric are chosen so that an electric field is created in the plasma that compensates the inhomogeneity caused by a standing wave accordingly. This is achieved by an attenuation of the electric field by

the strong dielectric in the center of the reactor.

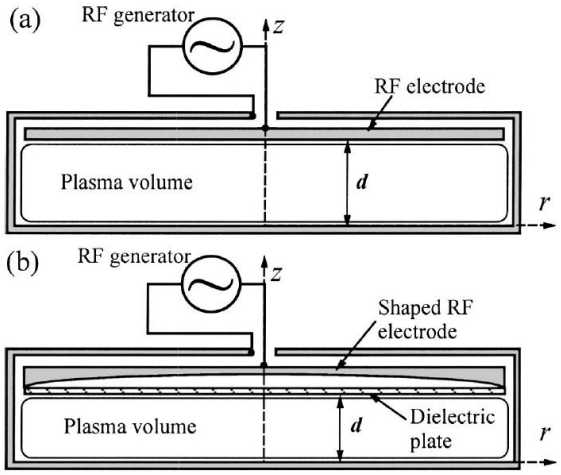

Figure 5.29: Model of a dielectric lens to compensate inhomogeneities in the plasma caused by standing waves [44].

- *Graded Conductivity*

  A technically simpler variant of a dielectric lens is achieved with a geometrically equally thick dielectric with different ϵ_r under the grounded electrode. This concept also has the disadvantage that the correction of the field distribution is fixed by the choice of the dielectric, either by the material thickness or by the ϵ, and thus only a certain operating point of the plasma is possible. Other operating modes require a complete rebuild of the entire system.

- *Distributed Electrodes*

  An alternative to this is concepts in which the high-frequency feed-ins are distributed over the area of the driven electrode. By matching, the HF current can thus be locally adapted, and an inhomogeneous density profile can be compensated.

5.2.5.3 Electrical Asymmetry

In high-frequency discharges, the voltages at the individual electrodes are set in such a way that the amount of charge within the sheaths is equal within an RF cycle. Only in this way is the conservation of the alternating current

ensured. When changing the area ratios, the voltages must be set differently, as only in this way can the amount of charge compensate for the change in area. When reducing the area, the voltage is increased so that the sheath expands and thus the enclosed charge increases again. This consideration, however, applies averaged over an RF cycle:

$$\frac{1}{T}\int_0^T \dot{Q}_\mathrm{a}\mathrm{d}t = \frac{1}{T}\int_0^T \dot{Q}_\mathrm{b}\mathrm{d}t \tag{5.92}$$

$$\bar{Q}\mathrm{a} = \bar{Q}_\mathrm{b} \tag{5.93}$$

In addition to a spatial variation, however, a temporal variation is also possible, which changes the voltages in the same way. This effect is referred to in analogy to the geometric asymmetry as electrical asymmetry [24]. First, consider a simple matrix sheath with a charge $\hat{Q}_\mathrm{a}$ that has an extension s_a:

$$\frac{\hat{Q}_\mathrm{a}}{A} = e\int_0^{s_\mathrm{a}} n\mathrm{d}z = e\bar{n}_\mathrm{a}\bar{s}_m athrma \tag{5.94}$$

This integral can take different values. We abbreviate this here and therefore use effective/averaged quantities $\bar{n}_\mathrm{a}$ and $\bar{s}_\mathrm{a}$. The voltage that drops across this matrix sheath is:

$$\hat{V}_\mathrm{a} = -\frac{e}{\epsilon_0}\int_0^{s_\mathrm{a}} nz\mathrm{d}z \tag{5.95}$$

The quantities $\hat{V}_\mathrm{a}$ and $\hat{s}_\mathrm{a}$ denote the points of the greatest amplitude of the voltage and extension of the sheath, respectively. These quantities are linked as:

$$\hat{V}\mathrm{a} = -\frac{1}{2}\frac{1}{e\epsilon_0}\left(\frac{\hat{Q}_\mathrm{a}}{A}\right)^2\frac{1}{\bar{n}_\mathrm{a}}\zeta_\mathrm{a} \tag{5.96}$$

ζ_a denotes a correction due to the difference between the real sheath and our assumption of a matrix layer for which $\zeta_\mathrm{a} = 1$ applies. The maximum voltage at the other sheath is:

$$\hat{V}_\mathrm{b} = -\frac{1}{2}\frac{1}{e\epsilon_0}\left(\frac{\hat{Q}_\mathrm{b}}{B}\right)^2\frac{1}{\bar{n}_\mathrm{b}}\zeta_\mathrm{b} \tag{5.97}$$

We define the ratio of the maximum voltages as the asymmetry parameter ϵ:

$$\epsilon = \left|\frac{\hat{V}_\mathrm{b}}{\hat{V}_\mathrm{a}}\right| = \left(\frac{A}{B}\right)^2\frac{\bar{n}_\mathrm{a}}{\bar{n}_\mathrm{b}}\frac{\zeta_\mathrm{b}}{\zeta_\mathrm{a}} \tag{5.98}$$

Here, we could shorten the charges $\hat{Q}_\mathrm{a}$, $\hat{Q}_\mathrm{b}$, since these must be equal because the current is conserved. If $\epsilon = 1$, we have a symmetric discharge, and values for $\epsilon \to 0$ mean a strongly asymmetric discharge with a small driven electrode, or for $\epsilon \to \infty$ a strongly asymmetric discharge with a large driven electrode. The expression for ϵ is analogous to the original derivation of the geometric asymmetry based on the Child-Langmuir sheath. There, under the assumption $\bar{n}_\mathrm{a} = \bar{n}_\mathrm{b}$, we had:

$$\epsilon = \left|\frac{\hat{V}_\mathrm{b}}{\hat{V}_\mathrm{a}}\right| = \left(\frac{A}{B}\right)^4 \tag{5.99}$$

One can see that the Child-Langmuir layer (exponent 4) and the matrix layer (exponent 2) again represent the two limiting cases for the dependence of the voltages on the area ratio.
Now consider a discharge with an external RF voltage V_rf and a self-bias V_SB that is set. The voltages across the two sheaths are V_a and V_b. If we choose the signs of the voltages such that they originate from the driven electrode, Kirchhoff's voltage law states:

$$V_\mathrm{rf} + V_\mathrm{SB} = V_\mathrm{a} + V_\mathrm{b} \tag{5.100}$$

For a geometrically symmetric reactor, the maxima of the voltages cancel each other out:

$$\hat{V}_\mathrm{b} = -\hat{V}_\mathrm{a} \tag{5.101}$$

For a strongly asymmetric reactor, on the other hand, we get:

$$\hat{V}_\mathrm{b} = -\epsilon\hat{V}_\mathrm{a} \tag{5.102}$$

The RF voltage now oscillates between the respective maxima $V_\mathrm{rf}^{(1)} = +\Phi_0$ and $V_\mathrm{rf}^{(2)} = -\Phi_0$, and for this the voltage of one or the other sheath becomes maximal, and the voltage of the opposite sheath becomes zero:

$$V_\mathrm{rf}^{(1)} + V_\mathrm{SB} = \hat{V}_\mathrm{a} \tag{5.103}$$
$$V_\mathrm{rf}^{(2)} + V_\mathrm{SB} = \hat{V}_\mathrm{b} \tag{5.104}$$

From these equations, we can now solve for the voltage for the self-bias using Eq. 5.102 and get:

$$V_\mathrm{SB} = -\frac{V_\mathrm{rf}^{(1)} + \epsilon V_\mathrm{rf}^{(2)}}{1+\epsilon} \tag{5.105}$$

We want to discuss the self-bias for some cases:

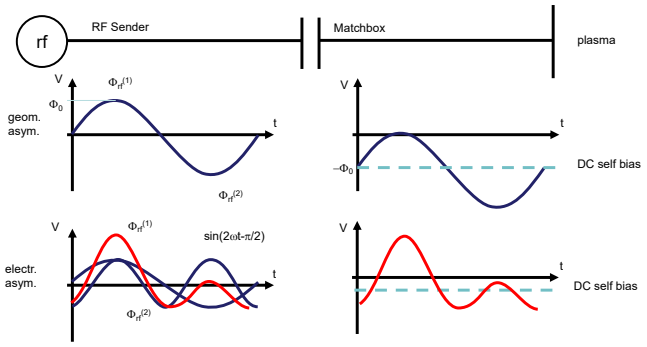

Figure 5.30: Illustration of the voltage curves at the generator (left) and at the electrode (right) for multifrequency discharges.

- *geometrically symmetric discharge,* $\epsilon = 1$

  In a geometrically symmetric discharge, $\epsilon = 1$. If we have a simple sine as an RF signal, then $V_{\mathrm{rf}}^{(1)} = -V_{\mathrm{rf}}^{(2)}$ and we get:

$$V_{\mathrm{SB}} = -\frac{V_{\mathrm{rf}}^{(1)} + V_{\mathrm{rf}}^{(2)}}{2} = 0 \tag{5.106}$$

  That is, as already discussed, V_{SB} disappears in a geometrically symmetric discharge:

- *geometrically asymmetric discharge,* $\epsilon \to 0$

  In an asymmetric discharge, let electrode a be smaller compared to b, or $\epsilon \to 0$. The self-bias then tends to $-V_{\mathrm{rf}}^{(1)}$. That is, the voltage at electrode a is shifted to the negative by a DC offset.

$$V_{\mathrm{SB}} = -\frac{V_{\mathrm{rf}}^{(1)} + \epsilon V_{\mathrm{rf}}^{(2)}}{1+\epsilon} \to -V_{\mathrm{rf}}^{(1)} = -\Phi_0 \tag{5.107}$$

- *geometrically asymmetric discharge,* $\epsilon \to \infty$

  In an asymmetric discharge, let electrode a be larger compared to b, or $\epsilon \to \infty$. Now the self-bias tends to $-V_{\mathrm{rf}}^{(2)}$. That is, the voltage at electrode a is shifted to the positive by a DC offset, since the voltage swing now occurs mainly in front of the grounded electrode.

$$V_{\mathrm{SB}} = -\frac{V_{\mathrm{rf}}^{(1)} + \epsilon V_{\mathrm{rf}}^{(2)}}{1+\epsilon} \to -V_{\mathrm{rf}}^{(2)} = \Phi_0 \tag{5.108}$$

- *electrically asymmetric discharge,* $\epsilon = 1$

  In this consideration, we have so far always assumed symmetric RF signals, such as a simple sine, etc. However, there is the possibility to assume any signal shapes. If, for example, a cosine is superimposed with higher harmonics, it turns out that the addition of even and odd harmonics results in different maxima of the voltages $V_{\mathrm{rf}}^{(1)}$ and $V_{\mathrm{rf}}^{(2)}$. Thus, the two maxima no longer cancel each other out, and we get:

$$V_{\mathrm{SB}} = -\frac{1}{2}\left(V_{\mathrm{rf}}^{(1)} + V_{\mathrm{rf}}^{(2)}\right) \neq 0 \tag{5.109}$$

  The possible superpositions are shown schematically in Fig. 5.30 and from the experiment in Fig. 5.31. In addition, it is also possible to change the phase between the individual harmonics. This changes the symmetry of these signals from a symmetric to an asymmetric shape, and the self-bias can thus be adjusted via the phase position.

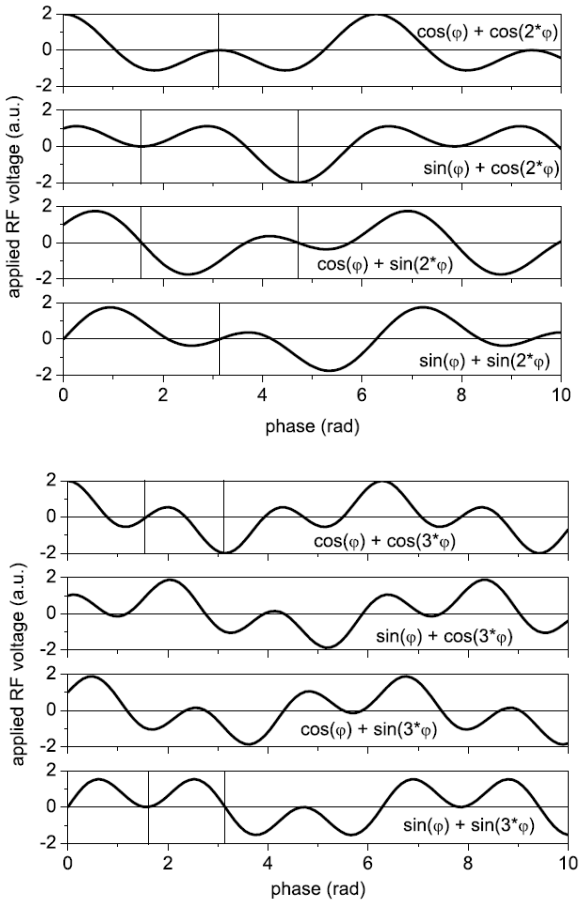

Figure 5.31: Voltage curves when superimposing two frequencies [24].

5.3 Inductively Coupled RF Discharges

5.3.1 Plasma Sources

In inductive discharges, an alternating magnetic field is generated via a coil in which an RF current j_{Spule} flows. This alternating field penetrates through a dielectric into a plasma and induces an electric field there. This electric field drives a current j_{Plasma} in the plasma. An inductive plasma is created (ICP: inductively coupled plasma). The plasma represents a single secondary winding of a transformer and is therefore also referred to as TCP (transformer coupled plasma).

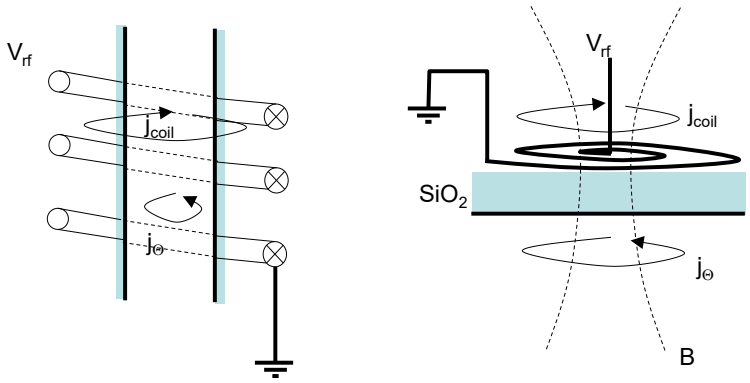

Figure 5.32: An inductive coupling is achieved in the simplest case via a coil (current j_{Spule}) around a quartz tube (left) or by a spiral on a quartz window. In any case, the plasma forms the secondary coil (current j_{Plasma}) of a transformer.

For this inductive coupling, there are cylindrical or planar configurations (see Fig. 5.32). The necessary coupling via a dielectric window is a significant limitation. To realize a plasma of a corresponding size, very large windows are necessary, which must be very thick for stability reasons. The resulting larger distance between coil and plasma reduces the magnetic field in the plasma at the same coil current and thus also the induced current. The window thickness could be reduced if a two-chamber system were chosen where 10 mbar prevails on the coil side and 1 Pa on the plasma side. Thus, the ignition criterion is only achieved on the plasma side, but the window can be made thinner again due to the smaller pressure difference. However,

this concept is very error-prone in practice and is therefore rarely used.
The most common applications of ICP are chemical processes in which one type of reactive particles is generated in a limited source. These then flow to the surfaces of the objects to be treated.
There are significant differences between an ICP and a CCP:

- *More efficient heating*

  The induced displacement current runs parallel to the surface of the dielectric and accelerates the electrons in this direction. This is in contrast to a capacitive discharge where the current runs in the direction towards the surface. In the capacitive case, the hot electrons can be lost in the direction towards the electrode.

  In addition, the electrons are heated twice per RF cycle and not just once as in the expansion of the sheath in a CCP.

- *Course of the HF currents*

  The RF current that the RF transmitter delivers to the system can, however, in an ICP discharge also flow directly from the coil to ground without being dissipated in the discharge. That is, with poor coupling of the plasma source, the RF transmitter delivers a large amount of power, but only a small part is absorbed in the plasma. This effect can lead to large hysteresis between coupled power and plasma density, as discussed further below.

- *Smaller sheath voltages*

  A significant advantage is also that the sheath voltages in front of the dielectric of an ICP become very small. At these small voltages, the sputtering of the dielectric window by the ions is low, and the process is not contaminated. This is particularly exploited in semiconductor etching. The sheath voltage is particularly small because the dielectric plus the sheath itself act like a capacitive voltage divider. The capacitance of the sheath increases with decreasing thickness at a high-density plasma. The voltage swing thereby becomes smaller, and thus the sheath voltage. That is, with a peak voltage of about $\simeq$ 1...2 kV, only $\simeq$ 50 V drops across the sheath. When igniting the discharge, the sheath is not yet present, and the voltage drop is almost 2 kV. This high voltage thus leads to a capacitive ignition of a plasma, which then transitions to the inductive mode with increasing electron density.

  When starting the discharge, the sheath voltages are initially still large, which can lead to erosion of the surfaces. For this reason, one tries to

block this part with so-called Faraday shields, as illustrated in Fig. 5.33. Between the supply and grounding of the coil, we have an electric field corresponding to the voltage swing. This is short-circuited by thin wires along the surfaces and can thus no longer penetrate into the plasma. The capacitive coupling is thus suppressed. However, these wires must be oriented in such a way that they do not simultaneously shield the induced current. That is, in the direction of the coil current, the wires must be interrupted. This results in a star in the case of a planar ICP electrode. A disadvantage of these Faraday shields, however, is the fact that at the same time the ignition of the plasma is made more difficult. In technical applications, these Faraday shields are therefore not actively grounded in microelectronics but left floating, so that the suppression of the capacitive coupling is not complete and the ignition of the plasmas becomes somewhat easier again.

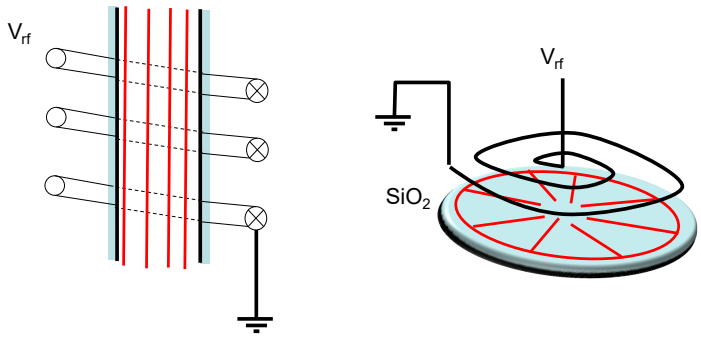

Figure 5.33: With a Faraday shield, the capacitive coupling in an ICP can be completely suppressed.

In processes in which metallic coatings are to be produced, the use of a dielectric window is not possible, as these will be coated and thus short-circuit both the capacitive component and the induced current. For this reason, internally located coils are used in these cases, which are located directly in the plasma. An application field is IPVD processes (IPVD ionized physical vapor deposition) in which a coil is added to a magnetron discharge to additionally ionize the charge carriers. This additional degree of ionization is necessary to ionize as many of the metal particles as possible, as in these processes deep holes on a processed chip are to be filled, which is only possible with a directed particle flow of the charged Cu^+ ions in the sheath.

5.3.2 Plasma Heating

5.3.2.1 E- and H-Mode

The absorbed power in the plasma depends on the efficiency of the transformer and the volume in which the plasma current flows. To consider this, we use a simple approach of ohmic heating by a current density j_{Plasma}, in a plasma of the charge carrier density n_{e} in a volume V:

$$P = \frac{1}{2} j_{\mathrm{Plasma}}^2 \frac{m\nu_{\mathrm{m}}}{n_{\mathrm{e}} e^2} V \tag{5.110}$$

In ICP, charge carrier densities in the range of 10^{12} cm^{-3} are generally generated. At these electron densities, the penetration depth of the electromagnetic wave can become smaller than the vessel dimensions.

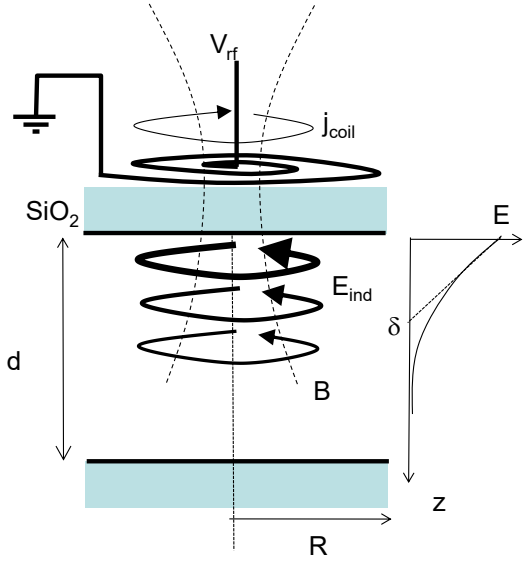

Figure 5.34: The electric field penetrates only within the skin depth into the plasma.

The refractive index $\tilde{n}$ of a plasma is given as:

$$\tilde{n}^2 = 1 - \frac{\omega_{\mathrm{p}}^2}{\omega^2} \frac{1}{1 - i\frac{\nu_{\mathrm{m}}}{\omega}} \tag{5.111}$$

The frequency at which these plasmas are operated (13.56 MHz) is usually smaller than the plasma frequency, so the wave is attenuated. The penetration depth, or skin depth $\boldsymbol{\delta}$, is defined as the decay of the amplitude of the wave to 1/e according to:

$$\exp(-\alpha x) \qquad \text{with} \qquad \alpha = \frac{1}{\delta} \tag{5.112}$$

In typical inductively coupled plasmas, $\omega < \omega_\mathrm{p}$ often applies. Thus, we get, depending on the ratio between collision frequency ν_m and RF frequency ω, the following estimates for the normal skin effect:

$$\nu_\mathrm{m} \ll \omega \qquad \delta = \frac{c}{\omega_\mathrm{p}} = \left(\frac{\epsilon_0 m c^2}{n_\mathrm{e} e^2}\right)^{1/2} \tag{5.113}$$

and the anomalous skin effect in which the penetration depth is frequency-dependent (cf. RF conductivity in metals):

$$\nu_\mathrm{m} \gg \omega \qquad \delta = \left(\frac{2\epsilon_0 c^2}{\omega \sigma_\mathrm{dc}}\right)^{1/2} \tag{5.114}$$

In both cases, however, the skin depth scales as $\delta \propto n_\mathrm{e}^{-1/2}$.
Next, we want to combine the individual possible contributions to heating in an ICP into an overall picture. The absorbed power is generally:

$$P_\mathrm{abs} = \frac{1}{2} j_\mathrm{plasma}^2 \frac{m\nu_\mathrm{m}}{n_\mathrm{e} e^2} V \tag{5.115}$$

The volume in which heating occurs can be either the entire reactor of height d, $V = R^2\pi d$ or only the volume into which the em-wave can penetrate, $V = R^2\pi\delta$ (see Fig. 5.34).

- *small power, capacitive coupling*

  At low power, the inductive coupling is not yet effective, and the power is absorbed via the capacitive effect. The entire RF current I_rf now flows directly through the discharge. The volume V through which the current flows is the entire plasma. Thus, we get:

$$P_\mathrm{abs} \propto \frac{1}{n_\mathrm{e}} I_\mathrm{rf}^2 \tag{5.116}$$

- *medium power, inductive coupling, $\delta > d$*

  At medium power, the inductive coupling becomes effective, but the charge carrier density is not yet so high that the field is completely

shielded. The RF current I_{rf} flowing through the coil is therefore not completely induced into the plasma. That is, only a part proportional to the charge carrier density and the coil current contributes to the current density in the plasma ($j \propto n_{\mathrm{e}} I_{\mathrm{rf}}$). Substituting this, we get:

$$P_{\mathrm{abs}} \propto \frac{1}{n_{\mathrm{e}}} \left(n_{\mathrm{e}} I_{\mathrm{rf}}\right)^2 = n_{\mathrm{e}} I_{\mathrm{rf}}^2 \tag{5.117}$$

- *high power, inductive coupling, $\delta < d$*

  At high power, the inductive coupling becomes effective, and the charge carrier density is so high that the field is completely shielded within the skin depth. The RF current I_{rf} flowing through the coil is completely induced into the plasma, but is absorbed only in a limited volume corresponding to the skin depth ($R^2\pi\delta$). The current density thereby becomes larger, since the entire RF current flows through a smaller area ($R\delta$). Substituting this and considering the dependence of the conductivity on the charge carrier density, we get:

$$P_{\mathrm{abs}} \propto \frac{1}{n_{\mathrm{e}}} \left(\frac{I_{\mathrm{rf}}}{R\delta}\right)^2 R^2\pi\delta = n_{\mathrm{e}}^{-1/2} I_{\mathrm{rf}}^2 \tag{5.118}$$

  Now the absorbed power decreases with increasing electron density, since the volume in which the coupled power can be absorbed becomes smaller and smaller.

In summary, the absorbed power can be expressed in the empirical form

$$P_{\mathrm{abs}} = \frac{1}{2} I_{\mathrm{rf}}^2 R_{\mathrm{abs}} \left(\frac{n_{\mathrm{ind}} n_{\mathrm{e}}}{n_{\mathrm{ind}}^2 + n_{\mathrm{e}}^2} + \frac{n_{\mathrm{kap}}}{n_{\mathrm{kap}} + n_{\mathrm{e}}}\right) \tag{5.119}$$

The resistance R_{abs} is set so that the absolute values of the power match the experiment, and the quantities n_{ind} and n_{kap} are adjusted so that the maxima and minima of the power are correctly reproduced (see Fig. 5.35).
This absorbed power is in equilibrium with the loss power through ionization and surface fluxes in the plasma according to:

$$P_{\mathrm{Verlust}} = k n_{\mathrm{e}} n_{\mathrm{g}} \left(E_{\mathrm{Ionisation}} + E_{\mathrm{sheath}}\right) \tag{5.120}$$

The operating point of a discharge then corresponds to the intersection of the two dependencies of P_{abs} and P_{Verlust} on the charge carrier density n_{e}, as illustrated in Fig. 5.35. With increasing current I_{rf}, the curve P_{abs} rises. At small values of I_{rf}, only one intersection point is created at small electron

densities, and the discharge burns in the capacitive mode. At high values, the intersection point moves directly to a high value for the charge carrier density and the discharge jumps into the inductive mode. This jump from the capacitive mode (E-mode) to the inductive mode (H-mode) leads to an increase in the charge carrier densities by two orders of magnitude and a correspondingly much more intense emission.

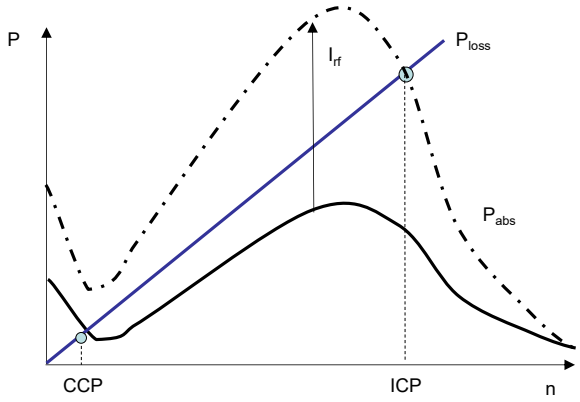

Figure 5.35: An ICP can be operated in a capacitive and inductive mode.

5.3.2.2 Stochastic Heating in ICP

The heating in an inductive discharge has so far been described very generally as ohmic heating. Even in the inductive discharge, there is stochastic heating, since the electrons move in the spatially and temporally changing decreasing field within the skin depth. This problem is much easier to treat than in the capacitive discharge, since there an electron falls from a field-free region onto a region with high field strength and is instantaneously reflected there. That is, all integrations over phases and velocities lead to large uncertainties due to the abrupt increase of the electric field to describe the problem in capacitive plasmas. In the stochastic heating in the inductive discharge, the electric field changes only slowly within the skin depth, so that no such large uncertainties arise from the integration.
First, the increase in velocity in a time-varying electric field over a time span $\tau = t_2 - t_1$ is given as:

$$\Delta v = \frac{q}{m} \int_{t_1}^{t_2} E \mathrm{d}t \tag{5.121}$$

This field decreases within the skin depth and oscillates with a frequency ω and a phase ϕ_0.

$$\Delta v = \frac{q}{m} \int_{t_1} t_2 E_0 e^{-\frac{z}{\delta}} \sin(\omega t + \phi_0) \mathrm{d}t \tag{5.122}$$

An electron is now reflected at a location z if it hits the oscillating electric field with a velocity v_z. This reflection at the time $t = 0$ can be expressed by a case distinction according to $t < 0 \rightarrow z = -v_\mathrm{z} t$ and $t > 0 \rightarrow z = v_\mathrm{z} t$. Thus, the difference in velocity becomes:

$$\Delta v = \frac{q}{m} \int_0^\infty E_0 e^{-\frac{v_\mathrm{z} t}{\delta}} \sin(\omega t + \phi_0) \mathrm{d}t + \frac{q}{m} \int_{-\infty}^0 E_0 e^{\frac{v_\mathrm{z} t}{\delta}} \sin(\omega t + \phi_0) \mathrm{d}t \tag{5.123}$$

This integration yields:

$$\Delta v = \frac{q}{m} E_0 \frac{2\tau \sin \phi_0}{1 + (\tau\omega)^2} \tag{5.124}$$

With τ the interaction time within the sheath $\tau = \delta / v_\mathrm{z}$. The energy gain is:

$$\Delta E = \frac{1}{2} m \left((v_\mathrm{z} + \Delta v)^2 - v_\mathrm{z}^2 \right) \tag{5.125}$$

Including the averaging over all phases $\langle \sin^2 \Phi_0 \rangle = 1/2$ we finally get:

$$\Delta E = \frac{q^2}{m} E_0^2 \frac{\tau^2}{\left(1 + (\tau\omega)^2\right)^2} \tag{5.126}$$

This is the energy gain for an electron that penetrates into the region of the skin depth with the velocity v_z. The total power is obtained by integrating over the energy transfer (ΔE) times the impact rate ($\propto v_\mathrm{z}$) weighted with the distribution function f_0 according to:

$$P_\mathrm{stoch} = \int_0^\infty \Delta E v_\mathrm{z} f_0 \mathrm{d}v_\mathrm{z} \tag{5.127}$$

With the assumption of f_0 as a Maxwell distribution, we get:

$$P_\mathrm{stoch} = \frac{q^2 E_0^2}{4m} \delta \frac{4\delta}{\bar{v}_\mathrm{e}} n_\mathrm{e} I(\alpha) \tag{5.128}$$

with $\alpha = \frac{4\delta 2\omega 2}{n_\mathrm{e} \bar{v}_\mathrm{e}}$ and

$$I(\alpha) = \frac{1}{\pi} \int_0^\infty \frac{x e^{-x}}{(x + \alpha)^2} \mathrm{d}x \tag{5.129}$$

In the case of inductive coupling, the skin depth $\delta \propto n_e^{-1/2}$. That is, the only dependence of the stochastic heating 5.128 on n_e is in this case in the expression $I(\alpha)$. This increases according to Fig. 5.36 with increasing electron density. In addition, the efficiency of this stochastic heating is shown, which is expressed as an effective collision frequency ν_{stoch}. For this purpose, the ohmic heating

$$P = \frac{1}{2}E^2\frac{n_e e^2}{m\nu_m} = \frac{1}{2}\int_0^\infty \left(Ee^{-z/\delta}\right)^2 \frac{n_e e^2}{m}\frac{\nu_m}{\nu_m^2+\omega^2}\mathrm{d}z \tag{5.130}$$

is replaced by an analogous expression with an effective frequency ν_{stoch}

$$P = \frac{1}{2}\int_0^\infty \left(Ee^{-z/\delta}\right)^2 \frac{n_e e^2}{m}\frac{\nu_{stoch}}{\nu_{stoch}^2+\omega^2}\mathrm{d}z = \frac{1}{4}\frac{n_e e^2\delta}{m}\frac{\nu_{stoch}}{\nu_{stoch}^2+\omega^2}E_0^2 \tag{5.131}$$

This can now be compared with Eq. 5.128 and ν_{stoch} can be quantified. This effective collision rate is normalized to $1/\tau = \frac{v_e}{\delta}$, the inverse residence time of the electrons in the layer with the thickness of the skin depth. This results in a measure of the efficiency of the stochastic heating according to $\nu_{stoc}/(v_e/\delta)$, as shown in Fig. 5.36. One can see that at medium densities the efficiency becomes large. At very high densities, the skin depth becomes small again, and the volume in which heating can take place becomes correspondingly smaller.

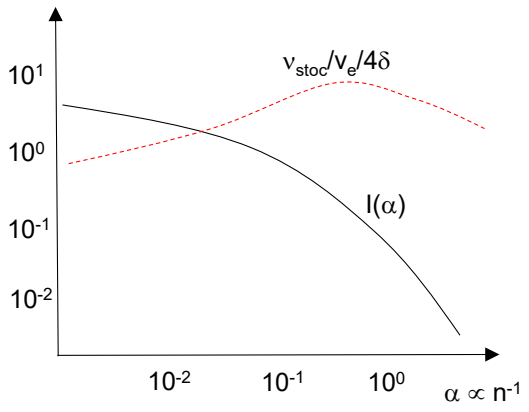

Figure 5.36: Integral $I(\alpha)$ according to Eq. 5.129 and efficiency of the stochastic heating expressed as effective collision frequency ν_{stoch} normalized to the frequency at which the electrons are in the skin depth.

5.3.3 EH Hysteresis and Instabilities in ICP Plasmas

When considering the heating of ICP, the transition from the E-mode, the capacitive coupling, to the H-mode, the inductive coupling, was already considered at the beginning. This transition is caused by the intersection points of the dependence of P_{Verlust} and P_{abs} on the charge carrier density. In the experiment, one often observes not only an instantaneous jump between the modes but even a pronounced hysteresis. In this hysteresis, the jump from the E-mode to the H-mode occurs at a higher RF current I_{rf} during the power increase compared to the jump from the H-mode to the E-mode during the power decrease. In addition, spontaneous oscillations between these two modes are also observed in some systems in the kHz range.
Such a hysteresis or oscillation can only occur if three intersection points are formed between P_{Verlust} and P_{abs}, as illustrated in Fig. 5.37. For this purpose, either the loss power or the absorbed power must become non-linear in the range of medium electron densities (if P_{Verlust} and P_{abs} are linear in n_{e}, a direct transition between the E- and H-mode occurs without hysteresis).

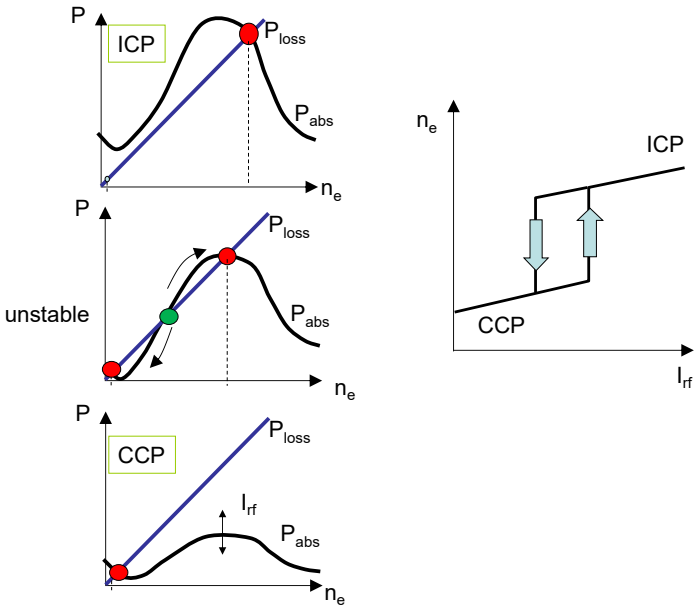

Figure 5.37: Hysteresis of an ICP discharge with a non-linear characteristic for the absorbed power.

This hysteresis is explained as follows. With a non-linear curve for P_{abs},

three intersection points can be created, of which the middle one is unstable. That is, a deviation to larger or smaller electron densities is amplified and the plasma either runs into the E- or H-mode. In the pure CCP mode, only one intersection point is obtained at small electron densities; with increasing I_{rf}, three intersection points are created. The discharge, however, remains in the E-mode; only when the lowest intersection point disappears with further increase of I_{rf}, the discharge jumps to the H-mode; if the current I_{rf} is now reduced again, the discharge remains in the H-mode, characterized by the operating point at the uppermost intersection point of P_{abs} and P_{Verlust}; only when this intersection point disappears with further reduction of I_{rf} one returns to the E-mode. That is, a pronounced hysteresis becomes visible (see Fig. 5.37).

5.3.3.1 Nonlinearity of the Absorbed Power

First, we consider the nonlinearity of the characteristics for P_{abs} as the cause of the hysteresis. Taking into account the capacitive coupling according to Eq. 5.119, the characteristic becomes slightly nonlinear and a small hysteresis becomes visible. This is often, however, hardly measurable.
A much larger effect is created by the coupling of the plasma with the RF transmitter via a matchbox. To consider this, we look at an equivalent circuit diagram of the arrangement, as shown in Fig. 5.38. One immediately recognizes two resonant circuits, which consist, on the one hand, of the matchbox and the coil, and, on the other hand, of the plasma itself, with a large inductive component. If the discharge is initially tuned for the operation of the inductive plasma, the power is optimally coupled into the second resonant circuit, since its resonance frequency matches the operating mode of the excitation. If, however, a small power is used with this setting so that the inductive mode does not start, power is coupled alone into the first resonant circuit. If the power is now increased, power is indeed absorbed in this first resonant circuit, but the plasma does not become more intense, since the coupling is poor. Only at a high power does the inductive coupling start; then the tuning is good, and the power is now optimally absorbed in the second resonant circuit. When reducing the power, the coupling remains good for a long time, and only at very low powers does one return to the initial state. That is, a hysteresis arises from the competition of the two resonant circuits. This effect can only be switched off by explicitly not using an adapted matchbox and strongly reducing the quality of the first resonant circuit. In this setting, the hysteresis suddenly disappears.

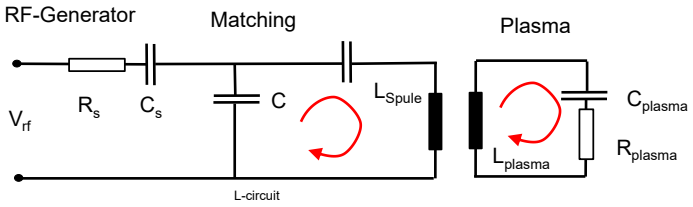

Figure 5.38: Equivalent circuit diagram of a drive of an ICP discharge.

5.3.3.2 Nonlinearity of the Loss Power

In addition to the nonlinearity in the characteristic of the absorbed power, there are also several non-linearities in the characteristics of the loss power.

- *Metastables*

  When metastables are formed in the discharge, a population of particles is created that has a lower ionization energy. That is, in the equation of the loss power, the average energy lost during an ionization decreases from a certain charge carrier density, and the curve bends down. This is shown in Fig. 5.39. This nonlinearity causes a hysteresis as motivated at the beginning.

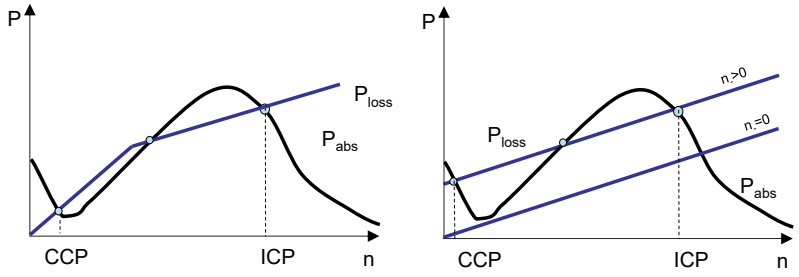

Figure 5.39: Formation of a hysteresis for a plasma with a significant population of metastables (left) or negative ions (right).

- *Negative Ions*

  When negative ions are formed, the characteristic P_{loss} is shifted upwards, since the following applies:

$$P_{\text{loss}} = k n_{\text{e}} n_{\text{g}} E_{\text{ionisation}} + v_{\text{B}} n_{+} E_{\text{sheath}} \tag{5.132}$$

For the case of a strongly electronegative plasma ($n_{\text{e}} \ll n_{-}$) $n_{+} = n_{-}$ applies and we get:

$$P_{\text{loss}} = k n_{\text{e}} n_{\text{g}} E_{\text{ionisation}} + v_{\text{B}} n_{-} E_{\text{sheath}} \tag{5.133}$$

That is, the characteristic shifts upwards. This again leads to three intersection points and thus to a hysteresis. In addition, a self-sustained oscillation is created at certain operating parameters. To consider this, we first look at a plasma in the ICP mode with a high electron density but low negative ion density. At the high electron density, negative ions are formed, and the loss curve slowly shifts upwards until the upper intersection point disappears. The discharge falls back into the capacitive mode, the electron density decreases, and thus also the density of negative ions and the loss curve decreases again. This happens until the lower intersection point disappears and the cycle can begin anew. The circulation frequency of this oscillation is typically a few kHz. A measurement in an electronegative SF_6-plasma is shown in Fig. 5.40.

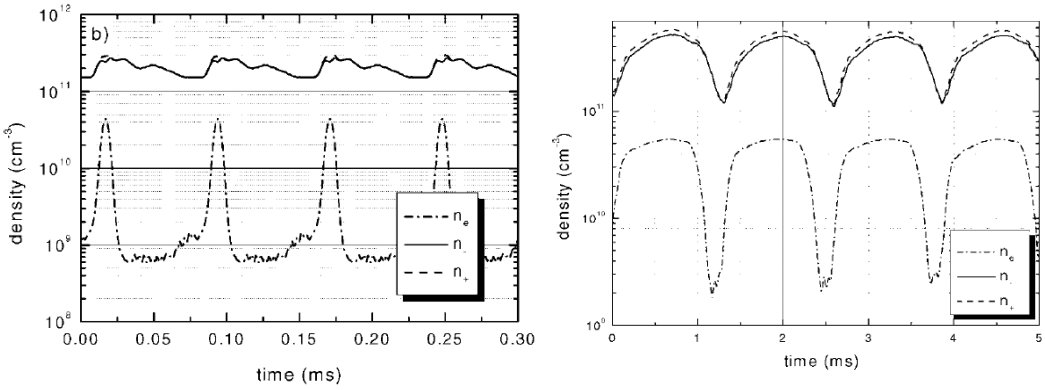

Figure 5.40: Oscillations of the charge carrier densities in electronegative SF_6-plasmas: Pure SF_6-plasma at 5 mTorr and 530 W (left); Ar/SF_6 (1:1) mixture at 5 mTorr and 550 W (right) [11].

5.4 Microwave Plasmas

5.4.1 Generation of Microwave Radiation

The generation of plasmas using microwaves (range GHz to several hundred GHz) has only been developed in the last few decades. It was not until the invention of radar that powerful sources of microwave radiation became available.

The most common sources of microwaves are **magnetrons** and **klystrons**. In both cases, an electron beam is initially generated, which, in a geometrically defined structure, produces an oscillation of an electric field in the microwave range.

In a **magnetron** (see Fig. 5.41), a central cathode is heated and emits electrons. These electrons leave the cathode and are deflected by a magnetic field. A ring current is formed around this cathode, which is enclosed by an anode. Small openings are made in this anode, in which (similar to an organ pipe) the electric field is excited to oscillations. Energy is transferred from the electron motion to the field oscillations, and the electrons group into packets. These oscillating fields are conducted away via waveguides and then form a microwave beam. Magnetrons are very simple and compact in design and are used in a variety of applications. Their frequency is not entirely precise, as the frequencies can shift slightly due to deviations in geometry and temperature fluctuations.

Alternatively, microwave radiation can also be generated with a **klystron** (see Fig. 5.41). Here, an electron beam is directly coupled into a resonance chamber and transfers its energy there again to oscillations of the electric field. This again leads to a grouping of the electrons (bunching), and the energy in the oscillating electric field is conducted away as microwave radiation.

However, the transmission of microwave radiation is quite complex. Initially, the attenuation of microwave radiation by matter is significant, so that transmission is usually carried out through waveguides. This is much more complex than simple cabling in the case of CCP or ICP.

A typical setup for supplying a plasma with microwaves is shown in Fig. 5.42: initially, the microwave transmitter must be protected from reflected power, which is achieved by a **circulator** that dissipates returning waves in a dump. Finally, a part of the wave energy is diverted via **directional couplers** to measure the intensities of the forward and reflected waves. A **stub tuner** ensures the matching/tuning between the microwave transmitter and the plasma. In a stub tuner, metallic pins are inserted into the microwave waveguide and short-circuit the field there. That is, a defined boundary

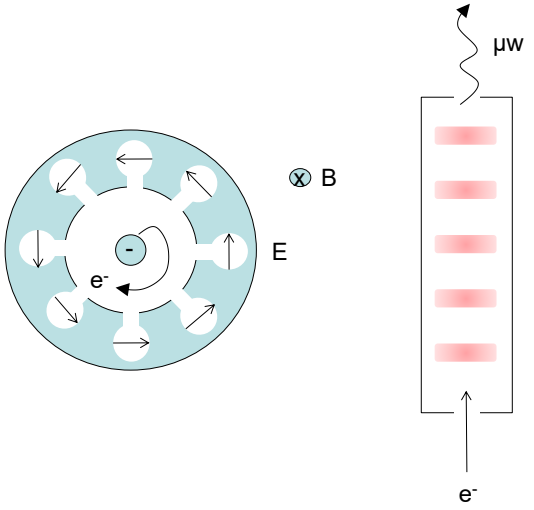

Figure 5.41: Magnetron, Klystron.

condition for the phase of the oscillating E-fields is locally created, which thus tunes the region between the stub tuner and the microwave transmitter on the one hand and between the stub tuner and the plasma chamber on the other hand. Under certain circumstances, a **mode converter** may also be found in the waveguide if transverse modes need to be converted into circular modes (example ECR plasmas, see below). Finally, the microwave is coupled into the low-pressure region of the plasma via a window. These windows should absorb as little microwave radiation as possible and are extremely stressed by direct plasma contact.
The penetration of microwave radiation into a plasma can be most easily derived from the refractive index of a plasma.

$$\tilde{n}^2 = 1 - \frac{\omega_p^2}{\omega^2} \frac{1}{1 + \imath \frac{\nu_m}{\omega}} \tag{5.134}$$

For the case $\nu_m \gg \omega$ we get:

$$\tilde{n}^2 = 1 + \imath \frac{\omega_p^2}{\omega \nu_m} \tag{5.135}$$

That is, the electric field decays with a decay constant α into the plasma:

$$E = E_0 e^{-\alpha z} \tag{5.136}$$

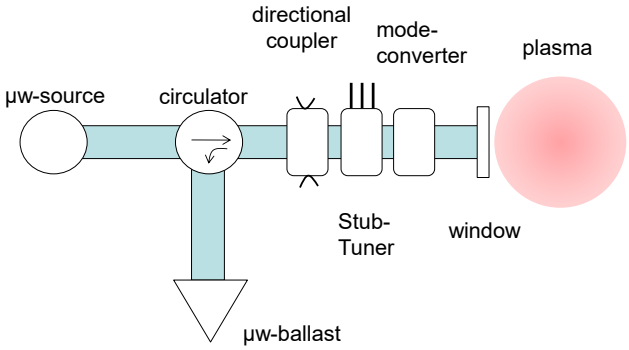

Figure 5.42: Elements of a microwave plasma.

The penetration depth δ is $\alpha = 1/\delta$. From the solution of the Maxwell equations for the propagation of the waves into the plasma, we can derive α for a planar arrangement as:

$$\alpha = \frac{\omega_p}{c}\sqrt{\frac{\omega}{\nu_m}} \tag{5.137}$$

This corresponds to typical penetration depths of centimeters at a microwave frequency in the GHz range.

5.4.2 Microwave Reactors

The wavelength of the coupled microwaves is typically 12 cm for 2.45 GHz. That is, this radiation is absorbed in a small volume in the plasma reactor. Without special measures, these microwave plasmas always burn in front of the coupling window.
There are now several concepts to overcome this strong localization of microwave plasmas, as illustrated in Fig. 5.43: (top left) in the simplest case, the radiation is absorbed behind the window, resulting in a small plasma ball; (top right) if the chamber itself is designed to be resonant for the coupled radiation, a field distribution can form in the plasma chamber that leads to a larger, more homogeneous plasma; (bottom left) via a mirror construction, the power of a microwave source is distributed over the surface of a microwave-transparent plasma vessel. This results in very homogeneous plasmas without heavily stressing the microwave source itself; (bottom right) A dual-chamber system is formed in which the microwave radiation is dis-

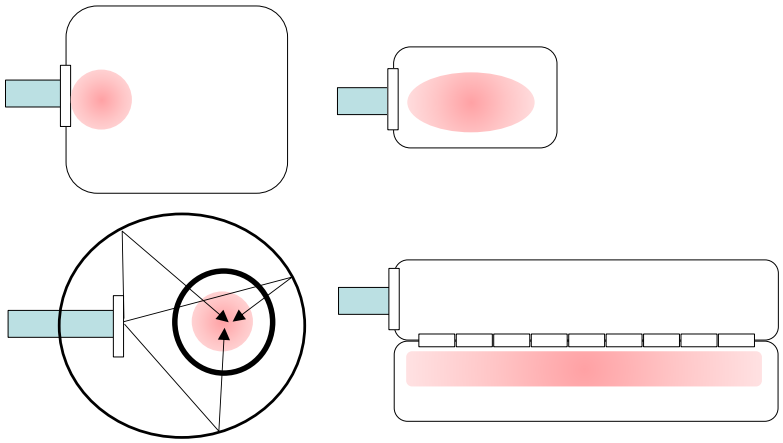

Figure 5.43: Microwave plasma reactors: (top left) formation of a plasma directly in front of the coupling window; (top right) in a resonant reactor, a standing wave and thus a large plasma can form; (bottom left) via a mirror arrangement, the microwave radiation can be guided to a transparent reactor at normal pressure; (bottom right) in a dual-chamber system, the microwave radiation is homogeneously distributed over a series of coupling windows.

tributed at normal pressure in one chamber and then coupled into the plasma chamber via a series of windows. The homogeneity of the plasma then depends on the homogeneity of the distribution of the microwaves in the first chamber.

Figure 5.44: Running discharge: in an evacuated waveguide, ignition is favored away from the coupling window. After the formation of the plasma, it runs through the cut-off to the coupling window.

Finally, there is an exotic concept, the **running discharge** (see Fig. 5.44). Consider a waveguide through which pulsed microwave power is passed. This waveguide is evacuated and at one end is the coupling window. At the other

end, the plasma is initially ignited, as the power is set such that only a local field enhancement at a tip or an efficient ignition condition through an additional magnetic field allows the formation of the plasma. After ignition of this plasma, the absorption of the microwaves causes the microwave power to be strongly absorbed on the side of the plasma facing the coupling window. A point is reached where the cut-off of the microwave radiation prevents further penetration, and the plasma can burn at that location without the presence of the additional "ignition device". This situation is unstable, and the plasma runs towards the coupling window, as the point at which the cut-off occurs continuously shifts in this direction. We get a running discharge that only comes to a stop when the plasma has reached the coupling window. Then, depending on the setting, the end of the power pulse is reached, and the plasma in front of the coupling window extinguishes. Only with the next power pulse does the cycle begin anew.

5.4.3 Surface Wave Plasmas

5.4.3.1 Wave Propagation

Tuning a microwave plasma to large volumes and large areas is difficult. With the concept of surface wave plasmas [54], however, one can exploit the special nature of wave propagation to generate a large-area homogeneous plasma.

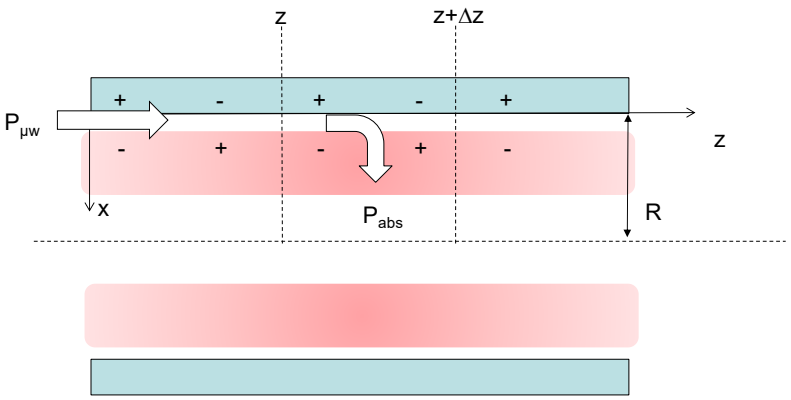

Figure 5.45: Surface wave plasma.

In a surface wave plasma, microwave radiation is coupled into a gas-filled quartz tube via a resonator. A plasma is formed not only inside the quartz

tube in the resonator, but it also spreads along the quartz tube. An elongated plasma is formed (see Fig. 5.47). The propagation of the plasma is carried by waves that propagate at the interface between the quartz tube and the plasma. Since these waves run on the surface, the cut-off cannot limit the size of the plasma along the tube.
In the oscillations of this wave, the charge in the plasma is compensated by a corresponding polarization charge in the dielectric (see Fig. 5.45). At the interface between the quartz tube and the plasma, the wave equation must be satisfied:

$$\nabla^2 \vec{E} + \frac{n^2}{c^2} \ddot{\vec{E}} = 0 \tag{5.138}$$

with the approach:

$$E = E_0 e^{\imath\omega t} e^{\alpha x - \imath k_z z} \tag{5.139}$$

Solutions must be found both in the dielectric (index d) and in the plasma (index p) according to a refractive index n_d and n_p, respectively. In the Fourier space, the wave equation becomes:

$$\alpha_\mathrm{p}^2 - k_\mathrm{z}^2 + \frac{\omega^2}{c^2} n_\mathrm{p}^2 = 0 \tag{5.140}$$

$$\alpha_\mathrm{d}^2 - k_\mathrm{z}^2 + \frac{\omega^2}{c^2} n_\mathrm{d}^2 = 0 \tag{5.141}$$

Since the amount of charge in the dielectric is proportional to $\epsilon_\mathrm{d} = n_\mathrm{d}^2$ and the amount of charge in the plasma is proportional to the decay constant α_p, the following must hold:

$$\frac{\alpha_\mathrm{p}}{\epsilon_\mathrm{p}} = -\frac{\alpha_\mathrm{d}}{\epsilon_\mathrm{d}} \tag{5.142}$$

or

$$\frac{\alpha_\mathrm{p}}{n_\mathrm{p}^2} = -\frac{\alpha_\mathrm{d}}{n_\mathrm{d}^2} \tag{5.143}$$

The reversal of the sign expresses that the opposite polarity is present in the plasma and in the dielectric, respectively (see Fig. 5.47). First, we transform Eqs. 5.140 and 5.141

$$\frac{\alpha_\mathrm{p}^2}{n_\mathrm{p}^4} - \frac{k_\mathrm{z} 2}{n_\mathrm{p} \text{`} 4} + \frac{\omega^2}{c^2} \frac{1}{n_\mathrm{p}^2} = 0 \tag{5.144}$$

$$\frac{\alpha_\mathrm{d}^2}{n_\mathrm{d}^4} - \frac{k_\mathrm{z}^2}{n_\mathrm{d}^4} + \frac{\omega^2}{c^2} \frac{1}{n_\mathrm{d}^2} = 0 \tag{5.145}$$

subtract them from each other:

$$\frac{k_z^2}{n_p^4} - \frac{\omega^2}{c^2}\frac{1}{n_p^2} = \frac{k_z^2}{n_d^4} - \frac{\omega^2}{c^2}\frac{1}{n_d^2} \tag{5.146}$$

This can be solved for k_z, and we get a wavenumber for the propagation along the plasma column of:

$$\boxed{k_z = n_d \frac{\omega}{c}\left[\frac{\omega_p^2 - \omega^2}{\omega_p^2 - (1+n_d^2)\omega^2}\right] 1/2} \tag{5.147}$$

with $n_p^2 = 1 - \frac{\omega_p^2}{\omega^2}$. The wavenumber becomes infinite in the case of resonance. This is achieved at:

$$\boxed{\omega_{\text{resonance}} = \omega_P \left(\frac{1}{1+n_d^2}\right) 1/2} \tag{5.148}$$

That is, the resonance frequency now depends on the dielectric constant of the dielectric. With increasing refractive index, the frequency decreases. This is intuitively understandable, as during the propagation of the waves not only the electrons in the plasma oscillate, but also the charges in the dielectric must be moved. That is, the inertia of the oscillation increases, which leads to a lowering of the resonance frequency.

5.4.3.2 Plasma Equilibrium

In the following, we want to consider the absorption of power in a surface wave plasma. Initially, a part of the microwave power that runs along the surface wave plasma is absorbed in the plasma. If the field strength varies according to

$$E = E_0 e^{-\beta z} \tag{5.149}$$

we obtain a change in power

$$P_{\mu w} = P_{\mu w}(z=0) e^{-2\beta z} \tag{5.150}$$

or

$$\frac{\mathrm{d}P_{\mu w}}{\mathrm{d}z} = -2\beta P_{\mu w} \tag{5.151}$$

Here, β is the decay length *along* the tube. This coupled power of the microwave is dissipated in the plasma. In the simplest case, this is:

$$\frac{\mathrm{d}P_{\mathrm{abs}}}{\mathrm{d}z} = n_{\mathrm{e}}(z) P_{\mathrm{e}} A \tag{5.152}$$

with P_{e} the power dissipated per electron and A the cross-sectional area of the tube (or the zone in which the incoming wave is absorbed in the plasma). In equilibrium, the power balance states $\mathrm{d}P_{\mathrm{abs}} = -\mathrm{d}P_{\mu\mathrm{w}}$. That is, we can set:

$$2\beta P_{\mu\mathrm{w}} = n_{\mathrm{e}}(z) P_{\mathrm{e}} A \tag{5.153}$$

To obtain a dependence on the electron density profile along the surface wave plasma, we differentiate this equation with respect to the location z, and obtain:

$$2\frac{\mathrm{d}\beta}{\mathrm{d}z} P_{\mu\mathrm{w}} + 2\beta \underbrace{\frac{\mathrm{d}P_{\mu\mathrm{w}}}{\mathrm{d}z}}_{-2\beta P_{\mu\mathrm{w}}} = A\frac{\mathrm{d}n_{\mathrm{e}}(z)}{\mathrm{d}z} P_{\mathrm{e}} + A n_{\mathrm{e}}(z)\frac{\mathrm{d}P_{\mathrm{e}}}{\mathrm{d}z} \tag{5.154}$$

Subsequently, we replace the derivatives with respect to z by derivatives with respect to n_{e} according to:

$$\frac{\mathrm{d}P_{\mathrm{e}}}{\mathrm{d}z} = \frac{\mathrm{d}P_{\mathrm{e}}}{\mathrm{d}n_{\mathrm{e}}}\frac{\mathrm{d}n_{\mathrm{e}}}{\mathrm{d}z} \tag{5.155}$$

etc. With this replacement, we solve for $\frac{\mathrm{d}n_{\mathrm{e}}}{\mathrm{d}z}$ and obtain:

$$\boxed{\frac{\mathrm{d}n_{\mathrm{e}}}{\mathrm{d}z} = -2\beta n_{\mathrm{e}}(z)\left[1 + \frac{n_{\mathrm{e}}}{P_{\mathrm{e}}}\frac{\mathrm{d}P_{\mathrm{e}}}{\mathrm{d}n_{\mathrm{e}}} - \frac{\mathrm{d}\beta}{\mathrm{d}n_{\mathrm{e}}}\frac{n_{\mathrm{e}}}{\beta}\right]^{-1}} \tag{5.156}$$

Assuming that the dissipated power per electron does not explicitly depend on the electron density itself ($\frac{\mathrm{d}P_{\mathrm{e}}}{\mathrm{d}n_{\mathrm{e}}} = 0$), we obtain:

$$\frac{\mathrm{d}n_{\mathrm{e}}}{\mathrm{d}z} = -2\beta n_{\mathrm{e}}(z)\left[1 - \frac{\mathrm{d}\beta}{\mathrm{d}n_{\mathrm{e}}}\frac{n_{\mathrm{e}}}{\beta}\right]^{-1} \tag{5.157}$$

The dependence of β on the electron density must now be calculated by an electromagnetic consideration of the propagation of the electric fields. For a cylindrical arrangement, an analytical approximation can be derived as:

$$\boxed{\frac{\mathrm{d}n_{\mathrm{e}}}{\mathrm{d}z} = -\frac{1}{0.2R}\nu_{\mathrm{m}} m_{\mathrm{e}} \omega \frac{\epsilon_0}{e^2}} \tag{5.158}$$

That is, the decrease in electron density is constant and does not explicitly depend on the distance z from the microwave coupling. This gradient $\frac{\mathrm{d}n_{\mathrm{e}}}{\mathrm{d}z}$ becomes stronger with the frequency or the collision rate and becomes flatter

with the radius of the cylinder. This result can be motivated. In the simplest picture, if $\beta(z) = const.$, the coupled power would decrease exponentially along the tube, as a certain fraction of the power is absorbed per path section Δz. However, the decrease in electron density leads to an increase in the penetration depth of the wave into the plasma and to a variation of β. That is, although the power decreases, a larger volume can now be heated. For a cylindrical arrangement, this results in exactly a linear decrease of $n_e(z)$, which has been found again in experiments and in model calculations, as shown in Fig. 5.46.

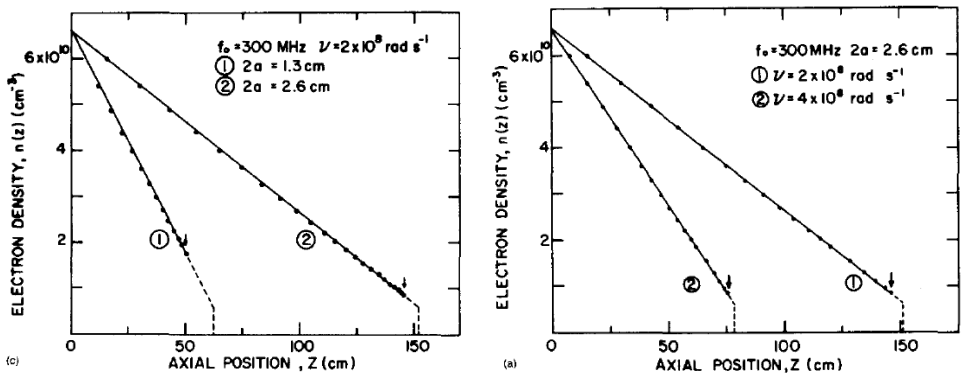

Figure 5.46: Modeling of the axial decrease of electron density in a plasma column [21].

As a technical realization of surface wave plasmas, there are initially **surfatrons**, in which a gas-filled quartz tube is passed through a microwave cavity (see Fig. 5.47). The wave propagates along the tube, and the plasma density decreases continuously.
A very elegant concept is the concept of the **plasmaline**. Here, the surfatron is inverted by initially coupling the microwave power directly into a quartz tube at atmospheric pressure. This quartz tube is passed into a vacuum vessel, and a plasma forms around the tube. The conductive plasma forms the walls of the microwave waveguide. With this concept, very extensive linear plasmas can be generated.
Furthermore, the concept of the **duo-plasmaline** can use the linear density decrease to generate a spatially homogeneous plasma by two opposing sources (see Fig. 5.47). That is, with a similar operation of both microwave transmitters at both ends of the quartz tube, a homogeneous density profile is obtained.

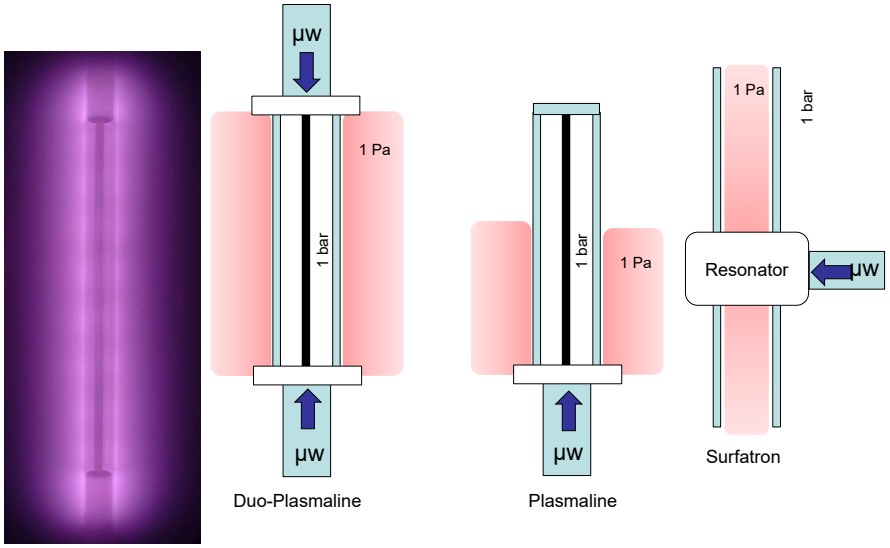

Figure 5.47: Duo-plasmaline, plasmaline, surfatron. Photo of a duo-plasmaline from IPF Stuttgart.

5.5 Magnetized Plasmas

5.5.1 General

The superposition of a plasma with a magnetic field is an additional control knob for setting the plasma density as well as the ion energy. In practice, these types of plasmas are rarely used, as the generation of magnetic fields leads to inhomogeneities in the discharge and, on the other hand, the generation of magnetic fields is generally expensive. Magnetic field strengths in the range of 100 mT are necessary for the gyration radius of the electrons to become smaller than the mean free path, in order to ensure efficient magnetization of the electrons. The cyclotron frequencies required for this are in the GHz range, i.e., the power coupling into these magnetized plasmas is usually carried out by irradiating microwaves.
The influence of the magnetic field on these plasmas can be divided into two areas - the increase in confinement as well as the increase in heating efficiency:

- *Confinement*

  In magnetized technical plasmas, often only the electrons are magnetized. Their transport perpendicular to the magnetic field lines is hindered, as for classical perpendicular diffusion the following applies:

  $$D_\perp = \frac{\pi}{8} r_c^2 \nu_m \propto \frac{\nu_m}{B^2} \tag{5.159}$$

  That is, for high magnetic fields, the perpendicular diffusion is suppressed, and only collision processes according to a collision frequency ν_m allow particle transport (see Fig. 5.48). This effect is used in several plasma types.

  In so-called **MERIE plasmas** (MERIE Magnetically enhanced reactive ion etching), a magnetic field is present parallel to a surface. This suppresses the loss of electrons. Due to the better confinement, the remaining electrons can be heated better, and higher temperatures and plasma densities are established.

  In the so-called **bucket source** [19], alternating magnets are distributed on the outside of a discharge vessel. This arrangement creates small magnetic mirrors as well as fields parallel to the surface that minimize the loss of charge carriers. Such bucket sources were used as sources for negative hydrogen ions in fusion. These sources were additionally superimposed with a magnetic filter field to separate hot

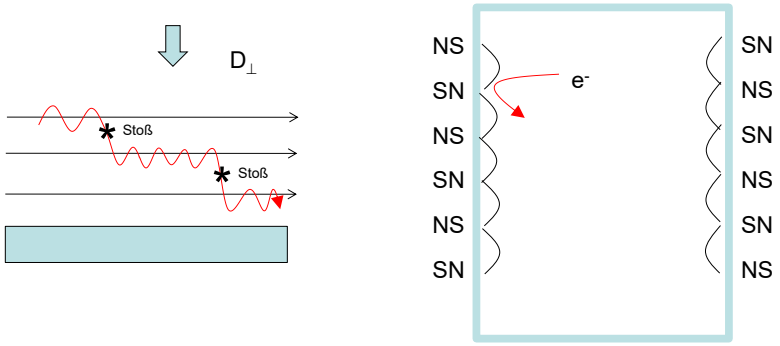

Figure 5.48: Magnetic confinement in a MERIE arrangement and in a bucket source.

electrons from cold electrons. It is precisely these cold electrons that lead to negative hydrogen ions through attachment reactions according to $e^- + H \rightarrow H^-$.

Finally, small magnets are still used in practice to make inhomogeneous plasma discharges more homogeneous. If the surface loss is large, a cosine profile is established as the density profile in the simplest case of a parallel plate arrangement, as the boundary condition $n_e = 0$ must be satisfied. Additional magnets locally improve the boundary condition at the surface, and the electron density no longer decreases as strongly towards the edge of the plasma.

- *Heating Efficiency*

  In addition to confinement, a magnetic field also increases the efficiency of heating, as resonant heating can be carried out at the cyclotron frequencies of the electrons or ions or the upper and lower hybrids. In particular, when heating at the ion cyclotron frequency or lower hybrid, the excitation frequency again falls into the MHz range, which is technically attractive.

5.5.2 Electron Cyclotron Resonance Plasmas (ECR)

5.5.2.1 Heating

A straightforward implementation of a magnetized plasma is the **Electron Cyclotron Resonance Plasma** (ECR). For this purpose, a wave is irradiated parallel to a magnetic field. At the cyclotron frequency, the right

circularly polarized wave is absorbed. In order to optimize the matching between the microwave transmitter and the plasma, a mode converter is therefore used in the feed line, which converts transverse waveguide modes into right circularly polarized light.
Usually, the magnetic field is not homogeneous, so that the absorption of power can only take place in a limited volume, the **resonance zone** with an extension Δz, as shown schematically in Fig. 5.49. In this volume, ohmic heating can now be carried out analogously to heating in high-frequency fields, where the power density can then be calculated as:

$$P = \langle j E_{\mu\mathrm{w}} \rangle \tag{5.160}$$

In addition to this ohmic heating, we also want to analyze the stochastic heating. According to this, an electron is efficiently accelerated near the resonance zone. If the resonance frequency and microwave frequency do not match exactly, the phase relationship between the circularly polarized microwave and the circular motion of the electrons shifts. If both fall out of phase, the heating effect ceases. This time span t_{res} in which they fall out of phase, together with the velocity v_{res} with which the electrons enter the resonance zone, determines the thickness Δz of the resonance zone. Based on this picture, we want to derive the stochastic heating. First, consider a spatially varying magnetic field, as shown in Fig. 5.49.
The gradient in the magnetic field can be expressed by a local variation of the cyclotron frequency:

$$\omega_{\mathrm{ce}} = \omega_{\mu\mathrm{w}}(1 + \underbrace{\frac{1}{\omega_{\mathrm{c}}}\frac{\partial \omega_{\mathrm{c}}}{\partial z}}_{\alpha} z) = \omega_{\mu\mathrm{w}}(1 + \alpha z) \tag{5.161}$$

The location z that an electron reaches, which flies through the resonance zone with the velocity v_{res} is given as $z = v_{\mathrm{res}} t$. The velocity or the gradient in the magnetic field is very large, i.e., $\alpha v_{\mathrm{res}} t \gg 1$, and we can write for the temporal development of the angle $\dot{\Theta} = \omega_{\mathrm{c}}$:

$$\dot{\Theta} = \omega_{\mu\mathrm{w}} \alpha v_{\mathrm{res}} t \qquad \text{or} \qquad \Theta = \omega_{\mu\mathrm{w}} \alpha v_{\mathrm{res}} \frac{1}{2} t^2 \tag{5.162}$$

This angle is given as $\tan\Theta = \frac{v_{\mathrm{y}}}{v_{\mathrm{x}}}$. If we assume that the time span t_{res} in which heating can take place is given by the phase separation up to 180 °, then we can derive with $\Theta = \pi = \omega_{\mu\mathrm{w}} \alpha v_{\mathrm{res}} \frac{1}{2} t_{\mathrm{res}}^2$:

$$t_{\mathrm{res}} = \left(\frac{2\pi}{\omega_{\mu\mathrm{w}} \alpha v_{\mathrm{res}}} \right)^{1/2} \tag{5.163}$$

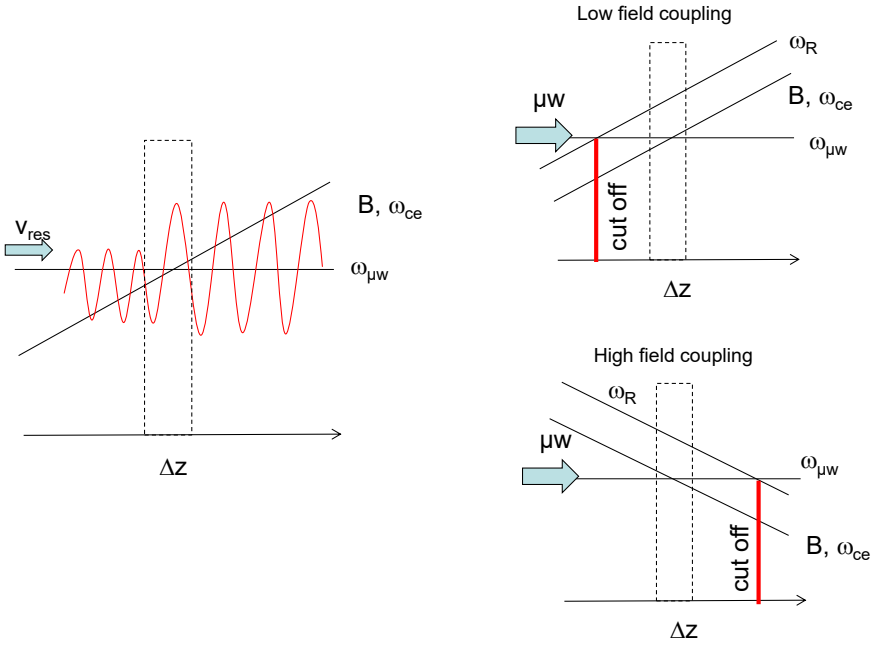

Figure 5.49: Spatial variation of the magnetic field or cyclotron resonance frequency and the microwave frequency. Different forms of microwave coupling relative to the gradient in the B-field.

From this, the thickness of the resonance zone Δz can be determined according to:

$$\Delta z = v_{\rm res} t_{\rm res} = \left(\frac{2\pi v_{\rm res}}{\omega_{\mu \rm w} \alpha} \right)^{1/2} \tag{5.164}$$

The increase in velocity during this time span is:

$$\Delta v = \frac{eE_{\rm r}}{m} \left(\frac{2\pi}{\omega_{\mu \rm w} \alpha v_{\rm res}} \right)^{1/2} \tag{5.165}$$

Thus, the energy increase per passage through the resonance zone is given as:

$$\Delta E = \frac{1}{2} m \Delta v^2 = \frac{e^2 E_{\rm r}^2}{m} \frac{\pi}{\omega_{\rm rf} \alpha v_{\rm res}} \tag{5.166}$$

The absorbed power is finally $P = n_{\rm e} v_{\rm res} \Delta E$:

$$\boxed{P = \frac{\pi n_e e^2 E^2}{m \omega_{\mu w} \alpha}} \tag{5.167}$$

It can be seen that the power becomes small if α is large, i.e., the magnetic field changes strongly locally. Furthermore, the heating is independent of v_{res}, as on the one hand the residence time in the resonance zone becomes smaller with increasing velocity, but on the other hand the number of electrons entering this resonance zone per unit time becomes larger.
This solution for stochastic heating is not quite self-consistent, as the electric field is weakened by absorption and decreases within the resonance zone.

5.5.2.2 Technical Realization of ECR Plasmas

For the technical realization of an ECR plasma, it must be noted that the coupled microwave radiation also reaches the location of the resonance zone. This is not necessarily given, as in addition to the resonance, the cut-off also occurs at the frequency ω_R. For this purpose, we consider the dispersion of the waves as shown in Fig. 5.50.

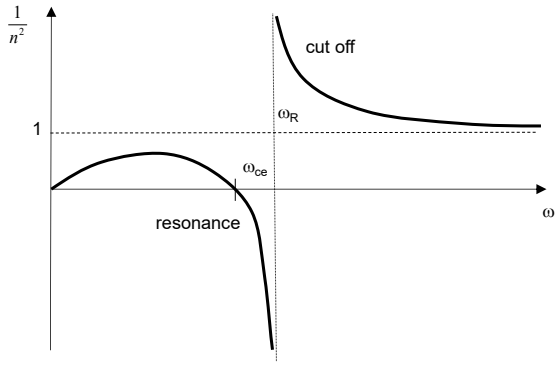

Figure 5.50: Dispersion of electron cyclotron waves.

It can be seen that the cut-off generally occurs at higher frequencies than the cyclotron resonance frequency. Since the magnetic field changes spatially, not only the location of the resonance changes, but also the location at which the cut-off occurs. For this purpose, we consider two cases as illustrated in Fig. 5.49. The line that marks the spatial course of the cut-off frequency is shifted upwards compared to ω_{ce}. That is, if we irradiate the microwave from those

regions in which the magnetic field or the cyclotron frequency is lower than the microwave frequency, we reach the cut-off *before* we reach the resonance zone, i.e., the wave is reflected without being able to heat. In the opposite case, if we irradiate the microwave from the side in which the magnetic field or the cyclotron frequency is greater than the microwave frequency, we reach the resonance zone undisturbed. For this reason, it is advisable to realize a so-called **high field coupling**, i.e., the coupling of the microwave from the high field side of a reactor.
A possible technical realization of an ECR plasma is shown in Fig. 5.51. In the center of a magnetic field, the microwave radiation is coupled in and thus reaches the resonance zone from the high field side. The magnetic field expands into the plasma chamber at the bottom of which the substrates are located. A difference in the plasma potential corresponding to the different electron densities in the region of the source and the substrate is established.

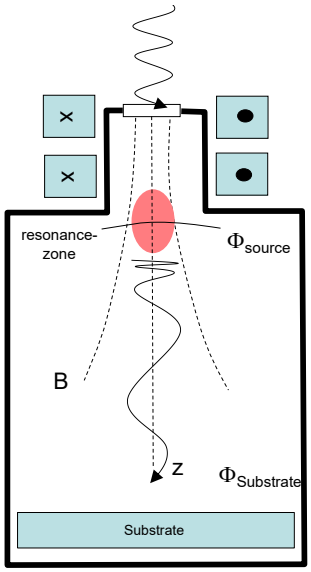

Figure 5.51: Typical configuration of an ECR plasma.

In ECR plasmas, the energy of the ions incident on the substrate can also be easily manipulated. Initially, the ion energy is accelerated by the difference in the plasma potential, as a high-density plasma and a correspondingly high plasma potential Φ_{source} are formed within the resonance zone. In the region of the substrate, the plasma density is correspondingly lower, and thus the local plasma potential $\Phi_{substrate}$ is lower. Furthermore, the energy of the ions is modified in the direction towards the substrate by the mirror effect in the

diverging magnetic field, as perpendicular velocity is converted into parallel velocity.

5.5.3 Helicon Plasmas

An exotic variant of magnetized plasmas is **Helicon plasmas**. For this purpose, consider waves that run parallel to the magnetic field, so-called **Whistler waves**. If these waves are spatially confined, standing waves are created and one speaks of **Helicon waves** or Helicon modes.
The refractive index for wave propagation parallel to B is again:

$$\tilde{n}2 = 1 - \frac{\omega_\mathrm{p}2}{\omega^2}\frac{1}{1 \mp \frac{\omega_\mathrm{c}}{\omega}} \tag{5.168}$$

The refractive index can also be expressed by a comparison with the vacuum wavenumber as:

$$\tilde{n}^2 = \frac{\omega^2}{c^2}k^2 = \frac{k^2}{k_0^2} \tag{5.169}$$

The most common application of Whistler waves is systems in which heating is carried out at the lower hybrids and thus at RF frequencies, i.e., $\omega < \omega_\mathrm{c}$. In this case, the following applies:

$$\frac{k^2}{k_0^2} = \frac{\omega_\mathrm{p}^2}{\omega_\mathrm{c}\omega} \tag{5.170}$$

The wave dispersion in a cylindrical plasma column results in an expression for obliquely running waves with:

$$k^2 = k_\perp^2 + k_\mathrm{z}^2 \tag{5.171}$$

of:

$$\boxed{\frac{kk_\mathrm{z}}{k_0^2} = \frac{\omega_\mathrm{p}^2}{\omega_\mathrm{c}\omega}} \tag{5.172}$$

The designation Whistler waves is derived from the whistle tone that can be heard when these waves run back and forth between the poles in the Earth's radiation belt. The refractive index scales with ω^{-1}, i.e., due to $v_\mathrm{phase} = \frac{\omega}{k}\tilde{n} \propto \omega^{1/2}$, waves with a high frequency are faster than those with a low frequency. If a thunderstorm in the southern hemisphere now triggers a plasma pulse in the radiation belt, we first hear a high tone and then the deep tone. That is, a falling pitch is perceived.

The spatial distribution of the electric fields of these waves can be expressed by

$$E = E_0 \exp \imath \left(\omega t - k_z z - m \frac{\Theta}{2\pi} \right) \tag{5.173}$$

For a field distribution in which the field strength remains axially symmetric, one obtains an $m = 0$ mode. For asymmetric field distributions, higher modes are obtained. Some modes are shown in Fig. 5.52.

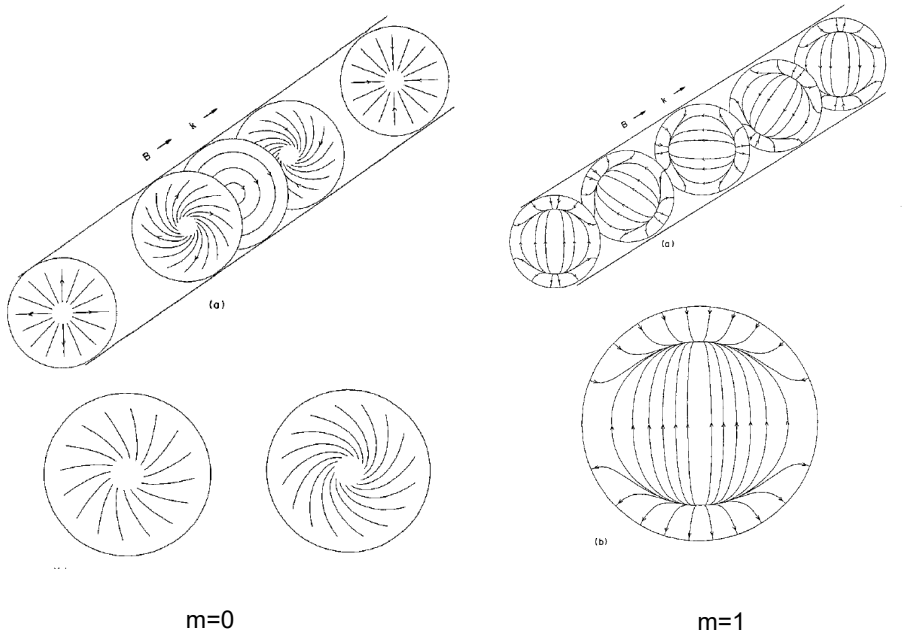

Figure 5.52: $m = 0$ and $m = 1$ modes of a Helicon plasma [13].

In practice, the $m = 1$ mode is often used, which is characterized by twisted current paths running counter to each other. A corresponding coil induces these currents in the plasma (see Fig. 5.53).
According to Eq. 5.172, the electron density of these waves scales linearly with the applied magnetic field. In Helicon plasmas, this dependence is now superimposed by standing waves along the plasma column. Therefore, a step-like behavior of the plasma density is observed in the experiment, as shown in Fig. 5.53, when each mode of the standing waves is hit.

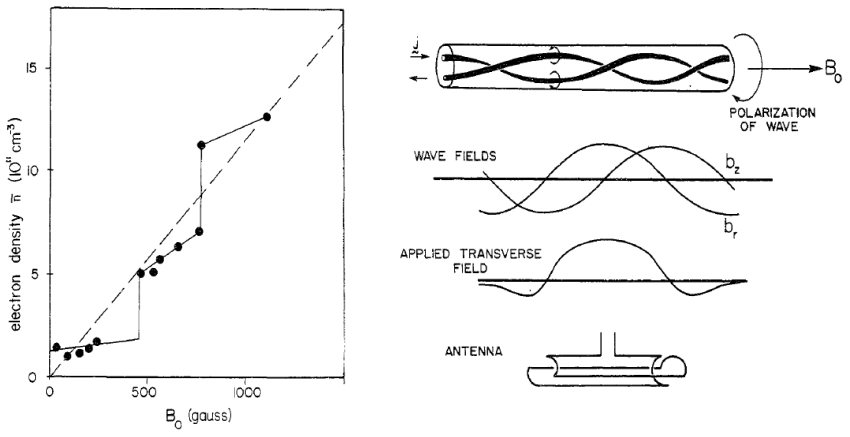

Figure 5.53: Helicon plasma $m = 1$ mode [5].

Chapter 6

Non-thermal Atmospheric Pressure Plasmas

Atmospheric pressure plasmas are divided into *non-thermal* plasmas and *thermal* plasmas. The latter are also referred to as arc plasmas, which are used for welding and cutting materials or for plasma chemistry. In this section, we will discuss non-thermal atmospheric pressure plasmas, in which the transition to an arc is fundamentally suppressed.

6.1 Streamer-to-Arc Transition

When considering a gas gap at atmospheric pressure, ignition is usually carried by the streamer mechanism. That is, a primary electron avalanche is amplified so strongly in the gas that a local electric field forms in the vicinity of the so-called streamer head, which is sufficient to ionize directly. That is, a self-sustaining mechanism has been created. Along the path of this streamer, a quasi-neutral plasma remains with a typical electron density of $n_e \simeq 10^{10}$ cm^{-3}. The time span for the buildup of this **streamer channel** is a few 10 ns. If this channel connects the two electrodes, a breakdown occurs, the so-called **channel breakdown**, and a high current flows. In this process, charge carrier densities up to $n_e \simeq 10^{14}$ cm^{-3} are formed, and sheaths with dominant secondary processes at the electrodes are created.
A streak image of a transition from a streamer to an arc is shown in Fig. 6.1 for a positive tip in front of a grounded surface. Initially, the streamer is seen starting at the cathode and moving towards the positive tip. The slope on the streak image can be used to read the propagation speed of this process, which is approximately 10^6 ms^{-1}. A current increase is also observed, which in this case is caused by displacement current. This first streamer forms a

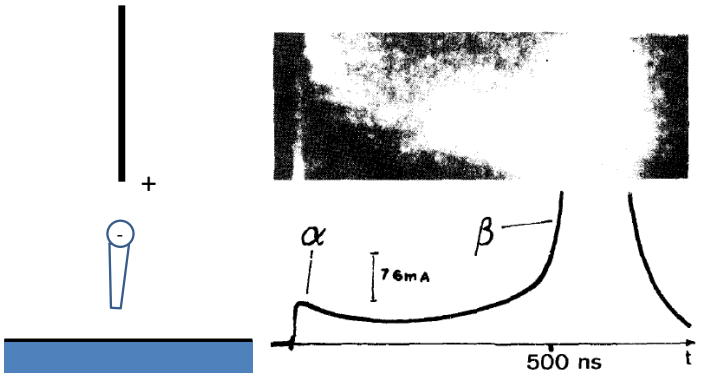

Figure 6.1: Streamer in a point-to-plate geometry. Streak image and current-time characteristic [32].

conductive channel. After this channel is closed, an ionization wave forms that runs from the anode to the cathode. This wave begins at the anode because the electric field strength there is very high. This ionization wave has a propagation speed of $10^{4...5}$ ms^{-1}, which is slower than the first streamer. A high charge carrier density of 10^{14} cm^{-3} builds up. The gas gap fills with plasma until the breakdown to an arc occurs. This process begins after approximately 500 ns.
If one wants to prevent this arc, there are now several possibilities. On the one hand, one can ensure that the conductive channel does not reach both electrodes, that the current is limited, or that the power supply only generates voltage pulses of at most 300 ns, so that the plasma is stopped before the arc can break through after 500 ns.
In the class of so-called **corona discharges**, very inhomogeneous electric fields are used with the aim that the field strength at least in front of one of the electrodes becomes so small that no streamer can form there.
The electrical possibilities to prevent the transition to an arc are shown in Fig. 6.2. If a resistor is inserted into the circuit, the voltage across the gas gap collapses exactly when a large current wants to flow in the arc. Alternatively, a coil can be inserted, which, when the current rises, compensates the externally applied voltage through self-induction and thus reduces the voltage across the gas gap again. Furthermore, a capacitor can be installed in the circuit, or a dielectric barrier can be inserted directly into the gas gap. In both cases, the charging of this capacitor through the current flow leads to a compensation of the externally applied voltage.
A current review article on the topic of streamer discharges can be found in

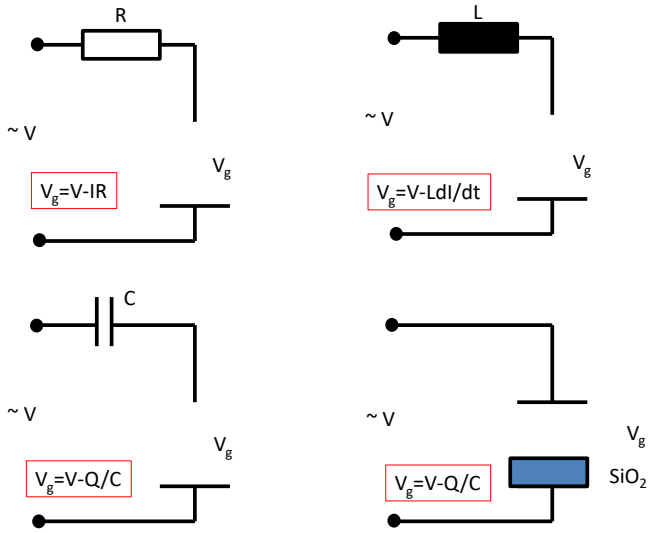

Figure 6.2: Electrical possibilities for the circuit of a corona or barrier discharge to prevent a transition from a streamer to an arc.

Nijdam et al. [37].

6.2 Corona Discharges

Corona discharges are atmospheric pressure plasmas that occur as short-term discharge channels in strongly inhomogeneous electric fields [12]. In nature, these corona discharges form in the vicinity of tips as a luminous phenomenon during a thunderstorm ("St. Elmo's Fire").

6.2.1 Positive and Negative Corona

As an example of an inhomogeneous electric field distribution, we first consider a tip opposite a grounded surface. If this tip is positively charged, this is referred to as a **positive corona**, and if the tip is negatively charged, as a **negative corona**. However, the ignition mechanisms of these plasmas are different.

- *Ignition of a Positive Corona*

  In a positive corona, electron avalanches move towards the positive tip. On their way, they are amplified and a negative streamer is formed.

The region around this tip in which the field strength is large enough to amplify an avalanche is referred to as the **active zone**. This has an extension with a radius $r_{\text{Active Zone}}$. For the formation of these negative streamers, we use the Meek criterion[1]:

$$\int_0^{r_{\max}} \alpha \mathrm{d}r \simeq 20 \tag{6.1}$$

with α the first Townsend coefficient for charge carrier multiplication in the volume. The ignition of the streamers occurs randomly, since the so-called *seed electrons* are first generated by cosmic radiation, etc. The running time of the streamers is approximately 10^{-8} s, while the frequency of the generation of seed electrons is typically 10^{-6} s. That is, on an oscilloscope, the streamers of a positive corona can be clearly perceived as individual pulses.

- *Ignition of a Negative Corona*

  In a negative corona, this picture is reversed, as now positive charge carriers are accelerated towards the tip. The electron avalanches are again triggered by seed electrons, but the negative electrons move away from the tip and run particularly in regions where the field strength becomes small again. Ions that hit the negative tip can release secondary electrons there and thus maintain the charge carrier density. That is, the ignition occurs according to the Townsend mechanism, as introduced in the derivation of Paschen's law. This ignition condition is:

$$\int_0^{r_{\max}} \alpha \mathrm{d}r = \ln\left(1 + \frac{1}{\gamma}\right) \tag{6.2}$$

  with α the first Townsend coefficient for charge carrier multiplication in the volume and γ the secondary electron emission coefficient. The Townsend mechanism is driven by the secondary electrons and thus by the ion bombardment. These processes are dominated by the inertia of the ions, i.e., the formation of such a discharge proceeds on the time scale of 10^{-6} s. Although the start is again random due to the seed electrons, which are also created on average every 10^{-6} s, the individual pulses can no longer be observed separately on an oscilloscope due to the time structure of the discharge.

[1] In a homogeneous electric field, we use the condition $\alpha d = 20$. In the inhomogeneous field around a tip, however, we must integrate along the electron avalanche, since the electric field changes and thus α also depends on the location.

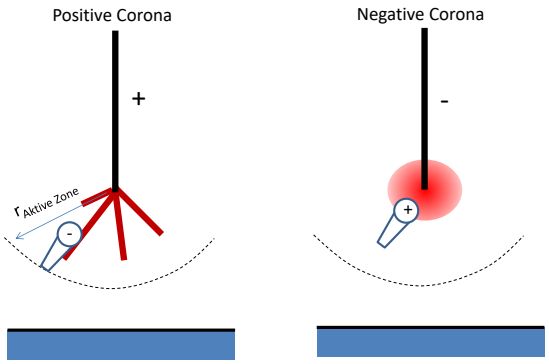

Figure 6.3: Positive and negative corona.

These different types of ignition are also evident in the appearance of the corona discharges. In a positive corona, long discharge channels are formed because the streamers form conductive channels along which the ionization waves propagate. In the negative corona, a smaller and more uniform glow margin is formed. This very general classification based on the external appearance is, however, not unlimitedly valid, as a negative corona can also show filaments when the geometry of the discharge or a different net current is changed. These filaments are then carried by positive streamers.
The microscopic description of the ignition criteria according to the Meek criterion or Townsend criterion is replaced in practice by an empirical formula that calculates the critical field strength necessary to ignite a corona discharge *in air*, the **Peek formula**:

$$\boxed{E_{\text{critical}}\left[\frac{kV}{cm}\right] = 31\delta\left(1+\frac{0.308}{\sqrt{\delta a[cm]}}\right)} \tag{6.3}$$

with $\delta = n/n_0$ the normalized gas density relative to the gas density n_0 at normal pressure and a the radius of curvature of a tip. This formula is valid in the range 0.1...10 bar or for radii of curvature of $a \simeq 0.01...1$ cm. According to this formula, for a radius of curvature of $a = 0.1$ cm, a critical field of $E_{\text{critical}} = 60$ kV cm^{-1} is obtained.
This critical field strength can now be realized in different arrangements. Considering, for example, a coaxial arrangement with an inner electrode of radius a and an outer electrode of radius R, we obtain an electric field between them of:

$$E = \frac{1}{r \ln \frac{R}{a}} V \tag{6.4}$$

with V the applied voltage and r the location in space between the two cylinders. In a point-to-plane geometry, the electric field becomes:

$$E = \frac{2V}{(a + 2x) \ln(2d/a + 1)} \tag{6.5}$$

with d the distance of the tip from the surface, a the radius of curvature of the tip, and x the location between tip and surface. If the Peek criterion is applied, for example, in a concentric arrangement, a critical voltage can be calculated that must be set so that the critical field strength is reached directly in front of the surface of the small electrode:

$$E_{\text{critical}} = \frac{V_{\text{critical}}}{a \ln \frac{R}{a}} \tag{6.6}$$

In the general case, the voltage V is set higher than the critical voltage V_{critical}, as the volume in which ignition occurs and streamers form is thus increased. With this relationship, the thickness of the active zone can be calculated for a concentric arrangement as:

$$x_{\text{Active Zone}} = \frac{V}{E_{\text{critical}} \ln \frac{R}{a}} \tag{6.7}$$

As an example, ICCD images of a positive corona discharge in the vicinity of a wire in front of a grounded surface are shown in Fig. 6.4. The position of the wire is marked with a thin white line, and the dashed line is the location of the grounded surface. In the sequence of images, the running of the ionization waves from the wire towards the surface can be seen. These waves are characterized by short bright luminous traces. After reaching the grounded surface, a second generation of ionization waves begins at the wire. These can only start when the first generation has faded, as the first generation shields the electric field behind it.
Corona discharges have numerous technical applications:

- *Parasitic Discharges Along High-Voltage Lines*

  High-voltage lines at 100 or 380 kV are partly surrounded by corona discharges, as the critical field strength can be reached at the surface of these conductors. These so-called parasitic discharges are a significant loss mechanism in the transmission of electrical power at high voltages.

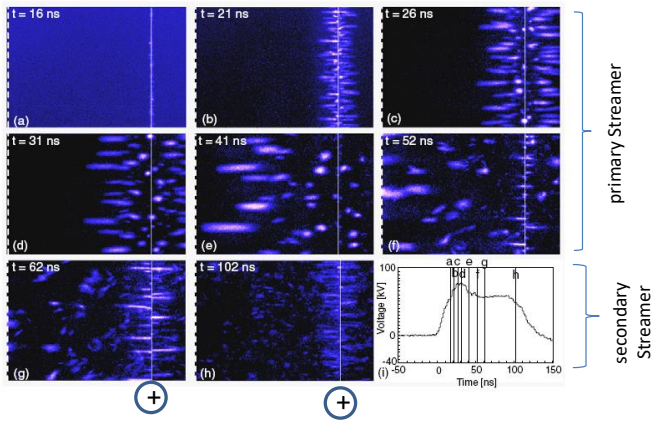

Figure 6.4: ICCD image of a positive corona. Positive wire (thin line) opposite a metal plate (dashed line) [52].

- *Charging in Copiers and Laser Printers*

  In a copier, electrical charge is sprayed onto a semiconducting surface of a drum via a corona discharge. A laser beam is then scanned over the drum and locally increases its conductivity so that the charge can flow off. An image of the page is created in the form of a charge layer on the surface. The drum moves on to a reservoir of toner particles, which adhere electrostatically to the remaining charged areas of the surface. Subsequently, the toner is pressed onto a paper.

- *Ozone Generation*

  The generation of ozone requires a very short reaction chemistry in air. That is, a short streamer in the range of 300 ns is sufficient to dissociate oxygen, which then reacts with O_2 to form ozone. The subsequent destruction of ozone is, however, strongly suppressed, as the plasma has already faded again. A more efficient form of ozone generation, however, is barrier discharges, as discussed further below.

- *Exhaust Gas Purification of Car Exhaust Gases*

  For some time, attempts were made to also purify car exhaust gases via corona discharges or to oxidize NO and CO to NO_2 and CO_2. In addition to problems with the energy requirement of a mobile application, additional toxic substances were also generated in the plasma-chemical processes, which made the use of this exhaust gas purification more complicated.

- *Exhaust Gas Dust Removal in Power Plants*

  A large-scale application of corona discharges is the removal of dust from exhaust gases of coal-fired power plants. In large washers, the dust particles in the exhaust gas are negatively charged via corona discharges and directed to large collectors via electric fields. From these collectors, they can be collected and fed back into the combustion.

6.2.2 Current-Voltage Characteristic of a Corona Discharge

Let us consider the current-voltage characteristic of a cylindrical corona discharge. For this purpose, we divide the corona into an **active volume** with radius $r_{\text{Active Zone}}$ and an outer region of the corona with a charge carrier density $n(r)$ (see Fig. 6.5). In this region, the field strength is so small that no electron avalanches can occur and thus the total current from the outer cylinder to the active zone remains spatially constant.

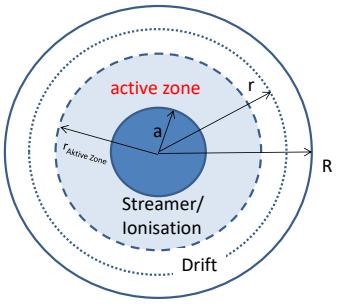

Figure 6.5: Cross-section of a cylindrical corona discharge.

The current in this outer region is given as:

$$I = en\mu E 2\pi r l \tag{6.8}$$

With μ the mobility and l the length of the central wire. Since the total current is conserved and must not depend on r, we can rearrange this equation and obtain a radial dependence of the electron density according to:

$$n(r) = \frac{I}{e\mu E 2\pi r l} \tag{6.9}$$

This equation is still not a unique determination of the charge carrier density, as the electric field $E(r)$ itself depends on the exact charge distribution

in the space. Assuming that space charge effects are small, we make the approximation:

$$n(r) = \frac{I}{e\mu E 2\pi r l} \simeq \frac{I \ln R/a}{e\mu V} \tag{6.10}$$

At this point, we have now inserted the electric field as it applies in a cylindrical arrangement *without* considering the space charge $n(r)$. With this approximate formula, we can now also calculate a new solution for $E(r)$, which takes into account the space charge density by inserting $n(r)$ into the Poisson equation:

$$\frac{1}{r}\frac{\partial}{\partial r} rE = \frac{I \ln R/a}{\epsilon_0 e\mu V} \tag{6.11}$$

Thus, we finally obtain an expression of the form

$$E(r) = \underbrace{\frac{V_{\text{critical}}}{r} \ln \frac{R}{a}}_{\text{without space charge}} + \underbrace{\frac{I}{l} \ln \frac{R}{a} \frac{1}{2\pi\epsilon_0 \mu V} \frac{r^2 - a^2}{2r}}_{\text{space charge correction}} \tag{6.12}$$

which consists of two parts, namely a component without space charge, corresponding to the minimum value of the voltage, the ignition voltage V_{critical}, and a component that arises from the correction due to the space charge. The voltage drop is again given by $\int_a^R E \mathrm{d}r = V$. We obtain a current-voltage dependence of:

$$\boxed{\frac{I}{l} = 4\pi\epsilon_0 \mu \frac{V(V - V_{\text{critical}})}{R^2 \ln \frac{R}{a}} \propto V(V - V_{\text{critical}})} \tag{6.13}$$

It can be seen that the current only increases above a voltage V_{critical} and increases quadratically at high voltages. This increase occurs as long as the active zone fills the cylindrical arrangement ($r_{\text{Active Zone}} \to R$) and the transition to the arc can occur.
The power that is converted in the corona discharge is then:

$$P = VI \propto V^2 (V - V_{\text{critical}}) \tag{6.14}$$

6.2.3 Pulsed Corona Discharge

A significant disadvantage of the corona discharge is its low power and thus its low plasma density. If the voltage were increased arbitrarily to convert more power, the active zone would reach the counter electrode and the transition to the arc would occur. A way out is pulsed discharges, which are operated

with high voltage but ensure through pulsing that the pulses are limited to at most 300 ns so that the arc breakthrough after 500 ns is not reached. This places high demands on the power supplies.

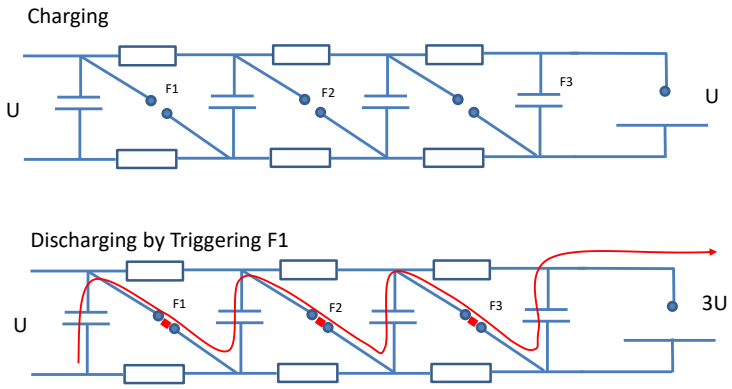

Figure 6.6: Marx generator.

A common variant for such a pulsed high-voltage power supply is a **Marx generator** (see Fig. 6.6): a parallel circuit of capacitors is charged via a DC voltage source with a voltage U. In addition, these capacitors are also connected in series via spark gaps F1...F3. All spark gaps are set so that they do not yet break down at the charging voltage U. That is, all capacitors are first simply charged over a period given by the internal resistance of the voltage source and the capacitance (RC time constant).
By means of an additional triggering (laser pulse, brief overvoltage, etc.), the first spark gap F1 is now caused to break down. As a result, the first two capacitors are suddenly connected in series and the voltage at the second capacitor doubles. This causes the second spark gap F2 to trigger and connect the third capacitor in series. This continues along the chain until a very high voltage is present for a short time at an electrode at the end.

6.2.4 Instabilities of a Corona Discharge

Corona discharges tend to exhibit instabilities at very low currents or voltages, which are in the range of 10...100 kHz. These instabilities are caused by space charge zones in the vicinity of the tips, which shield the field.

- *Flashing Corona*

In a positive corona, a space charge zone is formed from the remaining positive ions in the vicinity of the anode. This positive charge shields the electric field so that a second streamer cannot start immediately. Only when the drift of the ions to the grounded cathode empties the space of the gas gap does the electric field become large enough for a second streamer. This process is periodic and repeats itself with a frequency of 10 kHz.

- *Trichel Pulses*

  In a negative corona, a similar behavior is only observed if this corona burns in an electronegative gas such as air, for example. Here, negative ions are formed, which now shield the electric field in the vicinity of the negative tip in the same way. Only when these negative ions have disappeared through drift or recombination can the next streamer start. These pulses are referred to as **Trichel pulses**. Numerical simulations of this can be found, for example, in Napartovich [35].

6.3 Dielectric Barrier Discharge

A significant limitation of corona discharges was their low plasma densities and thus the low particle turnover. For this reason, so-called **barrier discharges** are often used, in which the transition to an arc is suppressed by an insulating barrier. They are also referred to as **DBD (dielectric barrier discharge)** [7]. In a DBD, individual discharge channels are generally formed, each of which is maintained for only about 300 ns and then extinguishes again. They are also referred to as **silent discharges (SD)** in contrast to thermal arcs, which can become very loud due to the strong heating of the air in connection with the resulting flows and instabilities. DBD discharges are intense but strongly localized. One speaks of a **filamentary discharge**. That is, for applications in which large areas are to be treated homogeneously, barrier discharges are ruled out. However, in recent years it has also been possible to cultivate barrier discharges that form a spatially homogeneous plasma. These two manifestations of barrier discharges are discussed below.

6.3.1 Filamentary Discharge

If the formation of an arc is to be prevented, this can be achieved by inserting a dielectric barrier into the gas gap. After the ignition of an electron avalanche, the electrons are deposited on the dielectric and thus reduce the field strength in the gas gap. The remaining ions can now flow to the cathode, and the discharge extinguishes again. These microdischarges occur in the form of individual filaments, which burn for only a short time in the range of nanoseconds and have a diameter of approximately 300 μm.
The individual phases of a DBD discharge are shown schematically in Fig. 6.7 for a parallel plate arrangement with a dielectric barrier on the anode. The distance between the two parallel plates is approximately 1 mm:

(i) the discharge begins again with the first electron avalanche near the cathode. The electrons are multiplied according to the first Townsend coefficient α;

(ii) then a negative streamer is formed, which runs towards the anode. The speed of this streamer is typically 10^6 ms^{-1};

(iii) when the streamer reaches the anode, it deposits negative charge there, which can no longer flow off at the surface of the dielectric. A conductive channel has formed, along which an ionization wave now runs from the anode to the cathode. This is referred to as the so-called **return**

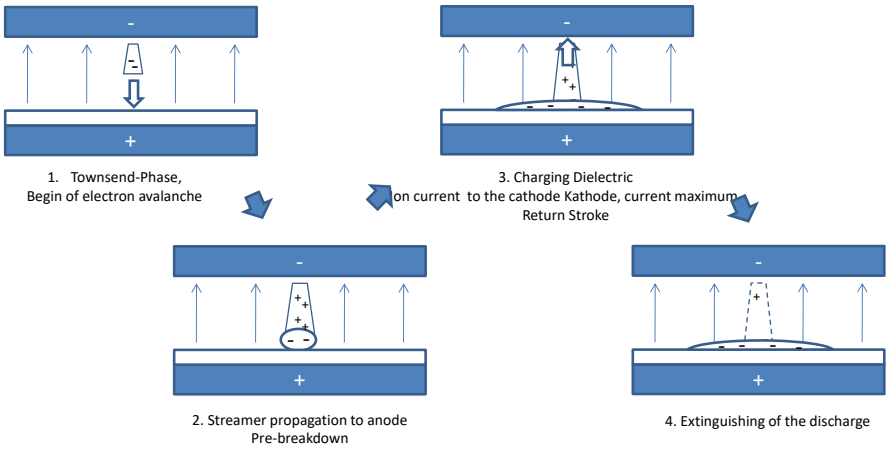

Figure 6.7: Individual stages of the buildup and decay of a DBD filament.

stroke. This wave is triggered by the strong electric field that is created when the streamer hits the anode. During this ionization wave, the main part of the ionization and current flow takes place. Current densities of 1000 A cm^{-2} and electron densities of 10^{14} cm^{-3} are achieved. Analogous to a DC discharge, the discharge scales in this phase with j/p^2. The speed of the ionization wave is in the range of $10^{4...5}$ ms^{-1};

(iv) the charging of the dielectric causes the externally applied electric field strength in the gas gap to be shielded and the discharge slowly extinguishes.

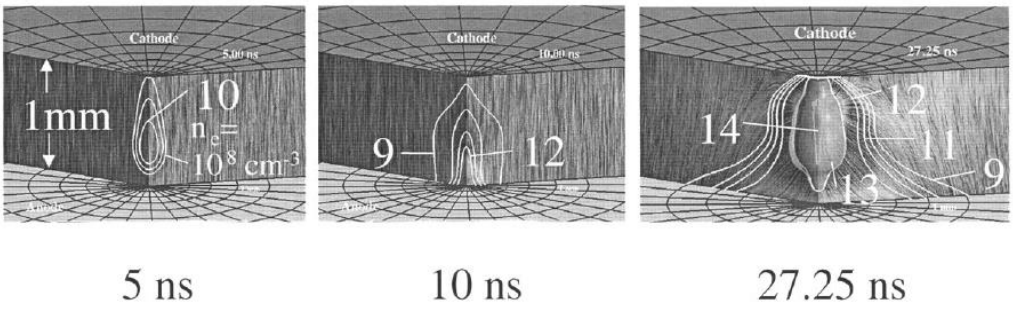

Figure 6.8: Modeling of the temporal evolution of a DBD filament [27].

The development of a barrier discharge has been compared with model calculations, as shown in Fig. 6.8. Initially, the formation of the streamer with a central electron density in the range of 10^{10} cm^{-3} is observed. When this streamer reaches the lower electrode with the dielectric, the return stroke begins and a plasma channel with an electron density of 10^{14} cm^{-3} forms.
A prominent form of barrier discharges is so-called **plasma bullets**. In this case, a barrier discharge is ignited in a quartz tube that is enclosed by two electrodes (see Fig. 6.9). In this case, the ionization wave runs along the tube and can thus run past one electrode and exit the quartz tube. A long, elongated plasma is observed. The ionization waves become visible when the plasma is observed with a time-resolved measurement. These plasma bullets run along the outflowing gas from the quartz tube. Plasmas with lengths of up to meters can be generated in this way. Essential for this are the very strong ionization waves, which can be achieved in particular by very steep edges of the high-voltage excitation. As an electrical phenomenon, the plasma bullets can also pass through glass panes, as these are polarized by the ionization wave.
The direct observation of a filament of a barrier discharge is, however, very difficult, as a filament is a one-time event whose beginning does not occur strictly periodically, and an observation in the sense of a simple PROES measurement is not possible. As explained above, the streamer is ignited by a seed electron, which is formed only in the *temporal mean* every 10^{-6} s. One could indeed ignite a filament through an external ionization source (such as a laser pulse), but the discharge would then no longer correspond to a DBD.
A direct observation of a single filament was developed using the so-called **cross-correlation spectroscopy (CCS)**. In this method, the light of an entire filament is first collected with a photomultiplier to use it as time information. Synchronously or with a small delay to this trigger signal, photons are counted in a second photomultiplier in single-photon mode and assigned to this time axis. This second photomultiplier is focused on a small area of the filament and can be moved spatially to scan the entire discharge. Now, a sequence of individual filaments is observed, and the counted photons are sorted into the correct spatial and temporal intervals. An image of the spatial and temporal sequence of the filament is created, as shown in Fig. 6.10.
The course of the discharge is again observed, which becomes very intense after the first streamer phase. The ionization wave begins again at the anode and runs along the channel to the cathode. Edge layers with maximum light emission at the edges are formed. At the end, the discharge extinguishes again.
In the technical realization of a barrier discharge, one wants to generate a regular sequence of filaments. With a DC power supply, a barrier discharge

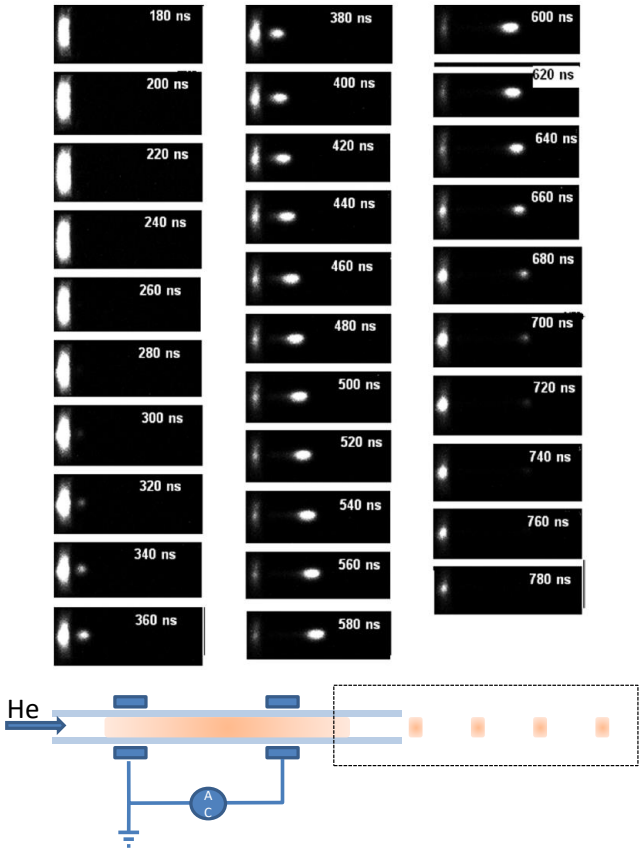

Figure 6.9: Formation of plasma bullets, which are formed in a coaxial DBD discharge [33].

cannot continue to burn, as after the charging of the dielectric, the electric field is shielded. Therefore, DBDs are always operated with AC voltages to break down the surface charges on the barrier again.
The typical current-voltage characteristics of a DBD are shown in Fig. 6.11. With increasing voltage, a series of fast current pulses is observed above the critical field strength, corresponding to the passage of the ionization waves through the individual channels formed in the gas gap by the streamers. After the charging of the dielectric, the discharge extinguishes. Only when the polarity is reversed again can a new series of current pulses begin, with the current direction reversing. A periodically igniting barrier discharge is obtained.
In addition to this temporal structure, a spatial structure can also form. In a microscopic analysis, it is observed that each new filament preferably begins

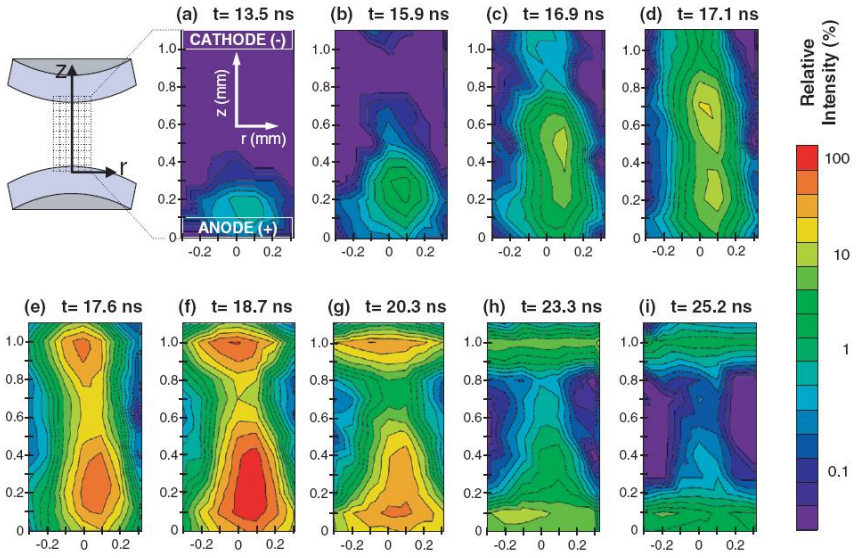

Figure 6.10: Spatial and temporal development of the light emission of a filament [6].

at the location where the filament from the previous phase of reversed polarity was ignited. This can be easily explained: the surface charges remaining from the first filament on the barrier *increase* the local electric field when the polarity is reversed. That is, the new filament burns at the same location.
This feedback between the location of origin of new filaments and the formation of surface charges can lead to a near-order of the filaments, as shown in experimental images in Fig. 6.11 above. Here, a regular arrangement of the filaments in the form of a hexagonal pattern is observed. In Fig. 6.11 below, the surface charges are shown, which exhibit an identical pattern to the filaments.
The voltage-charge characteristic during the reversal of the filaments results from a consideration of an equivalent circuit (see Fig. 6.11). The discharge corresponds to a series connection of capacitors, with C_g the capacitance of the gas gap and C_d the capacitance of the dielectric [30]. The total capacitance is:

$$\frac{1}{C_{\text{total}}} = \frac{1}{C_g} + \frac{1}{C_d} \tag{6.15}$$

For a parallel plate arrangement with a ϵ_r of the dielectric, the following is obtained:

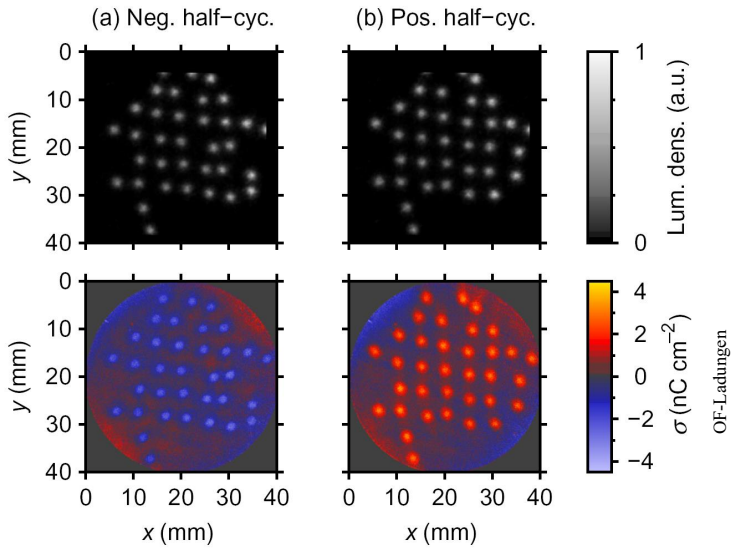

Figure 6.11: Spatial arrangement of DBD filaments [48].

$$C_{\text{total}} = \frac{C_{\text{g}}}{1 + \frac{d}{\epsilon_{\text{r}} g}} = \frac{C_{\text{d}}}{1 + \frac{\epsilon_{\text{r}} g}{d}} \tag{6.16}$$

With d the thickness of the dielectric and g the thickness of the gas gap, and ϵ_{r} the relative dielectric constant of the dielectric. During operation of the discharge, the equivalent circuit varies between two states: (i) while the filaments provide charge transport between the electrodes, the gas gap is short-circuited and the capacitance of the entire arrangement is given solely by C_{d}; (ii) in the phase in which the filaments cannot form, the total capacitance is dominated by the gas gap, and C_{total} is calculated according to the series connection. Since $C_{\text{total}} < C_{\text{d}}$ applies, the capacitance of the arrangement oscillates between these two extrema.
This results in a characteristic voltage-charge diagram of a barrier discharge, as shown in Fig. 6.12. The slope of the characteristic in this diagram corresponds directly to the capacitance of the arrangement in this phase ($C = \frac{\text{d}Q}{\text{d}U}$). When the current flow begins, the charge amount increases slowly, and the dielectric is charged. At some point, the charge amount is applied, and the discharge extinguishes. Now, the capacitance decreases abruptly ($C_{\text{total}} < C_{\text{d}}$) and the discharge voltage decreases at nearly constant charge amount. After reversing the polarity, the filaments begin to run again in the opposite direction after ignition, and the sequence of large and small capacitance is

repeated.

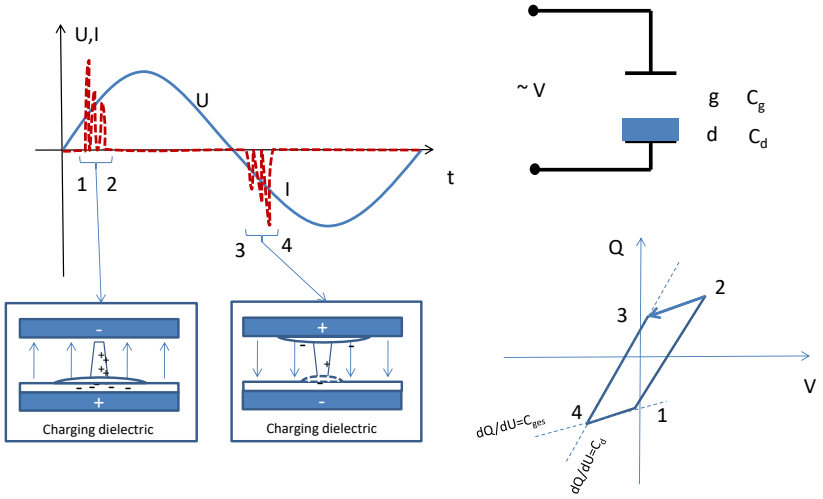

Figure 6.12: Charge-voltage characteristic of a DBD.

The power that is converted in the barrier discharge is given by the area enclosed by the current-charge characteristic according to:

$$W = \int_T U \mathrm{d}Q = C_{\mathrm{total}} \int U \mathrm{d}U \tag{6.17}$$

This area becomes larger the greater the difference in the capacitances C_{total} and C_{d} becomes. That is, a high dielectric constant of the dielectric produces very intense DBD discharges. A current description of the electrical equivalent circuit can be found in Pipa et al. [39].
A simple scaling of the coupled power was already derived by Manley. From the area of the charge-to-voltage characteristic, it can be derived that the absorbed power W scales as:

$$W = 4 f U_0 C_d \frac{C_d}{C_d + C_g} (U - U_0) \tag{6.18}$$

with the voltage of the plasma ignition U_0 and f the frequency of the discharge. This results in a linear dependence of the power on the voltage. For more complex discharge forms, the empirical scaling is used.

$$W \propto (U - U_0)^n \tag{6.19}$$

with n between 1 ... 3. In volume DBDs, as described above, $n = 1$. In surface DBDs, $n = 2$.

6.3.2 Applications of Barrier Discharges

DBD discharges have a wide range of applications:

Ozone Generation

An important application of the dielectric barrier discharge is ozone generation. This method is much more efficient than a corona discharge. In the short times of a local filament, the oxygen chemistry is only briefly initiated, and ozone has a significant probability of survival in these discharges. A typical course of the chemistry of ozone formation is shown in Fig. 6.13. Initially, oxygen atoms are formed, which subsequently recombine with O_2 in a three-body collision:

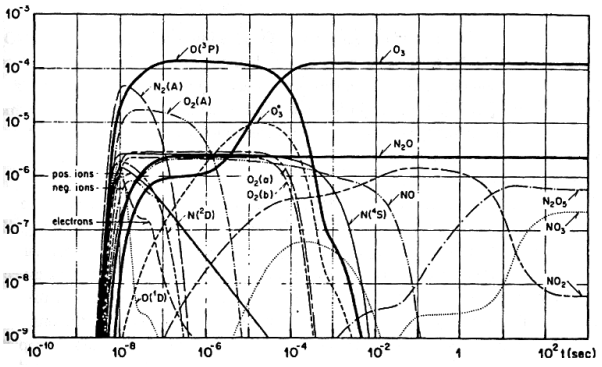

Figure 6.13: Dynamics of ozone generation in air [18].

$$O + O_2 + M \;\rightarrow\; O_3^* + M \rightarrow O_3 + M$$

This formation step competes with the mechanisms for the destruction of ozone according to:

$$\begin{aligned} O + O + M &\rightarrow O_2 + M \\ O + O_3 + M &\rightarrow 2O_2 + M \end{aligned}$$

That is, the oxygen concentration must not be too high, and ratios of O/O_2 $\simeq 10^{-4}$ are optimal. Another technical advantage is the fact that barrier discharges can be easily scaled.

Excimer Lamps

Due to the high pressures and short discharge times in the filaments, DBD plasmas are also very suitable for excimer lamps. In this case, for example, a xenon DBD is generated. Xe_2^*-excimers are formed according to the following reaction channels:

$$\begin{aligned} e^- + Xe &\rightarrow Xe^* + e^- \\ Xe + Xe^+ + M &\rightarrow Xe_2^+ + M \\ Xe_2^* &\rightarrow 2Xe + 172 \text{ nm photons} \end{aligned}$$

Surface Functionalization

Barrier discharges are used to functionalize polymers, with the polymer itself representing the barrier of the discharge. Polar groups are introduced into the otherwise non-polar polymers or plastics by air plasmas, which enable a subsequent step such as printing and coating.

Plasma Medicine

In the very new field of plasma medicine, plasmas are brought into direct contact with living tissue. One of the mechanisms of action is the formation of **reactive oxygen species (ROS reactive oxygen species)** in the aqueous medium. For this process, the introduction of charge carriers into these liquids is essential. In this case, electrons from the plasma react with oxygen dissolved in the water to form superoxide O_2^-:

$$\begin{aligned} e- + O_2 : H_2O &\rightarrow O_2- : H_2O \\ 2O_2- + 2H+ &\rightarrow H_2O_2 + O_2 \end{aligned}$$

The hydrogen peroxide H_2O_2 formed is very stable and can penetrate much deeper into the liquid medium compared to the plasma itself. Through the so-called catalytic **Fenton reaction**, H_2O_2 is then converted into OH radicals, as H_2O_2 can react with the iron atoms present in the biological medium:

$$H_2O_2 + Fe2+ \rightarrow OH + OH - + Fe^{3+}$$
$$\mathrm{H_2O_2} + Fe3+ \rightarrow OOH + H + + Fe^{2+}$$

These OH and OOH radicals can then react with pathogenic proteins and DNA components and thus sterilize a biological medium.

Plasma Display

In plasma displays, individual pixels are formed by small barrier discharges. In this case, energetic photons are initially generated analogously to an excimer lamp. These photons fall on the enclosing walls of the pixel and are converted there in a phosphor into visible light of different colors.

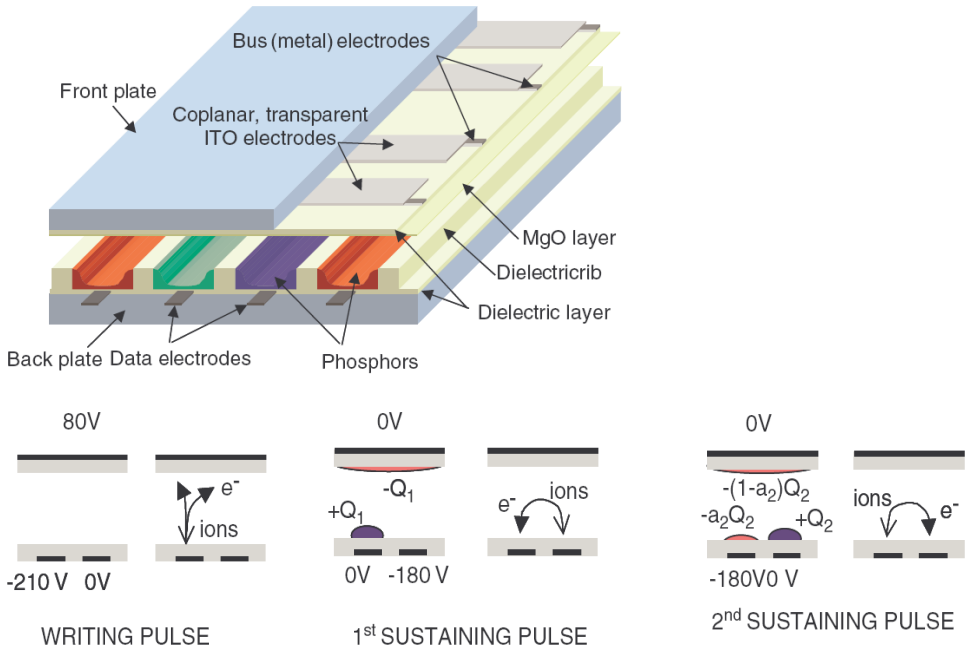

Figure 6.14: Plasma Display Panels [4].

However, a significant boundary condition of plasma displays is the fact that many millions of pixels must be switched simultaneously. For this reason, the scheme of the **coplanar plasma panels** was developed (see Fig. 6.14). In this case, it is a matter of two coplanar electrodes, between which an

AC voltage of 0...-180 V is applied, which can maintain a DBD discharge, the so-called *sustaining pulses*. These electrodes are located behind a glass plate that is additionally coated with MgO. This MgO has a good secondary electron emission coefficient, i.e., only low voltages are necessary to operate the pixel. However, the switching on and off of the pixels takes place in a separate cycle, as illustrated in Fig. 6.15.

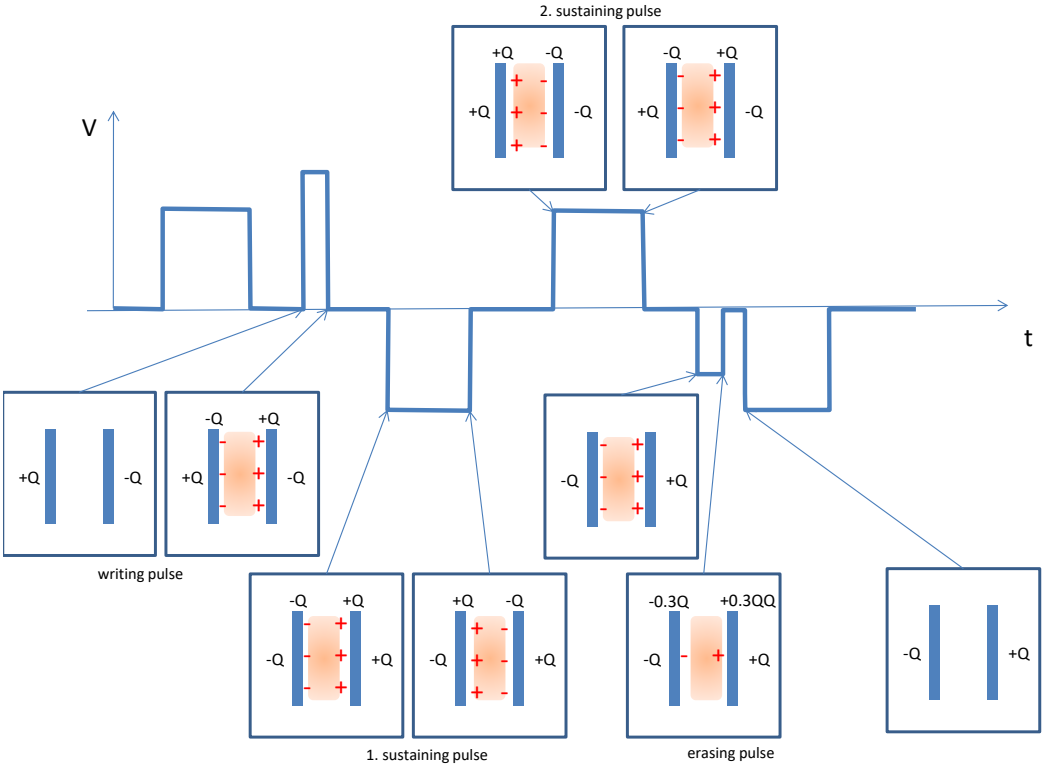

Figure 6.15: Switching cycles of a plasma display pixel.

- *Switching on Pixel*

  The AC voltage of 180 V is not sufficient to ignite the DBD. For this purpose, a voltage of -210 V, the *writing pulse*, is briefly applied to one of the coplanar electrodes, and a voltage of +80 V is applied to a third address electrode (data). These address and coplanar electrodes each form individual lines of a matrix, and the pixel at which +80 V and -210 V are simultaneously applied to the electrodes sees a high field strength and can ignite (see Fig. 6.14). Through this *writing pulse*, the dielectrics are charged to $\pm Q$ (see Fig. 6.15). When the subsequent

-180 V pulse is applied, the surface charge now causes $\pm 2Q$ to generate an electric field when the voltage is applied, so that the DBD can now be ignited. In the further course of the *sustaining pulses*, the reversal of the discharge always leads to a recharging of the surfaces by $\pm 2Q$, so that the plasma is reliably ignited in each *sustaining pulse*.

- *Switching off Pixel*

  If a certain pixel needs to be turned off, it is necessary, *before* the next *sustaining pulse*, to reduce part of the surface charge by a corresponding polarity. This is done with the *erasing pulse*, in which the barrier is recharged by $\pm Q$ (see Fig. 6.15). If the *sustaining pulse* is then applied, the surface charges are missing, and the electric field that is generated is no longer sufficient to ignite the corresponding pixel.

It can be seen that by skilfully manipulating the surface charges, the individual plasma pixels can be turned on and off.
The gas mixture of the pixels consists of 3%...15% xenon in neon. Here, the low ionization energy of neon is used for plasma formation and xenon as a UV emitter. These UV photons fall on the phosphor, which converts UV light into visible light.
The efficiency of plasma displays is very low. Based on 100 % of the power absorbed in the discharge, only 40 % goes into the electrons, 20 % ends up in the xenon excitation, and 15% is also emitted as UV photons. Of these photons, only a part reaches the phosphor, of which in turn only a small part is converted into visible light. In the end, 1.5 % of the originally coupled power reaches the viewer as light.

Plasma Aerodynamics

Atmospheric pressure plasmas are also being researched for aerodynamic purposes. An atmospheric pressure plasma can locally influence the pressure and viscosity conditions, as the plasma flows can induce a convective flow through friction with the neutral gas. From the Coulomb force $F = \rho E$ and the Maxwell equation $\nabla \cdot E = \rho/\epsilon_0$ an electrostatic pressure gradient p_e can be immediately derived, which arises from gradients in the electric field.

$$F = \frac{\mathrm{d}}{\mathrm{d}x}\frac{1}{2}\epsilon_0 E^2 = \nabla p_\mathrm{e} \tag{6.20}$$

Analogous to the Bernoulli equation, static pressure can be converted into dynamic pressure by the flow of a gas. Due to $\frac{1}{2}\rho v_0 2 = \frac{1}{2}\epsilon_0 E2$ we obtain:

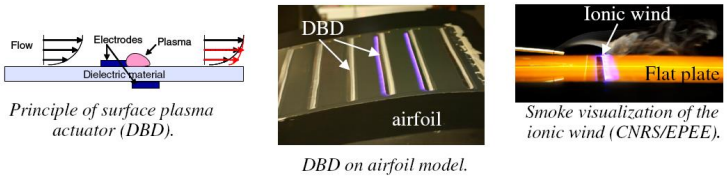

Principle of surface plasma actuator (DBD).

DBD on airfoil model.

Smoke visualization of the ionic wind (CNRS/EPEE).

Figure 6.16: Plasma Aerodynamics [10].

$$v_0 = E\sqrt{\frac{\epsilon_0}{\rho}} \tag{6.21}$$

That is, if we generate a gradient in the electric field, from a region with strong electric fields and regions with small electric fields, this leads to a corresponding flow of the surrounding gas. This is achieved with asymmetric barrier discharges, as sketched in Fig. 6.16. In this case, an electrode is located on one side of a so-called *airfoil*, the foil is the dielectric barrier, and below the foil a large counter electrode. If AC voltage is now applied to these electrodes, a barrier discharge is created between the edge of the upper electrode and the surface of the lower electrode. The electric field is localized precisely at the edge, and a corresponding flow direction of the gas, as indicated, is induced. This gas flow generates a recoil, opposite to the induced gas flow, and thus a forward movement of the airfoil. One can also motivate this recoil by the fact that the positive ions give their kinetic energy to the negative electrode upon impact. If the negative electrode is the one above the airfoil, this recoil takes place tangentially to the airfoil surface. In the reversed polarity, the sheath is distributed over a large area, and the recoil of the ions points in the direction of the airfoil.

6.3.3 Homogeneous Barrier Discharge

In atmospheric pressure plasmas, filamentation of the discharge usually occurs because the high power densities lead to local heating of the gas. This reduces the local particle density at the same pressure and improves the ignition criterion. A discharge channel is formed. However, for many applications, this filamentation is not desirable. Therefore, it is sought to also generate a so-called **APGD Atmospheric Pressure Glow Discharge** at atmospheric pressure. From the family of these plasmas, there are several variants, one of which is the homogeneous barrier discharge. A **filamentation** could be suppressed by several concepts:

1. If it is possible to start the individual streamers simultaneously so that the resulting discharge channels overlap, a homogeneous discharge would be created.

2. If the field strength can be kept small without a streamer being able to form completely but ignition is still possible, a homogeneous plasma could be generated. This situation is ensured, for example, by a **pre-ionization** within the gas gap. Such a pre-ionization can be formed by long-lived charge carriers that were created in previous plasma filaments. For this reason, one also speaks of a **memory effect**.

3. If the dimensions are made very small, no complete streamer can form and the gas gap is homogeneously filled by these Townsend avalanches.

4. In a gas with high thermal conductivity, the thermal instability is suppressed, and the discharge channels cannot burn so deeply into the gas. In the case of thermal instability, the heating by the plasma leads to a local reduction of the neutral gas density. Thus, the mean free path of the electrons increases, and ignition can be achieved at lower field strengths. An important representative of these concepts is helium plasmas, which can be easily brought into a homogeneous state.

5. The high-frequency voltage is chosen such that the inertia of the ions becomes too large for an arc discharge to form. This is referred to as the **pendulum effect**.

6. In the external circuit, the inductance is set such that a strong increase in current, as occurs in the filaments, is suppressed.

From the many concepts, we want to examine two more closely.

6.3.3.1 Memory Effect

An overlap of the individual streamers can be achieved if the density of primary electrons is large enough. If the number of electrons in a streamer head is 10^8, according to the Meek criterion, we need, according to the radius of the streamer head, at least an electron density of 10^6 cm^{-3} through the pre-ionization so that all electron avalanches overlap after their formation.
Such pre-ionization, before the breakdown begins, can be caused by volume or surface effects. In any case, the pre-ionization originates from a phase of the previous filaments.
In the case of the surface effect or **γ-effect**, it is assumed that surface charges can be more easily detached by the filaments and thus could fill the gas gap

to a small density. In the case of the **volume effect**, it is assumed that metastables form a reservoir of excited atoms in the discharge. These can continuously generate new electrons through **Penning ionization**. Penning ionization has a lower excitation energy, as illustrated by the example of a helium/nitrogen plasma:

$$\begin{aligned} e^- + He &\rightarrow He^* + e^- \\ He^* + N_2 &\rightarrow N_2^+ + He + e^- \end{aligned}$$

The longer lifetime ($\sim \mu s$) of the excited states compared to the lifetime of a single filament ($\sim$ ns) is decisive here.

6.3.3.2 Pendulum Effect

At medium frequencies in the kHz range, it is possible to generate uniform glow discharges at atmospheric pressure. The frequency must be chosen such that the electrons can reach the surfaces while the slower ions remain trapped in the oscillating E-field in the middle of the gas gap. In such a situation, a reduced electric field is obtained in the gas gap and the discharge ignites only in the sheath but does not break through. This inertia separation of electrons and ions can be estimated from the equation of motion:

$$m\ddot{x} + m\nu_\mathrm{m}\dot{x} = eE_0 \sin\omega t \tag{6.22}$$

This has the solution:

$$x(t) = -\frac{eE_0}{m}\frac{1}{\omega^2+\nu_\mathrm{m}^2}\sin\omega t - \frac{\nu_\mathrm{m}}{\omega}\frac{eE_0}{m}\frac{1}{\omega^2+\nu_\mathrm{m}^2}\cos\omega t \tag{6.23}$$

If the deflection is averaged over an RF period, the following is obtained for $\nu_\mathrm{m} \gg \omega$:

$$x_{rms} = \left(\int_0^{2\pi} x^2 \mathrm{d}t\right)^{1/2} = \frac{2}{\pi}\frac{eE_0}{m\omega\nu_\mathrm{m}} \tag{6.24}$$

The ions thus remain trapped in the gas gap if the deflection does not become larger than the width d of the gap ($x_\mathrm{rms} = d/2$). With the field strength at a voltage V_rms given as $E_0 = V/d$ one obtains:

$$\boxed{f = \frac{2e}{\pi^2 m}\frac{1}{\nu_\mathrm{m}}\frac{V_\mathrm{rms}}{d^2}} \tag{6.25}$$

That is, at a certain combination of frequency, voltage, and electrode spacing, a uniform glow discharge can be generated at atmospheric pressure.

The transition from a filamentary discharge to a homogeneous barrier discharge is clearly visible in the external appearance but also in the current-voltage characteristic, as illustrated in Fig. 6.16. In the homogeneous discharge, a broad current maximum is observed, corresponding to a uniform *return stroke* of the entire discharge.

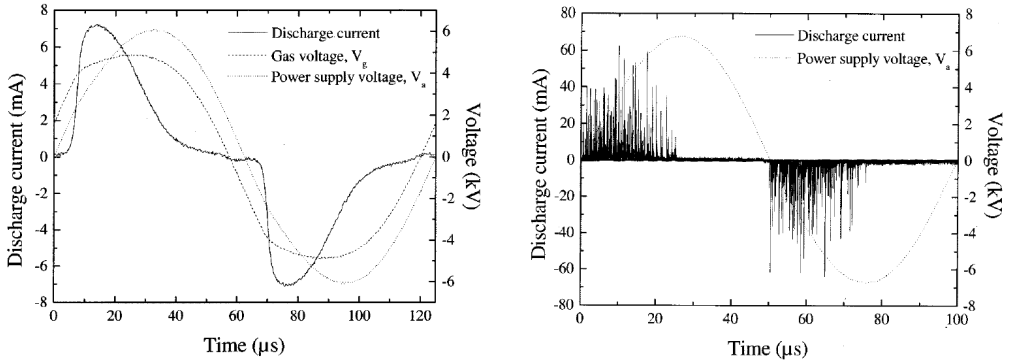

Figure 6.17: Current-voltage characteristics of a uniform DBD (left) and a filamentary DBD (right) [20].

6.4 Examples of Microplasmas

In the previous sections, it has already become clear that atmospheric pressure discharges are often very small due to the ignition mechanisms. Alone, the Paschen law requires that for ignition at atmospheric pressure, the dimensions of the discharge must be in the range of approximately 100 μm. The dimensions of the streamer channels, which are typical but also limiting for atmospheric pressure discharges, are in the same range if one wants to prevent an uncontrolled spark or transition to an arc discharge. The dimensions in the micrometer range, together with the high densities, lead to very strong interactions with the walls and thus reactions [49, 2]. In recent years, a large number of microplasmas have been developed and investigated due to the great potential range of applications. Two exemplary configurations are briefly presented here.

6.4.1 Atmospheric Pressure Plasma Jets

The first group of discharges are the so-called atmospheric pressure plasma jets. These discharges operate with a continuous gas flow, which is typically in the range of standard liters per minute (slm). The gas flow usually consists of a noble gas as a carrier medium and an admixture of a reactive gas. In particular, helium is used to reduce the tendency to instabilities. Molecular gases are usually used as reactive gases, very often nitrogen and oxygen, as the so-called reactive oxygen and nitrogen species (reactive oxygen and nitrogen species, RONS) are interesting for many applications. With the molecular radicals converted in the discharge, which are guided to a surface with the gas jet, various processes can be initiated. In particular, the field of plasma medicine is interesting here. The excitation of the discharges can be carried out with frequencies between DC and the microwave range. However, DC and microwave-excited plasmas often transition into a thermalized mode. These types are then less suitable for biomedical applications where the surface temperature must not exceed 37Â°C. Therefore, discharges with AC or RF excitation are the typical representatives here. A broad overview of these plasma jets can be found in Winter et al. [53].
If we focus here only on some examples of discharges, these should be of biomedical interest. There are two different configurations of the electric field, which also have consequences for the application, among other things. In the first case, the two electrodes are positioned one behind the other with respect to the gas flow. The field is thus oriented parallel to the axis (parallel-field) see Fig. 6.18 b,c).
In both cases, the two electrodes are parallel to the gas flow, so that the electric field is transverse thereto ("crossed-field" arrangement). In this configuration, dielectric coatings (also the glass walls of the gas guide) can be used, but do not have to be. In these cases, the significance of helium as a working medium is even greater.

6.4.1.1 Parallel-field Plasma Jets

Very often, the two electrodes are separated from each other and from the gas flow by a dielectric. Thus, essentially DBD-like behavior is observed. In this case, it can be either a volume DBD with a central electrode (Fig. 6.18b) or a so-called surface DBD with two electrodes arranged outside the dielectric (Fig. 6.18c). In any case, the excitation here is typically carried out in the AC range at a few 10 kHz and at excitation voltages in the kV range. Excitation in the MHz range is also possible. Through the gas flow, however, a relatively homogeneous formation of the discharge is observed.

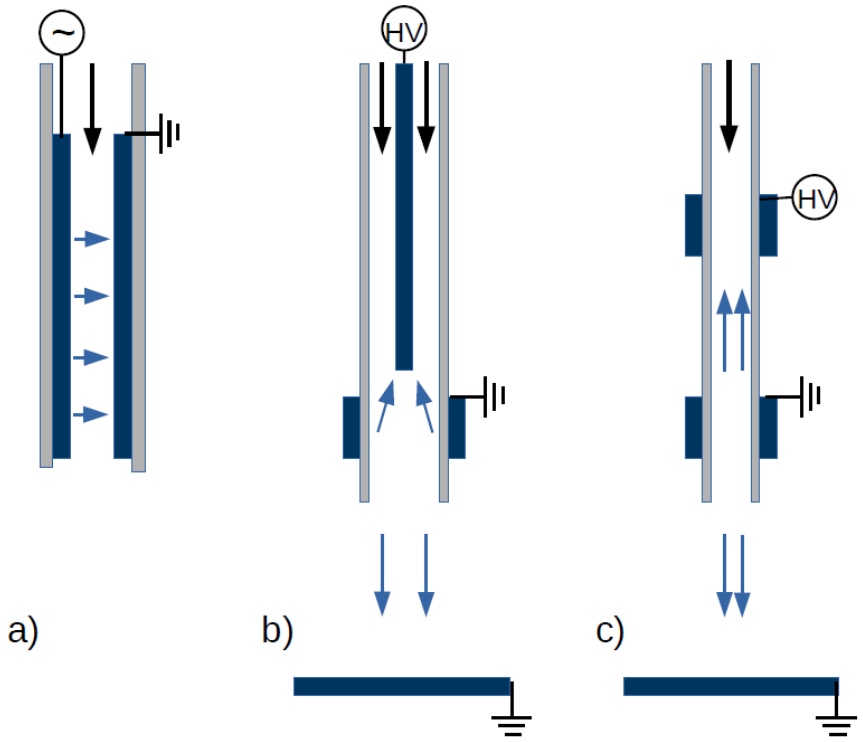

Figure 6.18: Field configuration of jet discharges. a) shows a so-called "crossed-field" arrangement, while the images b) and c) show two variants of the "parallel-field" arrangement.

With significant admixtures and impurities, the discharges become increasingly unstable.
An example of the latter discharge type (and configuration b) is the so-called "KinPEN"[41]. This very well-studied jet has been developed in particular for plasma-medical applications. In this case, even first so-called pre-clinical studies have been carried out, which corresponds to a first step towards the actual introduction in the medical field with its high requirements. An example of type c) with excitation in the kHz range is the so-called "PlasmaGun" [29].
In both configurations, when observed with sufficient time resolution, it is observed that the homogeneously appearing discharge is composed of streamers in the volume of the discharge. In addition, however, the luminous phenomenon also emerges from the actual jet volume into the free area. This is due to the fact that a field can form up to a surface positioned in front of

the jet (grounded). This field has several consequences. On the one hand, the electrons within this area can not only excite but also trigger additional processes (dissociation, ionization). On the other hand, atmospheric air can simultaneously penetrate into the gas stream and be converted there. This leads to a very efficient production of reactive species, which is, however, strongly dependent on external conditions. To reduce this, a surrounding gas jet of noble gas is sometimes used. On the other hand, the field at the surface can have direct effects, such as breaking up biological components. As a third aspect, the current flow, which is guided to the surface via the gas stream, should be mentioned.
In the "KinPEN" configuration with its high excitation frequency, the external luminous phenomenon is also generated by the formation of streamers. It thus typically remains limited to a few mm.
In the kHz-pulsed discharges, on the other hand, discharges with lengths of up to several meters can form. This is due to the fact that here ionization waves are induced, which then propagate along the gas jet. In particular, the propagation takes place at the interface between the gas jet and the environment. With each AC excitation pulse, such an ionization wave is generated, which then moves as a pulse with a few 104-105 m/s along the gas jet. Each pulse has electron densities of about 1016cm−3. This density is so high that when it hits a dielectric surface, a field can be induced even behind the surface through the charge carriers, which is sufficient to allow the ionization wave to propagate further.
Another consequence of the field and the particles driven by it is a frequently observed alignment and rectification of the gas jet (see Fig. 6.19). This depends on how the counter electrode is polarized to the jet electrode. The counter electrode is often the skin of a patient in medical applications.

6.4.1.2 Crossed-field Plasma Jets

In the "crossed-field" arrangement, direct excitation in the MHz range (especially 13.56 MHz) is also possible. Due to the arrangement, the interaction here only takes place in the actual discharge volume, so that in the effluent only processes in chemical equilibrium can take place. Perhaps the first of these jets was the so-called "Atmospheric pressure plasma jet (APPJ)" [47], which provided a guideline for other jets with an electrode spacing of one millimeter. A current version, which is characterized in particular by its good diagnosability with open optical access and integrated electrodes, is the so-called "COST-Jet" [22].
Fig. 6.20 shows in strongly simplified form the configuration of the electrode head. All components that may come into contact with the plasma are

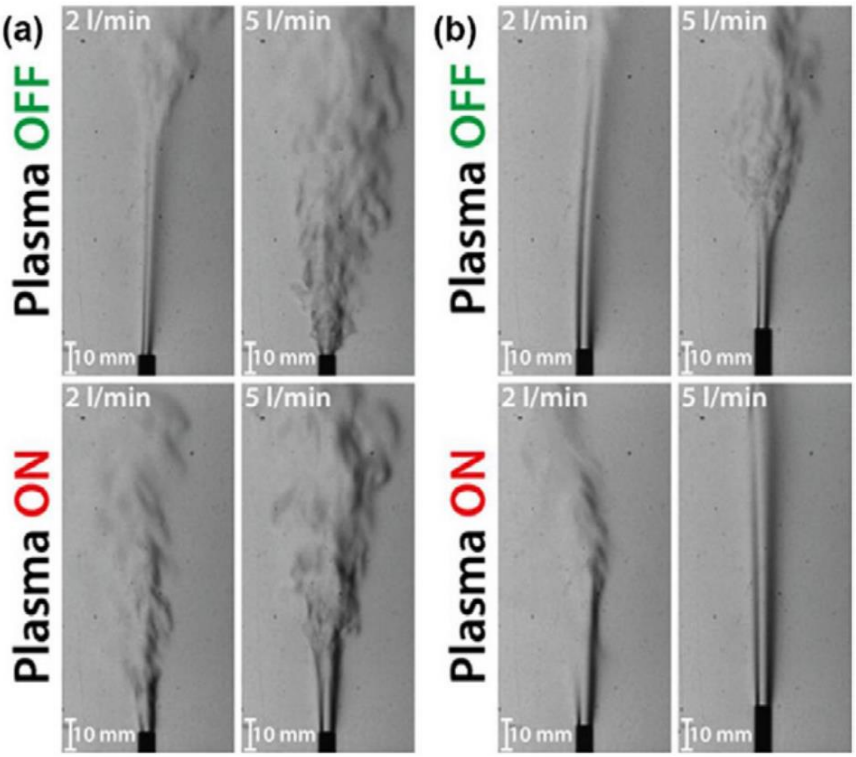

Figure 6.19: Schlieren images of a plasma gun in dependence on its polarity. The counter electrode is at the upper edge of the image. [42]

made of inert materials (stainless steel, ceramic, quartz). The stainless steel electrodes together with the quartz plates form the discharge space of 1x1x30 mm^3, for which there is free access for diagnostic purposes (optical). In a ceramic component, the electrodes are coupled to the stainless steel gas supply.
Parts of the matching network (resonant circuit) and a current and a voltage sensor are integrated into the head of the COST-Jet (Fig. 6.21). These allow the measurement of the power coupled into the electrode system by measuring current, voltage, and phase.
After ignition, the power first increases linearly with the applied voltage (Fig. 6.22). This corresponds to the α or 'Omega' mode, in which volume effects dominate. At somewhat higher powers, the power coupling then increases disproportionately. Here, the surface effects (γ-mode), or better the 'Penning' mode, become relevant. Here, the Penning ionization of the metastables provides an additional electron source. Finally, the discharge contracts.

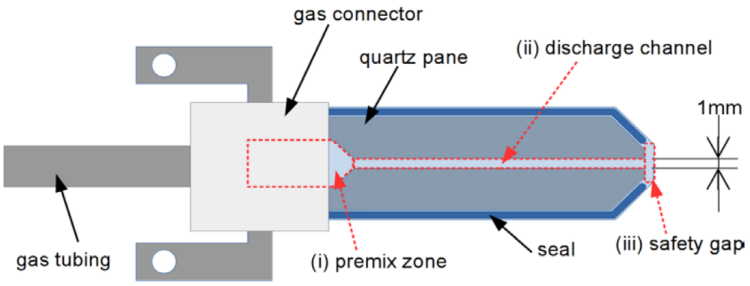

Figure 6.20: Schematic representation of the COST-Jet electrode configuration

In this type of discharge, it is observed that the typical admixtures of reactive gases are in the order of about 1%. For oxygen, the conversion maximum is at about 0.5 %. This type of discharge was introduced in particular as a reference for the many microdischarges investigated in various laboratories.

6.4.2 Microcavity Plasma Arrays

A second special type of non-thermal atmospheric pressure discharges is the so-called microcavity plasma arrays, abbreviated as "Micro arrays". In this case, configurations are involved in which many microscopically small cavities are distributed in a structured manner on a surface. The individual cavities have dimensions in the order of about 100 µm. Many of them (some 10 to millions) are arranged on the surface at distances of again 100 µm. An overview of the concepts and possibilities can be found, for example, in [17]. Very often, these arrays are produced with methods of microstructuring technology. This is intended to ensure a very high accuracy, precision, and reproducibility of the components. Silicon usually serves as the base material, into which the cavities are then impressed, for example, by chemical etching processes or by ion etching. For this purpose, the position, geometry, and dimension of the various cavities are predefined in each case via a mask. In the case of chemical (wet) etching, structures with right angles, so-called "inverse pyramids", are formed because the process can only develop along a crystal axis. In the case of ion etching processes, the geometry is much more flexible, but the flanks are essentially perpendicular. Above the silicon surface, there is then one or more dielectrics. Above this, a nickel layer of a

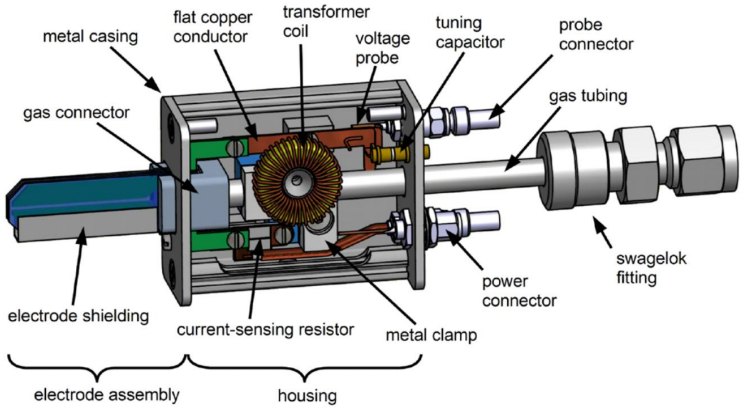

Figure 6.21: Overall representation of the COST-Jet head with integrated current and voltage sensors [32].

few µm thickness with the corresponding recesses for the cavities is usually applied. The nickel layer serves as a counter electrode to the silicon wafer typically used as a grounded electrode (see Fig. 6.23a and b).
If the cavity itself is not dielectrically coated, a discharge current can flow directly, and the array can thus also be used in DC operation. However, this leads to damage very quickly due to the small dimensions and the associated relatively high current densities. This can be due, for example, to the fact that inclusions of the working medium (He, Ar) are removed from the surface structure by ion bombardment. For this reason, an additional dielectric is often applied, and the array is thus converted into a dielectric barrier discharge. Depending on the operating conditions, the individual cavity can be compared with a volume or a surface DBD, or alternatively with a micro-hollow cathode discharge. The operating ranges are typically in the range of some 10 kHz and applied voltages of less than 1000 V. Another possibility to increase the lifetime is, for example, to assemble the system from a stack of nickel grid dielectric foil and a magnet (see Fig. 6.23c). In this case, the magnet serves as a grounded electrode and simultaneously holds the entire system together via its magnetic field. Due to the many collisions due to the pressure, the plasmas within the cavities are not magnetized despite the magnetic field. An advantage for investigations, in particular of surfaces, is that the system can be disassembled.
The advantage of microarrays lies in the fact that, unlike the chaotic or at best self-organized DBD discharges, the plasma processes can be specified much more precisely. At the same time, a very high surface-to-volume ratio

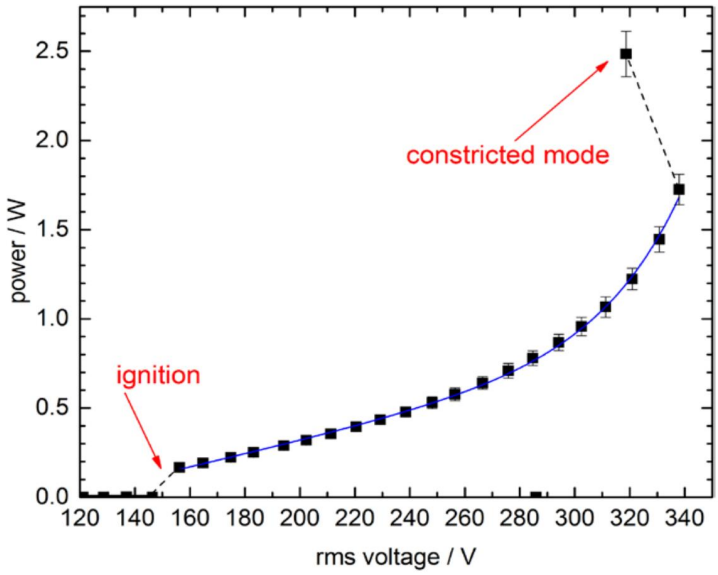

Figure 6.22: Power characteristic of the COST Jet.

results due to the dimensions. Together with operation at pressures in the atmospheric pressure range, surface processes can play a very important role. For this reason, the use of this type of discharge is in the foreground for material conversion. An example is the ozone synthesis for the purification of contaminated water with the help of such a system [26].

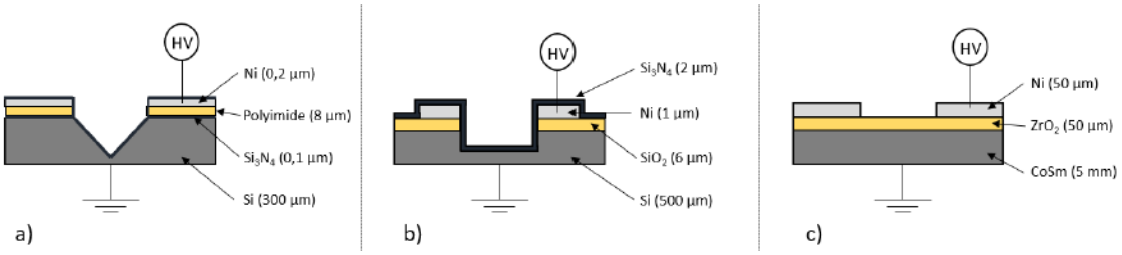

Figure 6.23: Configurations of microcavity plasma arrays

Although the individual cavities typically correspond to DBDs, it must be noted that the typical dimensions are smaller than those in conventional configurations. At the same time, the development of the streamers and structures formed thereon is limited by the geometric dimensions. Another

difference is the presence of further discharges at exactly predefined distances, which, as is also the case with surface DBDs, can lead to interactions.
The given asymmetry of the system leads to the fact that the two half-periods differ from each other. In the case of positive polarity of the nickel grid, electrons emerge from the cavity in a simplified representation and can even expand over the surface. In contrast, in the negative polarity, a contraction of the discharge into the cavity is observed. The discharges ignite in glow or Townsend-like form when a sufficient voltage is reached, i.e. sharp peaks or a relatively uniform emission are observed. The actual ignition voltage is also determined by the space charge generated in the previous half-period [3]. This leads to a similar memory effect as already discussed above. Essentially, charge carriers are assumed here, which settle on the surface and can recombine in the best case due to the dielectric coating but cannot flow off. In Fig. 6.25 the behavior for a neon-argon mixture is shown. In this case, short emission pulses are observed in both half-periods with bipolar excitation, but they differ significantly in size.

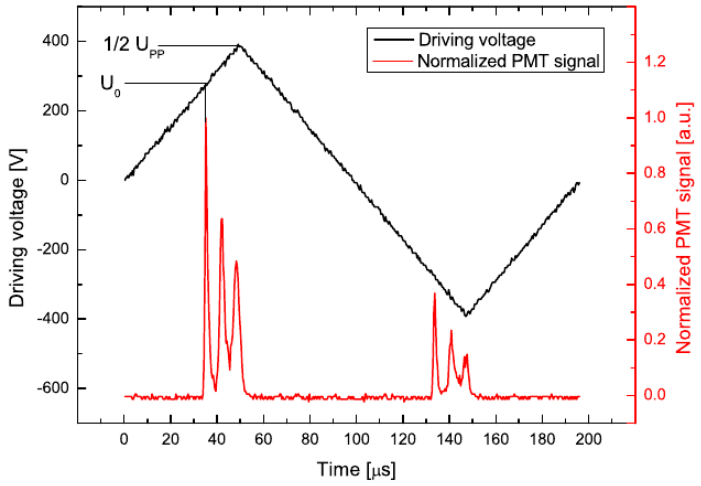

Figure 6.24: Voltage curve and emission characteristic of an array with inverse pyramids [3]

One of the most interesting observations that have not yet been fully understood is the formation of emission or ionization structures that move wave-like from one cavity to the next over the array (Fig. 6.25). Possible reasons for the propagation are the transport of particles or also photoemission of electrons in neighboring cavities under discussion. A purely electrical effect

is also not excluded, which, due to changes in the charge in the individual cavities and the resulting potentials in the environment, leads to ignition in the adjacent cavities.

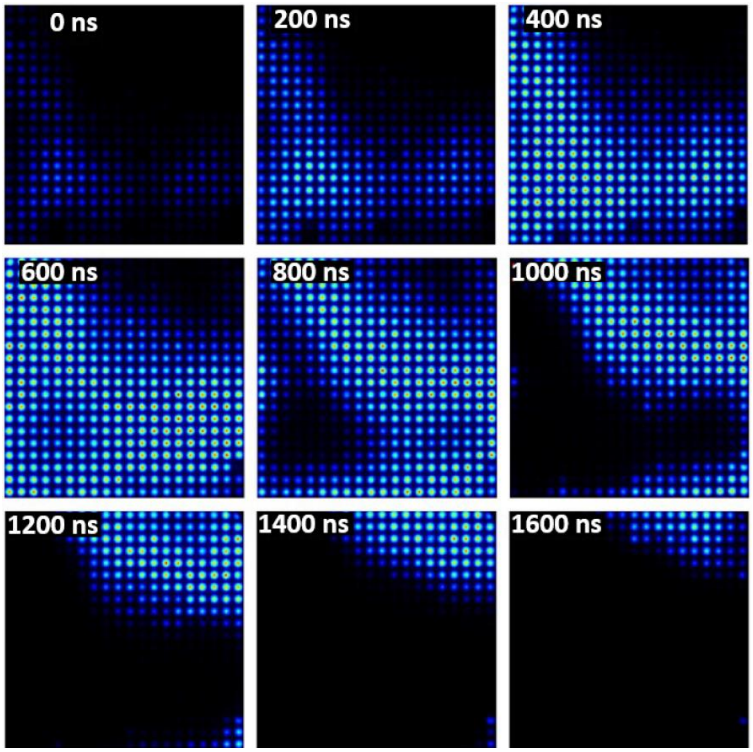

Figure 6.25: Wave propagation over a microcavity plasma array

In addition to the application possibility in plasma chemistry, applications in light generation, especially in the UV range, have also been presented. Here, the proximity to the plasma display panel already discussed comes into play.

Chapter 7

Plasmas in Contact with Liquids

7.1 Introduction

Closely related to atmospheric pressure plasmas, but also extending far beyond, are the so-called 'Plasmas in Liquids / Plasmas in Fluids' which are currently being investigated very intensively. In the following, only some of the most interesting aspects will be addressed. Their importance today lies in the multitude of envisaged applications, particularly in the fields of biology and medicine. The interesting aspect here is that the plasma generates reactive radicals directly in the liquid. Previously, the focus was mainly on electrolysis and the investigation of breakdown in dielectric liquids. An area that is still important today includes analytical chemistry. Here, the liquid electrodes of various discharges provide or excite their contents for subsequent analyses. Today, the main focus is on transferring energy into the system to drive reactions of the liquid towards a specific process. This alone clearly shows that a strong interaction between various scientific disciplines is required to describe these systems. A very good overview of this, which also forms the basis of this chapter, is provided by the review articles by Bruggeman and others [8, 9].
Very roughly, the complex 'Plasmas and Liquids' is divided into two areas:

- *Plasma-Liquid Interaction*: In the first, which is directly correlated with atmospheric pressure plasmas, the interaction of the species generated in a plasma with a liquid is investigated. In this case, various atmospheric pressure plasmas are used as excitation sources. The particular interest here lies in the fact that, in particular, the human skin

is always covered with a liquid film, which the species generated in the plasma must first penetrate.

Species can enter the liquid from the plasma. The processes that occur at the surface and subsequently in the liquid are diverse and not yet fully understood. Fig.7.1 shows a schematic representation of the species that occur in front of a liquid surface in the liquid and in the interface between them. An argon/moist air mixture was used as the gas medium. One of the problems is the extremely fast reaction rates caused by the high particle densities. As a consequence, mainly the end products of the process chain, such as H_2O_2, are observed.

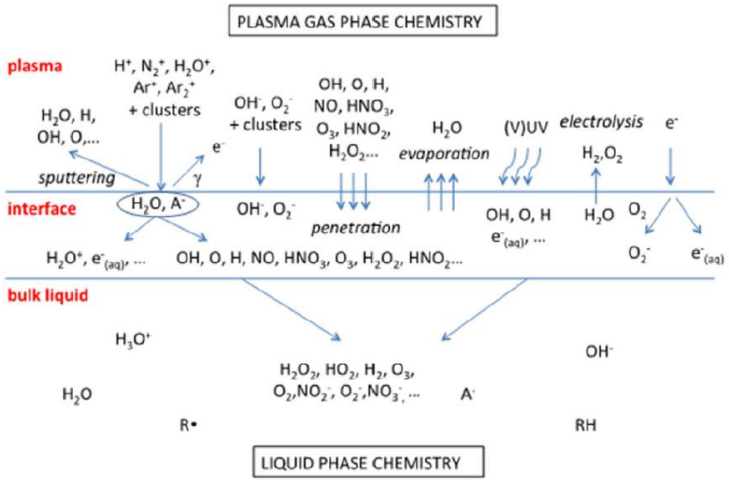

Figure 7.1: Schematic representation of the species that occur in an argon/moist air mixture in front of a liquid surface in the liquid and in the interface between them [8].

The transition probability is low when transitioning from the gas phase to the liquid. This leads to the concentrations of the species remaining low. The Henry's constant is a measure of this:

$$H = \frac{c}{p} \qquad \left[\frac{mol}{m^3 Pa}\right] \tag{7.1}$$

which compares the concentration c of a type of particle in the liquid with the partial pressure p above the liquid. This often leads to the contradiction that a certain type of particle may occur in high concentration in the gas phase but can hardly transition into the liquid due to

its small Henry's constant. For other species such as H_2O_2, the Henry's constant is large and the transfer from the plasma to the liquid phase is effective.

- *Plasmas in Liquids* In the second case, the direct generation of the plasma within a liquid is of interest. Here, the focus is on the efficiency of the coupling or generation and deposition of the plasma-generated species within the liquid. One possible solution is to attempt to ignite a plasma directly in the liquid. However, the high densities then require extremely high voltages ($\geq$ 10 kV) and very short voltage pulses ($\leq$ 10 ns). In this case, the discharges are driven by nanosecond-pulsed to DC voltages in the tens of kV range, but also by AC voltage and GHz microwave discharges. The operating range extends into the high-pressure range. If the discharge is ignited in a liquid, pressures up to the GPa range are formed in the plasma filaments. This then leads to the formation of bubbles in which plasmas/gas breakdowns can possibly form again. Sometimes it is also assumed that these discharges can form in other empty areas (voids).

  Due to the short times, pressure waves are then excited and observed in the liquid. Due to the short time scales and the small dimensions, observation and subsequent analysis and interpretation are extremely difficult.

7.2 Classification and Configuration

As with gas phase plasmas, there are various ways to classify the discharges. One possibility is based on the configuration, as this also strongly influences the type and intensity of the interaction. Fig. 7.2 shows some frequently used configurations.
These include, for example:

Discharges directly in the liquid

a) Discharges directly in the liquid

Discharges that trigger reactions in the liquid

b) Without direct contact

c) In direct contact

d) At the liquid surface (surface discharge)

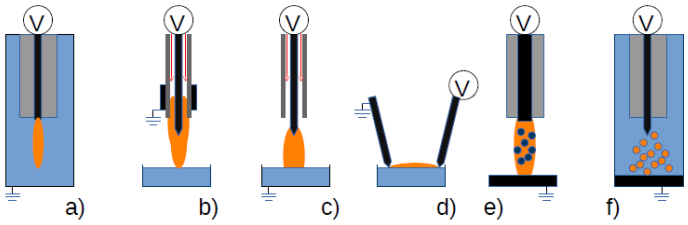

Figure 7.2: Schematic representation of different configurations of the interaction of plasmas with liquids (after [8]).

Discharges that involve multiple phases, such as

e) Dispersed liquids (aerosols) in gas phase plasma

f) Gas phase plasmas (bubbles) in liquids

7.3 Direct Liquid Discharges

These discharges typically require a very fast breakdown process. If this is generated with high-voltage pulses, it often corresponds to streamer or corona discharges. Pin-to-plane or pin-to-plate configurations are frequently used. Typical pulse lengths are in the microsecond range. Today, ns discharges are intensively investigated, which are driven, for example, with high-voltage pulsers.
In-liquid corona discharges often do not form a complete conductive discharge channel. The discharge current is conducted via slow ions and the displacement current.
The actual formation process is still under discussion and strongly depends on the conditions. It is often assumed that discharges first develop in already existing bubbles, as ns discharges are too fast to enable the formation of such a bubble. In these bubbles, the charge carrier density can quickly reach values of 10^{24} - 1026m−3 and the degree of ionization can reach about 10%. The gas temperature can rise to values of up to 5000 K. This leads to shock waves that indicate pressures of over 1 GPa.

Animation

Dynamics of a bubble formed by plasma ignition in a liquid.

Rayleigh-Plesset simulation of a cavitation bubble.

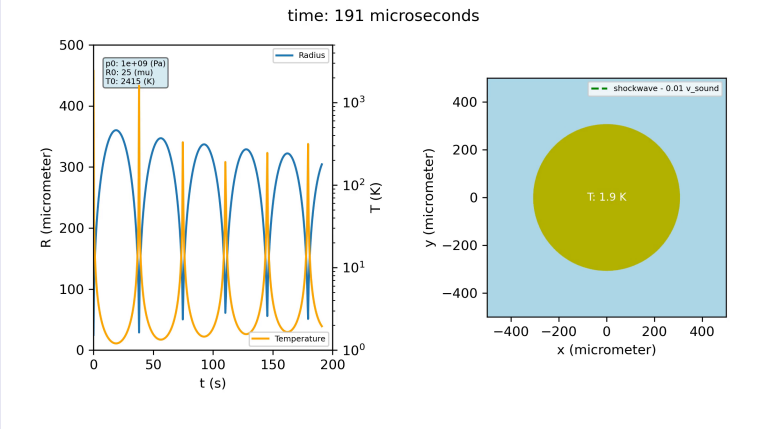

The in-liquid plasmas are generated directly in the liquid and in the transient vapor phase. This can produce significantly different reactive species than in gas-phase plasmas. The species generated directly in the liquid are capable of undergoing very short-term reactions with the medium or the species in the vapor phase. This leads to completely different rate constants than in the gas phase.

7.4 Gas Phase Plasmas in Contact with Liquids

In the configuration of Fig. 7.2 d), streamers can form that hit the surface at km/s. Here, species can be formed directly at the interface between gas and liquid at high rates, making this type of discharge efficient.
This looks different when using atmospheric pressure plasma jets (APPJ). Here, the reactive species are formed in the gas phase and then transported to the liquid in the so-called effluent/afterglow. The entry and interaction with the liquid is largely determined by diffusion. These jets can be operated both as DBD and with high-frequency excitation. A major difference here is the orientation of the electric field to the gas jet. With crossed fields, there is no direct interaction with the liquid, which can occur with linear orientation if the field can establish electrical contact there.
In addition to the species formed in the plasma and transported through the effluent, photolysis via UV photons is also a special feature here. These UV and VUV photons can be formed in atmospheric pressure discharges by the formation of excimers and their decay. These photons can lead to further processes.

7.5 Multiphase Plasmas

7.5.1 Discharges with Dispersed Liquid - Aerosol Plasmas

Aerosols are frequently used, for example in ICP's to identify atomic components by atomic emission spectroscopy or mass spectrometry. Today, non-equilibrium plasmas are used to convert the precursors contained in the aerosols. The droplets are often injected into the gas via 'electrospray' processes (Fig. 7.2 e)). Depending on the mode of operation and, for example, the liquid, different diameters are achieved. This diameter also defines the surface as the interaction interface.
However, it is not yet fully understood how the interaction with the droplets takes place. Here, in particular, the surface of the droplet with the interface between plasma-gas and the liquid is of importance. A model for the formation and the processes during the ignition of an ns discharge in a liquid in combination with the observed plasma parameters can be found, for example, in [23].
At sufficiently high voltages, discharges can also be generated with and around the droplets. This configuration then leads to a very efficient mass transfer of the active plasma species into the liquid. In the droplets, these species can then survive for a longer time.
Due to the large surface area and small volume, additional processes such as heating could trigger processes other than those occurring in pure surface plasmas.

7.5.2 Discharges in Bubbles and Foams

Bubbles, i.e. small gas inclusions, exist in every liquid. Through energy transfer through the surface during the plasma interaction, these bubbles can expand greatly (Fig. 7.2 f). However, bubbles are often also generated via so-called 'bubblers'. At sufficiently high voltage, streamer discharges then occur within the bubbles. This can happen both in bubbles that are still attached to the nozzle and in freely floating ones. These discharges tend to form as surface discharges along the gas-liquid interface.
Due to the high field strength and the high electron density in the streamer head, extreme interactions with the nearby liquid surface can lead to the formation of reactive species.
A particularly extreme case is the formation of plasmas in foams. Here, the various, directly touching bubbles form an extremely large surface that is

then available for the plasma interaction. Here, relatively low voltages are often required to ignite the discharge.

7.6 Transport of Species at the Gas-Liquid Transition

To obtain results for the transition region between gas and liquid, a large number of processes must be considered, such as fields, aerosols, atmospheric chemistry, evaporation, condensation, solubility, and so on. This must then be treated for liquids with different properties, with water being the most frequently investigated solvent.
In general, the kinetics of the transport processes to the gas and liquid volume are considered for the transition region, which is characterized in particular by strong density gradients, see Fig 7.3.

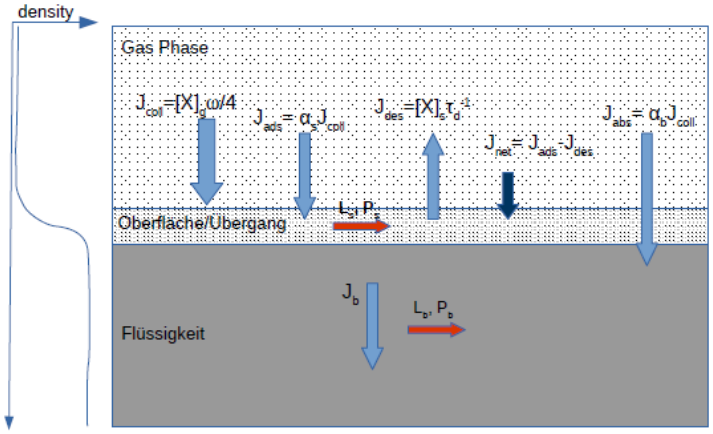

Figure 7.3: Schematic representation of the most important processes and flows during gas uptake, such as surface collisions J_{coll}, adsorption J_{ads}, and absorption J_{abs}. The red arrows show production (P) or loss processes (L) in the transition zone (s) or in the liquid volume (b) (after [8]).

The thickness of the transition zone indicated in the figure is only a few nm in reality. In addition to the flow due to gas kinetic collisions, the flows of the particles that are adsorbed in the interface or absorbed into the liquid volume must be considered, as well as those that desorb via the reverse process. Within the transition zone and in the liquid volume, reactive particles can then change their concentrations via generation and annihilation reactions.

For these reactions and transfer mechanisms, the various possible particle groups must be considered individually. The simplest concepts are naturally given for the *neutrals*, for which the known mechanisms such as Eley-Rideal or Langmuir-Hinshelwood are considered. Furthermore, a large number of surface and other coefficients are known. This is already different for the *ions*. For cations, it is assumed that they immediately lose their energy upon entry into the interface. The penetration depths of the ions are only a few nm and their mean free path is less than a micrometer. The transport of negative ions is even less clear, although they play a significant role in many plasmas (O^-). The third important plasma component, the *electrons*, can be grouped into two classes - high-energy electrons that can excite, dissociate, etc., and low-energy electrons that can be adsorbed and absorbed and possibly become so-called *solvated (solvated, aqueous) or hydrated* electrons. Here, too, the transport process is only poorly understood. In general, it is assumed that the solvated electrons are quickly neutralized at the surface by impinging ions. Apart from that, there are a large number of processes in which these electrons play a role. Their importance is largely dependent on the density of the absorbing particles (*scavengers*). In particular, in systems with a liquid electrode, the current of electrons into the surface can become significant.

7.7 Plasmas in Liquids

Due to their importance, we will take a closer look at the ignition directly in the liquid. In principle, a distinction must be made between two cases. In the first case, a gas bubble is formed by heating through the electric field, within which a discharge can then be ignited. This can be explained in principle with the already known streamer theories. For heating to occur, sufficient energy must be coupled over a sufficient period of time. Typical times here are μs. The situation is different if the electric field is only applied for a few nanoseconds. Here, no clear picture of the processes has yet been found, so we would like to present two possibilities here.

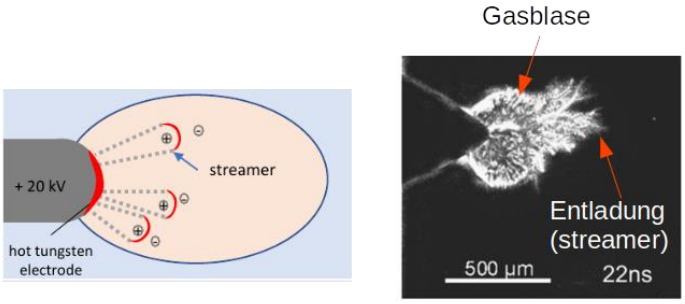

Figure 7.4: Ignition

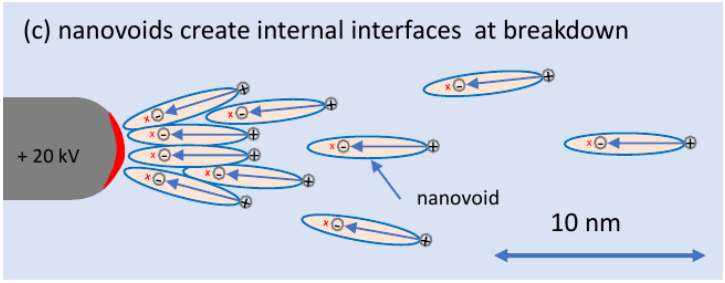

Figure 7.5: Cavitation

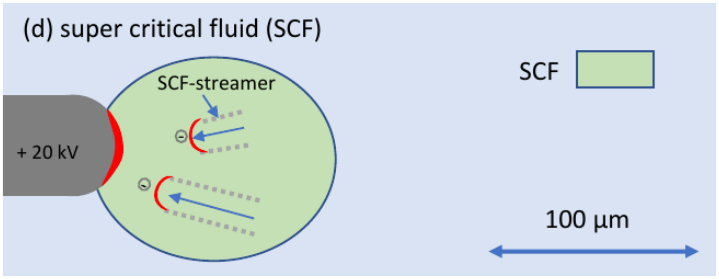

Figure 7.6: Supercritical

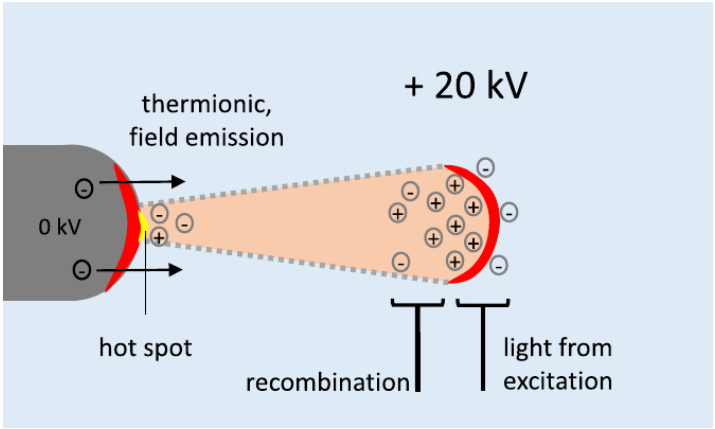

Figure 7.7: Streamer

Chapter 8

Thermal Plasmas

8.1 Plasma Equilibrium

In the case of thermal plasmas, one also speaks of an arc discharge. This term originates from the appearance of these plasmas. If two electrodes are brought horizontally close to each other, a very hot thermal plasma is ignited. The buoyancy causes this plasma to form in an arc between these two electrodes, hence the name.
In an arc discharge , the current density in a DC discharge has reached a value at which the heating of the electrodes leads to thermal emission of electrons. This means that a high voltage is no longer needed for electron multiplication in the gas phase, but the electrons are emitted directly from the cathode.

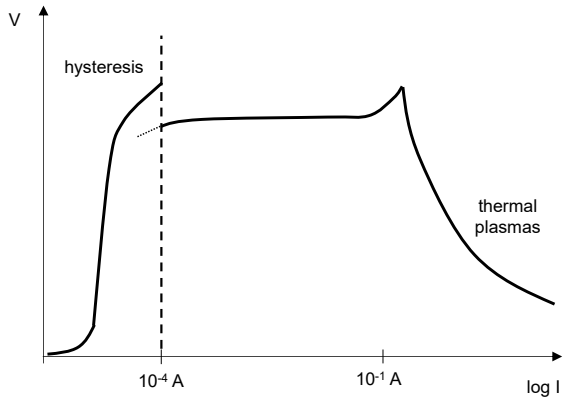

Figure 8.1: Characteristic curve up to the arc discharge

Thermal emission is described by the **Richardson Equation**:

$$j = AT^2 \exp\left[-\frac{e\Phi}{k_B T}\right] \tag{8.1}$$

Arc plasmas are usually operated at atmospheric pressure, and the high pressure implies a thermal equilibrium of the individual particle types, electrons, ions, and neutral gas.

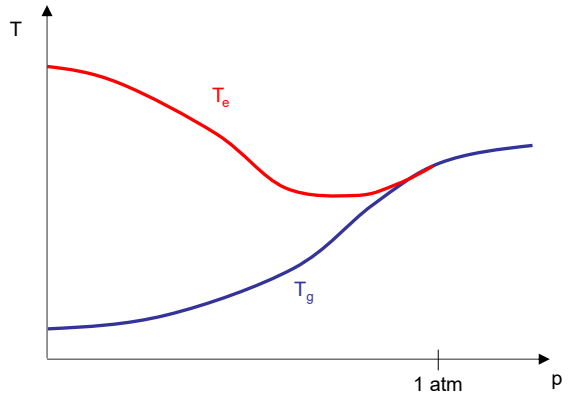

Figure 8.2: Equilibrium of neutral gas and electron temperature in an arc plasma

The stability of the arc is characterized by the MHD equilibrium, as sketched in Fig. 8.2.

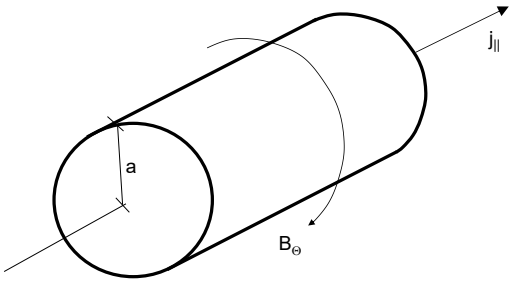

Figure 8.3: Equilibrium of a plasma arc

The current of the arc generates a magnetic field that, via $j \times B$ forces, confines the plasma. The magnetic field is given by:

$$B_\Theta = \frac{1}{2}\mu_0 j_| r \qquad r < a \tag{8.2}$$

$$B_\Theta = \frac{1}{2}\mu_0 j_| \frac{a^2}{r} \qquad r > a \tag{8.3}$$

and the MHD equilibrium as:

$$\vec{j} \times \vec{B} = \nabla p \tag{8.4}$$

Substituting Eq. 8.2, one obtains through integration for the pressure:

$$p(r) = \frac{1}{4}\mu_0 j_\parallel^2 (a^2 - r^2) \tag{8.5}$$

In the center of the arc, the following applies:

$$p(0) = p_0 = \frac{1}{4}\mu_0 j_\parallel^2 a^2 \tag{8.6}$$

The current flowing through the arc is $I = \pi a^2 j_\parallel$. Thus, one obtains:

$$p_0 = \frac{1}{4}\mu_0 \frac{I^2}{\pi^2 a^2} \tag{8.7}$$

This describes the pressure for a given expansion of the arc and impressed current. Often, the current in thermal plasmas of plasma technology is smaller than that required for the arc to be stabilized solely by MHD forces. Therefore, such an arc is stabilized by a gas flow, by a twisting of the magnetic field lines, by an external magnetic field, or by wall contact.
The arc attachment itself is usually smaller than the expansion of the arc. By localizing on the electrode surface, the current, and thus the temperature and the electron emission according to the Richardson equation, increase. A **Cathode Spot** is formed. This arc attachment creates a pressure gradient between the electrode and the plasma volume, driving the gas flow, the so-called **Electrode Jet**, as sketched in Fig. 8.4. The pressure difference is given by:

$$\Delta p = p_b - p_a = \frac{\mu_0 I^2}{4\pi^2}\left(\frac{1}{b^2} - \frac{1}{a^2}\right) \simeq \frac{\mu_0 I^2}{4\pi^2 b^2} \tag{8.8}$$

Using the Bernoulli equation, the pressure difference can be converted into an outflow velocity according to:

$$\Delta p = \frac{1}{2}\rho v_0^2 \tag{8.9}$$

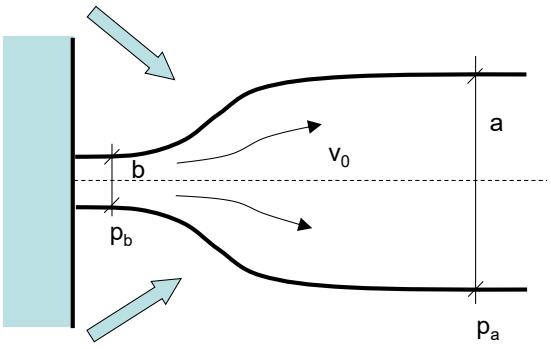

Figure 8.4: The pressure difference between the arc attachment point and the arc itself leads to a so-called electrode jet.

Thus, one obtains:

$$v_0 = \frac{I}{\pi b}\sqrt{\frac{\mu_0}{2\rho}} \tag{8.10}$$

This outflow velocity reaches up to 100 ms^{-1} and drives the gas mixing of the arc with the surrounding atmosphere (see Fig. 8.3).
These thermal plasmas tend to have strong fluctuations and instabilities, which must be suppressed by gas turbulence or magnetic stabilization. Moreover, the electrodes suffer from strong erosion at the arc attachment point. This is also attempted to be suppressed by moving the arc attachment point on the electrode through electrical forces.
In general, two designs are distinguished: the "transferred arc" and the "non-transferred arc". In the "transferred arc", the current flow is closed via the electrically conductive workpiece. The typical case is plasma welding. In a "non-transferred arc", the current flow is closed via an anode that surrounds a cathode. The gas flows through the gas gap and a plasma torch is formed. Here, the cooling of the anode is very important. Typical applications of these arcs are plasma spraying, where the workpiece itself should remain cold.

8.2 Applications of Thermal Plasmas

Plasma Cutting, Plasma Welding, Plasma 3D Printing

Thermal plasma arcs are used for **Plasma Cutting** and **Plasma Welding**. An arc is ignited between two coaxial electrodes, and the gas flowing through carries the flame onto the workpiece, which is either cut or welded depending on the power.
A modern variant of the application of plasma arcs is 3D printing. Here, welding spots are set by a robot that builds an object layer by layer. The pixel size is given by the diameter of a welding spot.

Arc Lamps

A traditional application of plasma arcs is so-called arc lamps. Here, an arc plasma is ignited between two graphite electrodes. These electrodes burn slightly, and their excitation produces a bright whitish emission. Another example is short arc lamps in projectors, where a Xe plasma serves as the light source.

Plasma Spraying, Spheroidization of Particles

Thermal plasmas are also used for material processing. One area is **Plasma Spraying**, where a powder is blown into the arc. The material melts during the flight from the injection point to the impact on the surface in the arc and then suddenly solidifies on the workpiece. These processes are used, for example, to produce ceramic coatings on turbine blades.
A variation of this method is the use of thermal plasmas for the spheroidization of particles. Here, irregularly shaped particles are blown in and only melted on the surface. Due to the surface tension, the particles become spherical and retain this shape upon rapid cooling. This makes the particles more free-flowing.

Thermal Treatment in Waste Disposal

Another possibility for material processing is the thermal decomposition of waste, where the material passes through the arc or the waste in a crucible is destroyed by the arc. This is particularly advantageous for highly hazardous substances that require a high temperature for decomposition (example: dioxins).

High-Temperature Synthesis, Ore Processing

Finally, thermal arcs are still used in the synthesis of new substances, as the arc has the advantage of being able to be used as a very homogeneous short-time reactor. Many non-equilibrium reactions require a limited reaction time to initiate a reaction, for example, from A $\rightarrow$ B, but to prevent further progression of the reaction B $\rightarrow$ C. Here, thermal plasmas can be very well controlled.
Another example would be the conversion of bauxite into aluminum using thermal plasmas or the reduction of iron ore in hydrogen plasmas.

Plasma Switches

A large area is also **Plasma Switches** used for switching large currents. In this application, it is important to prevent a plasma, as it leads to strong erosion of the electrodes when the switch is opened. For this purpose, the gas gap is filled with SF_6, which flows into the gap when the plasma switch is opened and efficiently extinguishes the resulting plasma, as fluorine, as a strongly electronegative gas, binds the free electrons.

Appendix A

Question Catalog

Introduction

- What possible classifications can you name for plasmas?
- How can the efficiency of energy coupling be assessed?
- How does the energy coupling depend on the excitation frequency?
- Give examples of high and low pressure discharges.

Collisions

- What do you use to describe collisions?
- Which collision processes are frequently considered in plasma physics?
- How do you describe transport in the fluid picture and the kinetic picture?

Ignition

- What distinguishes a self-sustained discharge from a non-self-sustained discharge?
- Which two processes work together in a Townsend discharge?
- What is not present in a Townsend discharge?
- What is the Townsend criterion?

- What does the Paschen curve describe in the DC case?
- What must be balanced to fulfill the requirements for RF discharges?
- Which physical effects determine the Paschen curve for the RF case?
- How does the drift influence the ignition field strength of an RF discharge?
- What is a streamer? What is a spark?
- How and why does a positive/negative streamer move?
- What does the Meek criterion state?

Plasma Boundary Layers

- How is an ion boundary layer structured?
- Which criterion must be fulfilled?
- How can it be fulfilled?
- What is the floating potential?
- What does the space charge region of an electronegative plasma look like?
- What influence does the geometry have on the potential distribution in a DC discharge?
- What distinguishes the Matrix/Child-Langmuir and the collision-dominated boundary layer?
- What does the energy distribution of ions hitting the wall look like?

Heating of a Plasma

- How does Ohmic heating change when transitioning to RF excitation?
- What must be fulfilled for the electrons in stochastic heating?
- Explain the energy gain in oscillating boundary layers?
- How can it be fulfilled?

- What is the initial idea behind plasma series resonance?
- Where does the nonlinearity of the boundary layer show in this picture?
- Which relationship describes the connection between wavenumber and frequency in the plasma?
- When do cut-offs and resonances occur? What do they mean for heating?
- Which quantities determine the energy transfer rate in wave heating?

Global Models

- What does a global model describe?
- Which balance equations determine the electron temperature and density in electropositive plasmas?
- How does the geometry influence the particle balance in the global model?
- What do typical approaches for ionization and dissociation look like in the global model?
- Which reactions must an electronegative plasma (e.g., in oxygen) at least contain?
- Why does the spatial distribution of species complicate the description of an electronegative plasma?
- How does the electron temperature behave when turning on a (pulsed) plasma?
- What does the turn-off behavior of a (pulsed) plasma depend on?

Low-Pressure Plasmas

- Describe the characteristic curve of a DC plasma.
- Describe the spatial structures of a DC plasma.
- What can be described using the j/p^2 law?
- What distinguishes α- and γ-mode?

- Describe the mechanism of thermal instability.
- What is the basic configuration of a hollow cathode discharge?
- How is a magnetron structured?
- What movements do the electrons perform in a magnetron discharge?
- What happens during target poisoning?
- How are current and voltage related in a capacitively coupled plasma (CCP)?
- What potential must the plasma assume in a CCP?
- What does the absorbed power in a CCP depend on? What consequences does this have, for example, for an application as an etching plasma?
- Can the voltage conditions at the electrodes of a CCP be influenced by the geometry?
- What is the DC self-bias in a CCP?
- Why is a matching network needed?
- When does the skin effect occur?
- How can the formation and consequences of standing waves in a CCP be reduced?
- What are the essential differences between a capacitively and an inductively (ICP) coupled RF plasma?
- How do E- and H-mode of an ICP differ?
- What determines the operating point of an ICP?
- Describe the EH hysteresis in ICP's.
- Describe the concept of a running discharge/surface plasma.
- Which conditions must be fulfilled for the stochastic heating of an Electron Cyclotron Resonance (ECR) plasma?
- What does the typical configuration of an ECR discharge look like?

Non-Thermal Atmospheric Pressure Plasmas

- Describe the ignition of a positive/negative corona.
- What does the concept of the dielectric barrier discharge (DBD) prevent?
- Describe the phases of a filamentary DBD discharge.
- Name application areas of the DBD.
- What are typical applications for other atmospheric pressure/low-pressure discharges?

Index